Structure, Organization and Dynamics of Functional Supramolecular Materials Studied by Solid-State NMR

Dissertation
Zur Erlangung des Grades
“Doktor des Naturwissenschaften”
im Promotionsfach Chemie

am Fachbereich Chemie, Pharmazie und Geowissenschaften
der Johannes Gutenberg-Universität Mainz

Ümit Akbey

Geboren in Çorum, Turkey

Mainz, (2008)

Tag der mündlichen Prüfung: 13.11.2008

Contents

Abstract:

Functional materials have great importance due to their many important applications. The characterization of supramolecular architectures which are held together by non-covalent interactions is of most importance to understand their properties. Solid-state NMR methods have recently been proven to be able to unravel such structure-property relations with the help of fast magic-angle spinning and advanced pulse sequences.

The aim of the current work is to understand the structure and dynamics of functional supramolecular materials which are potentially important for fuel-cell (proton conducting membrane materials) and solar-cell or plastic-electronic applications (photo-reactive aromatic materials). In particular, hydrogen-bonding networks, local proton mobility, molecular packing arrangements, and local dynamics will be studied by the use of advanced solid-state NMR methods.

The first class of materials studied in this work is proton conducting polymers which also form hydrogen-bonding network. Different materials, which are prepared for high ^{1}H conduction by different approaches are studied: PAA-P4VP, PVPA-ABPBI, Tz5Si, and Triazole-functional systems. The materials are examples of the following major groups;

- Homopolymers with specific functional groups (Triazole functional polysiloxanes).
- Acid-base polymer blends approach (PAA-P4VP, PVPA-ABPBI).
- Acid-base copolymer approach (Triazole-PVPA).
- Acid doped polymers (Triazole functional polymer doped with H_3PO_4).

Perylenebisimide (PBI) derivatives, a second type of important functional supramolecular materials with potent applications in plastic electronics, were also investigated by means of solid-state NMR. The preparation of conducting nanoscopic fibers based on the self-assembling functional units is an appealing aim as they may be incorporated in molecular electronic devices. In this category, perylene derivatives have attracted great attention due to their high charge carrier mobility. A detailed knowledge about their supramolecular structure and molecular dynamics is crucial for the understanding of their electronic properties. The aim is to understand the structure, dynamics and packing arrangements which lead to high electron conductivity in PBI derivatives.

To my family; Meliha, Duran and Murat...

Chapter 1:
Introduction

Since its discovery in 1946, Nuclear Magnetic Resonance (NMR) has become one of the most versatile spectroscopic techniques in terms of different types of systems and processes that can be investigated. With the variety of NMR active nuclei, NMR can provide information on the local structural properties and on different types of dynamic processes in a broad range of timescales (Schmidt-Rohr 94). Liquid-state NMR has been intensively used for the chemical characterization and been proved a very powerful technique (Ernst 87). For solid materials, solid-state NMR gains importance due to the current technical developments which make it possible to achieve high spectral resolution. With the help of fast magic angle spinning (MAS) (Andrew 58, Lowe 59) and advanced pulse sequences (Schnell 01a), one can extract a lot of information on supramolecular materials.

Functional supramolecular materials have great importance due to their many important applications. The characterization of supramolecular architectures which are held together by non-covalent interactions; i.e. electrostatic interactions, van der Waals forces, and hydrogen-bonding (Lehn 95) is of outmost importance to understand their properties. Solid-state NMR methods have recently been proven to be able to unravel such structure-property relations (Brown 01).

The aim of the current work is to understand the structure and dynamics of functional supramolecular materials which are potentially important for fuel-cell (proton conducting membrane materials) and solar-cell or plastic-electronic applications (photo-reactive aromatic materials). In particular, hydrogen-bonding networks, local proton mobility, molecular packing arrangements, and local dynamics will be studied by the use of advanced solid-state NMR methods.

Hydrogen bonding is one of the key interactions to be investigated in this work because it has an important role in many chemical and biological systems and many important phenomena develop with the help of it (Mingos 04). The motivating factor behind these studies is the structure stabilizing, or even structure-directing role of hydrogen bonds, which is as yet not fully understood, and represents one of the current frontiers of scientific research (de Greef 2008). Solid-state NMR has been used widely to understand the structure and dynamics of hydrogen bonded systems (Brown 2001, Schnell 2001a). Especially ^{1}H MAS NMR spectroscopy provides deep understanding on the hydrogen-bonding. In this work, different types of hydrogen bonded networks with different proton donor and acceptor groups will be identified which are formed from the pairs of O-H$\cdots$O, O-H$\cdots$N, N-H$\cdots$O, and N-H$\cdots$N in various proton conducting polymer systems.

The need for renewable energy sources makes fuel cells one of the pursuits as alternative energy sources. For such devices, one of the crucial components is the proton exchange membrane whose examples will be shown in the following chapters. Currently, the most commonly adapted polymer membrane electrolyte is the perfluorinated polymer Nafion®, a product of DuPont. In hydrated form, the membrane provides a high proton conductivity of about 0.19 S cm^{-1} (Yeo 83) at ambient pressures of 1 atm and at temperatures below 100 ° C. The high proton conductivity of Nafion membranes has allowed attainment of high power densities and efficiencies.

Since few membranes can retain sufficient water at temperatures above 120^{o}C for proton conduction (Yeo 83, Pourcelly 90), a new proton transport mechanism not depending on hydration and water diffusion is needed for membranes operating at high temperature. To meet this goal, several design concepts have been explored for the anhydrous proton-conducting polymeric electrolytes or membranes with fair conductivity at temperatures higher than 130 °C.

The first class of materials studied in this work is proton conducting polymers which also form hydrogen-bonding network. Different materials, which are prepared for high ^{1}H conduction by different approaches are studied: PAA-P4VP, PVPA-ABPBI, Tz5Si, and Triazole-functional systems. The materials are examples of the following major groups;

- Homopolymers with specific functional groups (Triazole functional polysiloxanes).
- Acid-base polymer blends approach (PAA-P4VP, PVPA-ABPBI).

- Acid-base copolymer approach (Triazole-PVPA).
- Acid doped polymers (Triazole functional polymer doped with H_3PO_4).

which are shown in Figure 1.1.

The study of the proton conducting polymers is targeted in general on the structural and dynamic factors governing proton conduction and hydrogen-bonding; (a) the understanding of the types of proton conducting mechanisms, (b) the acidity, or the degree of proton dissociation, (c) the effects of the local structures (e.g. hydrogen-bonding) and dynamics (e.g. local proton mobility).

Hydrogen bonding as well as proton conduction in polymeric materials can be studied by means of various spectroscopic techniques, e.g. IR spectroscopy (McQuade 97), X-Ray and neutron diffraction (Gebel 97, Serpico 02), impedance spectroscopy (Fontanella 93), and NMR spectroscopy (Hamilton 68, Becker 96). However, most of these techniques reflect only limited aspects of the proton conducting polymers, which are amorphous materials.

The proton conductivity monitored by impedance spectroscopy reflects the macroscopic conductivity which however, does not or only in rare cases coincides with the local proton mobility (Fontanella 93). Solid-state NMR in turn, is sensitive to the local chemical environment of the protons as well as to their local mobility (Traer 06, Ye 06, Goward 02). Especially solid-state ^{1}H MAS NMR under fast MAS conditions, $\nu_R \sim 30$ kHz, providing resolution of different proton sites in the systems helps to elucidate the local conduction mechanisms. Proton double-quantum NMR experiments supply information about spatial proximities and interactions of different proton sites as well as the nature of the hydrogen-bonding network. Moreover, variable temperature ^{1}H MAS NMR experiments help us to monitor the proton mobilities in different environments. With additional deuterium NMR studies after specific labeling with ^{2}H, more insight into the dynamics can be obtained with both static and magic-angle spinning experiments.

The first detailed solid-state MAS NMR study of proton conducting systems has been performed on imidazole-based materials by Goward et al. (Goward 02). This study proved that only the weakly hydrogen bonded sites in disordered areas of the material contribute to the proton conductivity, whereas strongly hydrogen bonded protons show only restricted local reorientations (Fischbach 04, Lee 07). Comparable studies by Hughes et. al. on H_3PO_4 doped poly(benzimidazole) derivatives confirmed the remarkable differences between macroscopic proton conductivity and the local mobility (Hughes 04). More recently the high-resolution solid-state MAS NMR study of poly(vinyl phosphonic acid) and its copolymers determined the mobility of P-OH groups and their crosslinking tendencies as well as the important role of disorder (Lee 07, Unugur 08).

Perylenebisimide (PBI) derivatives, a second type of important functional supramolecular materials with potent applications in plastic electronics, were investigated by means of solid-state NMR. The preparation of conducting nanoscopic fibers based on the self-assembling functional units is an appealing aim as they may be incorporated in molecular electronic devices. In this category, perylene derivatives have attracted great attention due to their high charge carrier mobility (Percec 02). A detailed knowledge about their supramolecular structure and molecular dynamics is crucial for the understanding of their electronic properties. The aim is to understand the structure, dynamics and packing arrangements which lead to high electron conductivity in PBI derivatives. Details on the properties of these materials will be given in chapter 7. ^{1}H MAS NMR, ^{1}H-^{1}H double quantum (DQ) NMR methods, and ^{1}H-^{13}C correlation experiments are powerful tools to investigate the structural and dynamics properties of similar semi-crystalline systems (Rapp 2003). These techniques combined with fast-MAS provide the spectral resolution needed to assign resonances and to obtain site specific structural and dynamics information to elucidate supramolecular systems with pronounced π-stacking effects.

In chapter 2, a theoretical description of the solid-state NMR techniques used in this thesis will be given in detail. After this general overview, the results of NMR experiments will be presented and discussed in chapter 3-7. The anhydrous proton conductor systems studied in this work will be presented in chapters 3-6. In chapter 7, the results on the structure and dynamics of the PBI derivatives will be presented. Finally, conclusions will be given in chapter 8.

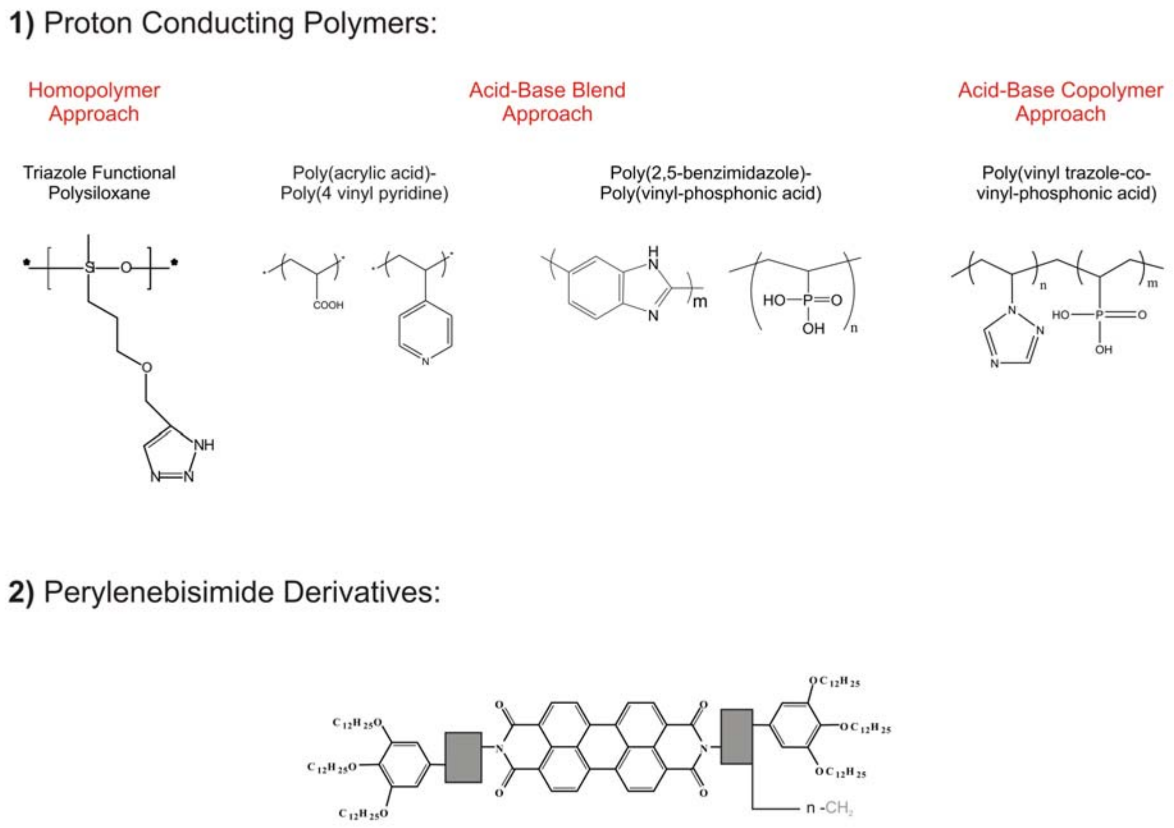

Figure 1.1: The schematic representation of the materials studied in this work. The chemical structures of different types of proton conducting polymers and photoconducting perylenebisimide derivatives are shown separately.

Chapter 2:
NMR Spectroscopy

The field of nuclear magnetic resonance (NMR) has grown rapidly after the pioneering experiments of F. Bloch and E. Purcell (Bloch 46, Purcell 46). There have been four Nobel prices awarded in the field of NMR since then. These prices went first in 1952 to Bloch and Purcell for their discovery of nuclear magnetic precision, then to R. Ernst in 1991 for his contributions to the development of the methodology of high resolution Fourier transform nuclear magnetic resonance (NMR) spectroscopy, in 2002 to K. Wuthrich for his development of nuclear magnetic resonance spectroscopy for determining the three-dimensional structure of biological macromolecules in solution and finally in 2003 to P. Lauterbur and P. Mansfield for their discoveries concerning magnetic resonance imaging techniques.

In the first issue of Journal of Magnetic Resonance 1969, editor Wallace S. Brey was stating, “At this point, we might ask: Is there any substantial body of new techniques or principles yet to be uncovered in magnetic resonance? Are there basically new instrumental methods to be invented, which will be described in these pages? It is obviously impossible to answer these questions …” From this time we have been witnessed many developments in this field and now NMR is a mature subject.

For a better understanding of the concepts discussed in the following chapters, in this section the basic nuclear spin interactions are summarized in a general and in a tensorial form. Detailed description can be found in the previously published text books (Abragam 61, Slichter 96, Mehring 83, Ernst 87, Schmidt-Rohr 94).

2.1 Nuclear Spin Interactions

The basic nuclear spin interactions can be divided into two general parts containing external fields, (e. g. spins interactions in the static magnetic field B_0 and the radiofrequency field B_1), and internal fields, e.g. chemical shift, dipolar coupling, quadrupolar coupling:

$$H = H_{ext} + H_{int}. \qquad \mathbf{1.1}$$

Where the interactions in the external fields are;

$$H_{ext} = H_Z + H_{rf}. \qquad \mathbf{1.2}$$

H_Z is the Zeeman interaction with B_0 and H_{rf} is the Zeeman interaction with B_1. The spin interactions with the internal fields depend on the properties of the nucleus studied, but generally it may be expressed as

$$H_{int} = H_{CS} + H_D + H_Q. \qquad \mathbf{1.3}$$

H_{cs} is the chemical shielding, H_D the dipolar and H_Q the quadrupolar interaction. There are in fact additional Hamiltonians as the one explaining J-coupling H_J, but this is usually negligible in this study because its effect is very small in solid state NMR.

The separation of external and internal interactions is useful because in the strong magnetic fields used today the magnitude of the external Hamiltonian is much larger than that of the internal Hamiltonian (*high-field* or s*ecular* approximation; $||H_0||>>||H_{int}||$ with the definition $||H|| = [Tr\{H^2\}]^{1/2}$). This secular approximation may be invalid when the investigated nucleus has a very strong quadrupolar coupling which is near or exceeding the Zeeman interaction. Within this work, this type of nucleus will not be studied (Antzutkin 99). All spin Hamiltonians mentioned above can be represented in a general form most conveniently in terms of second rank tensors, because of the orientation dependence of the interactions (Abragam 61, Slichter 78 and Mehring 83):

$$H = \mathbf{I}\bullet\mathbf{A}\bullet\mathbf{S} = \left(I_x, I_y, I_z\right)\begin{pmatrix} A_{xx} & A_{xy} & A_{xz} \\ A_{yx} & A_{yy} & A_{yz} \\ A_{zx} & A_{zy} & A_{zz} \end{pmatrix}\begin{pmatrix} S_x \\ S_y \\ S_z \end{pmatrix} \qquad \mathbf{1.4}$$

where I and S are vector operators and $\underline{\underline{\mathbf{A}}}$ is second-rank Cartesian coupling tensor. $\underline{\underline{\mathbf{A}}}$ can be broken up into three irreducible Cartesian tensors of rank 0, 1 and 2 (Haeberlen 76, Smith 92).

$$\underline{\underline{\mathbf{A}}} = \begin{pmatrix} A_{xx} & A_{xy} & A_{xz} \\ A_{yx} & A_{yy} & A_{yz} \\ A_{zx} & A_{zy} & A_{zz} \end{pmatrix} = A_{iso} \underbrace{\begin{pmatrix} 1 & 0 & 0 \\ 0 & 1 & 0 \\ 0 & 0 & 1 \end{pmatrix}}_{\textbf{rank 0}} + \underbrace{\begin{pmatrix} 0 & \alpha_{xy} & \alpha_{xz} \\ \alpha_{yx} & 0 & \alpha_{yz} \\ \alpha_{zx} & \alpha_{zy} & 0 \end{pmatrix}}_{\textbf{rank 1}} + \underbrace{\begin{pmatrix} \delta_{xx} & \delta_{xy} & \delta_{xz} \\ \delta_{yx} & \delta_{yy} & \delta_{yz} \\ \delta_{zx} & \delta_{zy} & \delta_{zz} \end{pmatrix}}_{\textbf{rank 2}} \qquad \textbf{1.5}$$

The specific components are as follows where u and v sum over the three axes chosen.

$$\begin{aligned} A_{iso} &= (1/3)(A_{xx} + A_{yy} + A_{zz}) = (1/3)\mathrm{Tr}\{\underline{\underline{\mathbf{A}}}\} \\ \alpha_{\mathrm{uv}} &= ½\,(A_{uv} - A_{vu}) \\ \delta_{\mathrm{uv}} &= ½\,(A_{uv} + A_{vu} - 2A_{iso}) \end{aligned} \qquad \textbf{1.6}$$

The first component in equation 1.5 is the isotropic part A_{iso}, which is equal to the one third of the trace of the Cartesian tensor. The matrix following A_{iso} is rank 0, thus a scalar. The rank 1 component is antisymmetric and contains three distinct components. The rank 2 component is symmetric and traceless, so it contains five distinct components. The elements of the tensors depend on the coordinate system used but this will not be discussed here in detail (Smith 92).

2.1.1 Zeeman Interaction

The coupling of the spin I with the external static magnetic field $B_0 = (B_x, B_y, B_z)$ which splits the degenerate energy levels into (2I+1) energy levels is called Zeeman interaction. It can be expressed as (in frequency units):

$$\mathrm{H}_Z = \mathbf{I}\bullet\mathbf{Z}\bullet\mathbf{B_0} = -\gamma_I \mathbf{I}\bullet\mathbf{B_0} = -\gamma_I I_z B_0 = \omega_0 I_z \qquad \textbf{1.7}$$

where $\omega_0 = \gamma_I B_0$ is the *Larmor frequency*. Usually the Zeeman interaction exceeds all internal interaction which leads to a simplified Hamiltonian after the secular approximation. For a nucleus in a B_0 filed greater than 1 Tesla, the dominant contribution to the spin Hamiltonian H is the Zeeman interaction (Schmidt-Rohr 94).

2.1.2 Chemical Shift

The chemical shift results from the shielding of the external magnetic field B_0 by the electrons surrounding the nucleus. The local field at the position of the nucleus is described by $\underline{\mathbf{B}_{loc}} = \underline{\mathbf{B}_0} - \underline{\underline{\sigma}} \bullet \underline{\mathbf{B}_0}$. This feature has a lot of applications since it depends on the electronic environment of the nucleus. Change in the chemical shift for different molecules supplies important information on the chemical structure. In general the charge distribution is not spherically symmetric, thus the chemical shift is anisotropic. This means that the chemical shift depends on the orientation of the molecule with respect to the magnetic field. With a magnetic field in the z direction only the σ_{zz} component leads to a secular contribution which is a first-order frequency shift. Within this approximation, the shielding Hamiltonian of the spin I is the coupling of the spin with the magnetic field B_0 with the shielding tensor $\underline{\underline{\sigma}}$:

$$\mathrm{H}_{\mathrm{CS}} = \gamma \underline{\mathbf{I}} \bullet \underline{\underline{\sigma}} \bullet \underline{\mathbf{B_0}} = \gamma I_z \sigma_{zz} \underline{\mathbf{B_0}} = -\omega_0 I_z \sigma_{zz} = \omega_{CS} I_z \qquad \mathbf{1.8}$$

where, γ is the magnetogyric ratio of the spin and I_z is the z component of the spin operator $\underline{\mathbf{I}}$. The chemical shielding tensor is no longer a unit matrix which is the case for Zeeman interaction. Because the coupling is established with the electronic surrounding, the careful investigation of the shielding tensor can give information about the electronic states and thus the chemical structure.

Usually, the trace of the chemical shift tensor is not zero and not symmetric. However this tensor can be separated into isotropic, antisymmetric and symmetric parts as:

$$\underline{\underline{\sigma}} = \gamma_1 \begin{pmatrix} \sigma_{xx} & \sigma_{xy} & \sigma_{xz} \\ \sigma_{yx} & \sigma_{yy} & \sigma_{yz} \\ \sigma_{zx} & \sigma_{zy} & \sigma_{zz} \end{pmatrix} = \underbrace{\sigma_{iso} \begin{pmatrix} 1 & 0 & 0 \\ 0 & 1 & 0 \\ 0 & 0 & 1 \end{pmatrix}}_{\textbf{rank 0}} + \underbrace{\begin{pmatrix} 0 & \alpha_{xy} & \alpha_{xz} \\ -\alpha_{xy} & 0 & \alpha_{yz} \\ -\alpha_{xz} & -\alpha_{yz} & 0 \end{pmatrix}}_{\textbf{rank 1}} + \underbrace{\begin{pmatrix} \delta_{xx} & \delta_{xy} & \delta_{xz} \\ \delta_{yx} & \delta_{yy} & \delta_{yz} \\ \delta_{zx} & \delta_{zy} & \delta_{zz} \end{pmatrix}}_{\textbf{rank 2}} \qquad \mathbf{1.9}$$

The rank 0 tensor is scalar, rank 1 tensor is zero because of symmetry reasons (Vold 1979) and rank 2 tensor is both traceless and symmetric. By changing to the principal axis system of the chemical shift tensor, the internal coordinate system in which $\underline{\underline{\sigma}}$ is diagonal, rank 1 component will usually also become zero (Hafner 98).

$$\underline{\underline{\sigma}} = \sigma_{iso} + \delta_{CS}\begin{pmatrix} -\frac{1+\eta_{CS}}{2} & 0 & 0 \\ 0 & -\frac{1-\eta_{CS}}{2} & 0 \\ 0 & 0 & 1 \end{pmatrix} \qquad \mathbf{1.10}$$

in which the anisotropy parameter δ_{CS} and asymmetry parameter η_{CS} are as follows:

$$\delta_{CS} = \omega_L(\sigma_{zz}^{PAS} - \sigma_{iso}) \text{ and } \eta_{CS} = \frac{\sigma_{yy}^{PAS} - \sigma_{xx}^{PAS}}{\sigma_{zz}^{PAS} - \sigma_{iso}} \qquad \mathbf{1.11}$$

It is useful to write the chemical shift tensor in terms of chemical shift anisotropy (CSA), which is the symmetric part of the tensor. Fast isotropic motions, as found in liquids and solutions, averages this anisotropy to zero, however in solids where this motion is absent, the CSA depends on the orientation and leads to broad resonances. Orientation dependent frequency of a spin is given by

$$\sigma_{zz}(\theta,\phi) = \sigma_{iso} + \frac{\delta_{CS}}{2}(3\cos^2\theta - 1 - \eta_{CS}\sin^2\theta\cos\ 2\phi) \qquad \mathbf{1.12}$$

where θ and ϕ are polar coordinates in the principal-axes system of $\underline{\underline{\tilde{\sigma}}}$. For a molecule with axial symmetry (η=0) the last term in 1.12 vanishes and the value depends only on the θ angle (between “z axes of principal-axes frame” and “B_0 direction in the laboratory frame”). In a powder sample where all angles are possible, the powder-average can be calculated which results in a powder lineshape from which the principal-axes values can be determined. In the case of more than a single site, the powder lineshapes may overlap and the assignment becomes difficult. In Figure 2.1, the characeristic lineshapes (calculated by Bloembergen 53) for symmetric and asymmetric tensors can be seen. The principle values of the CSA can be identified from the line shape. A convention for the line shape analysis (Spiess 78, Haeberlen 76, and Schmidt-Rohr 94) requires $|\sigma_{xx}| \le |\sigma_{yy}| \le |\sigma_{zz}|$. This results in $0 \le \eta \le 1$, and for $\eta = 0$ this conventions always identifies the unique principal axis as z-axis.

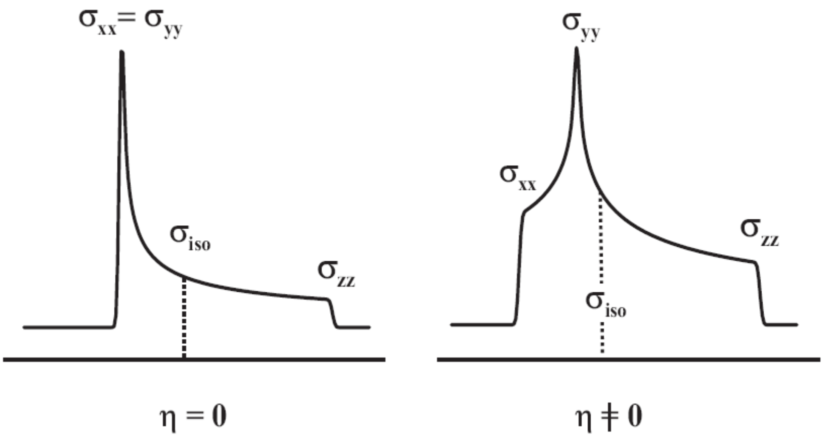

b)

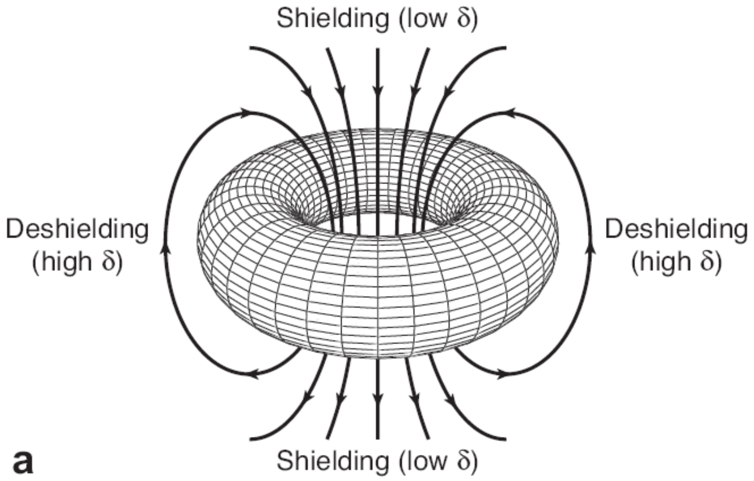

c)

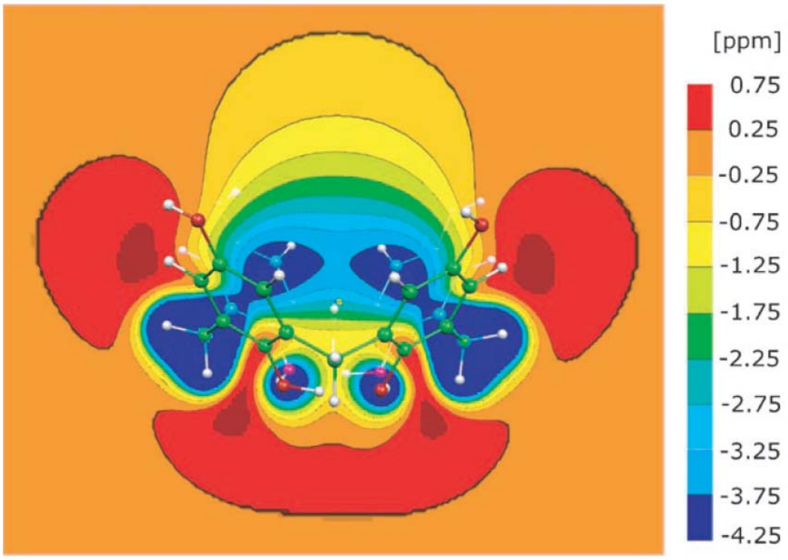

Figure 2.1: a) Theoretical lineshapes for isotropic samples for a symmetric (left) and asymmetric (right) CSA tensor. Principle values are also shown. **b)** Representation of the ring currents observed in aromatic systems (from Parkinson 07). **c)** The NICS map of an isolated calixhydroquinone (from Sebastiani 05).

There is a strong influence of the surrounding of a nucleus on its chemical shift value. Usual chemical shift ranges of ~10-15 ppm for ^{1}H and ~200 ppm for ^{13}C are observed. When a nucleus is nearby to a strong electronegative atom (O, Cl …), an increased field is experienced by the nucleus which results in an observation of increased chemical shift, σ. In particular, in hydrogen-bonded systems this kind of shifted proton chemical shift values can be observed commonly.

In addition to the hydrogen-bonding, π-packing has also significant influence on the observed chemical shift values. The ring currents of aromatic systems induce additional magnetic fields, which cause chemical shift alteration even if the influenced atom is not chemically bonded. When a nucleus is close to the axis of symmetry of an aromatic ring passing from the center of the ring, the local field experienced by that nucleus is decreased which causes observation of lower chemical shift values (shielded). However, a nucleus close to the plane of the aromatic ring experiences an increased field which causes observation of higher chemical shift values (deshielded). This effect can give valuable information on the molecular packing, examples will be shown later.

It is possible and popular these days to calculate the chemical shifts by ab-initio quantum chemical calculations. With an optimization of the molecular geometry of a particular system, the information about the electronic structure is also known. After this procedure, chemical shifts can be calculated in a conventional way or in a nucleus independent chemical shift (NICS) maps manner for each atom in space (Schleyer 96, Sebastiani 05). Without a need to specific the effected nucleus, a quantitative degree of shielding and deshielding is represented in the NICS maps, shown in Figure 2.1c.

2.1.3 Dipolar Coupling

The interaction of two spins, I and S, through space is known as a direct or dipolar coupling. This interaction has a $1/r^{3}$ dependence on the distance and linear dependence on the γ values of spins. The Hamiltonian of the dipolar coupling is

$$\mathrm{H}_{D} = \underline{\mathbf{I}} \bullet \underline{\underline{\mathbf{D}}}_{IS} \bullet \underline{\mathbf{S}} \qquad \mathbf{1.13}$$

The Hamiltonians can be expanded into the *dipolar alphabet* (Abragam 61) as

$$\begin{aligned}
\mathrm{A} &= (1\text{-}3\cos^2\theta)\, I_z S_z \\
\mathrm{B} &= \frac{1}{2}(1\text{-}3\cos^2\theta)\,(I_z S_z - \mathbf{I}\bullet\mathbf{S}) \\
\mathrm{C} &= -\frac{3}{2}\sin\theta\cos\theta e^{-i\phi}(I_z S_+ + I_+ S_z) \\
\mathrm{D} = \mathrm{C}^* &= -\frac{3}{2}\sin\theta\cos\theta e^{i\phi}(I_z S_- + I_- S_z) \\
\mathrm{E} &= -\frac{3}{4}\sin^2\theta e^{-i2\phi} I_+ S_+ \\
\mathrm{F} = \mathrm{E}^* &= -\frac{3}{4}\sin^2\theta e^{i2\phi} I_- S_-
\end{aligned} \qquad \mathbf{1.14}$$

$$\mathrm{H}_D = D\,[\mathrm{A+B+C+D+E+F}] \qquad \mathbf{1.15}$$

D is given below. Only the A and B terms contribute to the NMR spectrum from the fundamental secular commutator $[\mathrm{H}_Z, \mathrm{H}_{D,\sec}] = 0$, C-F are non-commuting terms and cancelled out.

$$\underline{\underline{\mathbf{D}}} = -2D \bullet \begin{pmatrix} -\frac{1}{2} & 0 & 0 \\ 0 & -\frac{1}{2} & 0 \\ 0 & 0 & 1 \end{pmatrix} \qquad \mathbf{1.16}$$

where

$$D = -\frac{\mu_0 \gamma_I \gamma_S \hbar}{4\pi r_{IS}^3} \qquad \mathbf{1.17}$$

In the case of homonuclear dipolar interaction in the PAS, the tensor D is axially symmetric and $Tr\{\mathbf{D}\} = 0$ within the secular approximation.

$$\begin{aligned}
\mathrm{H}_{D,\mathrm{homo}} &= -\frac{\mu_0 \gamma_1 \gamma_2 \hbar}{4\pi r_{IS}^3}\frac{1}{2}(1\text{-}3\cos^2\theta)(3 I_z^i I_z^j \text{-} \underline{\mathbf{I}}^i \bullet \underline{\mathbf{I}}^j) \\
\mathrm{H}_{D,\mathrm{hetero}} &= -\frac{\mu_0 \gamma_1 \gamma_2 \hbar}{4\pi r_{IS}^3}\frac{1}{2}(1\text{-}3\cos^2\theta)\, 2 I_z S_z
\end{aligned} \qquad \mathbf{1.18}$$

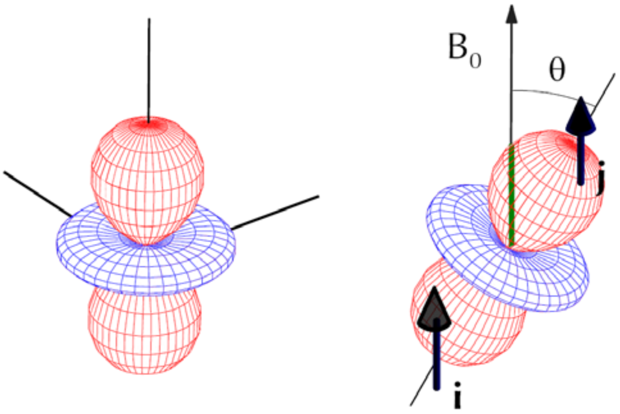

Figure 2.2: Angular dependency of the tensor of dipolar interaction $\underline{\underline{\mathbf{D}}}$.

The spin part of the dipolar Hamiltonian contains a static term (I_zS_z) and a flip-flop (exchange) term. In the homonuclear case, both exist and in the heteronuclear case, only the static-term exists. The static-term describes the interaction of a spin with the dipolar field of the other spin. Depending on the orientation of the second spin two energy levels can arise which lead to a doublet splitting. The exchange-term couples states differing only in polarization and if the energy difference is small, the dipolar field of one spin can flip the magnetic moment of the second spin and both spins change their sign of their states without change of the overall energy. In the heteronuclear case, the difference between the Larmor frequencies can be several orders of magnitude larger than the dipolar coupling so that the Hamiltonian is further truncated by cancellation of the exchange-term (*second averaging*).

2.1.4 Quadrupolar Coupling

Nuclei having spin $I \geq 1$ posses an electric quadrupolar moment Q and are called quadrupolar nuclei. They interact with the electric field gradient V at the place of the nucleus. The Hamiltonian for the quadrupolar interaction is written

$$\mathrm{H}_Q = \underline{\mathbf{I}} \bullet \underline{\underline{\mathbf{Q}}} \bullet \underline{\mathbf{I}} \qquad \mathbf{1.19}$$

and using the quadrupolar interaction tensor, $\underline{\underline{\mathbf{Q}}}$ given by:

$$\underline{\underline{\mathbf{Q}}} = \frac{eQ}{2I(2I-1)\hbar} \cdot \underline{\underline{\mathbf{V}}} \qquad \mathbf{1.20}$$

in which e is the elementary charge, Q is the quadrupolar moment. The electric field gradient tensor $\underline{\underline{\mathbf{V}}}$ has the cartesian component

$$(\mathbf{V})_{\alpha\beta} = \frac{\partial^2 \Phi}{\partial\alpha\partial\beta} \qquad \mathbf{1.21}$$

where α, β are the x, y, z and Φ is the electric potential.

The quadrupolar interaction is an anisotropic interaction in which the electric field gradient EFG tensor has a PAS like the chemical shift tensor whose trace is zero so has no isotropic component. $\underline{\underline{\mathbf{Q}}}$ can also be represented in PAS as

$$\underline{\underline{\mathbf{Q}}} = \delta_Q \cdot \begin{pmatrix} -\frac{1+\eta_Q}{2} & 0 & 0 \\ 0 & -\frac{1-\eta_Q}{2} & 0 \\ 0 & 0 & 1 \end{pmatrix} \qquad \mathbf{1.22}$$

In equation 1.22 δ_Q is the anisotropy and η_Q is the asymmetry of the interaction ($0<\eta_Q<1$) and δ_Q is given by

$$\delta_Q = \frac{e^2 qQ}{2I(2I-1)\hbar} \qquad \mathbf{1.23}$$

The first-order quadrupolar Hamiltonian can be written with the orientation dependence term as

$$\mathrm{H}_Q = \frac{e^2 qQ}{2I(2I-1)\hbar} \cdot \frac{1}{2}(1\text{-}3\cos^2\theta + \eta_Q \sin^2\theta \cos 2\theta) \cdot (3\mathbf{I}_\mathbf{z} \bullet \mathbf{I}_\mathbf{z} \text{-} \mathbf{I} \bullet \mathbf{I}) \qquad \mathbf{1.24}$$

The only quadrupolar nucleus investigated in this thesis is the deuteron which has spin I = 1. The quadrupolar splitting is around 130 kHz, which is smaller than the Zeeman interaction but stronger than the chemical shift interaction. In solids, the quadrupolar coupling leads to typical lineshape, the Pake-pattern (Pake 48) as shown in Figure 2.3. In the presence of molecular motion changes in line shape are observed and with a careful analysis the geometry and timescale of the motion can be obtained (Spiess 85).

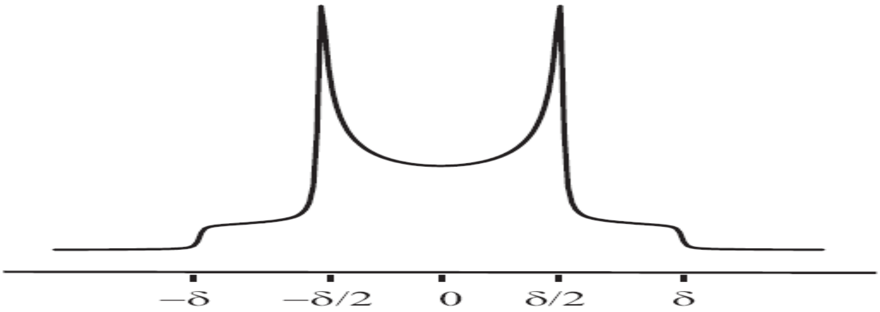

Figure 2.3: Pake-pattern of static deuterium sample.

2.2 Spherical Representation of Interaction Tensors

So far, the interaction tensors have been represented in terms of Cartesian tensors. For spherical applications it is more convenient to represent them as irreducible spherical tensors. The need for this new representation will be understood when dealing with the rotations commonly used in the description of most solid-state NMR experiments, like sample rotation or application of RF pulses.

It is advantageous to divide the Hamiltonians into a space part A and a spin part T as $\mathrm{H} = A \cdot T$. Transformations from PAS frame to LAB frame (z-axes is parallel to B_0) are needed sometimes because all interactions are defined in their PAS frame and the reference frame is given by the LAB frame. It is possible to do rotation transformations in Cartesian notation but it is much more convenient to perform it in spherical representation. In the spherical representation the space part and the spin part are split into three irreducible parts, as the interactions are at maximum second rank tensor,

$$A = A_0 + A_1 + A_2$$

1.25

$$T = T_0 + T_1 + T_2$$

in which; A_0, T_0 are scalar, A_1, T_1 antisymmetric and A_2, T_2 are symmetric (Smith 92). Each A_L term is composed of 2L+1 components $A_{L,M}$ which have the same properties of spherical harmonics in terms of transformations (Rose 57). The Hamiltonian can be written as follows

$$\mathrm{H} = \sum_{k=0}^{2} \sum_{q=-k}^{+k} (-1)^q A_{kq} T_{k-q} \qquad \textbf{1.26}$$

When equation 1.26 is written down explicitly, nine terms appear and also from equation 1.4 nine terms will be obtained. The advantage in using the spherical tensor description is that they can easily be arranged according to their rotational symmetries and easily handled while rotations.

In the case of dipolar interaction, because $Tr\{D_{\alpha\beta}\} = 0$ and $D_{\alpha\beta} = D_{\beta\alpha}$ (symmetric), A_{00} and A_{1q} terms vanish leaving only the terms k=2. In the case of quadrupolar interaction, again only the k=2 terms contribute. However, in the case of chemical shielding, which has a non-vanishing trace and antisymmetric components, A_{00} and A_{1q} terms have to be considered (Smith 92).

In dipolar and quadrupolar interactions the Hamiltonians can be expressed by $A_{2,0}$ and $T_{2,0}$ only, because of the absence of isotropic and antisymmetric part. The first-order secular approach reduces the order to m=0 because

$$[I_z, A_{2,m}] = mA_{2,m} \qquad \textbf{1.27}$$

In spherical tensor representation, using of the property stated in equation 1.27, the secular part of the internal interaction becomes

$$\mathrm{H}_{\mathrm{int}} = A_{00}T_{00} + A_{10}T_{10} + A_{20}T_{20} \qquad \textbf{1.28}$$

All the other terms in equation 1.26 vanish because they do not commute with B_0.

2.3 Density Matrix Representation

In quantum mechanics the system is described in terms of wave functions. It is more convenient to describe the system in terms of a density operator $\widehat{\rho}(t)$ (Sakurai 85). By using the density operator notation, a combination of quantum mechanics and statistical mechanics is obtained and this gives a more complete picture.

In thermal equilibrium at a temperature T and with a Hamiltonian H, the density operator is

$$\widehat{\rho}_{eq} = \frac{1}{Z} e^{-\mathrm{H}/kT} \qquad \textbf{1.29}$$

where $Z = Tr(e^{-\mathrm{H}/kT})$. In the high temperature approximation (T > 1 K), after a series expansion for $\frac{1}{T}$ and taking only the linear terms into account, $\widehat{\rho}_{eq}$ can be described by

$$\widehat{\rho}_{eq} \sim (\hat{\mathbf{1}} + \frac{\hbar \lambda B_0}{kT} I_z) \qquad \textbf{1.30}$$

in which the unity operator commutes with all operators and is thus irrelevant in most cases. Physical observables of operators are obtained from the density operator by taking the trace

$$\langle \widehat{A} \rangle = Tr(\rho\mathbf{A}) = \sum_i (\rho\mathbf{A})_{ii} = \sum_i \sum_j \rho_{ij} A_{ji} \qquad \mathbf{1.31}$$

The time evolution of the density matrix is described by the Liouville-von-Neumann equation as

$$\frac{d}{dx}\widehat{\rho} = -i[\mathrm{H}, \widehat{\rho}] \qquad \mathbf{1.32}$$

from which a formal solution for a time-independent Hamiltonian is given by:

$$\widehat{\rho}(t) = e^{-i\mathrm{H}t}\,\widehat{\rho}(0)e^{i\mathrm{H}t} \qquad \mathbf{1.33}$$

The operator which pushes the operator ahead in time is $\widehat{U}(t) = e^{-i\mathrm{H}t}$, is called propagator. The initial state of $\widehat{\rho}(0)$ is taken from equation 1.30 (Abragam 61).

2.4 Effect of Radio-Frequency (rf) Pulses

Radio-frequency pulses play an important role in pulsed NMR. The rf field which is used in NMR is perpendicular to B_0 field,

$$B_1\,(t) = 2B_1.\cos(\omega_{rf}t + \phi) \qquad \mathbf{1.34}$$

According to

$$\cos(\omega_{rf}t + \phi) = \frac{1}{2}e^{i\omega_{rf}t+\phi} + \frac{1}{2}e^{-i\omega_{rf}t+\phi} \qquad \mathbf{1.35}$$

the harmonic oscillation can be decomposed into two rotating fields with angular frequencies of $+\omega_{rf}$ and -ω_{rf}. The negative one can be neglected because the magnetization is only influenced by fields rotating with frequencies close to Larmor frequency ω_L. In order to make the B_1 field appear static, a transformation into the rotating frame is needed.

In the rotating frame, the actual field acting on the magnetization is the vector sum of two different components. The first is the B_1 field and the second is the remainder of the B_0

field which has not been removed by transforming into the rotating frame because of off-resonance effects. Nevertheless, the off-resonance field can be neglected since B1 is large compared to $\omega_L - \omega_{rf}$.

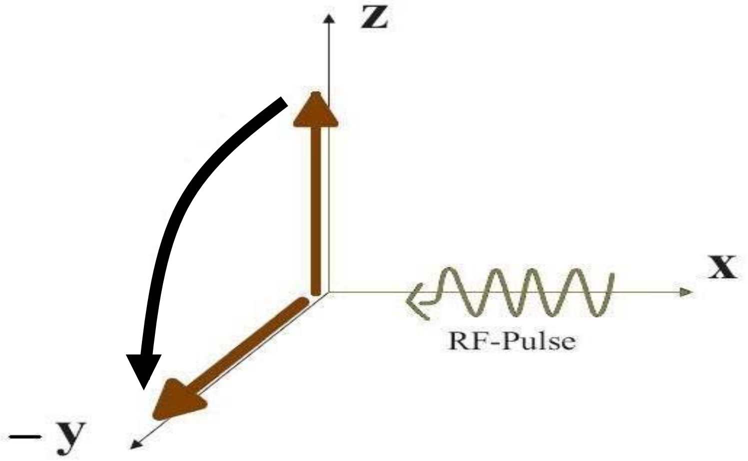

Figure 2.4: The effect of 90° x-pulse to the state initially on z direction. The direction of rotation is stated with the right-hand-rule always.

The effect of a pulse is rotation around an axes in the xy-plane, depending on the phase of the pulse. The pulse may be applied in "+" or "-" direction, which represents the phase of the pulse. The rotation direction is by convention used throughout this thesis given by the "right hand rule": the thumb is pointing at the direction of the RF-pulse and the index finger is pointing at the direction of the initial magnetization, the middle finger points at the direction of the magnetization after the pulse. The effect of the pulse length t, is a rotation of the z-magnetization to xy plane by an angle $\alpha = \omega_1(t)t = -\gamma B_1(t)t$. More interestingly a 90 degree pulse corresponds to

$$\frac{\pi}{2} = \gamma B_1 t_{pulse} \qquad \textbf{1.36}$$

The effect of pulses is usually calculated with the help of the density matrix representation.

With the Hamiltonian operator of a +x pulse given by $\mathrm{H} \sim I_x(\alpha)$, the propagator is $\widehat{U} = e^{-i\alpha \hat{I}_x}$. The equilibrium density matrix ($\widehat{\rho}_{eq} \sim I_z$) evolves during the x-pulse is as

$$\rho(t) \approx e^{-i\alpha I_x} I_z e^{i\alpha I_x} \qquad \textbf{1.37}$$

which describes a rotation in the spin part. By using the formalism introduced by Ernst and co-workers (Sorensen 83) called "product operator formalism" in which the rotations in spin space are described by the propagator of $\widehat{U}(t)\hat{\boldsymbol{\rho}}(0)\widehat{U}^{-1}(t)$, it will be easier to continue in a sequence of pulses.

The effect of rotation of z-magnetization by an x-pulse is as follows

$$\hat{I}_z \xrightarrow{\alpha \hat{I}_x} \hat{I}_z \cos\alpha - \hat{I}_y \sin\alpha \qquad \mathbf{1.38}$$

2.5 Magic Angle Spinning (MAS)

In the solid phase a nuclear spin experiences a great number of interactions as stated in equation 1.3. The main three interactions that we will encounter mostly in this work (dipolar, chemical shift anisotropy, quadrupolar) often lead to very broad and featureless lines, because they are anisotropic and depend on the crystalline orientation. In liquids, e.g. a solution of an organic compound, most of these interactions will average out because of the rapid isotropic molecular motion that occurs. In the solid-state these interactions can be averaged by manipulating the spin part (with rf pulses) or space part (with specimen rotation). The manipulation of the space part can be done by applying magic angle spinning, which mimics to some extend the orientational averaging in solution. In this way, the anisotropic interactions described by the second Legendre polynomial are averaged out by rotating the sample at an angle of 54.7° with respect to the magnetic field. Complete averaging of the anisotropic interaction to zero is achieved only when the sample is spun with a spinning speed much greater than the characteristic frequency of interaction, i.e. $\omega_r \gg \omega_\lambda$.

The theoretical description of MAS conveniently can be done by using the spherical tensor representation is given in equation 1.26 and 1.28. The antisymmetric part A_{10} can be neglected because it does not contribute in first order (Mehring 83) and the isotropic part $A_{00} = -\frac{1}{\sqrt{3}} Tr\{A_{ij}\}$ is invariant under motion, so that only the A_{20} term needs to be calculated. More detailed descriptions of MAS are available in the book of Mehring (Mehring 83) and other literature (Maricq 79). For the moment, the following description will be given. For special interactions like chemical shift anisotropy, dipolar coupling, and quadrupolar coupling $\widehat{T}_{10} A_{10} = 0$, and the interaction Hamiltonian reduced to

$$\widehat{\mathrm{H}}_\lambda = \widehat{T}_{00} A_{00}^{\lambda} + \widehat{T}_{20} A_{20}^{\lambda} \qquad \mathbf{1.39}$$

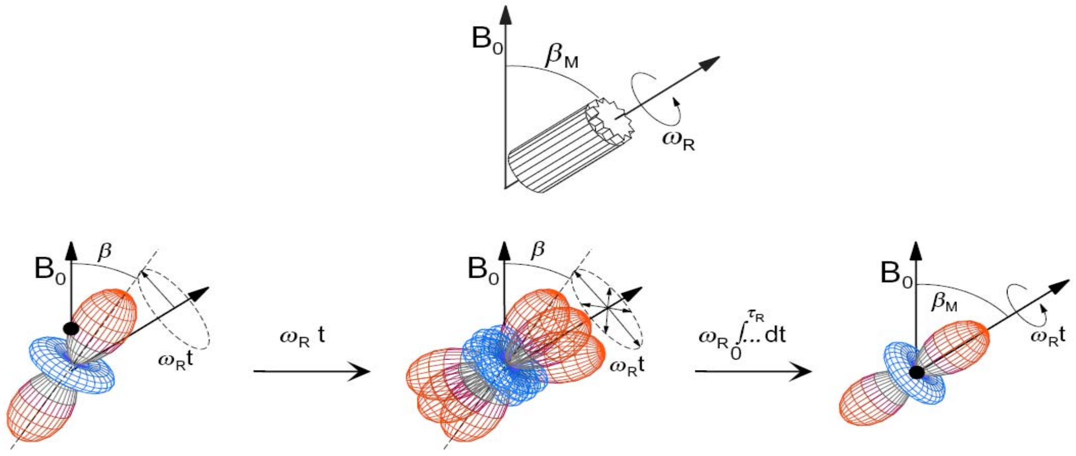

Figure 2.5: Averaging of NMR interactions by MAS.

Time dependence is introduced to the space part of the interaction Hamiltonian with MAS. So equation 1.33 is no longer a solution of the Liouville-von-Neumann equation (equation 1.32). Nevertheless, still average Hamiltonian theory can be used to calculate an average time-independent Hamiltonian when the problem is cyclic, which is the case for MAS. Cycle time t_c for MAS is a rotor period, τ_r. The average Hamiltonian ($\overline{H}$) for a single rotor period is determined by

$$\widehat{U}(t_c) = e^{-i\widehat{H}_n\tau_n}\dots e^{-i\widehat{H}_2\tau_2}e^{-i\widehat{H}_1\tau_1} = e^{-i\widehat{\overline{H}}_r\tau_r} \qquad \textbf{1.40}$$

$\widehat{U}$ is called the propagator. Since the average Hamiltonian is time-independent, it commutes with itself at arbitrary times, $[\widehat{\overline{H}}(t_1), \widehat{\overline{H}}(t_2)] = 0$, and the propagator for N rotor periods can be written as

$$\widehat{U}(N\tau_r) = e^{-i\widehat{\overline{H}}N\tau_r} \qquad \textbf{1.41}$$

It is not easy to calculate $\widehat{\overline{H}}$, because usually $\widehat{H}_i$ and $\widehat{H}_j$ do not commute. The propagator of two non-commuting Hamiltonians can be expanded according to Baker-Campbell-Hausdorff relationship:

$$e^{\hat{A}}e^{\hat{B}} = \exp(\hat{A}+\hat{B}+\frac{1}{2}[\hat{B},\hat{A}]+\frac{1}{12}([\hat{A},[\hat{A},\hat{B}]]+[[\hat{A},\hat{B}],\hat{B}])+...) \qquad \mathbf{1.42}$$

By using this relationship the resulting average Hamiltonian can be written as a sum of different orders, with order i which is indicating the number of nested commutators involved:

$$\widehat{\overline{\mathrm{H}}} = \widehat{\overline{\mathrm{H}}}^{(0)} + \widehat{\overline{\mathrm{H}}}^{(1)} + \widehat{\overline{\mathrm{H}}}^{(2)} + ... + \widehat{\overline{\mathrm{H}}}^{(i)} \qquad \mathbf{1.43}$$

where the zeroth-order average Hamiltonian is

$$\widehat{\overline{\mathrm{H}}}^{(0)} = \frac{1}{\tau_r}\sum_{i=1}^{n}\hat{\mathrm{H}}_i\tau_i \qquad \mathbf{1.44}$$

The $\hat{\mathrm{H}}_i$ are not constant during the time interval τ_i under MAS, as a result the problem can be treated only in the limit of $\tau_i \rightarrow 0$ and n → 0. By assuming that the zeroth-order average Hamiltonian can be calculated because the commutator $[\hat{\mathrm{H}}(t),\hat{\mathrm{H}}(t+\Delta t)]$ vanishes for infinitely small time steps. In the limit of $\Delta t \rightarrow 0$, the full average Hamiltonian can be written as a sum of integrals, which is known as the Magnus expansion. The first three terms:

$$\begin{aligned}
\widehat{\overline{\mathrm{H}}}^{(0)} &= \frac{1}{\tau_r}\int_0^{\tau_r} dt\hat{\mathrm{H}}(t) \\
\widehat{\overline{\mathrm{H}}}^{(1)} &= -\frac{i}{2\tau_r}\int_0^{\tau_r} dt_1\int_0^{t_1} dt_2[\hat{\mathrm{H}}(t_1),\hat{\mathrm{H}}(t_2)] \qquad \mathbf{1.45} \\
\widehat{\overline{\mathrm{H}}}^{(2)} &= -\frac{1}{6\tau_r}\int_0^{\tau_r} dt_1\int_0^{t_1} dt_2\int_0^{t_2} dt_3([\hat{\mathrm{H}}(t_1)[\hat{\mathrm{H}}(t_2),\hat{\mathrm{H}}(t_3)]+[\hat{\mathrm{H}}(t_3)[\hat{\mathrm{H}}(t_2),\hat{\mathrm{H}}(t_1)]])
\end{aligned}$$

At this point it is useful to state that the inhomogeneous interactions like chemical shift anisotropy, dipole-dipole coupling of an isolated spin pair, and quadrupolar coupling, the $[\hat{\mathrm{H}}(t_1),\hat{\mathrm{H}}(t_2)]$ commutator vanishes (Maricq 79). For these interactions the higher-order terms in Magnus expansion vanish leaving only the zeroth-order average Hamiltonian for describing the evolution under a given interaction (λ) and MAS at an arbitrary time:

$$\widehat{\overline{\mathrm{H}}}_{\lambda}^{(0)} = \frac{1}{t}\int_0^{t} dt\hat{\mathrm{H}}_{\lambda}(t) = \hat{T}_{00}A_{00}^{\lambda,LAB} + \hat{T}_{20}\cdot\frac{1}{t}\int_0^{t} dtA_{20}^{LAB}(\omega_r t) \qquad \mathbf{1.46}$$

The knowledge about the space part of the interaction in the laboratory frame, A_{20}^{LAB}, is needed for the calculation of the average Hamiltonian according to the above formula. So a transformation from the principle axis system (PAS) to the laboratory frame (LAB) is necessary. This involves three Euler angle transformations; from PAS to molecular frame (MOL) which describes tensor orientation, then from MOL to rotor frame (ROT) which is the powder averaging, and finally from rotor frame to laboratory frame which is needed for the MAS:

$$\mathrm{PAS}\xrightarrow[\text{tensor orientation}]{(\alpha_{PM},\beta_{PM},\gamma_{PM})}\mathrm{MOL}\xrightarrow[\text{powder average}]{(\alpha_{MR},\beta_{MR},\gamma_{MR})}\mathrm{ROT}\xrightarrow[\text{MAS}]{(\omega_r t,\beta_M,0)}\mathrm{LAB} \qquad \mathbf{1.47}$$

Only in the last transformation the time dependence enters, where the Euler angle α_{RL} depends on the rotor phase, $\alpha_{RL}=\omega_r t$, which varies with time. The benefit of using the irreducible tensor representation is clearly seen at this step, because it is relatively simple to do the transformations from one reference frame to other by using it. The transformed tensor is given by a linear combination of components with the same rank L:

$$A_{Lm}^{Y} = \sum_{m'=-L}^{L} A_{Lm'}^{X} D_{m'm}^{(L)}(\Omega) \qquad \mathbf{1.48}$$

where the $D_{m'm}^{(L)}(\Omega)$ are elements of the Wigner rotation matrices;

$$D_{m'm}^{(L)}(\alpha,\beta,\gamma) = d_{m'm}^{L}(\beta)e^{-im'\alpha}e^{-im\gamma} \qquad \mathbf{1.49}$$

with the reduced matrix elements $d_{m'm}^{L}(\beta)$, which are listed in many NMR textbooks like the book of Mehring (Mehring 83). A_{20}^{LAB} is obtained after three subsequent rotations as

$$\begin{aligned} A_{20}^{\lambda,LAB}(t) &= \sum_{m=-2}^{2} A_{2-m}^{\lambda,ROT} \times e^{-im\omega_r t} d^{2}_{-m0}(\beta_M) \\ &= \sum_{m=-2}^{2}\left[\sum_{m'=-2}^{2} A_{2m'}^{\lambda,MOL} D^{(2)}_{m'm}(\Omega_{MR})\right]\times e^{-im\omega_r t} d^{2}_{-m0}(\beta_M) \\ &= \sum_{m=-2}^{2}\left[\sum_{m'=-2}^{2}\left[\sum_{m''=-2}^{2} A_{2m''}^{\lambda,PAS} D^{(2)}_{-m''-m'}(\Omega_{PM})\right] D^{(2)}_{-m'-m}(\Omega_{MR})\right]\times e^{-im\omega_r t} d^{2}_{-m0}(\beta_M) \end{aligned} \qquad \textbf{1.50}$$

If there is more than one interaction is present, all three transformations are needed, otherwise, transformation from PAS to ROT and then to LAB frame is enough. The Hamiltonian under magic angle spinning is given with the following general formula

$$\widehat{\mathrm{H}}_{\lambda,MAS}(t) = \widehat{T}_{00}A_{00}^{\lambda,LAB} + \widehat{T}_{20}.\frac{1}{t}\int_{0}^{t} dt A_{20}^{LAB}(\omega_r t) = \widehat{T}_{00}A_{00}^{\lambda,LAB} + \widehat{T}_{20}.\frac{1}{t}\sqrt{\frac{3}{2}}.\Phi_{\lambda} \qquad \textbf{1.51}$$

$$\begin{aligned} \Phi_{\lambda}(t) &= \frac{C_1}{\omega_r}(\sin(\gamma+\omega_r t)-\sin\gamma)+\frac{C_2}{2\omega_r}(\sin(2\gamma+2\omega_r t)-\sin 2\gamma) \\ &-\frac{S_1}{\omega_r}(\cos(\gamma+\omega_r t)-\cos\gamma)+\frac{S_2}{2\omega_r}(\cos(2\gamma+2\omega_r t)-\cos 2\gamma) \end{aligned}$$

$$\begin{aligned} \mathrm{C}_1 &= -\frac{\delta_\lambda}{\sqrt{2}}\sin 2\beta(1+\frac{\eta_\lambda}{3}\cos 2\alpha) \\ \mathrm{C}_2 &= \frac{\delta_\lambda}{2}\sin^2\beta-\frac{\delta_\lambda\eta_\lambda}{6}(1+\cos^2\beta)\cos 2\alpha \\ \mathrm{S}_1 &= \frac{\sqrt{2}\delta_\lambda\eta_\lambda}{3}\sin\beta\cos 2\alpha \\ \mathrm{S}_1 &= \frac{\delta_\lambda\eta_\lambda}{3}\cos\beta\sin 2\alpha \end{aligned} \qquad \textbf{1.52}$$

The integrated phase, Φ_λ, is greatly reduced for dipolar coupling and for most of the quadrupolar couplings, if $\eta_\lambda = 0$. After the cancellation of oscillating terms with the effect of MAS for dipolar and quadrupolar couplings ($A_{00}^{quad,LAB} = A_{00}^{dip,LAB} = 0$), equation 1.51 can be re-written in the following form

$$\widehat{\mathrm{H}}_{MAS} = \widehat{T}_{20}A_{20}^{\lambda,R}d_{00}^{(2)}(\theta) = \widehat{T}_{20}A_{20}^{\lambda,R}.\frac{1}{2}(3\cos\theta^2-1) \qquad \textbf{1.53}$$

The spin part is independent of the rotor modulation and can independently be modulated by rf pulses. The anisotropic parts of the interactions which is manipulated with the second Legendre polynomial $P(\theta)=\frac{1}{2}(3\cos^2\theta-1)$ are averaged out by rotating the sample with an axis inclined with angle θ (”magic angle” 54.7°) with respect to the magnetic field. The phenomenon of modification of signals in a rotating specimen as a result of the time dependence imparted to the local fields as $\mathrm{H}_{loc}=\sum_n \mathrm{H}_n e^{in\omega_r t}$ for liquid samples (Carr 53). MAS in solids was first introduced by Andrew (Andrew 58) and Lowe (Lowe 59) independently who were interested in removal of dipolar broadening. For a complete averaging, sufficiently high spinning speeds needed, $\omega_r \gg \omega_\lambda$. Commercially 35 kHz spinning speed is available, and in the literature spinning speeds up to 70 kHz have been reported (Bruker 97, Ernst 01, Samoson 03).

The technique of sample spinning at the magic angle averages interactions causing a shift in the energies of Zeeman spin functions. Chemical shift anisotropy, heteronuclear dipolar coupling and quadrupolar coupling are this kind of interactions. Moreover, MAS has also effect on the interaction which mix Zeeman functions like homonuclear dipolar coupling.

Spinning the sample at the magic angle with a rotation speed lower then the frequency spread of the shielding anisotropy results in isotropic chemical shift peak with a series of sidebands separated by the spinning frequency. The sideband intensities can supply valuable information about the chemical shift anisotropy. Herzfeld and Berger described a general procedure to correlate the CSA with the intensities of sidebands (Herzfeld 80a, 80b). Although spinning sidebands contain valuable information, sometimes they make the spectrum complicated and need to be removed. Removing sidebands can be managed in three different ways: First, spinning sample much faster than the anisotropy or coupling, but for this the manageable spinning frequency will sometimes be not sufficient. The second way is to sample the FID in a rotor synchronized manner which can be achieved by setting the dwell time equal to the rotor period (spectral width will be equal to spinning frequency). The last way is using advanced pulse sequences like TOSS (Dixon 82, Antzutkin 94).

2.6 Basic NMR Experiments

After the theoretical description, now it is time to concentrate on the basic NMR experiments used in this thesis. First the general procedure for the simplest NMR experiment, the one-pulse experiment, will be discussed (section 2.6.1). After this the cross-polarization technique will be explained which is an essential technique in the observation of low abundance nucleus like ^{13}C (2.6.2). In section 2.6.3 and 2.6.4 the dipolar decoupling techniques will be explained and finally in the last section, 2.6.5, the echo experiments will be introduced which are essential in deuterium NMR spectroscopy.

2.6.1 One-Pulse Experiment

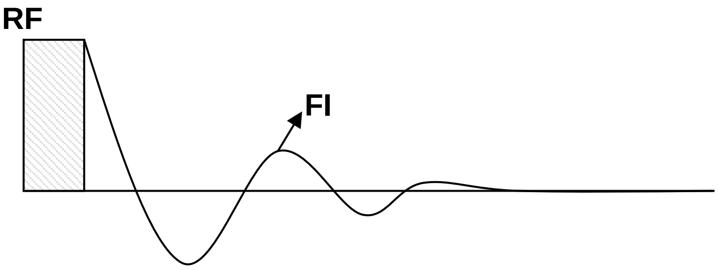

Figure 2.6: One-pulse experiment.

The one-pulse NMR experiment is the simplest nuclear magnetic resonance technique. A 90^o pulse ($\hat{I}_z \xrightarrow{\pi/2\hat{I}_x} -\hat{I}_y$) can flip the spins, which are in thermodynamic equilibrium to the x-y plane (transverse-plane) and they start to precess in this plane with the Larmor frequency. With precession, the time derivative of the magnetic moment changes and this result in the formation of an alternating current with the frequency of ω_L in the coil. The signal is mixed with the reference carrier frequency, to obtain the free inducting decay (FID) at low frequency. x and y components of the precessing magnetization can be detected in a phase sensitive detector (quadrature detection).

Quantum mechanically transverse magnetization is an observable and its expectation value is

$$\left\langle \hat{I}_+ \right\rangle = Tr\{\hat{I}_+ \hat{\rho}\} = \frac{1}{\sqrt{2}}\left(Tr\{\hat{I}_x \hat{\rho}\} + iTr\{\hat{I}_y \hat{\rho}\}\right) = \frac{1}{\sqrt{2}}\left(\left\langle \hat{I}_x \right\rangle + i\left\langle \hat{I}_y \right\rangle\right) \qquad \textbf{1.54}$$

Fourier transform of the time dependent shift operator ($\left\langle \hat{I}_+ \right\rangle(t)$) gives a spectrum with full phase information.

2.6.2 Cross Polarization

Cross-polarization (CP) (Pines 73) is usually used to facilitate the observation of dilute spins (low-γ, low abundance, e.g. **S** = ^{13}C) by polarization transfer from an abundant spin like protons (high-γ, high abundance, e.g. **I** = ^{1}H). One advantage of cross-polarization in most cases is the shorter recycle time. In this type of experiments only the relaxation time of proton limits the repetition rate of the experiment and not the S spin relaxation time, which is in many cases much longer then that of the proton. In cases where many scans are needed, this can be crucial.

In the CP experiment the polarization transfer is mediated by the dipolar interaction between **I** and **S** spins. Because of this reason the MAS spinning speed should be limited, otherwise high spinning speeds will remove the dipolar interaction and the efficiency of the polarization transfer will be much less.

The polarization phenomenon was first suggested by Sven Hartmann and Erwin Hahn in 1960 (Hartmann 62). The Hartmann-Hahn condition stated there is

$$\omega_1(S) = \gamma_S B_1(S) = \gamma_I B_1(I) = \omega_1(I) \qquad \textbf{1.55}$$

This means the Zeeman splittings in the spin-lock field become degenerate; so I and S precess with the same frequency and this leads to the magnetization transfer, even though the precession frequencies of I and S in the lab-frame are widely apart.

The maximum signal enhancement is given by the factor $\gamma(S)/\gamma(I)$. By increasing the contact time (t$_{cp}$), S magnetization first increase with a time constant (T_{IS}, which is characteristic for the strength of the dipolar couplings), but because of the relaxation there is an optimum value for t$_{cp}$. The dependence of CP efficiency to relaxation parameters is formulated as

$$M_S(t_{CP}) = \frac{M_0}{\lambda}\left[1 - e^{-\frac{\lambda t_{CP}}{T_{IS}}}\right] e^{-\frac{t_{CP}}{T_{1\rho}^{I}}} \qquad \textbf{1.56}$$

where $T_{1\rho}^{I}$ and $T_{1\rho}^{S}$ are relaxation constants in rotating frame, and λ is (Slichter 96)

$$\lambda = 1 + \frac{T_{IS}}{T_{1\rho}^{S}} + \frac{T_{IS}}{T_{1\rho}^{I}} \qquad \textbf{1.57}$$

The cross-polarization mechanism under MAS conditions is different from the plain CP. Under MAS, the Hartmann-Hahn condition is modified to

$$\omega_1(S) = \omega_1(I) \pm n\omega_r \qquad \textbf{1.58}$$

This matching in CP-MAS can easily be missed. If the spinning frequency is high, the matching condition becomes difficult to obtain, because of the narrow linewidth of protons. This problem can be solved by using the ramped-amplitude cross-polarization sequence (RAMP-CP) as was first introduced by Metz et. al. (Metz 94). In this technique the amplitude of the spin-lock field increased slightly during the contact time and this avoids to miss the matching condition.

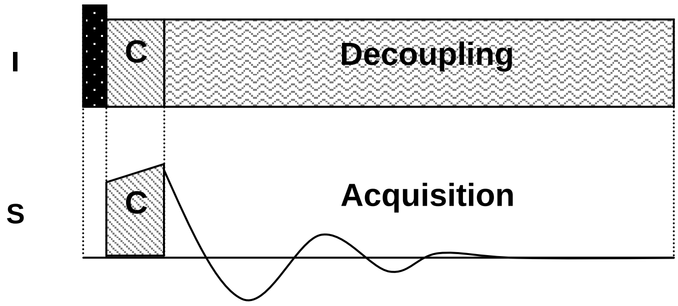

Figure 2.7: Pulse sequence cross-polarization MAS NMR experiment.

2.6.3 Heteronuclear Dipolar Decoupling

When investigating the low abundant nuclei like ^{13}C the homonuclear couplings can safely be neglected because of the very low natural abundance (~ %1) of NMR active carbon nucleus. However, the dipolar coupling of the dilute spin with abundant spin like ^{1}H can cause a broadening even under fast magic angle spinning conditions. In this case the effect of coupling can be removed by rf irradiation with special pulse sequences.

High-power continuous-wave decoupling is the simplest technique, which removes the effect of heteronuclear coupling. The method is simply applying continuous irradiation of high power at the proton resonance frequency during the acquisition of the S spin FID. This irradiation frequency does not need to be broad-band (containing wide frequency range) because of homonuclear dipolar coupling between protons will transmit the effect of rf-pulse among all coupled protons. For effective decoupling the rf amplitude needs to be around three times higher than the largest heteronuclear coupling. For example, a directly bonded H-

C spin pair has a dipolar coupling of around 22 kHz and needs an rf amplitude of 66 kHz for effective decoupling.

Under MAS conditions, there may be interference between physical rotation and rotation of spins via rf. Most interference occurs at the rotary resonances of $n\omega_r = \omega_1$ and/or $\frac{1}{2}\omega_r = \omega_1$ (Dusold 00). The decoupling frequency should be set at least twice the spinning frequency. In the biological research areas, instead of cw high-power decoupling, low-power CW decoupling combined with fast MAS is much more attractive. This power will be much lower than the spinning frequency (Ernst 01).

Pulse sequences have been introduced which can manage the decoupling with reasonable rf powers. The following pulse sequences are mainly designed to be used under MAS conditions. The first one is “two pulse phase modulation” (TPPM, Bennet 95) and the second is XiX (Detken 02). Both of these sequences have better performance than the CW decoupling even at similar power levels.

The TPPM sequence consists of irradiation with two pulses of flip angle θ_p and phases which differ by $\Delta\phi_p$. From the experimental investigations the optimal values can be found for flip angle θ_p and for $\Delta\phi_p$. θ_p is often around 170$^{\text{o}}$ and $\Delta\phi_p$ can vary between 10-70$^{\text{o}}$. These values depend on the sample and on the spinning speed, so they need to be optimized on each sample. The TPPM sequence is sensitive to rf inhomogeneities and rf instabilities, nevertheless, it usually gives better performance than simple CW high-power decoupling with the same power.

XiX also uses continuous, high-power rf irradiation with two pulses differing in phase by 180$^{\text{o}}$. The performance of the XiX sequence only depends on the ratio of pulse length to the rotor period of the sample spinning t_P / t_r. The XiX scheme is effective for t_P / t_r larger than one, but integer multiples of $t_r / 4$ should be avoided as these points correspond to resonances at which decoupling efficiency is severely reduced. The optimal value of t_P / t_r again should be determined experimentally, but good starting values are t_P / t_r =1.85 or 2.85. This sequence is insensitive to rf inhomogeneities and instabilities. At spinning speeds higher than 30 kHz, XiX has better performance than TPPM, but for lower spinning speeds TPPM is a better choice. Comparison of TPPM and XiX can be found in the literature (Detken 02, Ernst 03).

Besides TPPM and XiX, other decoupling sequences are presented in the literature like FMPM (Gan 97), SPARC (Yu 98), $C12_2^{-1}$ (Eden 99), SPINAL (Fung 00), and amplitude-Modulated TPPM (Takegoshi 01). All of these sequences have similar effects like TPPM sequence (Duer 04).

2.6.4 Echo Experiments

A technical problem exists, when trying to observe the rapidly decaying FID in NMR spectroscopy. Ringing of the coil prevents the measurement of the signal during a short delay time which is called *dead-time* after a pulse. If the FID decays fast, a big portion of the signal is lost in this dead-time interval. The method of choice for this problem is the acquisition of an echo, which is basically a 90^o or 180^o degree pulse applied after a time period τ after the initial 90^o pulse. These pulses will rotate the magnetization component so that the components refocus after another period τ. This τ delay must be long enough to be away from the dead-time of the probe, and after this the FID can be recorded from the echo maximum.

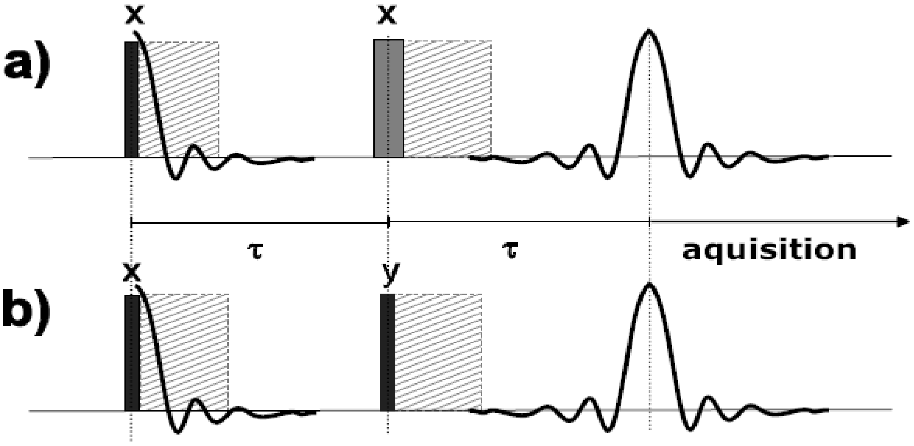

Figure 2.8: Echo Experiments pulse sequences for **a**) Hahn-echo, **b**)Solid-echo. The dead time is shaded area.

Two types of echo pulses have been used, the Hahn *spin-echo* (Hahn 50) and the *solid-echo* or *quadrupolar-echo* (Powles 63, Davis 76). The spin-echo ($90_x^o - \tau - 180_y^o - \tau - acquire$) is used for lines broadened by chemical shift anisotropy or heteronuclear dipolar coupling, i.e. interactions linear in the observed spin operators. The solid echo ($90_x^o - \tau - 90_y^o - \tau - acquire$) used for lines broadened by quadrupolar or homonuclear dipolar couplings, i.e. interactions bilinear in the observed spin operator. Detailed theoretical explanation can be found in literature (Schmidt-Rohr 94).

The important echo experiments for the current purpose is the solid-echo experiment which is used in deuterium NMR spectroscopy for molecular dynamics investigations in terms of correlation times in the range of $1/\delta_Q < \tau_c < 10\tau$. Spiess et. al intensively investigate deuterium static NMR (Spiess 85). By using simulation programs or packages, the type of molecular motion can be estimated from these experiments (Macho 01, Bak 00).

2.6.5 Multidimensional NMR Experiments

In NMR we observe the time evolution of coherences between Zeeman functions of the spin system. The only coherence, which can be observed directly is the m=-1. coherence. Although we can only observe -1. order coherence, we can create many different quantum orders and observe their evolution indirectly. This is one of the general ideas behind multidimensional NMR experiments. There are different types of two-dimensional experiments like correlation, separation and exchange experiments.

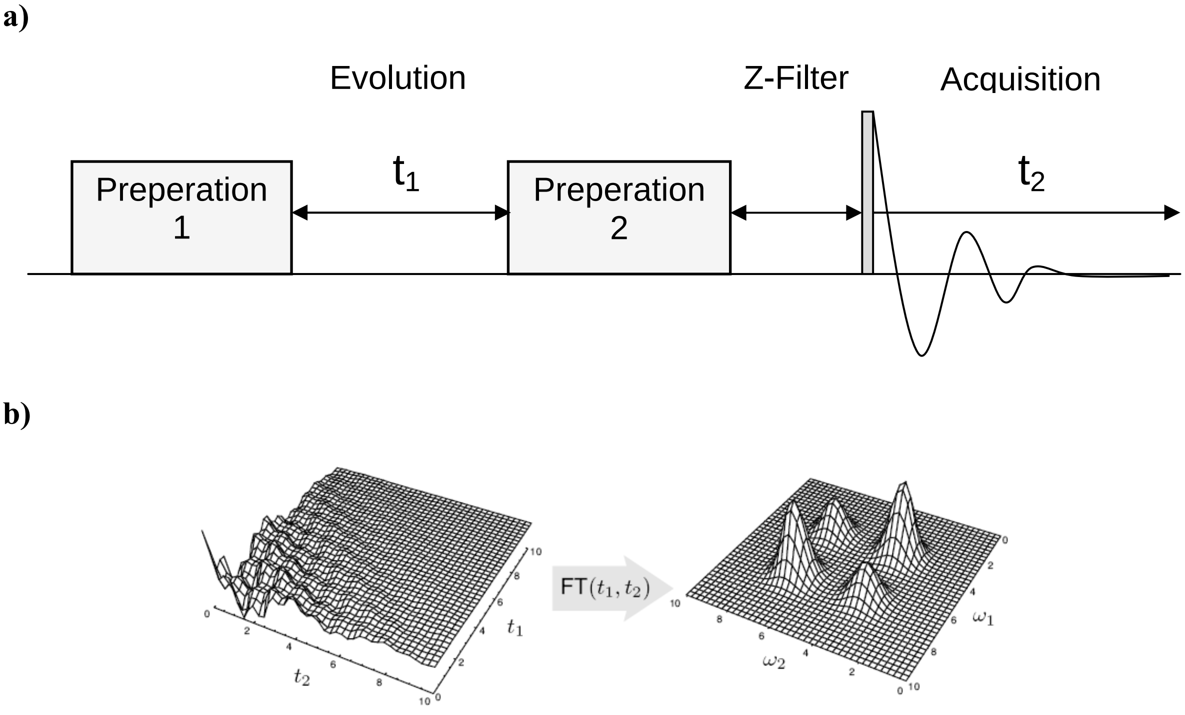

Figure 2.9: **a)** Schematic representation of Two Dimensional NMR experiment. **b)** The representation of the Fourier transformation performed to obtain the two-dimensional spectra.

In two dimensional experiments, an initial preparation period creates a non-equilibrium spin state. Then comes an evolution period of t_1 duration, in which the coherences are allowed to evolve. The desired coherence order is selected by applying the appropriate phase cycling. In the second preparation period, the selected n-quantum coherence is transformed into the observable single-quantum coherence for the observation during t_2. Repeating the experiment for different values of t_1, a two-dimensional time domain data set is obtained. The information of the evolution of single-quantum coherence will be in the t_2 dimension, and the information of the evolution of the n-quantum coherence will be in the t_1 dimension. Finally, the two-dimensional time-domain dataset will be transformed to the frequency domain by two subsequent Fourier transformations to produce a two-dimensional frequency spectrum.

2.7 Advanced NMR Experiments

After describing some basic NMR techniques in the previous chapter, we now need to introduce some more advanced solid-state NMR techniques used throughout this thesis. First, a general overview of recoupling techniques will be given, then multiple quantum techniques will be described and finally the method used in this study, the BaBa technique will be described.

2.7.1 Recoupling Methods under MAS Condition

In section 2.6 the methods of line narrowing techniques were mentioned, which are crucial in obtaining high resolution spectra. This high resolution is obtained by MAS at the expense of losing valuable structural and dynamical information, the orientational dependence and distance information. Methods which supply high resolution and at the same time also selectively reintroduce the desired information are needed. This is achieved by *recoupling techniques*. Some examples for the homonuclear DQ MAS NMR spectroscopy are BABA (Sommer 95, Feike 96), C7 (Lee 95), DRAMA (Tycko 91), DRAWS (Gregory 95) and HORROR (Nielsen 94). Levitt and co-workers have recently introduced a very helpful classification system for the rotating-frame pulse sequences, based on symmetry principles, which covers sequences like C7 and HORROR (Brinkmann 00, Carravetta 00).

The one-pulse MAS ^1H spectrum is not well suited to get information about dipolar interactions, because the detected signal contain only limited information about the spin-pair character of dipolar coupling. One of the first methods to gather this kind of information is off-MAS methods or slow MAS methods (Stejskal 77, Blumich 90). The recoupling approach was introduced later (Gullion 89b). In these recoupling methods the space part is modified by MAS and at the same time the spin part is synchronously modified by rf pulses. These pulses are capable of reintroducing the interaction of interest by supplying kind of a "counter rotation" in spin space (Gullion 97, Lee 95, deAzavedo 99, Dusold 00, Schnell 01a, Saalwachter 02c). The pulse sequences can be divided mainly into two classes, laboratory frame pulse sequences and tilted rotating frame pulse sequences. For the laboratory frame pulse sequences, the average Hamiltonian is calculated in the laboratory frame. It is important to supply the condition of δ-pulses, which have short pulse lengths in the recoupling sequences compared to the MAS rotor period. At increasing spinning frequencies this might be instrumentally difficult to achieve. However, for the tilted rotating frame pulse sequences, nutation frequency of the longer pulses are matched (synchronized) to multiples of MAS frequency. The selection of desired interaction is achieved by the symmetry arguments (symmetry based pulse sequences) that different NMR interactions intrinsically have. We will mainly consider the former case, because it is used in the current study, the detailed description of the later case can be found in the literature (Brinkmann 00, Zhao 01).

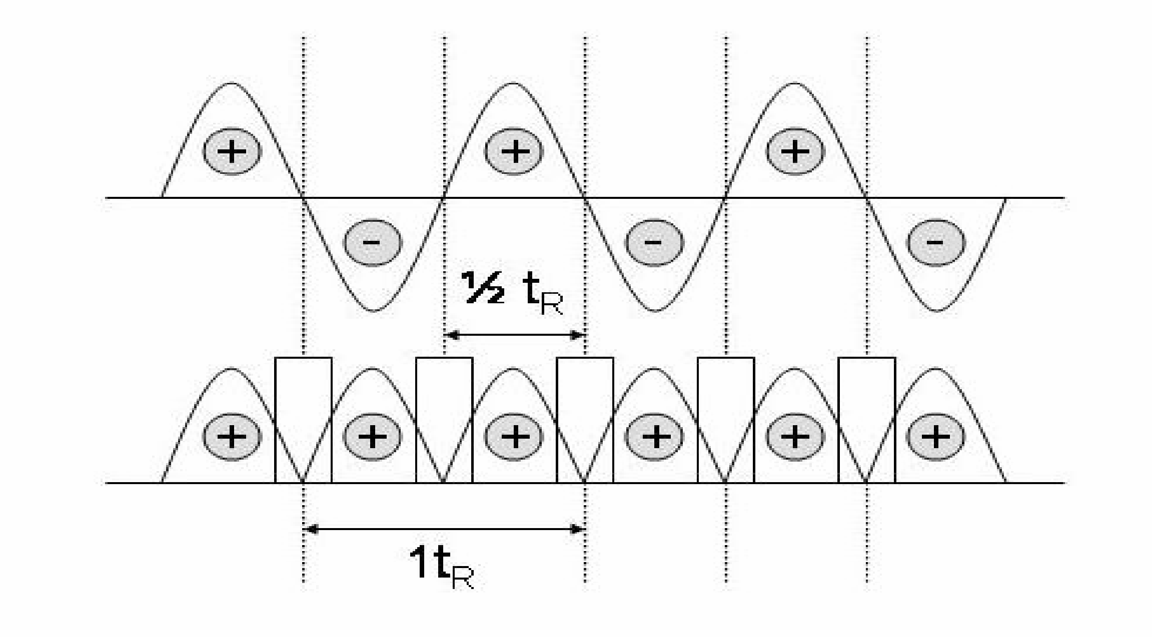

Figure 2.10: Recoupling by π pulses trains in a rotor synchronized way.

Recoupling pulse sequences are based on the application of rotor-synchronized pulses with a spacing of half or quarter rotor periods to recouple the ω_r modulated and $2\omega_r$ modulated art of the spin Hamiltonian under MAS, respectively. Anisotropic interactions which are averaged to zero can be reintroduced with these pulse schemes. The sine ω_r

modulation of the anisotropic part of the interaction Hamiltonian is schematically represented in Figure 2.10, with the mathematical sign of the sine-oscillation labeled "+" and "-" respectively. The REDOR (Rotational Echo DOuble Resonance) experiment uses the pulse spacing of half a rotor period (Gullion 89a, 89b, 97) for the heteronuclear dipolar coupling recoupling with π pulse. The similar type of pulse sequence can be used to recouple the chemical shift anisotropy (deAzavedo 99, Hong 00). By changing the π pulses with $\pi/2$ pulses homonuclear recoupling can also be obtained (Feike 96). This change leads to a time-reversal of the homonuclear dipolar coupling during the second half of each rotor period.

In the following, the mathematical formulation of the recoupling effect of REDOR pulse sequence will be represented. The averaged Hamiltonian of an interaction λ under MAS is given by

$$\widehat{\mathrm{H}}_{\lambda,MAS} = \widehat{T}_{00} A_{00}^{\lambda,LAB} + \widehat{T}_{20}.\frac{1}{t}\sqrt{\frac{3}{2}}.\Phi_{\lambda} \qquad \mathbf{1.59}$$

The first and the second terms are the isotropic and the anisotropic contributions to the averaged Hamiltonian of an interaction λ under MAS (eq. 59). With MAS, a sine(w_r) modulation on the anisotropic part of the interaction Hamiltonian imposed. The time dependence of the acquired phase angle $\Phi_{\lambda}(t)$ is given by eq. 1.52, and by setting the $t=\tau_r$ it is clear that acquired phase over a full rotor period is zero, so that the anisotropic part of the interaction Hamiltonian is refocused. The first and the second half of the rotor period cancel under MAS, the anisotropic part of the interaction Hamiltonian is averaged to zero (refocused) after an integer number of rotor period without the application of any RF pulses. However with an application of suitably placed RF pulses the sign of the spin part of the $\widehat{\mathrm{H}}_{\lambda,MAS,aniso}$ can be inverted every $\tau_r/2$, hence the anisotropic contribution of the interaction is reintroduced (recoupled).

$$\int_{t}^{t+n.\tau_r} \widehat{\mathrm{H}}_{\lambda,MAS,aniso}(t)dt = 0 \text{ and } \int_{t}^{t+n.\tau_r} \widehat{\mathrm{H}}_{\lambda,MAS+RF,aniso}(t)dt \neq 0 \qquad \mathbf{1.60}$$

The nature of the applied pulses to recouple an interaction depends on the nature of the spin part of the respective interaction. For heteronuclear dipolar coupling and chemical shift anisotropy (interactions linear in $\hat{I}$) π-pulses are needed and for homonuclear dipolar coupling (interactions bilinear in $\hat{I}$) π/2-pulses are needed. Instead of a single π/2 pulse, multiple π/2 pulses with orthogonal phases may be used which lead to a higher recoupling efficiency compared to that achieved with a single π/2 pulse.

2.7.2 Multiple Quantum Techniques

In solids, multiple-quantum coherences are commonly excited by recoupling pulse sequences. MQ methods have been applied for a long time in solution-state NMR (Bodenhausen 81) and solid-state NMR (Weitekamp 82, Munowitz 87). Experiments of *multiple quantum coherence* (MQC) evolution are intrinsically two dimensional (shown in Figure 2.11), because MQC cannot be detected directly. An *m-quantum coherence* involves a change in overall multiple-spin quantum number M by m. In unperturbed systems transitions with $\Delta m > 1$ are forbidden, but they become weakly allowed under the influence of a coupling interaction. First a MQC is excited in the excitation period, then during the incremented evolution period t_1 the created coherences evolve. In the reconversion period MQCs are converted (reconversion period is the time reversal of excitation sequence to prevent destructive interference of many MQCs) into single-quantum (SQ) coherences which is detected in the t_2 acquisition period.

To select the desired coherence transfer pathways, a phase cycling scheme is employed (Bodenhausen 79). Pure absorption-mode two dimensional line shapes are ensured by the selection of symmetric pathways such that the time-domain signal is amplitude modulated in t_1 (Ernst 87). Sign discrimination can be restored in the indirect dimension by the time proportional phase incrementation, TPPI (Marion 83) or States-TPPI (Marion 89) methods, which are for the evolution of DQC in t_1, involve incrementing the phases of all excitation pulses by 45° after recording each t_1 point for the double-quantum experiments. In TPPI the sine and cosine components are detected alternatingly from slice to slice, so the effective increment (Δt_1) is doubled and the spectral width in the indirect dimension is divided by two ($SW(F1)=1/(2\Delta t_1)$). States-TPPI method should be used for a larger spectral width in the indirect dimension in which the SW is $SW(F1)=1/(\Delta t_1)$ (Schmidt-Rohr 94).

Double-quantum (DQ) spectroscopy is the special case of MQC spectroscopy in which the minimum number of coupled spins is two. By this method the dipolar couplings can be analyzed in pair wise manner with respect to chemical shifts of involved nuclei.

2.7.3 Back-to-Back as a MQ Technique for Homonuclear Dipolar-Recoupling

From many recoupling techniques for homonuclear dipolar couplings listed in section 2.7.1, the Back-to-Back (BaBa) pulse sequence was chosen, because it is robust under high spinning speed up to 30-35 kHz which is needed for ^{1}H DQ spectroscopy. As seen in Figure 2.11, the BaBa pulse sequence consists of the repeating $90_x - \tau_r/2 - 90_{-x}90_y - \tau_r/2 - 90_{-y}$ unit (in short; $x - \bar{x}y - \bar{y}$). An appropriate phase cycling must be applied for the selection of the desired coherence pathway (Ernst 87). The name BaBa is refers to the fact that the pulses are placed back-to-back. BaBa consists of half a rotor periods where an evolution period is managed by two 90^o pulse with the phases adjacently shifted by 90^o. The phase shift is crucial because it supplies the negation of the spin-part of the Hamiltonian, which exactly compensated the negation of space part by MAS. There are one and more rotor period excitation time versions of BaBa sequence. A complete description of BaBa can be found in the literature (Feike 96, Hafner 98, Brown 01, Schnell 01a).

The theoretical description of BaBa is as follows: A DQ Hamiltonian is tailored from the homonuclear dipolar coupling by BaBa according to the zero-order average Hamiltonian approach

$$\widehat{\mathrm{H}}_{dip,\mathrm{hom}} = T^{ij}_{20}.\frac{1}{t}.\int_0^t A^{LAB}_{20} = T^{ij}_{20}.\frac{1}{t}.\sqrt{\frac{3}{2}}\Phi_{dip,\mathrm{hom}} \qquad \mathbf{1.61}$$

where the integrated phase is

$$\Phi_{dip,\mathrm{hom}} = -\sqrt{2}D_{ij}\frac{\sin 2\beta}{\omega_r}.(\sin(\gamma+\omega_r t)-\sin\gamma)+D_{ij}\frac{\sin^2\beta}{2\omega_r}..(\sin(2\gamma+2\omega_r t)-\sin 2\gamma) \qquad \mathbf{1.62}$$

in which $\delta_{dip,\mathrm{hom}}$ is replaced by $D_{ij} = \frac{1}{2}\delta_{dip,\mathrm{hom}}$. For the $x - \bar{x}y - \bar{y}$ BaBa sequence the average Hamiltonian can be derived as (Schnell 01b)

$$\widehat{\mathrm{H}}_{BaBa} = \frac{1}{\tau_r}.3.\Phi_{dip,\mathrm{hom}}\Big|_0^{\frac{\tau_r}{2}}(T^{ij}_{2,+2}+T^{ij}_{2,-2}) = \frac{\Omega^{ij}(0,\frac{\tau_r}{2})}{\tau_r}.(T^{ij}_{2,+2}+T^{ij}_{2,-2}) \qquad \mathbf{1.63}$$

where, $\Omega^{ij}(0,\frac{\tau_r}{2}) = 3.\Phi_{dip,\mathrm{hom}}\,|_0^{\frac{\tau_r}{2}}$, which is a more common notation found in the literature.

The order m=±2 in the tensor component represents the generated DQ coherences and $\Omega^{ij}(0,\frac{\tau_r}{2})$ is need to be calculated from

$$\Omega^{ij}(0,\frac{\tau_r}{2}) = \frac{3\sqrt{2}D_{ij}}{\omega_r}\sin 2\beta_{ij}\sin\gamma_{ij} \qquad \mathbf{1.64}$$

The Ω^{ij} term is needed for the calculation of the amplitude modulation of the DQ coherence in the form of $\sin\Omega^{ij}_{exc}$ during the excitation and $\sin\Omega^{ij}_{rec}$ during the reconversion. Application of the BaBa Hamiltonian to a system, $\rho^{ij}_0 \propto I^{(i)}_z + I^{(j)}_z$, results in the generation of DQ coherences. The double-quantum signal intensity of the N rotor period of excitation and reconversion time can be described by the multiplication of these modulation terms;

$$S^{(ij)}_{DQ}(t_1) \propto \left\langle \sin(N\Omega^{ij}(0,\tau_{ext})).\sin(N\Omega^{ij}(t_1,t_1+\tau_{rec}))\right\rangle_{\beta,\gamma} \qquad \mathbf{1.65}$$

with the brackets indicating the orientational averaging (powder average) needed for the powder samples. Due to the symmetry of the dipolar interaction only the β and γ Euler angles need to be considered.

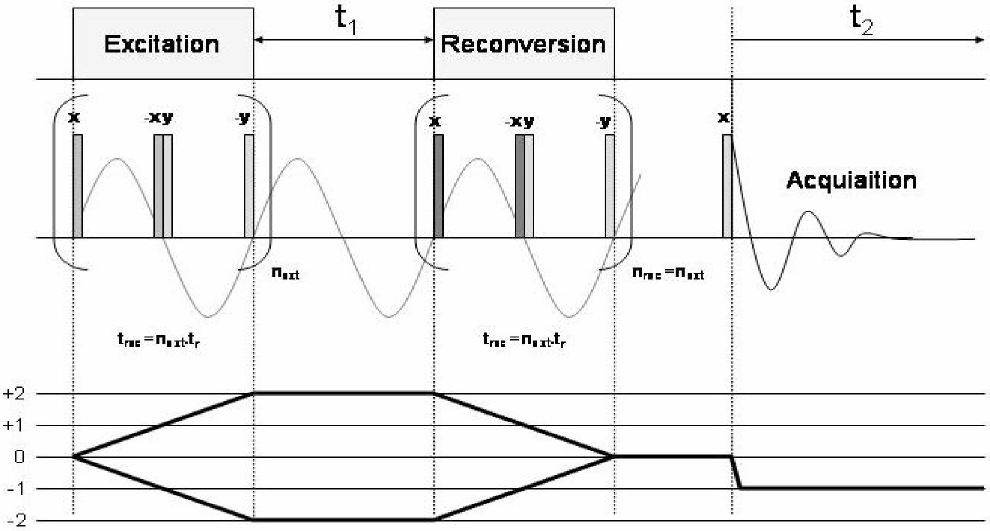

Figure 2.11: The BaBa pulse sequence. Top is the general structure of MQ experiment; middle is the BaBa pulse sequence; bottom is the coherence transfer pathway diagram for DQ excitation

The signal intensity of the DQ signal depends on the t_1 evolution time, which results in the possibility of conducting this experiment in different ways depending on the setting of t_1 and t_1-increment. The first possibility is setting $t_1=0$, which will result in a one-dimensional experiment in which double-quantum filtration applied. The comparison of MAS spectra to the ^{1}H double-quantum filtered (DQF) MAS spectra allow to distinguish mobile and rigid protons. Second and third ways are two-dimensional experiments which can be made in a rotor synchronized manner by setting the t_1 increment equal to the rotor-period τ_R or in a non-rotor synchronized manner to get sideband pattern by setting t_1 increment less than the rotor-period τ_R.

Rotor-synchronized 2D DQ MAS is recorded in a way that no spinning sidebands are observed in the spectrum by setting the spectral width in F1 equal to spinning frequency. By this way the spinning sidebands in F1 are folded back onto the centerband position. This experiment correlates the evolution of the selected DQ coherence during the first spectral dimension (t_1) with the SQ signal detected during the final acquisition period (t_2).

The spectral position in t_1 is governed by the isotropic chemical shift evolution of the DQ coherence with the resonance frequency being the sum of the resonance frequencies of the two involved spins. It is therefore convenient to display the 2D rotor synchronized spectrum in such a way that double quantum dimension axis (t_1 dimension) is scaled by a factor of two as compared to the single quantum dimension axis (t_2 dimension) (Fischbach 03).

2.7.4 Double-Quantum Buildup Curves

When the t_1 evolution time set to zero ($t_1=0$), a special version of the BaBa experiments is performed. In this one-dimensional version, there is no evolution time between the excitation and reconversion time periods. As a result the integrated phases become identical $\Omega^{ij}_{ext} = \Omega^{ij}_{rec}$. This form of the BaBa experiment serves as a double-quantum filter (DQF). The intensity of the DQ-filtered signal is given by:

$$\begin{aligned} S^{(ij)}_{DQ} &\propto \left\{\sin(N\Omega^{ij}\tau_{ext/rec})\right\}^2 \\ &\approx \left\{N\Omega^{ij}\tau_{ext/rec}\right\}^2 \\ &\propto \left\{D_{ij}\tau_{ext/rec}\right\}^2 \\ &\propto r_{ij}^{-6}\tau_{ext/rec}{}^2 \end{aligned} \qquad \textbf{1.66}$$

The first approximation can be performed at the limit of short excitation/reconversion times, in which the weak dipolar couplings can be neglected, $D_{ij}\tau_{ext/rec} \ll 1$. Only the stronger dipolar couplings contribute to the signal for shorter recoupling times. For the longer recoupling times, weaker dipolar couplings also contribute to the signal. The DQ signal intensity as a function of recoupling time results in a double-quantum build-up curve (Schnell 01b), from which the strength of dipolar couplings can be determined.

In rigid ^{1}H samples, the dense network of dipolar couplings is obviously a further and important reason for the observed deviations from a pure spin-pair buildup behavior. It is clear that with increasing excitation times, i.e., with increasing evolution time under dipolar recoupling conditions, the system develops its multi-spin character, and the buildup oscillations are damped out. The formula given before (eq. 66) which describes the relative intensity of the double-quantum signal is only the first term of a series expansion which results from the evolution of a multi-spin system (Schnell 01b). The truncation is only valid for the short recoupling times where only the double-quantum terms dominate.

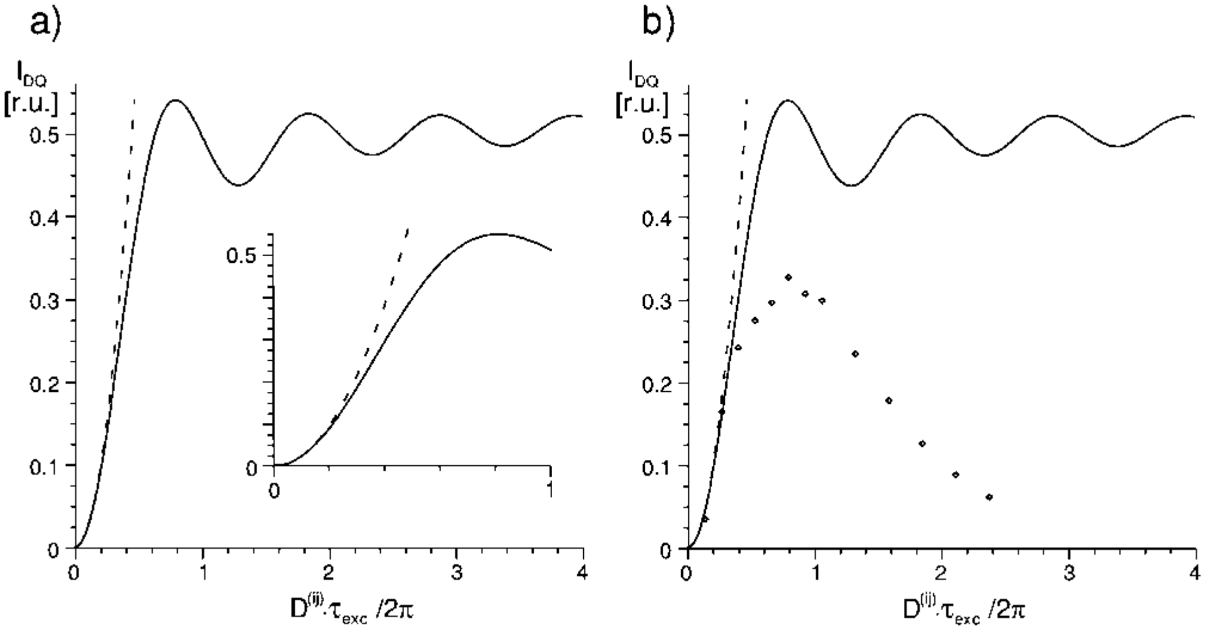

Figure 2.12: (a) Calculated DQ intensities for a single spin pair (solid line) and for the leading two-spin term in the series expansion for multi-spin systems (dotted line). The initial slope where two-spin behavior predominates is magnified in the inset. (b) Comparison of calculated and experimentally observed DQ signal intensities. The experiments (data points) were performed on tribromoacetic acid, which is a H-H spin-pair model compound with a dipolar pair coupling of $D^{(i\,j)}=2\pi.6.5$ kHz. In both diagrams, I_{DQ} is normalized with respect to the signal of a one-pulse experiment. (The figure is adapted from Schnell 01b).

A more complicated formula has to be used to fit the observed build-up curve in the presence of multi-spin effects:

$$S_{DQ}^{(ij)} = A.(D_{ij}.\tau_{ext/rec})^2 \exp\left\{-\frac{\tau_{ext/rec}}{T_1^{DQ}}\right\} \qquad \mathbf{1.67}$$

The cofactor A is fixed for a series of experiments and contains several constants. The decay of the DQ coherence is described by the exponential term with a time constant T_1^{DQ}. Usually for different dipolar coupled spin pairs, relative strength of the dipolar coupling can be estimated since the constant A is usually unknown (Graf 98a). In "real" ^{1}H systems, DQ buildup curves are expected to be damped for long excitation times because of the destructive interference of pair couplings of different strengths and the generation of higher order coherences. While for short excitation times the two-spin approximation is valid for multi-spin systems of arbitrary geometry, the onset of the breakdown of this approximation for longer excitation times depends on the overall dipolar coupling in the system (Schnell 01b).

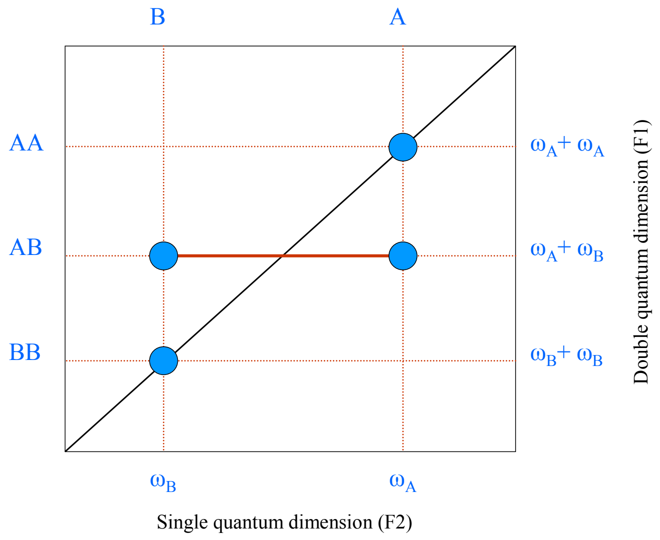

Figure 2.13: Schematic representation of rotor-synchronized 2DBaBa spectrum. The diagonal peaks are arising from DQ coherence between like spins (AA, BB) and cross peaks are arising from a DQ coherence between two unlike spins (AB).

2.7.5 Two-Dimensional Rotor-Synchronized Double-Quantum MAS Spectra

When the t_1 increment is set equal to one rotor period ($t_1=\tau_r$), rotor-synchronized two dimensional spectra are obtained. By this way ($SW(F1) = 1/\Delta t1 = 1/\tau R = \omega R$), in the indirect dimension of the spectrum, no spinning sidebands are observed due to the fact that the sidebands are fold back to the centerband position. This also means that the peak positions in the indirect dimension depend only on the DQ evolution during the t_1 period under the influence of isotropic chemical shift and dipolar coupling interactions. Additionally, the evolution of the DQ coherence between two involved spins (i and j), under the influence of respective chemical shifts result in a modulation of the form $\exp\left\{i(\omega_{CS}^{i}+\omega_{CS}^{j})t_1\right\}$. When ($i$ $=j$), it is clear that a DQC does not evolve under a dipolar coupling which is part of the coherence, since in a DQC the spin pair ($i\ j$) and the mediating coupling $D^{(i\,j)}$ behave as a single entity. However, any coupling to a spin outside the coherence gives rise to an evolution of the DQC during t_1 and, in this way, usually leads to a loss of signal, because the reconversion only reverses the effects of dipolar couplings, which have occurred during the excitation period τ_{exc}, but not any dipolar evolution thereafter. The spectral position in t_1 is purely governed by the isotropic chemical shift evolution of the DQ coherence with the resonance frequency being the sum of the resonance frequencies of the two involved spins. For short excitation times, the detected DQ signal intensity I_{DQ}^{AB} is given by the sum over all DQ intensities I_{DQ}^{AB} with (i,j) =**AB** (Schnell 01b):

$$I_{DQ}^{AB}=\sum_{\substack{i<j\\(ij)=AB}} I_{DQ}^{(ij)} \propto \sum_{\substack{i<j\\(ij)=AB}} (D^{(ij)}\tau_{exc})^2 \propto \tau_{exc}^2 \sum_{\substack{i<j\\(ij)=AB}} \frac{1}{r_{ij}^6} \propto \frac{\tau^2_{exc}}{r_{AB\mathrm{eff}}^6} \qquad \mathbf{1.68}$$

The sum over all pair distances $r_{i\,j}$ suggests the definition of an effective distance ($r_{AB\mathrm{eff}}$) between the spin pairs of the type AB. The contribution of each real distance $r_{i\,j}$ is weighted by the reciprocal sixth power, thereby ensuring a rapid convergence of the sum for increasing distances. Under fast MAS conditions, DQ coherences are observed up to a proximity of 3.5 Å for protons.

A schematic representation of the rotor-synchronized DQ spectrum is presented in Figure 2.13. The peak positions are given in the form of (ω_2, ω_1), where ω_2 is the SQ frequency and ω_1 is the DQ frequency of any resonance. A DQ coherence between spins with like chemical shifts give rise to a *auto-peak* at the position of (ω_A,2 ω_A) on the diagonal, whereas a DQ coherence between spins with different chemical shift values give rise to a pair of *cross-peaks* at the positions of (ω_A, $\omega_A+\omega_B$) and (ω_B, $\omega_A+\omega_B$) symmetrically on both side of the diagonal. Since the intensity of the cross-peaks depends on the number of involved spins, both cross-peaks have equal intensity if there is no relaxation process involved.

2.7.6 Double-Quantum Spinning-Sideband Patterns

The spinning sideband patterns can be obtained in the indirect dimension of a two-dimensional DQ spectrum by incrementing the t_1 evolution time in small steps $\Delta t_1 < \tau_r$ (Geen 94, Geen 95). Depending on the total recoupling time and the dipolar coupling present, the intensity of the sidebands can be varied and quantitative information on the dipolar coupling strength can be obtained (Friedrich 98).

The normal sideband generation mechanism, evolution rotor modulation (ERM) (Friedrich 98), can not result in the sideband patterns observed in DQ experiments, since the isolated spin-pair has no anisotropic evolution of the DQ coherence during t_1. The sidebands generated by ERM are due to the evolution of anisotropic interactions under MAS. This is observed in one-pulse MAS experiments with slow spinning speeds, which produces ERM sidebands due to the underlying chemical shift anisotropy. Under fast MAS, however, almost no contribution from the ERM is found.

The sidebands observed for the ^{1}H DQ experiments are due to another mechanism called reconversion rotor encoding (RRE) or γ-encoding. RRE results from the rotor-phase dependence of the average Hamiltonians used for the excitation and reconversion periods. BaBa (a laboratory frame pulse sequence) forms sideband patterns by RRE because its average Hamiltonian depend on the initial rotor phase, however, the tilted frame pulse sequences (e.g. C7) do not depend on the initial rotor phase so no sidebands occur with RRE mechanism.

The rotor-synchronized version of the DQ experiment has the same initial rotor phase for excitation and reconversion period, which is manifested in the integrated phase, Ω^{ij}. The rotor phase for the reconversion phase changes with the incrementation of t_1, which result in different integrated phases for excitation and reconversion periods:

$$\begin{gathered}\Omega^{ij}_{exc}(0,\frac{\tau_r}{2}) = 3\sqrt{2}D_{ij}\sin 2\beta_{ij}\sin\gamma_{ij} \\ \neq \\ \Omega^{ij}_{rec}(\frac{\tau_r}{2}+t_1,\tau_r+t_1) = \frac{3\sqrt{2}}{\omega_r}D_{ij}\sin 2\beta_{ij}\sin(\gamma_{ij}+\omega_r t_1)\end{gathered} \qquad \textbf{1.69}$$

It is clear from these formulas that rotor echoes occur in the t_1-signal for evolution times $t_1 = n\tau_r$ with sidebands spaced by multiples of the rotor period in the indirect dimension. The DQ signal is now given by

$$\begin{aligned} S_{DQ}^{(ij)}(t_1) &\propto \sin(N\Omega^{ij}(0,\frac{\tau_r}{2})).\sin(N\Omega^{ij}(\frac{\tau_r}{2}+t_1,\tau_r+t_1)) \\ &\propto \sin(C_{ij}\sin(\omega_r t_1+\gamma)) \end{aligned} \qquad \textbf{1.70}$$

C_{ij} contains all of the terms which do not depend on t_1, for simplicity. By using the following relationship (Abramowitz 72),

$$\sin(x\sin(\omega_r t_1+\gamma)) = 2\sum_{n=0}^{\infty} J_{2n+1}(x)\sin((2n+1)\omega_r t_1+(2n+1)\gamma) \qquad \textbf{1.71}$$

DQ signal intensity can be rewritten as a Fourier series, whose terms contain Bessel functions of *n*th order:

$$S_{DQ}^{(ij)}(t_1) \propto 2\sum_{n=0}^{\infty} J_{2n+1}(C_{ij})\sin((2n-1)\omega_r t_1+(2n+1)\gamma) \qquad \textbf{1.72}$$

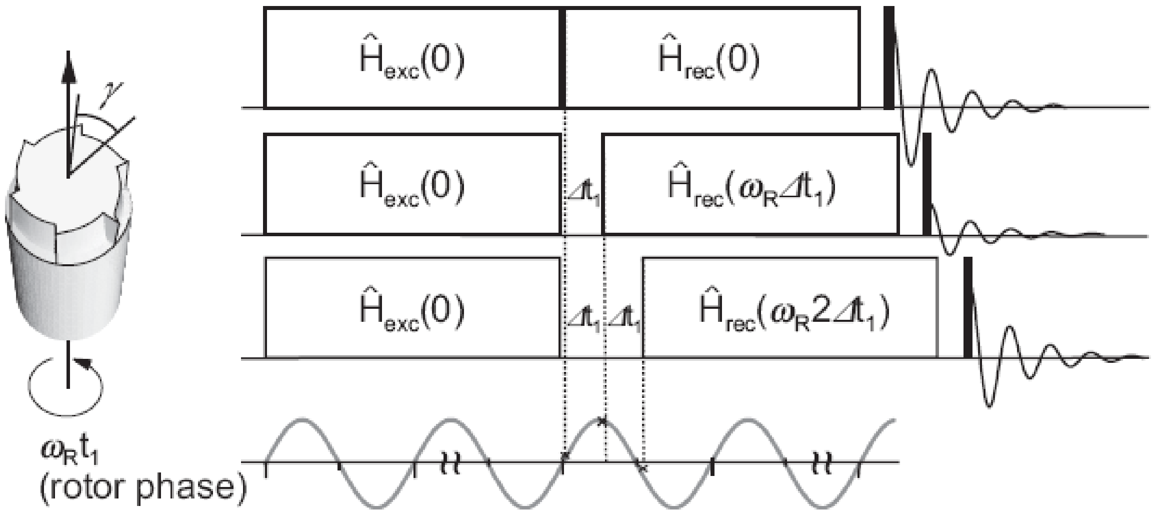

Figure 2.14: Schematic representation of the principle of reconversion rotor encoding (RRE) (The figure is adapted from Fischbach 03).

It is clear from the above equation that the modulated DQ signal contains only odd multiples of the spinning frequency, as a result the sideband patterns only consist of odd-order sidebands.

The distribution of the intensity among the sidebands is determined by the coefficient C_{ij} and Bessel functions. DQ sideband patterns contain information on sample orientation and dipolar coupling strength because, the coefficient C_{ij} depends on the orientation (β, γ) and on the ratio D_{ij}/ω_r. By choosing suitable excitation time, the number of the observed sidebands can be changed which depends on the product of $D_{ij}\tau_{exc}$. It was shown that it is advantageous to have $D_{ij}\tau_{exc}$=1.2, which is a compromise between enough sidebands for numerical simulations to extract dipolar couplings and not too many sidebands over which the intensity is distributed.

By assuming an isolated spin-pair, analytical simulations can be performed to extract the dipolar couplings. The isolated spin-pair approximation rarely exists in organic solids which are extensively studied throughout this thesis. The effect of remote protons is sometimes significant, and this may reduce the validity of spin-pair approximation. Under fast-MAS mostly the strong dipolar couplings remain, ideally as an isolated spin-pair form. Even if the weak couplings are present, they only contribute to the first-order sidebands. By considering higher-order sidebands, reliable values can still be extracted. The multi-spin effect is another issue which needs to be discussed, and which might cause the observation of even-order sidebands. These sidebands arise from ERM mechanism, from the evolution of DQ coherence during t_1 under the influence of dipole-dipole coupling to other spins (Fischbach 04b). Faster MAS would cause a reduction in the multi-spin effects, since ERM is suppressed by MAS.

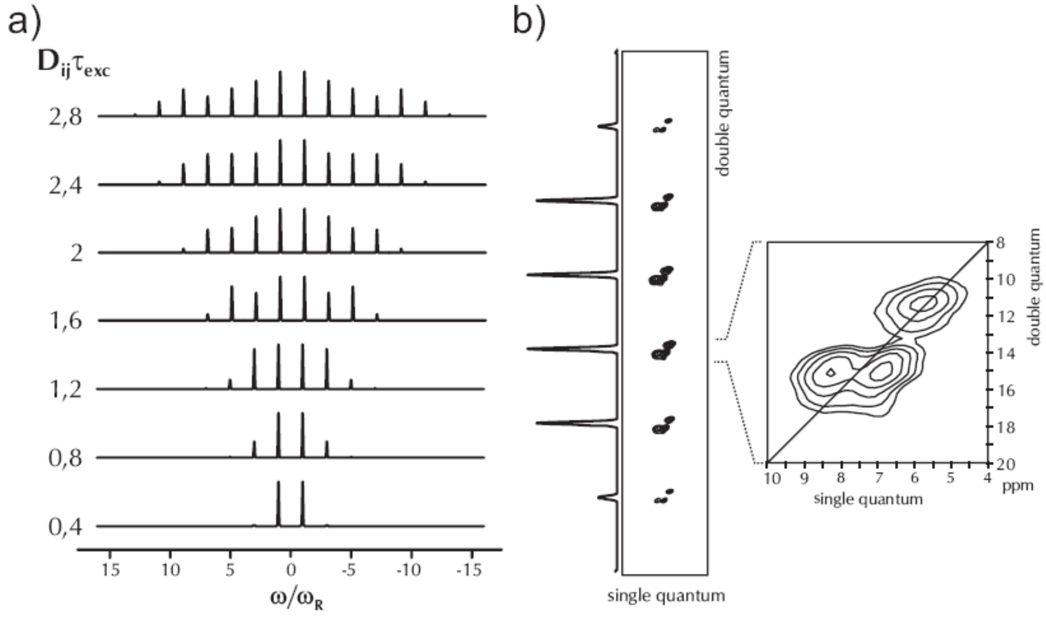

Figure 2.15: **a)** DQ sideband patterns which are calculated using the spin-pair approximation for various $D_{ij}\tau_{exc}$.

b) Full two-dimensional DQ sideband spectrum. The magnification represents one of the central sidebands, which consists of a full chemical shift resolved spectrum (The figure is adapted from Fischbach 03).

These experiments are typically done by using t_1 increments of $\Delta t_1=\tau_r/n$, where n is being 20-25. The chemical shift evolves during the t1 period, and in order to obtain chemical shift resolution in the indirect dimension, the rotor-encoding of many rotor periods is needed in order to obtain both the chemical shift and rotor encoded information (usually 512 or more t_1 increments are used for the indirect dimension). The schematic representation of a DQ sideband pattern spectrum is shown in Figure 2.15.

2.7.7 Heteronuclear Dipolar Recoupling Techniques based on REDOR

The recoupling of heteronuclear dipolar couplings between two nuclei (I and S) by using different experimental techniques will be presented in this section. Compared to the ^{1}H homonuclear dipolar recoupling experiments which are described in the previous sections, the heteronuclear dipolar recoupling experiments have the advantage of higher chemical shift resolution due to the S nuclei (^{13}C, ^{15}N, and ext.). Combined with the fast-MAS (ω_r > 20 kHz), the presented techniques supply a way of recoupling of the already averaged heteronuclear dipolar couplings by the usage of REDOR-type π pulse-trains (Jaroniec 00).

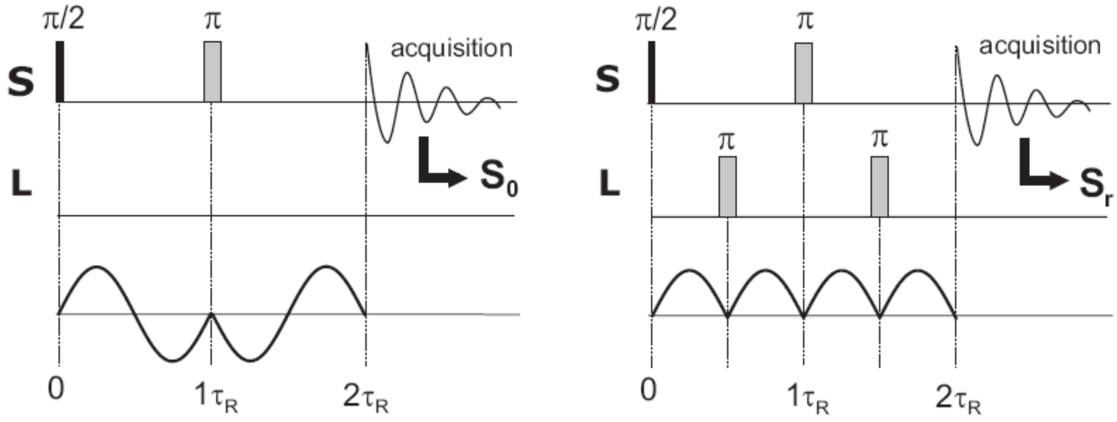

Figure 2.16: Schematic representation of a REDOR experiment for a heteronuclear dipolar coupling case (reproduced from Rapp 2004).

In the heteronuclear case suitably placed π pulse-trains are used for the recoupling purposes. A reference experiment, is a simple spin-echo experiment and no recoupling is done, is usually compared to an experiment recoupling is done. In the normal experiment to be compared to the reference experiment, π pulses are applied in two other channel at the half integer multiples of the rotor-period to recouple the dipolar couplings and as a result the local dipolar field is inverted in every half rotor-period and is not averaged to zero after each rotor-period. The observed signal is dipolar dephased and reduced compared to the reference experiment. After a comparison to reference experiment, the information of the strength of the dipolar coupling can be obtained. A schematic presentation of a REDOR experiment for heteronuclear dipolar coupling case is given in figure 2.16.

First a description of an average Hamiltonian under a REDOR-type π pulse-train will be given here. The evolution over one rotor-period of the recoupling π pulse-train which starts from initial proton transversal magnetization is:

$$\begin{aligned}
\hat{I}_x &\xrightarrow{\Phi 2\hat{I}_z\hat{S}_z} \hat{I}_x\cos\Phi + 2\hat{I}_y\hat{S}_z\sin\Phi \\
&\xrightarrow{\pi\hat{S}_x} \hat{I}_x\cos\Phi - 2\hat{I}_y\hat{S}_z\sin\Phi \\
&\xrightarrow{\Phi' 2\hat{I}_z\hat{S}_z} \hat{I}_x(\cos\Phi\cos\Phi' + \sin\Phi\sin\Phi') - 2\hat{I}_y\hat{S}_z(\sin\Phi\cos\Phi' + \cos\Phi\sin\Phi')
\end{aligned} \qquad \mathbf{1.73}$$

$$\begin{aligned}
\mathit{when}\ \ \Phi = \Phi' \quad &= \hat{I}_x\cos 2\Phi - 2\hat{I}_y\hat{S}_z\sin 2\Phi \\
&\xrightarrow{\pi\hat{S}_y} \hat{I}_x\cos 2\Phi + 2\hat{I}_y\hat{S}_z\sin 2\Phi
\end{aligned}$$

The $\Phi = -\Phi_{D_{is}}\Big|_0^{\frac{\tau_r}{2}}$ and $\Phi' = -\Phi_{D_{is}}\Big|_{\frac{\tau_r}{2}}^{\tau_r}$ are used in the above formulas for simplicity. As a result of the effective inversion of the space part of the Hamiltonian by MAS, $\Phi = -\Phi'$ holds. The above formula explicitly shows the effect of two π pulses and the evolution periods in between. To be able to describe a full cycle which is a full rotor period, the second π pulse is also included in the above formula. An average Hamiltonian can be written which describes the evolution over one rotor period of the recoupling π pulse-train:

$$\hat{\bar{H}}_{is} = \bar{\Phi} 2\hat{I}_z\hat{S}_z \frac{1}{\tau_r} \quad \text{and} \quad \bar{\Phi} = 2\Phi = -2\Phi_{D_{is}}\Big|_0^{\frac{\tau_r}{2}} = \frac{D_{is}}{\omega_r} 2\sqrt{2}\sin 2\beta \sin\gamma \qquad \mathbf{1.74}$$

and the evolution over a pulse-train of N rotor-periods is given by:

$$\hat{I}_x \xrightarrow{\hat{\bar{H}}_{is} N\tau_r} \hat{I}_x\cos(N\bar{\Phi}) + 2\hat{I}_y\hat{S}_z\sin(N\bar{\Phi}) \qquad \mathbf{1.75}$$

Cosine-modulation of the initial coherence and a sine-modulated antiphase coherence are generated by the first π pulse-train. In the reconversion period the antiphase coherence is converted back into a transverse coherence state. Neither the phase nor the channel where the π pulses are applied have any influence on the average Hamiltonian. This gives a great freedom which can be used to implement different experiments with the desired advantages, like compensated for offsets, CSA, and pulse imperfections. In all of the different experiment types, the (xy-4) phase cycling scheme (Gullion 90) is proven to be very useful.

Various types of experiments exploit the fact, that different coherences can be created and probed during the t_1 evolution period. The nucleus from which the recoupling process is started (from ^{1}H or X-nucleus whose polarization is enhanced by cross-polarization), the detected nucleus (conventional X or indirect ^{1}H detection), and the coherence state probed in the indirect dimension of the 2D experiment determines the type of the experiment. Figure 2.17 shows the different types of experiments with the coherence states present in the indirect dimension.

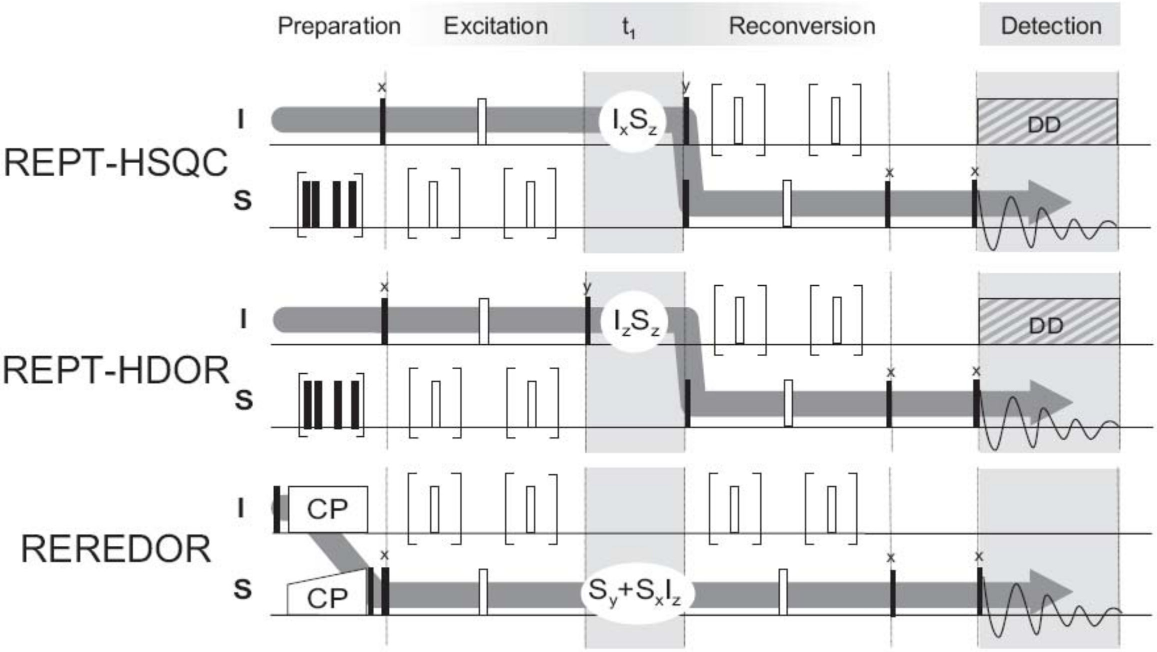

Figure 2.17: Different types of REDOR based pulse sequences for heteronuclear dipolar recoupling. Possible pathways for the transverse components of the coherence states present in the indirect dimension t_1 are indicated by the grey arrows (reproduced from Fischbach 04).

One of the first type of such experiments, TEDOR (Hing 92), has the disadvantage of not-producing the sidebands by reconversion rotor encoding due to the placement of the evolution period at the beginning of the experiment. It will not be discussed further. The other experiments can be classified further by the coherence transfer pathway and by the question whether the polarization is transferred between the nuclei. Only the DIP type of experiments (Saalwachter 01b) have the direction of recoupling from S to I and back to S and are symmetric with respect to the recoupling procedure. Other experiments have the polarization transfer from I to S nuclei and are asymmetric with respect to the recoupling procedure. The REPT (recoupled polarization transfer) technique uses an initial proton magnetization for the generation of HMQ coherences, with which the polarization is later transferred back to carbon channel. The advantage of this technique is that it does not rely on the initial cross-polarization step, which is usually not very efficient under fast-MAS. Inverse detection techniques recently introduced by Schnell (Schnell 01a) are symmetric with respect to the recoupling procedure. From all of these techniques, Rept-HSQC, Rept-HDOR, and REREDOR experiments will be explained in detail, which have been used intensively throughout this thesis.

2.7.7.1 REPT-HSQC

The heteronuclear equivalent experiment of the BaBa experiments, described in detail in the previous sections, is the Rept-HSQC experiment (Saalwachter 01a). Its general structure is represented in Figure 2.17. This experiment can also be performed in three distinct ways by selecting different evolution times, t_1. The 2D version of the experiment is described here which was used in the current study, in which the t1 is incremented in full rotor periods so a heteronuclear correlation (HETCOR) spectrum correlates S chemical shift in the direct dimension with I chemical shift in the indirect dimension.

For a better understanding of the experiment and the properties of the observed signal, the t_1 dependence of the detected S nucleus needs to be considered. The first π pulse-train creates the antiphase coherence $\hat{I}_x\hat{S}_z$. This coherence evolves during t_1 under the influence of the chemical shift and dipolar couplings of the remote spins. Considering the isotropic chemical shift evolution of the I spins, the x- and y- components of the signal are modulated by cosine and sine factors in the form of $\omega_{CS,I}t_1$. After the reconversion to observable SQ coherence, the two components of the S-detected signal are:

$$S_x(t_1) = \left\langle \sin(N_{ext}\overline{\Phi}_0)\sin(N_{rec}\overline{\Phi}_{t_1})\cos\omega_{CS,I}t_1 \right\rangle$$
$$S_y(t_1) = \left\langle \sin(N_{ext}\overline{\Phi}_0)\sin(N_{rec}\overline{\Phi}_{t_1})\sin\omega_{CS,I}t_1 \right\rangle \qquad \textbf{1.76}$$

The phase sensitive detection is achieved by TPPI for the indirect dimension which will acquire both sine and cosine modulated components. A heteronuclear correlation spectrum is obtained, if the spectrum is recorded in a rotor-synchronized manner. The t_1 dependent signal is only modulated by the isotropic chemical shift of the I spins. The strength of the dipolar coupling determines the strength of the correlation peaks as well as the number of recoupling cycles as multiples of the rotor period. Through-space distances can be probed due to the fact that the probed interaction is a through-space dipolar coupling. At short recoupling times (~ 1 rotor-period) only directly bonded ^{1}H-^{13}C pairs are observed. With increasing recoupling time, more distant spin-pair information can be probed, which will fit well for the spectral editing purposes.

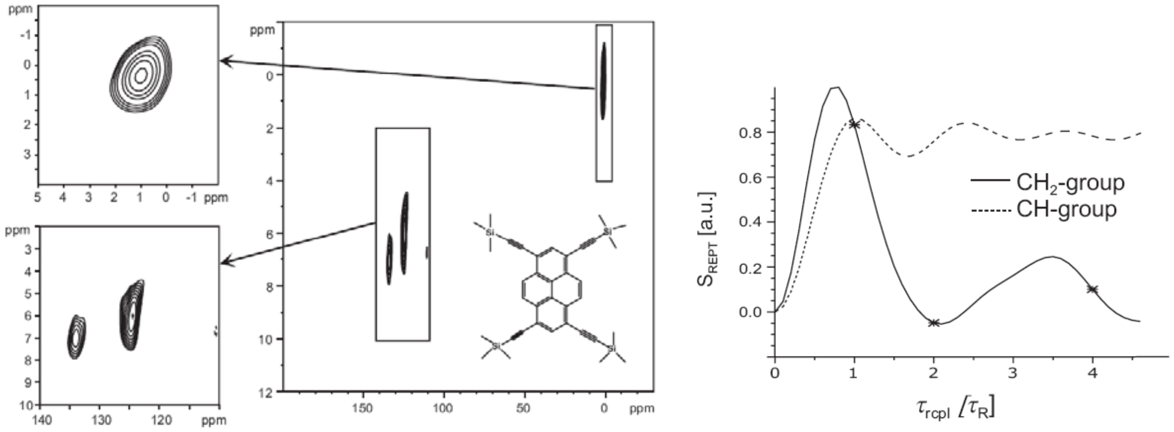

Figure 2.18: **a)** Heteronuclear correlation spectrum of a pyrene derivative obtained with the REPT-HSQC sequence at 30 kHz MAS and a excitation time of 1τ_r (Reproduced from Fischbach 04). **b)** Theoretical HSQC build-up curve for a CH group and a CH$_2$ group at 25 kHz MAS. Note that at a recoupling time of two rotor periods the CH$_2$ signal becomes zero.

An example of a spectrum recorded by the Rept-HSQC pulse sequence is presented in Figure 2.18 with additional information of the effect of recoupling times to the observed signal intensities for different C-H sites in supramolecular systems. The calculated build-up behavior for the rigid and directly-bonded CH$_2$ groups shows strong deviations from the spin-pair approximation. For the calculation of CH$_2$ and CH$_3$ groups, higher number of spins should be included to the calculations. Very interestingly, the buildup curve for CH_2 group has null signal intensity at recoupling times longer than 2 rotor-periods. This problem is circumvented by the use of REREDOR approach, described in the following sections, which can still give signal where Rept-HSQC fails.

2.7.7.2 REPT-HDOR

Despite the created antiphase coherence $\hat{I}_x\hat{S}_z$ in the Rept-HSQC experiment, a state of dipolar order $\hat{I}_z\hat{S}_z$ is created in the Rept-HDOR experiment during t_1 period. Initially an antiphase coherence, $2\hat{I}_x\hat{S}_z$, is formed during the excitation time, which is converted into a state of longitudinal dipolar order, $\hat{I}_z\hat{S}_z$, by a 90^o pulse on the I spin. After the t_1 evolution, the longitudinal dipolar order is converted back into antiphase coherence, $\hat{I}_z\hat{S}_y$, by a 90^o pulse on the S spin. Finally, by the reconversion period, the observable SQ coherence is formed. The advantage of the heteronuclear dipolar order state formed is that it does not evolve during t_1. As a result, the signal detected in a HDOR experiment becomes:

$$
\begin{aligned}
S_x(t_1) &= \left\langle \sin(N_{ext}\overline{\Phi}_0)\sin(N_{rec}\overline{\Phi}_{t_1}) \right\rangle \\
S_y(t_1) &= \left\langle \sin(N_{ext}\overline{\Phi}_0)\sin(N_{rec}\overline{\Phi}_{t_1}) \right\rangle
\end{aligned}
\qquad \mathbf{1.77}
$$

The amplitude modulation measured in this experiment is as a function of t_1 and is due to rotor encoding which leads to odd-order spinning sidebands centered around zero offset frequency in the indirect dimension. More importantly, no phase sensitive detection in t_1 is needed due to the absence of the I spin chemical shift contribution, which reduces the experimental time by a factor of two due to the detection of only *cosine* data set. Additionally, the signal in t_1 is periodic with respect to the rotor period, apart from a signal decay arising from T_1 relaxation of respective spins. Since the T_1 relaxation times are usually much longer than the timescale of the MAS, decay is mostly not observed. The sideband patterns obtained by Rept-HDOR experiment can be fitted to get the heteronuclear dipolar coupling constant. In **Figure 2.19 t**hese kind of sideband pattern is shown together with an extracted sideband pattern. The sidebands calculated for Rept-HDOR experiment deviates from those obtained for BaBa experiment due to the difference between homonuclear and heteronuclear dipolar coupling by a factor of 3/2. A suitable recoupling time is chosen in such a way that $D_{IS}\tau_{rcpl} \approx 1.6$.

In the case of multi-spin systems, a more complicated formula must be used for the detected signal (Saalwachter 01a). The CH_2 groups again exhibit zero signals also in Rept-HDOR experiment at higher recoupling times. The REREDOR approach solves this problem for CH_2 groups, which will be discussed in the following section.

2.7.7.3 REREDOR

The Rotor Encoded REDOR experiment (REREDOR) is obtained by inserting a t_1 delay after both recoupling periods (Saalwachter 02). Spinning sidebands can be generated by the reconversion rotor encoding mechanism. The time evolution can be calculated by summation of the phases acquired under the action of the whole sequence (excitation – t_1 – reconversion – t_1):

$$S \propto \left\langle \prod_i \cos(N_{ext}\bar{\Phi}_0^{(i)} - \bar{\Phi}^{(i)} \big|_0^{t_1} - N_{rec}\bar{\Phi}_{t_1}^{(i)} - \bar{\Phi}^{(i)} \big|_{t_1}^{2t_1}) \right\rangle \qquad \mathbf{1.78}$$

The possibility of couplings to more than one spin is already included by the product. The REREDOR experiment has the advantage compared to Rept-HDOR experiment, that the CH_2 groups do not vanish for longer recoupling time. As a result, sufficient sidebands can be created to extract the dipolar couplings. Moreover, the even order sidebands are also observed in addition to the odd order sidebands. By neglecting the two $\bar{\Phi}^{(i)} \big|_{t_a}^{t_b}$ terms, which can be done under fast MAS conditions and/or weak dipolar couplings since these terms describe the residual dipolar evolution during the two t_1 periods (Saalwachter 02). By restricting to only the dominant recoupling terms and a single spin-pair interaction, former equation becomes:

$$\begin{aligned} S &\propto \left\langle \cos(N_{ext}\bar{\Phi}_0 \;- N_{rec}\bar{\Phi}_{t_1}) \right\rangle \\ &\propto \left\langle \sin N_{ext}\bar{\Phi}_0 \;\sin N_{rec}\bar{\Phi}_{t_1} \right\rangle + \left\langle \cos N_{ext}\bar{\Phi}_0 \;\cos N_{rec}\bar{\Phi}_{t_1} \right\rangle \end{aligned} \qquad \mathbf{1.79}$$

It is clear that both the odd-order (sin-sin term) and even-order (cos-cos term) sidebands are created. The REDOR sideband pattern can be decomposed into a sum of a Rept-HDOR (only odd-order sidebands) and a RELM (only even-order sidebands) experiment. One other crucial experimental fact is that REREDOR experiment starts from S spin, whereas REPT-HDOR experiment starts with I spin. As a result the behavior of the

a)

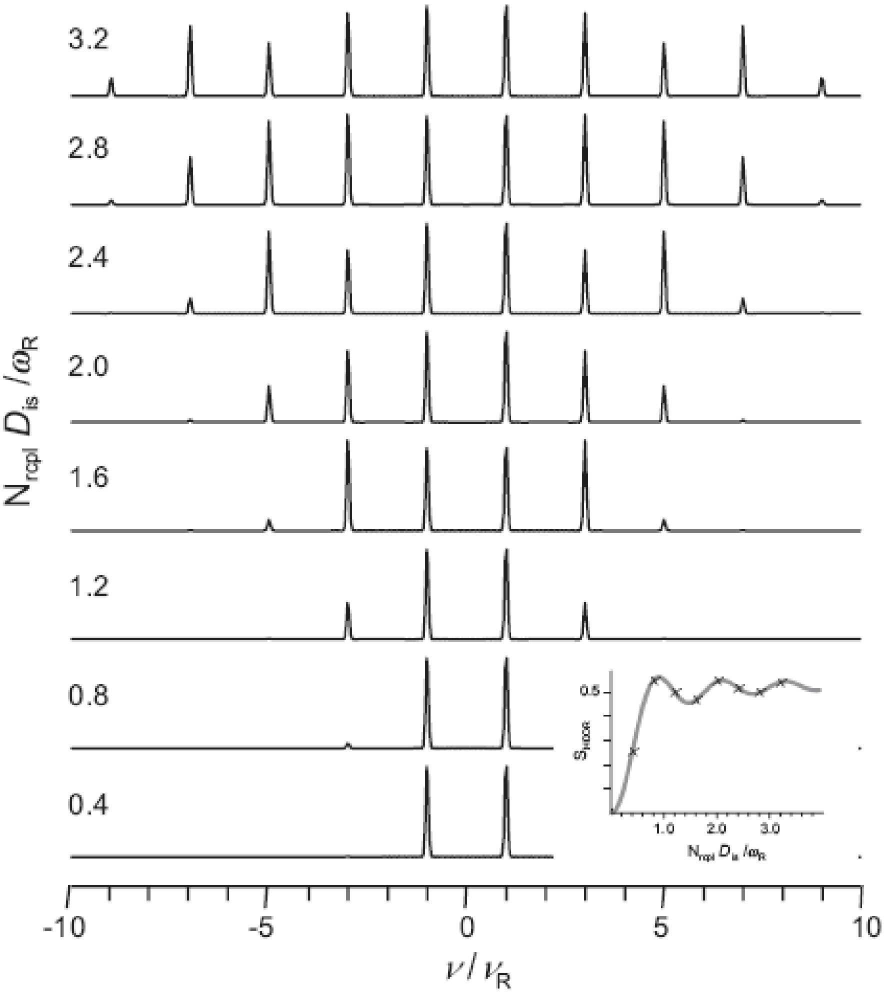

b)

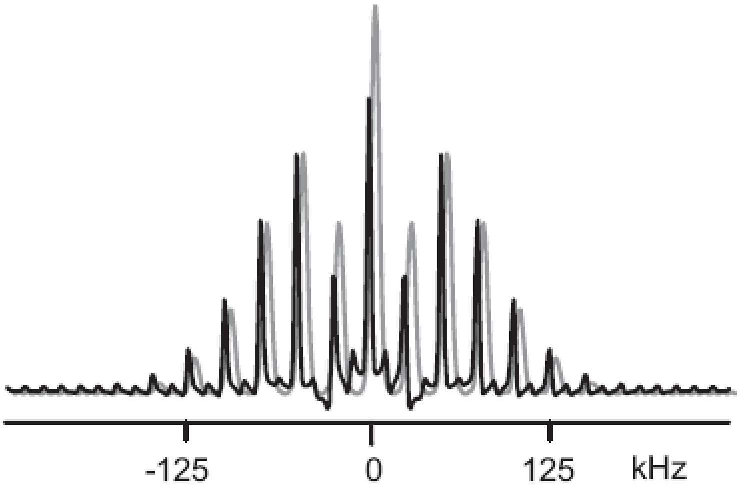

Figure 2.19: a) Calculated REPT-HDOR sideband patterns for various $D_{IS}\tau_{rcpl}$. The inset shows the corresponding build-up curve with the experimentally accessible points marked by asterisks. b) REREDOR sideband patterns of the CH group in L-Alanine measured at 25 kHz MAS and $\tau_{rcpl} = 2\tau_R$. The underlying grey pattern is a simulation with Dis/2π = 21kHz (From Fischbach 2003).

spins evolves differently under the influence of the remote spins in these two different experiments. Different spin-dynamics are active in these two experiments.

It can be concluded that the REREDOR experiment should be more sensitive than the other heteronuclear recoupling methods here due to the fact that it generates more sidebands, provided that the initial cross-polarization step is efficient. In some mobile samples this initial CP step sometimes become very problematic. In Figure 2.19 REREDOR sideband pattern of the CH group in L-Alanine is represented.

Chapter 3:

Structure and Dynamics of Anhydrous Proton Conducting Triazole-Functional Siloxane Polymer

In this chapter a promising type of proton conducting material is investigated by solid state NMR. The material is triazole-functional polysiloxane which exhibit water-free proton conductivity higher than those previously reported (Granadas 07). The system has an approach in which the functional unit is an amphoteric triazole heterocycle. Proton transport within heterocyclic hydrogen-bonded networks occurs under both anhydrous and low relative humidity conditions and could thus be used to develop polymer membranes that are highly conductive at temperatures above the boiling point of water. The triazole functional unit can lead to a higher conductivity compared to the imidazole and benzimidazole functional units (Zhou 06), which made us to investigate this system in detail. This system is an example of the homopolymer approach to achieve high proton conductivity with triazole functional units. The structure of the system is shown in Figure 3.1 with all of the three different possible conformations which differ from each other in terms of the nitrogen atom with the proton attached to it.

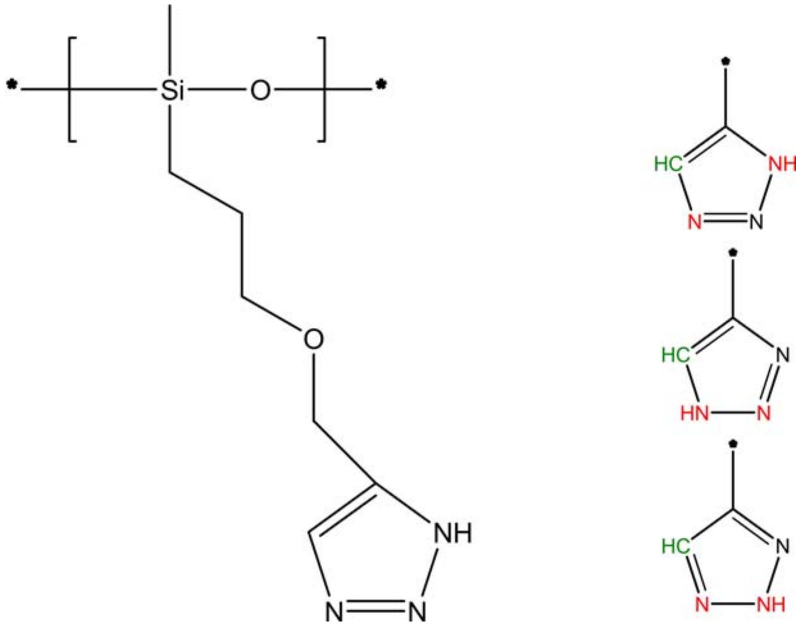

Figure 3.1: Chemical structure of the Tz5Si material studied, and its three different tautomers with different protonated nitrogen sites.

3.1. General Introduction to Proton Conductors

One promising solution, towards a clean portable energy source, is the polymer electrolyte membrane fuel cell, (PEMFC), having many applications already in the automotive and electronic industries (Colombon 92, Steininger 07). At ambient temperatures (up to 80 ^{o}C), Nafion® and similar acid-functionalized hydrophilic polymers are being used in PEMFC systems, exhibiting high proton conductivity and moderate stability (Carette 01, Mauritz 04). Next to the Nafion ionomer, arylene main-chain sulfonated polysulfone (sPSU, Udel®) (Linkous 93) and sulfonated poly(etheretherketone) (sPEEK, Victrex®) (Helmer-Metzmann 93) systems are available which show better stabilities compared to Nafion. However, they suffer from high cost (Ye 06), CO poisoning (Kreuer 97), and methanol crossover disadvantages (Apple 96). Methanol crossover and CO poisoning may be prevented by modifying the membranes with inorganic particles like H_3PO_4 oxoacids (Antonucci 99, Dimitrrova 02, Kreuer 96), using costly noble electrolyte materials, or much more easily by increasing the PEMFC operation temperature. Thus, proton conducting polymers with acceptable cost and performance is still a topic of ongoing research which is being away from complete.

Shifting the operation towards higher temperatures removes most of the problems, but causes the evaporation of crucial solvents from the membrane materials. In order to produce an operable proton conducting membrane at medium or high temperatures, a transport mechanism not depending on water has to be employed. One attempt is the replacement of water with alternative proton solvents (imidazole, pyrazole, benzimidazole or triazole) (Kreuer 98, Gunday 06, Zhou 06, Schuster 03). In this case, the operation temperature is limited by the boiling temperature of the solvent, especially in open fuel cell systems. Kreuer et. al. shows that the use of imidazole as the base component in place of water can provide not only higher proton conductivity in sulfuric acid solution, but also displayed better temperature stability due to the fact, that imidazole is a stronger Brønsted base compared to water (Kreuer 98). The use of amphoteric protonic materials with high self-dissociation constant as base in the presence of highly self-dissociable acid accomplishes fast proton conduction in the order of 10^{-2} S/cm (Yamada 05).

Organic-inorganic hybrid systems also have been proved to have many advantages compared to other systems, and have shown stability at high temperatures with high conductivity (Lee 05). Poly-benzimidazole (PBI) treated with H_3PO_4 showed high conductivity in the absence of water (Wainright 95, Wang 96). The polybenzimidazole-phosphoric acid membranes (Kerres 99) are now being pursued by developers of stationary fuel cells (Kerres 96). Leaching of the dopant material is the main problem in this type of materials.

Acid-base interaction is one of the material design concepts, where the protons are only weakly bound to the action of a base functional group. The use of amine base complexes with protonic acid system as a proton conductor in non-aqueous state was reported earlier, where it was shown that the complexes of triethylenediamine with H_2SO_4 exhibit proton conductivity (Lassegues 89, 92). The observation that conductivity can change remarkably with the composition of base or acid in the system has attracted significant attention. This has been largely attributed to the transient protonic defects as well as to the mobility in these small molecule solvated systems.

More recent development has been carried out on acid/base oligomer systems by Honma et. al (Honma 99), and on polymer blend systems bearing acid/base functional groups by Kerres et. al (Kerres 99). The fact that protons are not stationary, but show long range transport between acid/base complex is clearly demonstrated by a layer-by-layer deposition of alternating acid and base polymers (Takahashi 76, Lassegues 89, Tiitu 05).

Cesium hydrogen sulfate and other inorganic acid salts that undergo a superprotonic phase transition have been investigated by Haile et. al (Haile 97, 98). Takahashi et al. have investigated bisulfates of diethylenediamine and hexamethylenetriamine and found that organic amine salts of protic acids are capable of proton conduction over a wide temperature range (Takahashi 76). Lassegues et al. have investigated the structure of a variety of polymeric amine salts by infrared spectroscopy and have shown that proton conduction can readily occur through ionization and re-organization of hydrogen-bonded networks (Lassegues 89). The latter studies were restricted to temperatures below 100 °C.

Recently, new anhydrous proton conducting material based on polyimide and phosphoric acid composite have been explored. Sulfonated polyimides (sPI) have already been used as proton conducting materials (Takahashi 76, Lassegues 89). However, sPI do not show proton conduction in absence of water. Based on the same conducting principle of polybenzylimidazole, doping PI with phosphoric acid in the anhydrous state, a reasonable conductivity in the order of mS/cm is established suitable for medium temperature fuel cell. In the system, the phosphoric acid interacts with polyimides mainly by hydrogen bonds rather than by protonation of PI at room temperature (Hong 05).

The current system studied here is Triazole functional polysiloxane which is a promising alternative heterocyclic whose structure is similar to imidazole but contains three nitrogen atoms in the ring (Structure is shown in Figure 3.1). Recently, Triazole was used as a protogenic solvent in a blend with acidic polyelectrolytes to generate high temperature resistive and electrochemically stable free-standing films. Polymer electrolyte membranes consisting of an acidic polymer host and Tri allowed for long range proton transport via structural diffusion (Gunday 06, Kim 07, Granadas 07, Celik 08).

3.2. Results

In this section, the results obtained with solid-state MAS NMR techniques will be presented. Understanding the origin of the proton conduction on the molecular level will be supplied. The microscopic information obtained by the advanced NMR methods will be compared to the macroscopic conductivity information obtained by other conventional methods, like impedance spectroscopy.

^{1}H MAS NMR spectra will supply valuable chemical shift information of different proton sites. This information is extremely important due to the sensitivity of the proton chemical shift value to the supramolecular non-covalent interactions, like hydrogen-bonding and ring-current effects due to π-π packing of aromatic moieties (Brown 01). In addition to this information, ^{1}H variable-temperature (VT) MAS NMR will elucidate the local proton mobilities and timescale of molecular motions, which will be compared to conductivity measurements. Additionally, exchange processes of the acidic protons will be clarified with a detailed analysis of the proton line shapes obtained at various temperatures. The comparison of MAS spectra to the ^{1}H double-quantum filtered (DQF) MAS spectra will allow us to distinguish mobile and rigid protons. Moreover, the proton proximities will be obtained in a semi-quantitative manner by the use of 2D ^{1}H DQ MAS NMR.

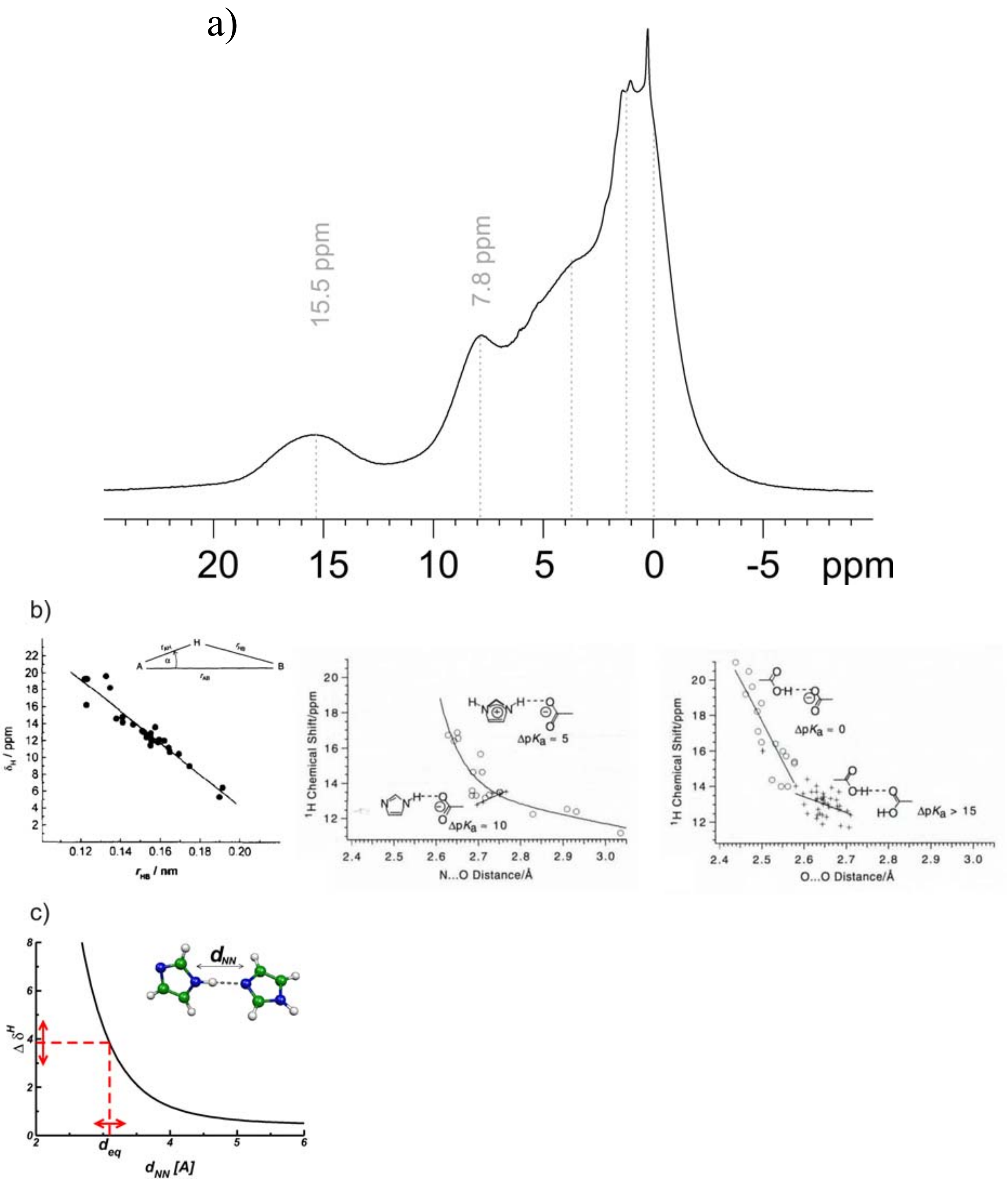

Figure 3.2: a) ^{1}H MAS NMR spectrum of Tz5Si recorded at 233 K (T_g-47 K) and 25 kHz of magic-angle spinning frequency. **b)** The correlation between the distance of O-H···O, O-H···N, N-H···N and the proton chemical shift value in a variety of solids (adapted from Brunner 98 and Wei 99) **c)** The correlation between the distance of N-H···N and the hydrogen-bonded proton chemical shift in a crystalline imidazole material (Sebastiani 08). The figure shows the chemical shift difference from an imidazole calculated by quantum chemical calculations in the gas phase which has a NH proton chemical shift of ~10 ppm.

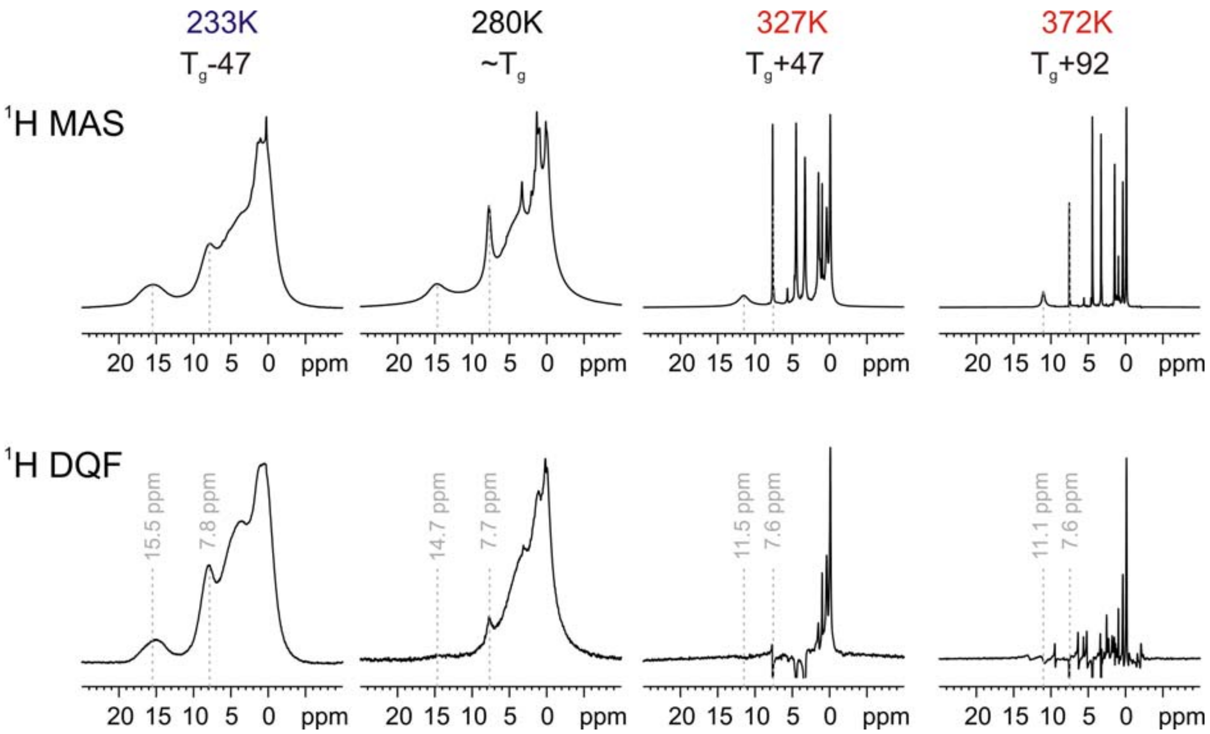

Figure 3.3: ^{1}H MAS and DQF spectra of Tz5Si at various temperatures (233, 280, 327, and 372 K) and 25 kHz MAS. The DQF spectra recorded with one rotor-period BaBa pulse sequence to recouple the dipolar-couplings.

By selective deuteration of the acidic NH protons at the triazole ring, a site selective probe was added to the system to gather information on motional processes. ^{2}H MAS NMR results will be analyzed to obtain deeper understanding on the ring-flipping and proton-hopping processes of the triazole ring and acidic NH proton. Moreover, the motion of the acidic ring NH will able to be monitored in a unique manner without bothering the additional effects of remote protons and ring motion, which are the case in proton linewidth analysis.

3.2.1 One-dimensional ^{1}H MAS & DQF MAS NMR: Structure of the System

The proton chemical shift value is very sensitive to the supramolecular interactions, hydrogen-bonding in the current system. High-resolution ^{1}H MAS NMR spectra can be obtained under fast magic-angle spinning. In the presence of hydrogen-bonding, low-field shifted chemical shift values are observed (Brown 01). The degree to which a ^{1}H resonance is shifted to higher frequency has been found to correlate with the strength of the hydrogen bond in which it is involved. There is a well established correlation between the distance of the two electronegative atoms (O$\cdots$O, O$\cdots$N or N$\cdots$N) involved in hydrogen-bonding and observed proton chemical shift value which is attached to one of the two atoms (Berglung 80, Jeffrey 86, Harris 88), shown in Figure 3.2b. For the N-H$\cdots$N case (Benedict 98, Kimura 00, Goward 01, Sebastiani 08), this correlation is particularly important to estimate the distance in the current system (Figure 3.2c, with the equilibrium value of N···N distance ~3.1 Å). Previously chemical shift values between 14 and 18 ppm were obtained for a hydrogen-bonded NH proton (Unugur 08, Akbey 08).

In Figure 3.2, the ^{1}H MAS spectrum of ***Tz5Si*** is represented recorded at 233 K (in the rigid solid phase at a temperature ~50 ^{o}C below T_g) and 30 kHz MAS. Due to the rigid nature of the sample at this low temperature, the proton resonances are broad. However, the resonances at different proton sites are clearly separated for aliphatic (H_a), OCH_2 (H_b), aromatic CH (H_c) and NH (H_d) protons at around 2, 4, 8 and 15.5 ppm, respectively. The high chemical shift value of the triazole NH at ~15.5 ppm indicates that this proton is involved in a strong hydrogen bond and allows us to estimate the distance between the two N atoms involved in the hydrogen bond to be ~2.8 Å according to a quantum chemical calculations of an imidazole material forming N-H···N type of hydrogen bonding (Sebastiani 08), which is similar to the triazole material. The separate chemical shift values observed for aromatic CH and NH protons will allow us to study the dynamics of aromatic ring and hydrogen-bonding separately, which will be explained in detail in the coming sections.

The ^{1}H MAS and DQ-filtered MAS NMR spectra recorded at various selected temperatures are represented in Figure 3.3. At low temperatures, ~50 ^{o}C below T_g, there is no difference between these two spectra, meaning that the protons are rigid. At temperatures near T_g (280 K), however, a complete loss of the hydrogen-bonded NH proton resonance and a significantly reduced intensity for the aromatic CH proton is observed. This clearly shows that the NH resonance is already mobile and has motional timescale at least in the range of the timescale of the ^{1}H DQF NMR experiment, which is ~ 80 μs (for a DQF experiment with one rotor-period of recoupling time). Resonances other than the NH proton remain after the application of DQF, so the dipolar interactions are not reduced much for those by any kind of molecular motions. At temperatures above T_g, all resonances in ^{1}H MAS become narrower due to increased molecular mobility. As a result the dipolar couplings of those protons are reduced significantly which can be seen in the DQF spectra at those temperatures, given in Figure 3.3. The line narrowing effects and chemical shift changes will be explained in more detail later.

3.2.2 Two-dimensional rotor-synchronized ^{1}H DQ MAS NMR: Proton Proximities and Order in the System in the Solid-Phase

To get information on spatial proximities, a two-dimensional rotor-synchronized ^{1}H

DQ MAS spectrum was recorded with one rotor period BaBa recoupling time at 25 kHz MAS and 233 K (the ***Tz5Si*** material is in solid-phase at this temperature). As expected, strong auto-peaks are observed for the aliphatic and OCH_2 protons at 1/2 and 4/8 ppm in the SQ/DQ dimensions, and a cross-peak between these two types of protons. For the aromatic CH proton, a weak auto-peak is observed which shows that the ring protons are still in the close proximity to each other. Two cross-peaks are observed for CH protons indicating the close proximity of this proton to both OCH_2 and aliphatic protons. The latter cross-peak at 9 ppm in DQ dimension is somewhat interesting to observe and not easy to understand, because one normally would not expect this resonance. The chemical shift of 9 ppm is the sum of the ring CH proton chemical shift (8 ppm) and the $–CH_2$ proton (1 ppm) chemical shift, of the CH_2 group directly attached to the siloxane polymer backbone. This indicates that in solid-phase of the material the triazole rings has interactions to the polymer spacer CH_2 units.

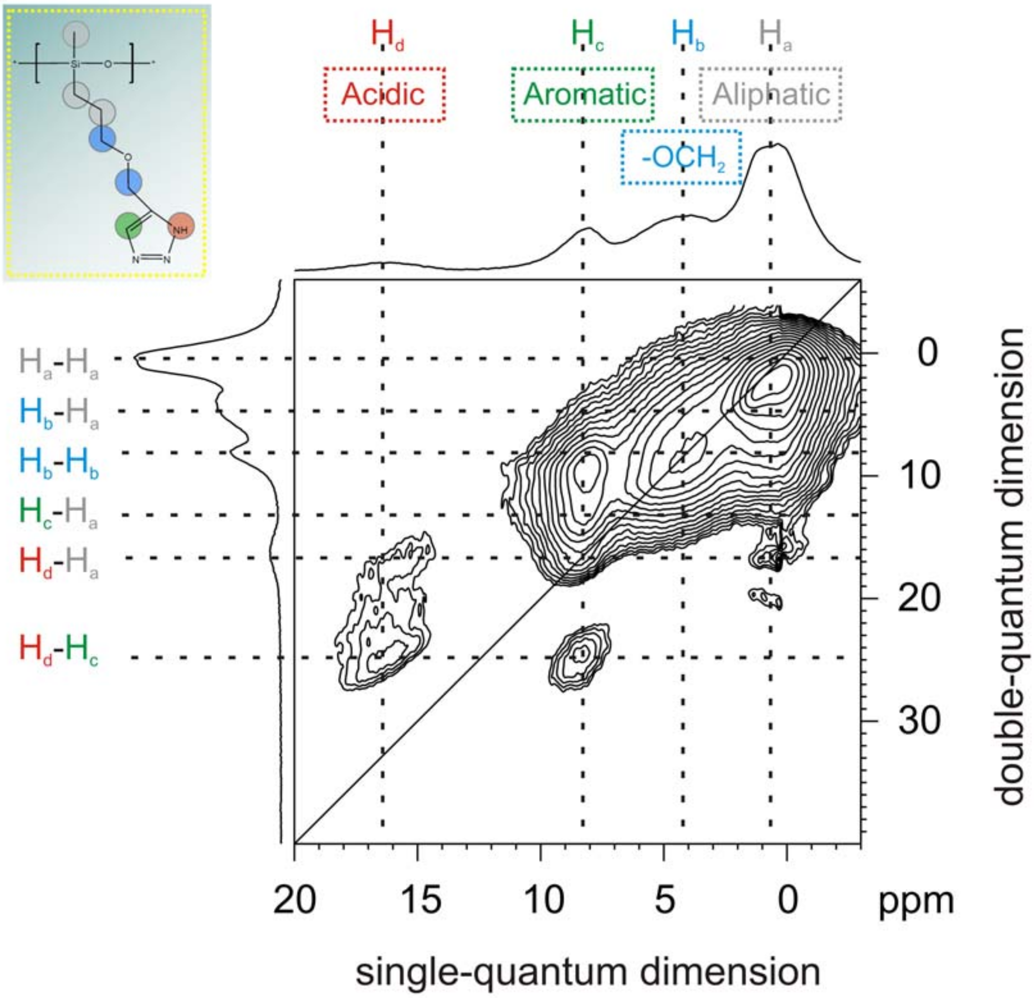

Figure 3.4: 2D ^1H DQ MAS NMR spectra of ***Tz5Si*** recorded at 233K and 25 kHz with one rotor-period of BaBa recoupling pulse sequence.

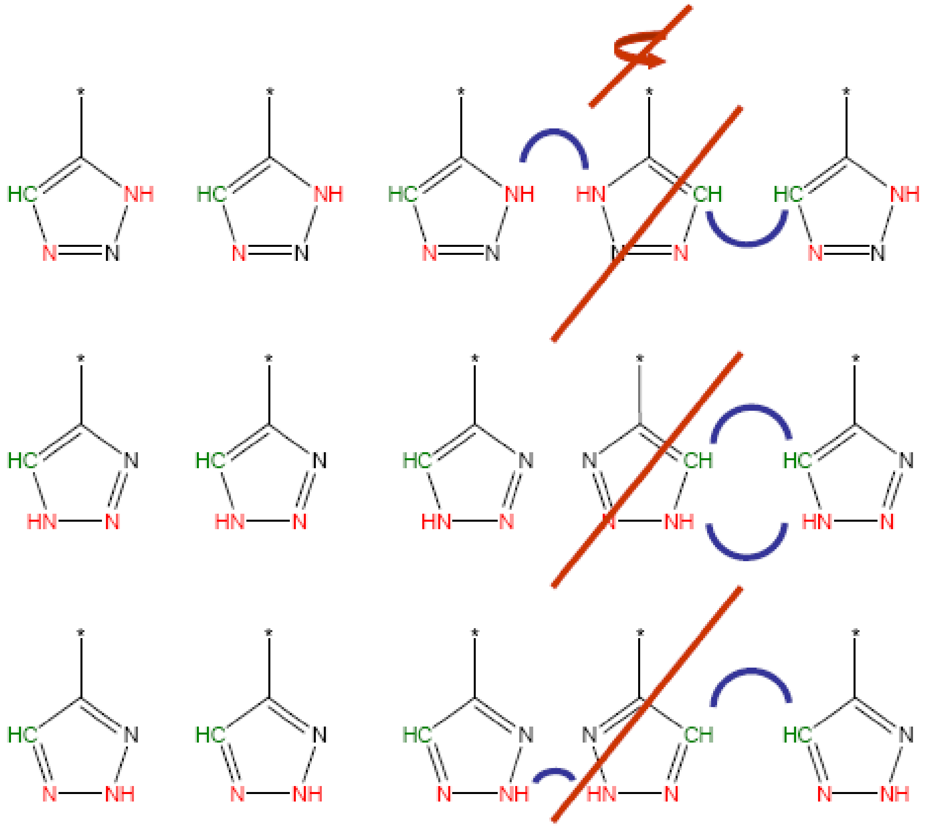

Figure 3.5: Schematic representation of the molecular ordering in ***Tz5Si*** material according to the proton proximity information obtained from ^{1}H DQ MAS NMR result. Three different triazole conformations are presented in which the acidic proton attached to triazole ring nitrogen atom is at different positions.

Finally, the acidic NH proton also does not show an auto-peak which would be expected at ~15/30 ppm in SQ/DQ dimension, meaning that the triazole ring form a hydrogen-bonded structure that is based on single and spatially separated N–H···N bridges in contrast to dimer-like structures, comparable to found in Imi-nEO materials (Goward 2002). The triazole NH protons form a hydrogen-bonded structure among themselves but still having close proximities to the aliphatic protons, most probably to the spacer –CH_2 protons, similar to the situation observed for the ring CH. This observation is different from the Imi-nEO case in which such proximities were not found.

The observed proton interactions from 2D ^{1}H DQ MAS NMR spectra are illustrated schematically in Figure 3.5, in a somewhat simplified manner. Three different triazole tautomers are presented in which the acidic proton attached to triazole ring nitrogen is at different positions. In the case of a ring flip preserving the NH hydrogen-bond at any arrangement is additionally represented in the figure. It would result in the observation of an auto-peak due to NH dimer and additionally an auto-peak due to the close proximity of the nearby protons of triazole ring CH protons. As these are not observed, it can be proposed that the arrangement of the triazole rings in the solid-phase of ***Tz5Si*** material are rather in a continuous ordered manner, in which the NH and CH protons are apart from each other and do not see each other to result in an auto-peak. At elevated temperatures, ordered packing of the triazole ring is disturbed by ring flipping motion as a result proton hopping becomes more probable. These aspects will be discussed in the following sections in more detail.

3.2.3 Variable Temperature ^{1}H & ^{13}C MAS NMR: Dynamics in the System & Chemical Exchange

The variable temperature ^{1}H MAS NMR spectra of ***Tz5Si*** recorded at 25 kHz MAS are shown in Figure 3.6a in the temperature range of 233 – 373 K. A continuous line narrowing with increasing temperature is observed for all proton resonances except for the NH proton resonance. The NH spectral region is shown separately in Figure 3.6b.

Several trends are observed after a careful consideration of the lineshapes and chemical shift changes of the resonance. The resonances of aliphatic, OCH_2 and aromatic protons exhibit a marked line narrowing especially above the glass-transition of the ***Tz5Si***. At very high temperatures, far above T_g, narrow resonances with full-width at half maximum values similar to those in liquid-state NMR are observed. No significant changes in chemical shift were observed for those resonances. In contrast, the acidic NH proton shows a much more complex behavior. From 233 K up to 269 K, a line narrowing and from 269 K up to 301 K a line broadening is observed. Above this temperature up to 373 K, the line narrows again. Throughout all of these temperatures, a gradual chemical shift change is observed in addition to the line width changes. The chemical shift of the NH changes by ~4.3 ppm (~3 kHz) from 15.3 ppm (at 233 K) to 11.03 ppm (at 373 K).

^{1}H DQ-filtered MAS NMR spectra recorded at various temperatures are also presented in Figure 3.3. The dipolar coupling of a specific proton must be constant for a duration exceeding the total recoupling time (sum of excitation and reconversion, in the current case 80 μs) to give rise to a signal. Thus, any motion on this timescale (rates of ~10 kHz or faster) will interfere with the experimental timescale and result in a loss of the DQF signal. The DQF spectrum recorded at 233 K clearly shows the presence of both the triazole NH and CH protons. However, with increasing temperature, the intensity of these two resonances decrease remarkably, and above the glass-transition temperature (~280 K) both signals disappear beneath the noise level. It should also be noted that, both the NH and CH

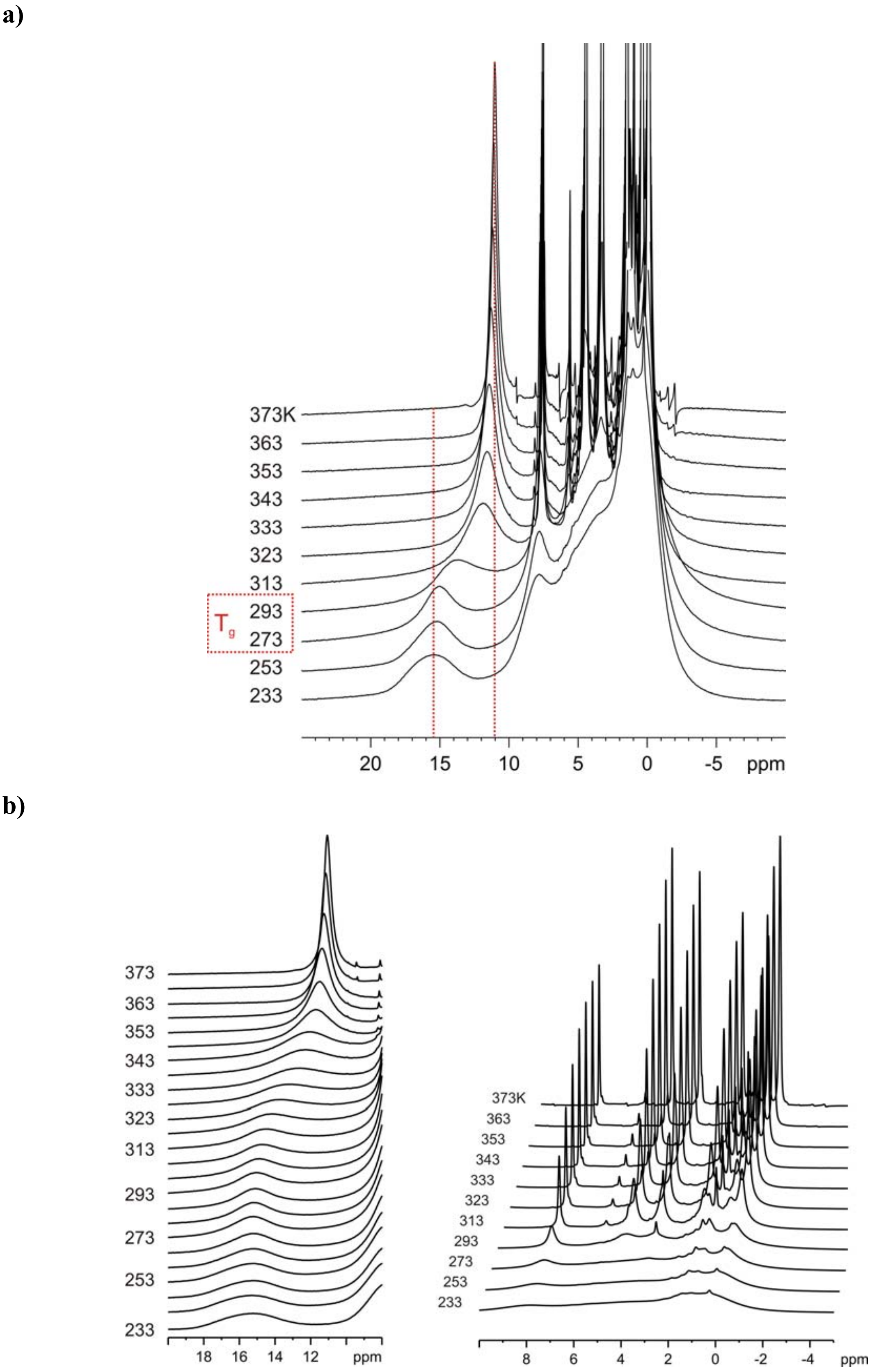

Figure 3.6: a) ^{1}H variable-temperature MAS NMR spectra of ***Tz5Si*** recorded at 25 kHz MAS. Pronounced line narrowing at all proton resonances can be seen at elevated temperatures. **b)** Acidic region and the remaining regions (aromatic and aliphatic) of the spectra are represented separately.

DQ signal vanish at the temperatures where pronounced high-field shift of NH signal is observed in ^{1}H MAS spectra.

Variable-temperature ^{13}C CP-MAS NMR spectra of the ***Tz5Si*** are given in Figure 3.7. The efficiency of the polarization transfer from protons to carbons strongly depends on the strength of the dipolar coupling between these two nuclei. With increasing temperature, the molecular mobility of nearly all different sites in the system increase significantly which reduces the dipolar coupling strength and thus the CP-MAS signal. This situation can clearly be seen in Figure 3.7, where the signals of ring, OCH_2, and two other spacer carbon signals nearly disappear at 260 K, and above ~290 K the last signal in the spectrum, the methyl carbon attached to the siloxane backbone, vanishes as well. This observation proves the gradual increase of the mobility of the system with temperature increase which manifests itself as a line narrowing effect in ^{1}H MAS spectra.

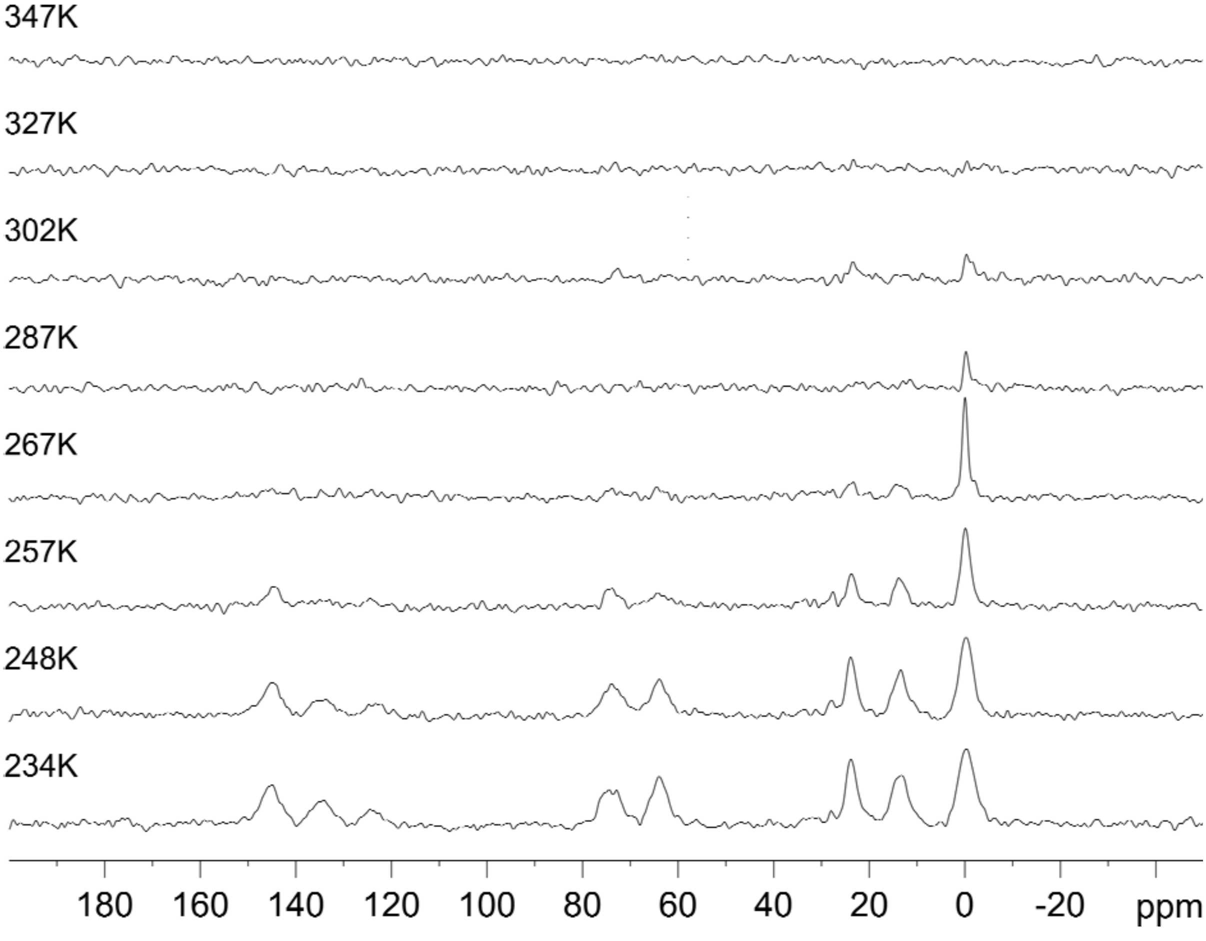

Figure 3.7: ^{13}C variable-temperature cross-polarization (CP) MAS NMR spectra of ***Tz5Si*** recorded at 20 kHz MAS with a CP contact-time of 2 ms.

3.2.4 ^{2}H NMR Results: Acidic Ring ND Dynamics

Figure 3.8 shows variable temperature ^{2}H MAS NMR spectra of *Tz5Si* recorded at 25 kHz MAS and at 107.47 MHz ^{2}H Larmor frequency. Due to the selective deuteration of the acidic NH proton, only resonances from this position are observed in the ^{2}H MAS spectra. The spectra were recorded over a wide temperature range from 233 K up to 373 K. At low temperatures, no ND signal is observed. Above T=303 K, slightly above the glass-transition temperature, the ND resonance starts to grow and show a continuous line narrowing with increasing temperature up to 373 K.

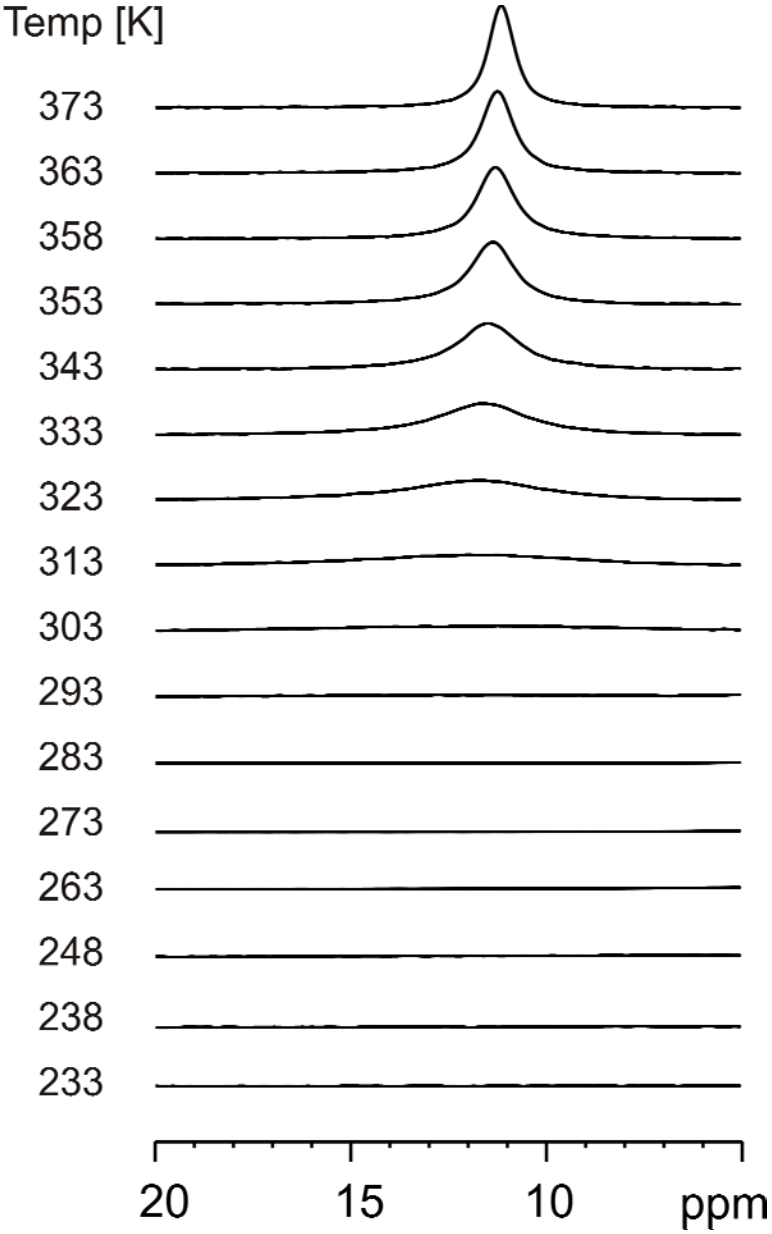

Figure 3.8: Variable temperature ^{2}H MAS NMR spectra of deuterated-***Tz5Si*** material recorded at 25 kHz of MAS.

The absence of the ND resonance at lower temperatures is due to the broadening of the deuterium linewidth by not averaged deuterium quadrupolar-coupling, because of the interference of the mobility and echo-formation. After certain temperature, however, due to the increased molecular mobility at the deuterium sites, the linewidth of the resonance significantly sharpens and becomes visible. More detailed linewidth analysis will be performed in the following sections, and the obtained activation energy will be compared to the value obtained from ^{1}H variable temperature linewidth analysis.

^{2}H static NMR experiments were also performed for the deuterated material to understand more about the dynamics of the deuterium site (ND) at lower temperatures. However, due to substantial broadening of the lines at lower temperatures, no signal was observed. No additional information was observed.

3.3. Discussion & Interpretation

A detailed analysis of the NMR results will be given in this section to understand the details of the processes active in the studied system. Special emphasis will be placed on the chemical exchange which has a great importance in the proton conduction mechanism.

3.3.1 Chemical exchange of the triazole ring NH protons

In Figure 3.9a, as it was stated before, at 233 K the acidic ring NH resonance appears at 15.3 ppm and at 373 K the same resonance is observed at a much different chemical shift value, at ~11 ppm. Additionally, the linewidth of this resonance is changing remarkable by the temperature elevation, first a slight line narrowing is observed until the temperature of ~270 K, then a subsequent line broadening which is followed again by a line narrowing above ~300 K. Moreover, a dramatic DQ signal intensity loss is observed for this particular resonance, in which case after 290 K the signal is more or less removed from the spectrum. These observations will now be described in detail by an exchange process in which there is equilibrium between a hydrogen-bonded and a free NH at each temperature with different populations.

The following chemical equation (eq. 1) is representing the exchanging species:

$$NH \cdots N \underset{k_b}{\overset{k_f}{\rightleftarrows}} NH + N \qquad (1)$$

where k_f and k_b are the rate constants (in units of Hz, s^{-1}) for the breaking of hydrogen-

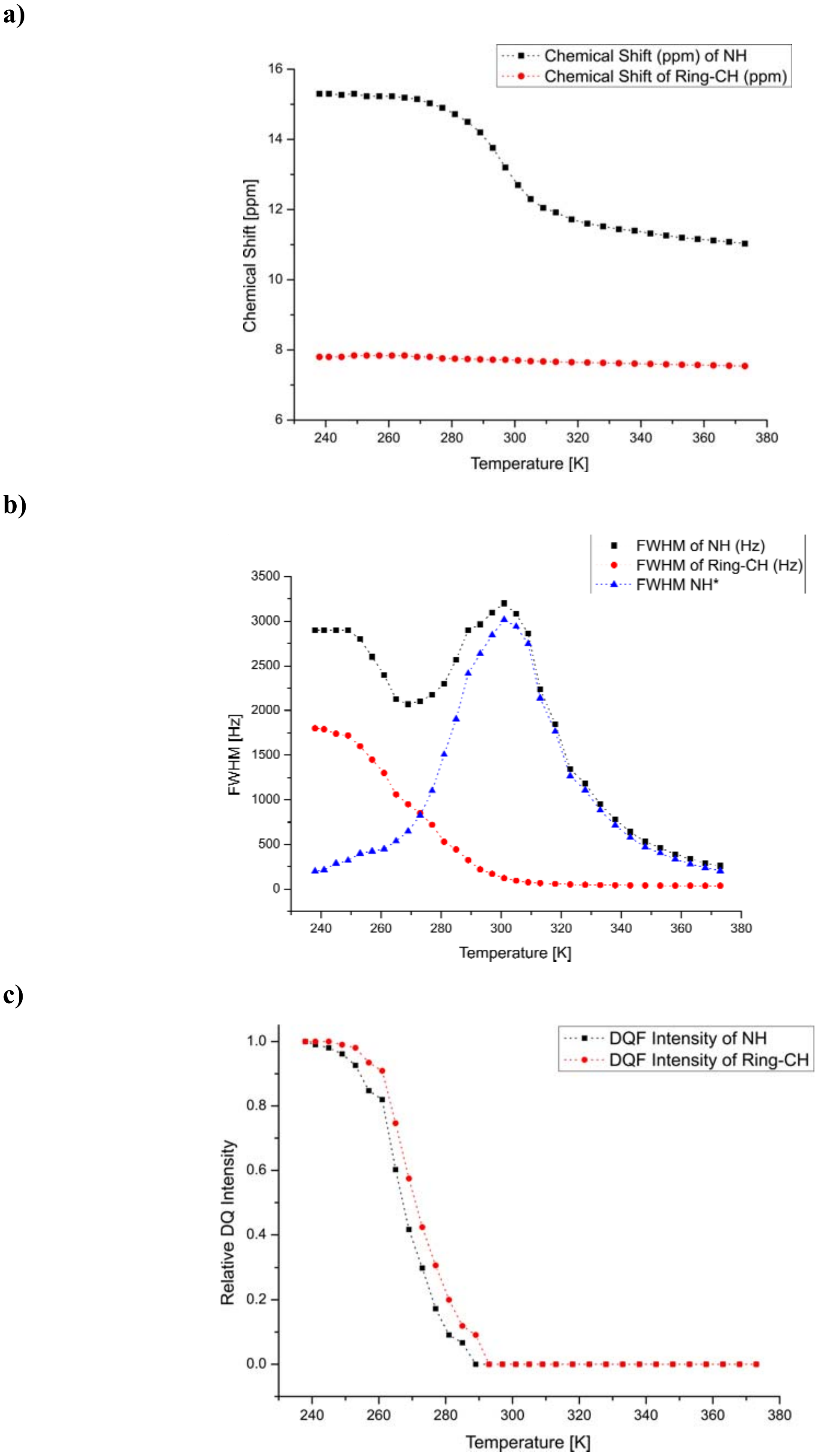

Figure 3.9: The effect of temperature on different spectral observables for both triazole ring CH and NH protons. **a)** Chemical shift changes at various temperatures. **b)** Full width linewidths changes at half maximum at different temperatures. **c)** Relative double-quantum intensity changes at different temperatures.

bonding (forward reaction, k_f) and for the formation of hydrogen-bonding (back reaction, k_b) (Brown 2001, Harris 94). Depending on the ratio of hydrogen-bonded and free NH, the position of the observed chemical shift changes in the spectra. This behavior can easily be formulated (eq. 2):

$$\delta_{ave} = (1\text{-}a).\ \delta_{hb} + a.\ \delta_f \tag{2}$$

where ***(1-a)*** and ***a*** are the populations of the hydrogen-bonded and free NH protons.

Assuming that the system is in equilibrium at each temperature after a sufficiently long equilibration delay (typically 5-10 minutes of waiting period prior to measurements), the ratio of the rate constants can be equated to obtain the equilibrium constant (K) at each individual temperature. The values of ***a*** can be calculated at a temperature from the observed chemical shift value with knowledge of the chemical shift values of the hydrogen-bonded and free NH proton. At the lowest temperature only the hydrogen-bonded NH exists and its chemical shift value is determined to be 15.3 ppm. At the highest temperature, nearly a plateau at 11.03 ppm is obtained above ~350 K in the chemical shift value, ascribed to the slightly hydrogen-bonded NH species. The formula for the equilibrium constant is;

$$K = \frac{k_f}{k_b} \tag{3}$$

In Figure 3.10, the rate constant for the chemical exchange, k_{ex}, and the lifetime, τ_{mean}, of the hydrogen-bonded NH dimer in terms of micro-second are represented, which are *kinetic* parameters of the exchange process. It should be keep in mind here that due to the dominating dipolar couplings and additional line-broadening in the intermediate-exchange limit, the analysis is only applicable in the fast exchange limit which is reached after the temperature of T=301 K. In fact, when a correction to the linewidth of the NH proton resonance is applied, by simply subtracting the linewidth of ring CH from NH, the corrected linewidth values without residual dipolar couplings can still be obtained, but this procedure will not further be analyzed. It is sufficient to state here that, symmetric patterns are observed after this correction in the line width of NH (the red lines are due to the corrected line widths).

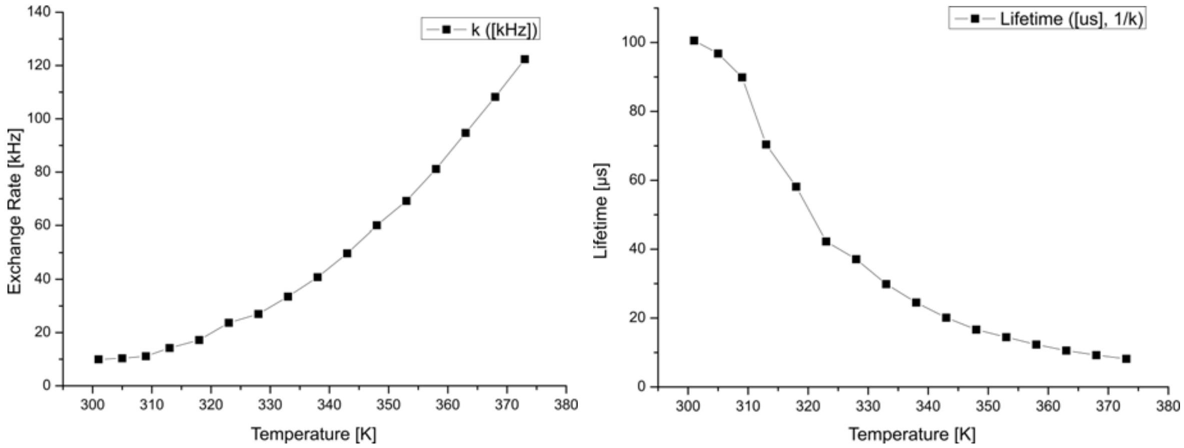

Figure 3.10: The rate constant, k_{ex} (in the unit of kHz), and the lifetime (τ) of the hydrogen-bonded NH dimer in terms of μs ($\tau_{mean}=1/k_f$), in the temperature range of 300 – 373 K.

Table 3.1: The values of the lifetime, τ_{mean} (in μs), and the exchange rate, k_f (in Hz), of the hydrogen-bonded NH proton at specific temperatures.

Temperature (K)	Exchange rate, k_{ex} (kHz)	τ_{mean} (μs)
301	9.9	100.6
313	14.2	70.4
323	23.7	42.2
333	33.5	29.9
343	49.7	20.1
353	69.2	14.5
363	94.7	10.6
373	122.4	8.2

The values extracted from Figure 3.10 for rate constants and lifetimes are given in Table 3.1, together with the populations at each temperature, for comparison. The gradual increase in the magnitude of the exchange rate is obvious, which results in a decrease in the mean lifetime of a hydrogen-bonded NH proton. The exchange rate at 301 K has a comparable magnitude to the difference in the chemical shift values of the free and hydrogen-bonded NH proton resonance (free NH resonance was taken to be at ~9 ppm) (~4500 Hz at 700 MHz Larmor frequency, $\Delta\nu\approx 6.5$ ppm corresponding to a lifetime of ~100 μs). At this specific temperature, the broadest linewidth is observed due to the interference of the exchange. After this temperature, narrower linewidths are observed with an increasing temperature, which shows that the exchange-limit goes away from the intermediate limit to the fast limit. As exchange rates approach the fast-exchange regime, the observed linewidth and as a result the exchange rate constant can be given by the following formulas (Harris 94):

$$\Delta \nu_{FWHM} = \frac{1}{2}\pi(\nu_{hb} - \nu_f)^2 k^{-1}$$
$$k = \frac{\pi(\nu_{hb} - \nu_f)^2}{2\Delta \nu_{FWHM}} \qquad (4)$$
$$\tau = \frac{1}{k}$$

Additionally, the lineshape analysis in the slow-exchange limit (represented in Figure 3.9b, below 300 K) can still be performed and information about the position and shape of the resonances can be determined by using the following equation (Goward 02);

$$g(v) = \frac{2\tau_A(v_{hb} - v_f)}{(v - \frac{1}{2}(v_{hb} + v_f))^2 + \pi^2 \tau_A{}^2 (v - v_{hb})^2 (v - v_f)^2} \qquad (5)$$

The calculated lineshape, ***g(v)***, depends on the lifetime τ_A (eq. 4) in seconds and the frequencies of the hydrogen-bonded and free proton resonances, ν_{hb} and ν_f respectively. The lineshapes before the coalescence in the current system show both the shift and the line-broadening effects as a function of temperature until ~300 K. One should still keep in mind that additional dipolar coupling that the pure ring NH proton experiences at low temperatures causes additional line shape changes (broadening-narrowing effects) in the slow- and intermediate-exchange limit. The effect of dipolar coupling is not included in the given formula, eq. 5. In the current case, additionally, the populations of the hydrogen-bonded and free NH are changing at each temperature causing additional changes at the calculated spectra, which is also not included in the given eq. 5.

3.3.2 The Comparison of Microscopic and Macroscopic Conductivity

The conductivity value determined by Impedance spectroscopy reflects the behavior of the system at a macroscopic level. The activation energy calculated by this method represents the activation energy for proton motion at the macroscopic level. The macroscopic properties, however, might be different from the microscopic mechanisms which NMR can successfully probe as shown in previous studies comparing both methods (Goward 02). The activation energy values for proton motion determined by NMR linewidth-analysis reflect the microscopic behavior of the system, and are directly related to the molecular processes in the studied systems.

In the fast-exchange limit, where all proton resonances are well resolved, the linewidth of the resonance depends strongly on the temperature. After plotting the linewidth at full width half maximum against the inverse temperature (1000/T), a linear relationship can be obtained, due to the fact that the linewidth is characterized by the effective transverse relaxation time, T_2^*, which is inversely proportional to the exchange rate. Such a plot is shown in Figure 3.11a, with a black colored line (the blue line shows the same calculation after a linewidth correction as described before) in the same temperature range where the activation energy calculation was performed. The activation energy of the microscopic local motion can be estimated with an Arrhenius relation of the temperature with linewidths as represented by the following formula;

$$\Delta \nu_{fwhm} = \frac{1}{\pi T_2^*} = k = k_0 e^{(-\frac{E_a}{RT})} \tag{6}$$

An activation energy of ~32 ± 1 kJ/mol for the local proton motion was obtained by this formula in the fast-exchange limit. The corresponding exchange rate, k, increased from ~5 kHz (at 301 K) up to ~70 kHz (at 373 K). To be able to compare this value to the macroscopic conductivity obtained from Impedance spectroscopy, the eq. 6 was slightly modified to analyze those results, as follows;

$$\sigma = \sigma_0 e^{(-\frac{E_a}{RT})} \tag{7}$$

The conductivity plots in Figure 3.11a and 3.11b show Arrhenius type linear temperature dependence in the analyzed temperature range. The activation energy for the bulk (macroscopic) proton mobility is obtained to be ~29.5 kJ/mol, as shown in Figure 3.11c by a VTF fit of the conductivity values obtained by impedance spectroscopy. This value is smaller than the value obtained by NMR, meaning that there should be additional processes involved additional to the local proton mobility (which is described by the T_2^*) and facilitating the macroscopic conductivity. More description on additional processes happening at the same time with the chemical exchange of NH protons and the model of proton conduction will be described in the following sections.

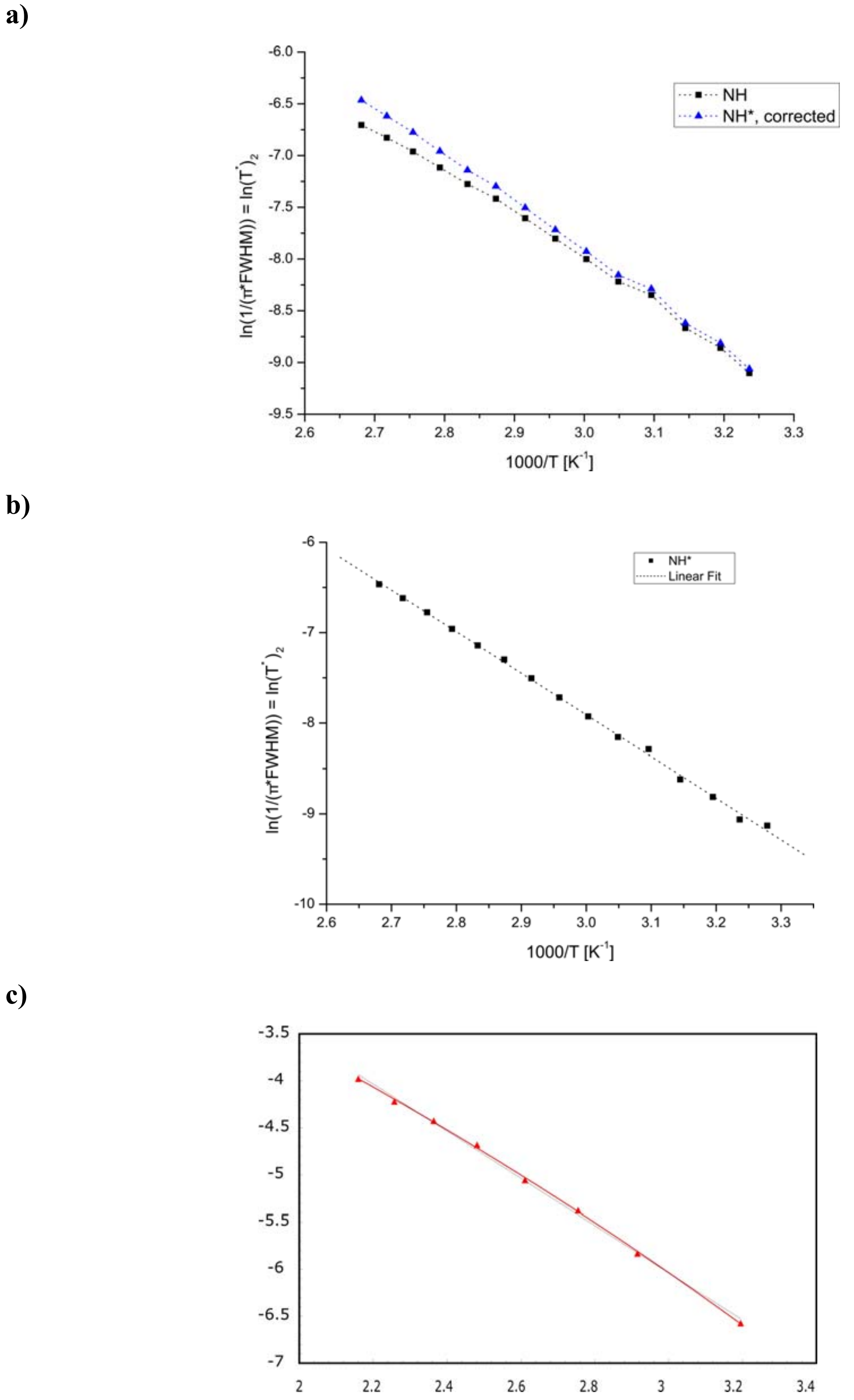

Figure 3.11: a) The logarithm of NH linewidths against 1000/T to get the E_a value for NH mobility. **b)** The linear fit of logarithm of linewidths against 1000/T. **c)** The VTF fit plot of conductivity data from impedance spectroscopy results (Obtained from Granados-Focil), logarithm of conductivity against 1000/T.

3.3.3 The activation processes monitored by selective deuteration of acidic NH proton: ^{2}H NMR

Detailed analysis of ^{2}H linewidths will be performed in this section for the variable temperature ^{2}H MAS NMR spectra represented in Figure 3.8. As represented by eq. 6, the deuterium linewidths can also be used to extract the activation energies of corresponding motional processes, which is the exchange of acidic ND deuterium in the current case. One should keep in mind that, the values which will be obtained by ^{2}H lineshape analysis might be slightly different from the values obtained from ^{1}H linewidth analysis due to the fact that deuterium is a heavier nucleus than proton (isotope effect, Yuan 05).

The absence of ^{2}H NMR signal at lower temperature might arise from the un-complete averaged quadrupolar couplings causing extreme line-broadening. In the same temperature region, where the deuterium line is missing, the proton resonances show first a line narrowing, and then a line-broadening. One should keep in mind that dipolar and quadrupolar couplings have different magnitudes (quadrupolar coupling is nearly 5-6 times larger compared to dipolar coupling), and the signal loss effects due to interference of molecular motional timescale and those interactions might happen at different timescales (so at different temperatures).

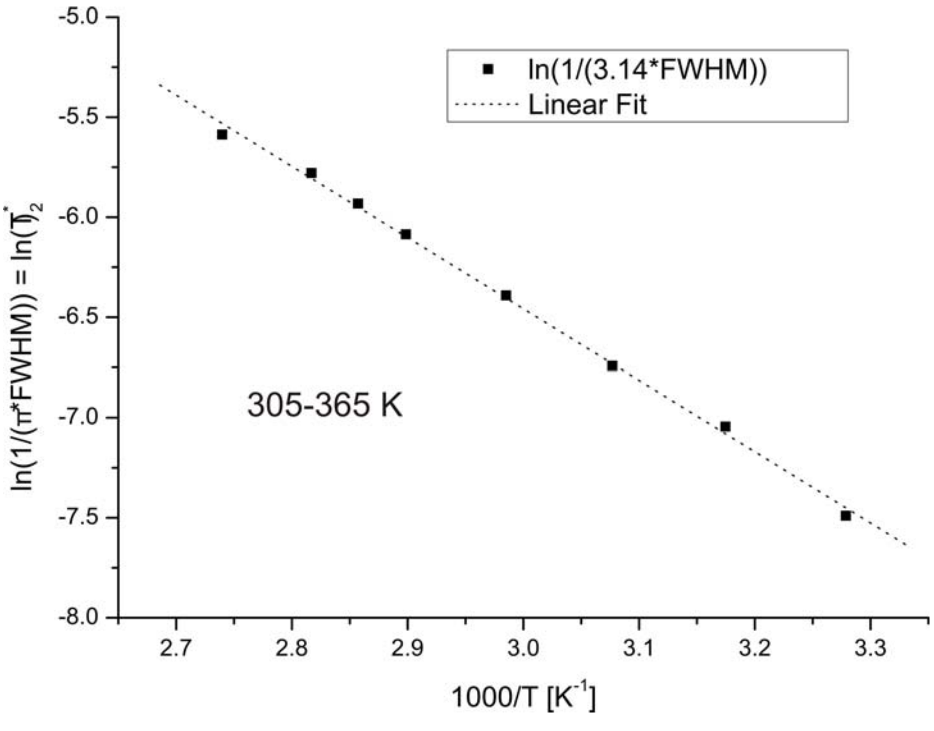

Figure 3.12: Fitting of the ^{2}H linewidths against 1000/T to get E_a value for acidic ND deuterium mobility. The linewidth values are extracted between the temperatures of 305 – 365 K.

a)

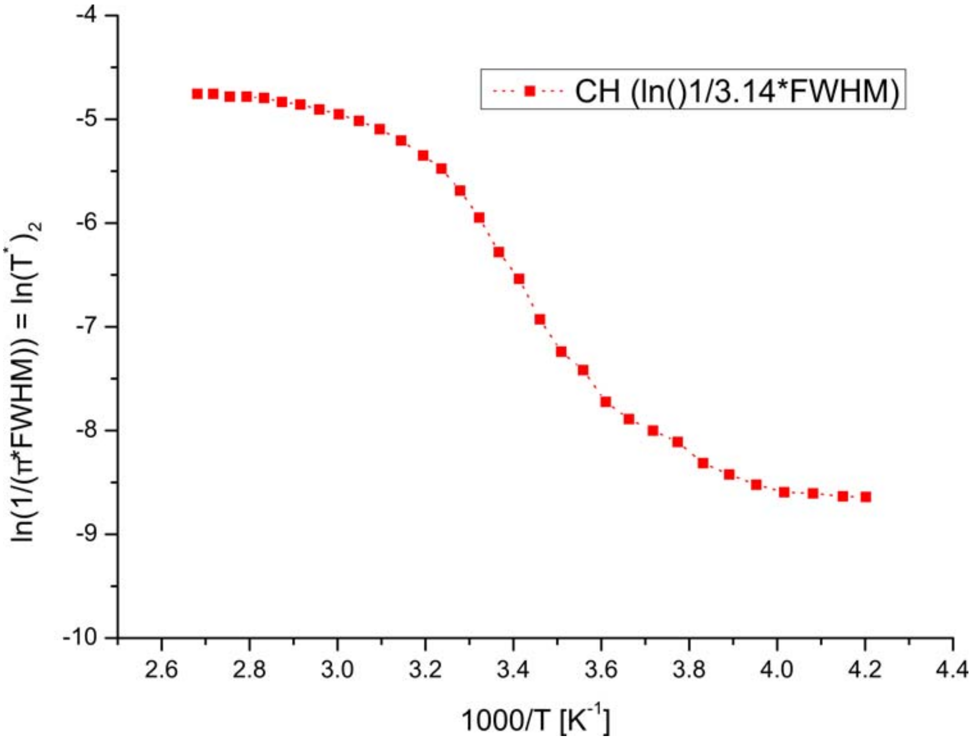

b)

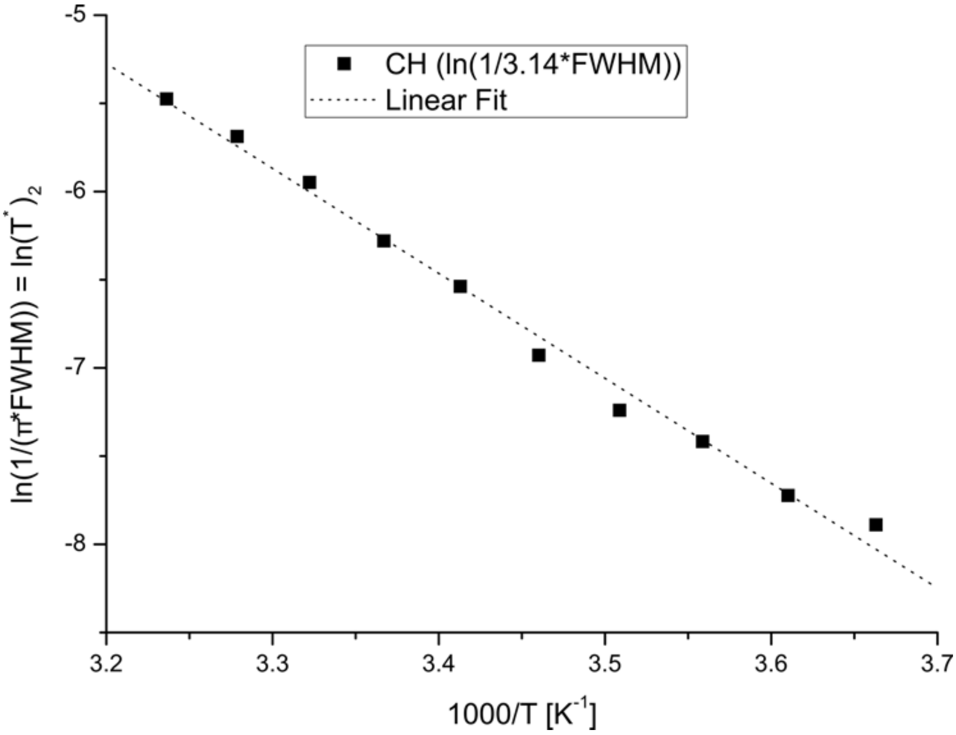

Figure 3.13: a) Logarithm of aromatic CH proton linewidths against 1000/T. b) The fitted curve from CH linewidths in the linear region (270–310 K).

The plot of $\ln(T_2^*)$ against 1000/T is represented in Figure 3.12. From a linear fitting of the data points, activation energy for the deuterium motion is obtained with a value of 29.5 ± 0.5 kJ/mol by using eq. 6. This value is similar to the activation energy of the proton at the same site (which was 32 ± 1 kJ/mol), despite the fact that deuterium is a heavier atom compared to proton. Moreover, this value is very similar to the activation energy for the macroscopic proton mobility obtained by Impedance spectroscopy.

3.3.4 The motional processes at the triazole ring:

The triazole derivative studied in the current work is advantageous in terms of the possible molecular probes which can be used to understand the molecular level dynamics of the system. As mentioned in the previous section, acidic triazole NH proton is a probe for the chemical exchange process. If the NH proton is selectively deuterated, it can also supply additional information on the dynamics of proton hopping mechanism. The triazole ring CH proton is an independent probe to monitor the ring flip-motion, which is difficult to determine with acidic NH proton linewidth analysis due to interfering effects of chemical exchange process to this type of ring-flip motion. Both of these processes, proton-hopping and ring-flip, seem to have crucial importance in the proton conduction mechanism in current triazole functional siloxane system.

For the CH proton, contrary to the acidic NH proton, a continuous line narrowing is observed which reaches a plateau linewidth value of ~40 Hz at a temperature of ~310 K, shown in Figure 3.6b and 3.9b. In fact, up to 269 K both CH and NH signals follow a similar line narrowing trend with increasing temperature, indicating that the molecular mobility increases at the triazole ring. However, between T= 269 K and T= 301 K, the ring CH proton continues its line narrowing behavior, whereas the acidic NH has an opposite line broadening effect due to the interference of the chemical exchange and NMR timescales. Above 301 K, once again both resonances show the line narrowing effect, but for the CH signal the final linewidth is much narrower compared to the acidic NH (linewidth at 373 K for NH proton is ~260 Hz).

The continuous line narrowing of the CH proton resonance is evidence of increasing ring-flipping motion throughout the covered temperature range. With a careful analysis of the linewidths using eq. 6, the activation energy for a temperature activated ring-flip process can be estimated in the temperature range where the line-narrowing follows Arrhenius behavior. Such a plot is represented in Figure 3.13. A value of 49±2 kJ/mol is obtained from the best-fit straight line which has a correlation coefficient of the linear regression, R, equals to 0.996.

a)

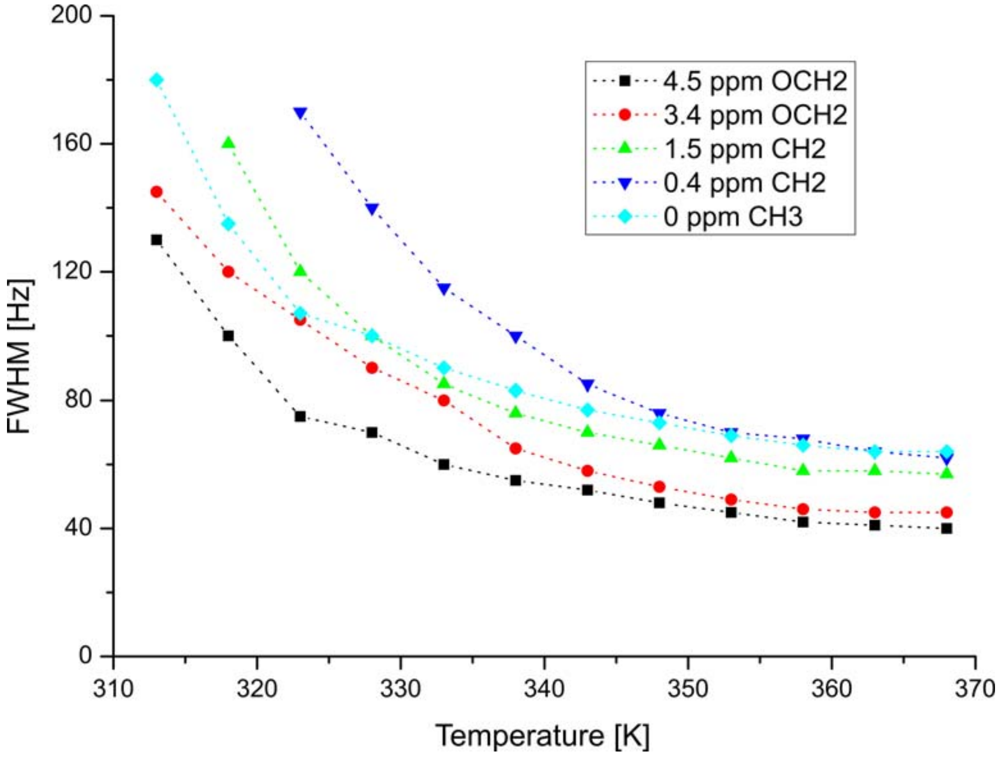

b)

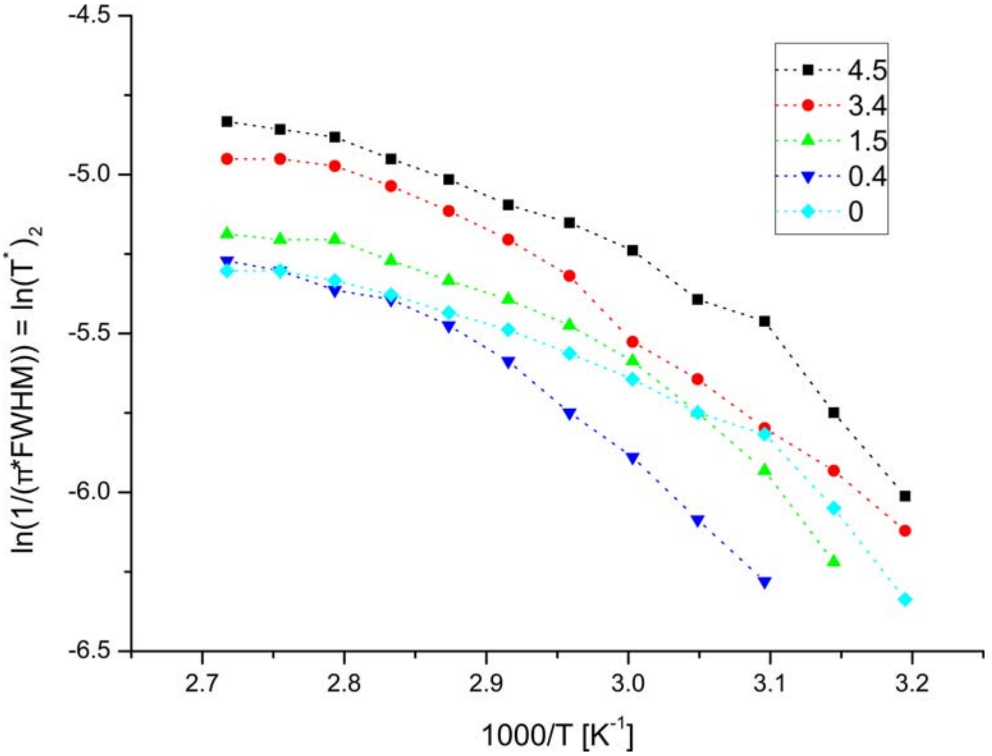

Figure 3.14: a) FWHM changes for different aliphatic sites against temperature, **b)** Logarithm of FWHM against inverse temperature (between 313 and 368 K). The non-linear behavior of the curves can clearly be seen.

This activation energy value is significantly higher compared to the activation energy for the proton mobility of the acidic NH proton, due to the fact that two processes are significantly different from each other, former is ring-flipping and latter is proton hopping.

From Figure 3.9 it is clear that the ring flip is fast with NH proton intact. Between 230 K and ~270 K, the ring flipping is active which cause significant line narrowing both in ring CH and NH protons. The ring-flip motion does not cause any chemical shift change for NH until 270 K, meaning that by this process the acidic NH proton ends in an equivalently strong hydrogen-bonding site. Above 270 K due to the additional exchange process of acidic NH protons between hydrogen-bonded and free sites, the NH proton linewidths broadens up to 300 K due to the intermediate exchange regime. Above 300 K up to 370 K, in the fast exchange regime of NH proton, again a line narrowing occurs, where in the same temperature interval the ring CH does not show any linewidth change. As a last point, comparing the exchange rates of the proton hopping and ring-flipping processes, it can be concluded that the ring flipping is in the same orders of magnitude with the NH proton exchange process. The ring-flipping starts at much lower temperatures already, where the acidic NH is still strongly hydrogen-bonded (at 270 K). The calculation of the rate constant of the ring-flipping was done for T=270 K in the linear temperature regime by using eq. 4 and assuming 1 kHz of distance between different ring CH sites.

3.3.5 Mobility of the Spacer and Backbone of the System:

In Figure 3.14a and 3.14b, the changes of FWHM and logarithm of proton FWHM against temperature are represented for different aliphatic groups (CH_2 or CH_3) in Tz5Si material at different spacer and backbone positions. A schematic representation of the proton sites are represented additionally for clarity. It can clearly be seen from Figure 3.14a that the linewidths strongly depend on the temperature and represent significant line narrowing effects with increasing temperatures. All of the specific aliphatic proton resonances reach a plateau value in proton linewidth at high temperatures which are ~40 Hz for spacer OCH_2 protons and ~60 Hz for the spacer CH_2 and backbone CH_3 protons.

Additionally, in Figure 3.14b, the logarithm of changes in proton linewidths are represented against inverse temperature in a similar form which was done for aromatic CH and NH protons to obtain more information from the activation energies of the motional processes for those specific sites, by basically following eq. 6. However, for the aliphatic proton resonances the dependence of the logarithm of linewidths to the inverse temperature is not linear in the studied temperature range, from 313 K up to 368 K. It can be concluded that the motion along the spacer is not uniform.

3.4. Conclusions

With the help of the solid-state NMR methods, detailed information on structure and dynamics of the triazole functional polysiloxane system is obtained. The presence of the strong hydrogen bonding in the solid phase of the material at low temperature was determined with the existence of the 15.5 ppm ^{1}H resonance. Moreover, the molecular organization at low temperature was determined by the 2D ^{1}H DQ NMR spectroscopy, which indicates that the triazole functional units arrange in such a way that the NH protons do not see each other. This means that they are away in space from each other, and they do not form hydrogen-bonded dimers.

After these structural insights have been obtained, additional effort was done to elucidate the dynamics of the materials. ^{1}H variable-temperature NMR results indicate that significant molecular mobility increase appears in all of the proton sites in the system, due to the increased motion of the system, which led to ^{1}H line narrowing. More surprisingly, the acidic NH resonance displayed line narrowing (249-269 K), broadening (269-301 K) and again narrowing (301-373 K), which was explained with the two site exchange between the hydrogen bonded NH sites and the free NH sites. Different motional exchange timescales (regimes) were obtained which led to different line-shape changes with temperature increase. A kilohertz range motion is observed in the fast exchange regime (301-373 K) for the acidic NH proton.

Finally, activation energies (E_a) were calculated from the linewidth analysis. The E_a for the aromatic CH motion is ~49 kJ/mol. Moreover, the activation energy obtained from impedance spectroscopy, ^{1}H and ^{2}H MAS NMR for the acidic NH proton is all ~ 30 kJ/mol. The similar values obtained from different methods for the acidic NH proton motion indicate that there is no phase separation in the material which would give different activation energies at the macroscopic (E_a value obtained from impedance spectroscopy) and microscopic level (E_a value obtained from NMR). In a previously studied system, very different activation energies were obtained from NMR and impedance spectroscopy for proton motion due to the crystalline-amorphous phase separation (Goward 02). Fast ring-flipping process is proved while NH proton is attached to the ring, whereas the breaking of NH hydrogen-bonds is in the same orders of magnitude as the ring-flipping. Only the latter process is responsible for proton conduction in Triazole material.

Chapter 4:

Anhydrous Proton Conducting Acid-Base Poly(acrylic acid)- Poly(4-vinyl pyridine) Polymer Blend System: A Study of Hydrogen Bonding and Proton Conduction

Acid-base polymer complexes gained great interest due to their numerous potential applications. One of the most appealing applications is their use in the field of fuel cells as anhydrous proton conducting polymeric materials for proton conducting membranes. In the current work, NMR studies of structure and dynamics of the system composed of acid polymer PAA [poly(acrylic acid)] and basic polymer P4VP [poly(4-vinyl pyridine)] are presented. This system is an example of an anhydrous proton conducting membrane which can be used at elevated temperatures where the proton conduction of hydrated membranes breaks down.

The applied spectroscopic NMR methods involve various nuclei, e.g. ^{1}H, and ^{13}C. The ^{1}H NMR measurements have been preformed under fast magic angle conditions to achieve sufficient resolution and the applied ^{1}H NMR methods vary from simple ^{1}H magic angle spinning (MAS) to double-quantum filtered (DQF) methods and two dimensional ^{1}H double-quantum (DQ) spectroscopy. The dynamic behavior of the systems has been investigated via variable temperature ^{1}H MAS NMR and ^{2}H static/MAS NMR. ^{13}C cross-polarization MAS NMR provides additional aspects of dynamic and structural features to complete the picture.

Different types of acidic protons have been identified in the studied PAA-P4VP systems that are involved in the formation of hydrogen bonds. Solid-state NMR is able to distinguish non-hydrogen bonded free acidic protons, hydrogen bonded dicarboxylic dimers and protons forming hydrogen bonds between carboxylic protons and ring nitrogens. The conversion of dimer structures in PAA to free carboxylic acid groups is accomplished at temperatures above 340 K. However, the stability of hydrogen-bonding strongly depends on the hydration level of the polymer complex. An inverse proportionality between hydrogen-bonding strength and proton conduction in the PAA-P4VP acid-base polymer blend systems is established.

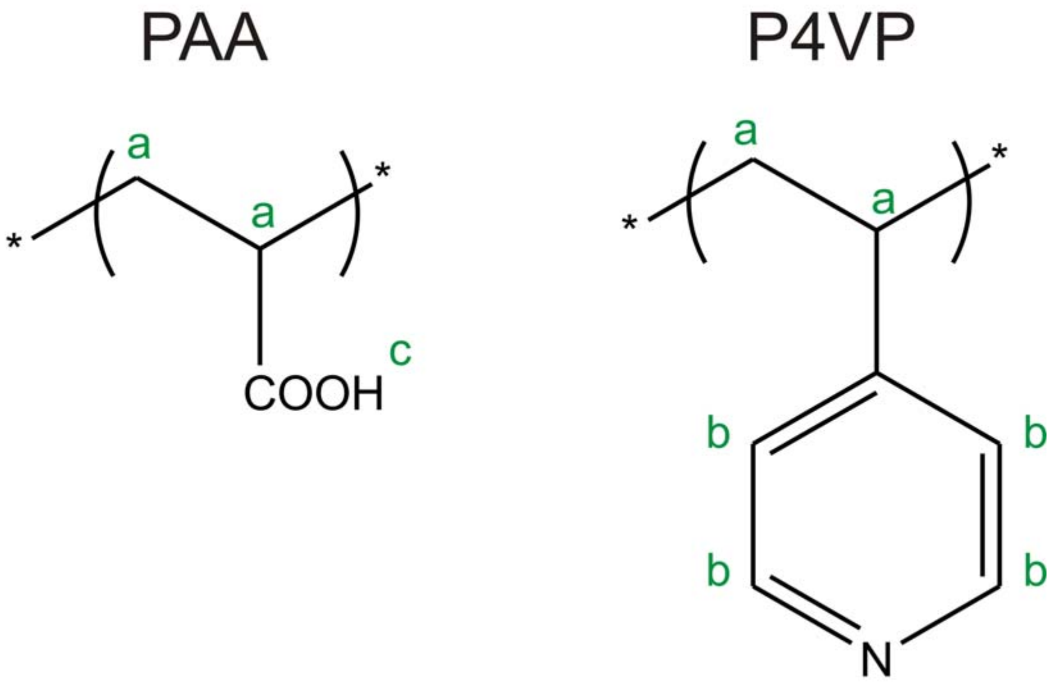

Figure 4.1: Chemical structure of parent polymers: Poly(acrylic acid) and poly(4 vinyl pyridine).

4.1. Introduction

In the quest of new materials for high-temperature and low humidity operation, tethering of proton conducting units to a polymer backbone was also introduced. These systems have the advantage of non-evaporating solvents at high-temperatures in the fuel cell. Ethylene oxide tethered imidazole heterocycles (Imi-n-EO) was one of the first type of these kinds of materials (Schuster 01). Other new possibilities supply the proton conduction through phosphoric acid units tethered to the backbone of polymers. Poly(vinyl phosphonic acid) (PVPA) is the first of its kind (Bingol 06). However, anhydride formation of phosphonic acid units is an intrinsic problem of these materials.

A new approach is being developed, based on the usage of acidic and basic polymer blend systems which will supply superior physical properties compared to previously reported doped systems (Pu 03, Kerres 99). These blends gained great interest due to their numerous favorable properties compared to previously reported systems (Carrette 01). These advantages, reported by Kerres (Kerres 99), are for example lower methanol-permeability than Nafion and superior physical properties (Walker 99).

An issue of importance is the process of forming macromolecular complexes in aqueous media due to hydrogen bonding. An ever growing interest has occurred in introducing hydrogen bonding into the polymers which originally lack donor or acceptor groups. It has been demonstrated that for such polymer solutions a transition from separated coils to complex aggregates takes place when the content of introduced interaction sites reaches a threshold level. In the solid state, the blends involve controllable hydrogen bonding; the immiscibility-miscibility-complexation transitions occur upon progressive increase in the density of hydrogen bonds. Physical properties are also found to strongly depend on the complexation via hydrogen bonding, e.g., the glass transition temperature is usually found to increase substantially in these complex systems. Due to the fact that the proton in hydrogen bonded systems exhibits different degree of liability, an issue of particular interests is the proton mobility. The present work is focused on studying the proton mobility and conducting behavior in the macromolecular complexes established by hydrogen bonding. The degree of complexation and thus the proton environments bears direct relevance on the proton conductivity. In contrast to acid containing ionomers, the conductivity does not follow the acid concentration, but is governed by the degree of complexation.

This chapter presents studies of structure and molecular dynamics of systems composed of poly (acrylic acid) (PAA) as acid polymer and poly (4-vinyl pyridine) (P4VP) as basic constituent. Their chemical structures are summarized in Figure 4.1. The anhydrous proton conductor system PAA-P4VP is of particular interest for proton conductor membranes at elevated temperatures.

4.2. Materials

The acid polymer poly (acrylic acid) (PAA) with a molecular weight of 450,000 g/mol was purchased from Aldrich whereas the poly (4-vinyl pyridine) (P4VP) was synthesized in the lab (Chu 08). The PAA-P4VP blends with different mixing ratios in order to understand the effect of complexation on the proton conduction mechanism in acid-base blend polymer systems were prepared as described elsewhere (Chu 08). The chemical characterization data for the different samples are shown in Table 4.1. Since the samples showed a strong influence on water content and on annealing, all samples have been kept for one week at 60°C under vacuum prior to the NMR investigation.

Table 4.1: Molecular composition of the materials investigated.

	% PAA	**% P4VP**
PAA	100	0
80-20 (4:1)	80	20
50-50 (1:1)	50	50
P4VP	0	100

4.3. Results

4.3.1 Structure of the PAA-P4VP System via SQ ^{1}H MAS and ^{13}C CP-MAS NMR

The hydrogen bonds between carboxylic groups of organic acids have long been investigated, and it is well-known that cyclic dimers exist in the liquid and solid states (Wainright 95). Interactions like hydrogen-bonding or aromatic π- π stacking effects lead to pronounced changes in the electronic structure. For protons involved in hydrogen bonding or in close proximity to aromatic systems, substantial difference in chemical shift can be detected (Spiess 04). In the solid phase, where configuration and conformation are mostly frozen, NMR spectra provide rich structure and dynamic information that will be lost due to rapid averaging in the liquid phase. Chemical shifts thus provide the first hints to understand packing and hydrogen bonding formation in the solid state (Schmidt 06).

In Figure 4.2, ^{1}H solid state NMR spectra of the parent polymer compounds are displayed. The ^{1}H NMR signals of the different sites in the polymers are well resolved in the spectrum. The aliphatic backbone protons (a-type) of both PAA and P4VP appear at ~2 ppm, the aromatic protons (b-type) of P4VP appear at ~8 ppm, and the carboxylic acid protons (c-types) of PAA are observed at 7-8 ppm, 10 ppm, and 12 ppm. The resonances in the low field region of the spectrum (10 ppm and 12 ppm) of PAA show the presence of different hydrogen bonding arrangements in the polymer, which have been previously identified via infrared and Raman studies by Dong et al. (Dong 97) In ^{1}H NMR, free, non-hydrogen bonded protons are observed at 8 ppm (c1 type), the strong hydrogen-bonded cyclic dimers of –COOH are observed at 12 ppm (c3 type), and the resonance appearing at 10 ppm (c2 type) is due to the exchange of the hydrogen-bonded and free types of acidic protons. Furthermore, it is generally accepted that three different states of water are present in polymers, known as "bound", "intermediate", and "free" water, respectively.

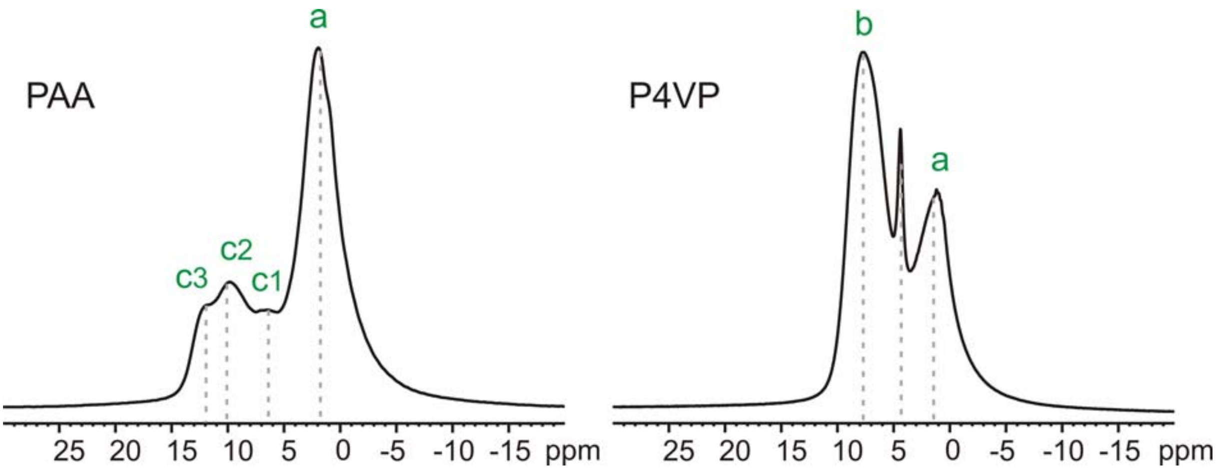

Figure 4.2: ^{1}H SQ MAS NMR spectra of parent polymers, PAA and P4VP, recorded at 30 kHz MAS frequency and at room temperature. For the assignment of the hydrogen bonded protons (c1-c3), see text.

On the basis of these previous works, we anticipate that there are different types of protons and they may be associated or not associated with hydrogen bonds in the hydrated PAA. In presence of a proton acceptor, P4VP polymer, the possible H-bonding configurations multiplies. As a result of the different arrangements we are facing a multitude of hydrogen bonding configurations, and a large spread of proton chemical shifts ranging from 8 ppm for

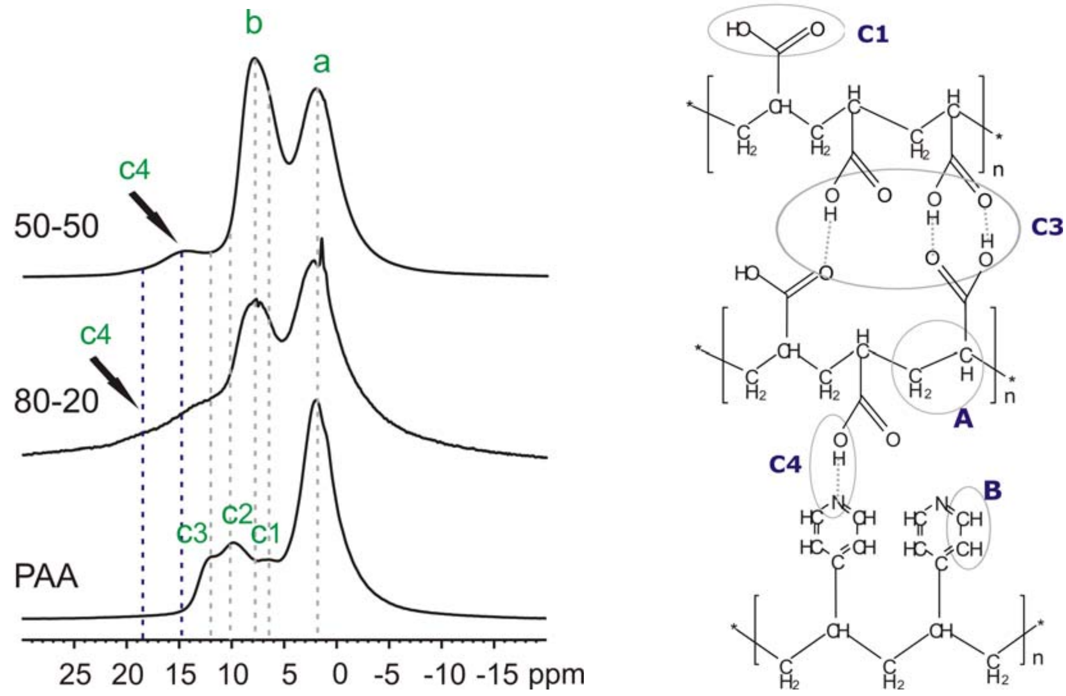

Figure 4.3: ^{1}H MAS NMR spectra of PAA, and complexes; 50-50, and 80-20. The spectra recorded at 30 kHz MAS frequency and room temperature. Additionally, schematic representation of the proton interactions in the PAA-P4VP system is also included on the right side of the figure. The resonance appearing at 10 ppm (c2 type) is due to the exchange of the hydrogen-bonded and free types of acidic protons, and is not represented in the schematic representation on the right side of the figure.

the unbound acidic proton up to 20 ppm for those protons involved in very strong hydrogen bonding can be observed.

Figure 4.3 displays the appearance of numerous hydrogen bonded protons. The chemical shift value directly reflected the proton acidity as well as the strength and the geometry of the hydrogen bonding (Berglung 80, Becker 96b, Yamauchi 00). Four different arrangements of the acidic protons can be identified: (Represented in Figure 4.3 and 4.11)

c1: Non hydrogen bonded, free carboxylic acid protons.

c2: The resonance appearing due to the exchange of hydrogen-bonded and free –COOH protons.

c3: Hydrogen bonded protons between two carboxylic acid groups which may originate from intra-chain or inter-chain configurations.

c4: Hydrogen bonded protons between carboxylic acid proton of PAA and pyridine nitrogen on P4VP.

4.3.2 Formation of the Acid-Base Polymer Complex and the Hydrogen Bonding

With blending the hydrogen-bonding donor PAA and the hydrogen-bonding acceptor P4VP, a homogeneous complex is formed predominantly driven by hydrogen bond formation. A similar phenomenon has been observed in poly (benzimidazole) (PBI) blended with P4VP, in which the miscibility and formation of the complex was attributed to the hydrogen bonding between the components (Makhija 90). Pu et al. also showed that in the PBI-P4VP system, different proton conduction mechanisms (hopping and/or segmental motion of the polymer) are active depending on the basic polymer composition (Pu 03). Recently, Kerres et al. studied the application of different types of acid-base polymer blends for PEMFC use and concluded that the ordered channels in these systems facilitate proton conduction (Kerres 99).

Table 2: Different proton types existing in PAA-P4VP polymer systems, their chemical shift values and assignments.

Proton Type	**A**	**B**	**C1**	**C2**	**C3**	**C4**
Chemical Shift (ppm)	2	7-8	7-8	10	12	≥15
Assignment	Backbone	Aromatic	Free COOH	Due to Exchange	H-Bonded COOH	H-Bonded COOH

With the complexation of the polymers, one (or more) additional proton types can be identified in the ^{1}H NMR spectrum. The signals occurring in the range of 15 ppm up to 20 ppm have not been observed neither in completely dry PAA nor in the P4VP homopolymer. These signals are assigned to carboxylic acid protons hydrogen-bonded to the pyridine nitrogen (c4 type). The spectra of pure PAA and its complexes with P4VP with two different mixing ratios are shown in Figure 4.3. From the width of the c4 peak it can be concluded that the chemical shift of these protons is broadly inhomogeneously distributed.

Traditionally, ^{13}C NMR spectroscopy is used to infer hydrogen bonding complexation. Although not directly attached, the carbonyl carbon is sensitive to the hydrogen bonding strength. ^{13}C CP-MAS spectra for PAA-P4VP complexes with different compositions are shown in Figure 4.4. Here the carboxylic acid of pure PAA is shown and from this it can be seen that the dimer (c2 or c3) type appearing at 184 ppm is dominant compared to the free (c1) type of carboxylic acid which is at 178 ppm. By blending P4VP with PAA, the dimer ratio changes as clearly seen in Figure 4.4b. The dimer structure is affected by P4VP addition with an introduction of an additional hydrogen-bonding arrangement (c4-type) between –COOH and ring –N. For instance, at a ratio of 4:1 PAA:P4VP (in the 80-20 case), the amount of free -COOH formed by pure PAA is increased. At the 1:1 ratio (in the 50-50 case), c4-type is the dominating hydrogen-bonding interaction appearing at ~184 ppm as a strong resonance.

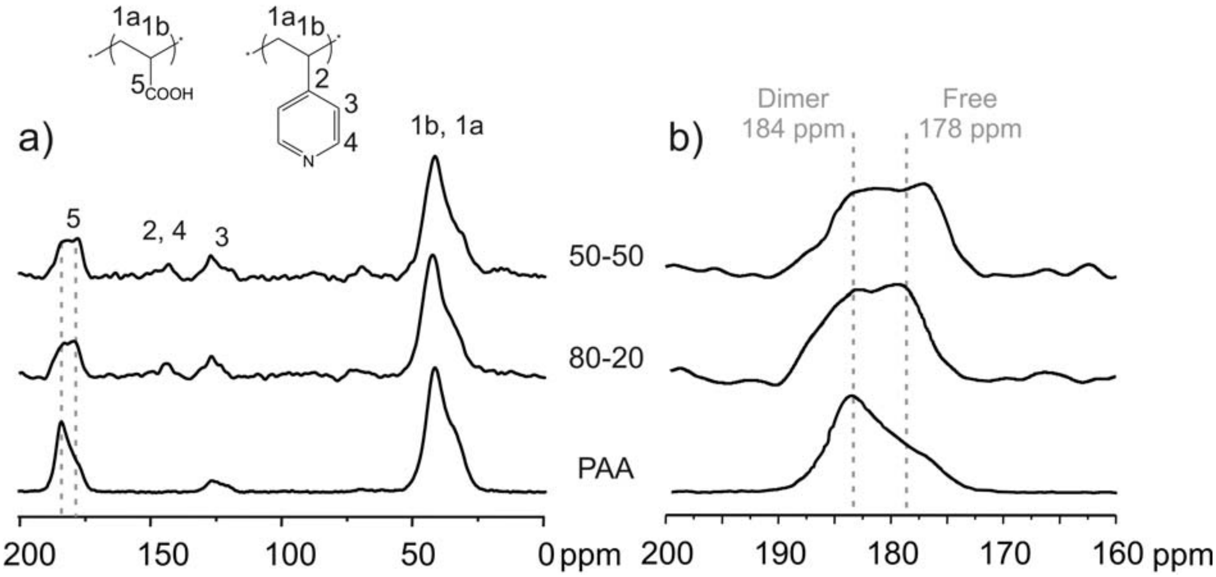

Figure 4.4: ^{13}C CP MAS NMR spectra of PAA, 50-50 and 80-20 samples at 10 kHz MAS frequency at room temperature. Contact time is 1 ms. **a**- Stacked plot of the spectra in full range, **b**- Zoomed region of carboxylic acid carbon.

4.3.3 ^{1}H MAS DQF Spectra and the Molecular Mobility

Since proton conductivity is of interest, proton mobility of the various types of hydrogen bonding was investigated. ^{1}H MAS-NMR spectra give information about the different types of ^{1}H sites in the samples. The BaBa homonuclear DQ recoupling pulse sequence was applied for one-rotor period (corresponding to an excitation and reconversion time-period of 33 μs) (Feike 96) at 30 kHz to excite and reconvert the ^{1}H-^{1}H DQ coherences (DQC), for getting more information about the local dipolar couplings. Only protons that are driven to a DQC during the excitation period and retain their DQC until the end of the reconversion period can give rise to a signal in DQF spectra. Thus, signals from mobile protons are suppressed compared to the rigid ones, additionally isolated protons are also filtered out from spectra with DQ filtration. This is the case, if the local motion of a given proton site occurs in the range of 10-100 kHz (which is in the range of experimental timescale). By comparing ^{1}H spectra with the one-dimensional double-quantum filtered BaBa spectra, mobile and rigid protons can easily be distinguished.

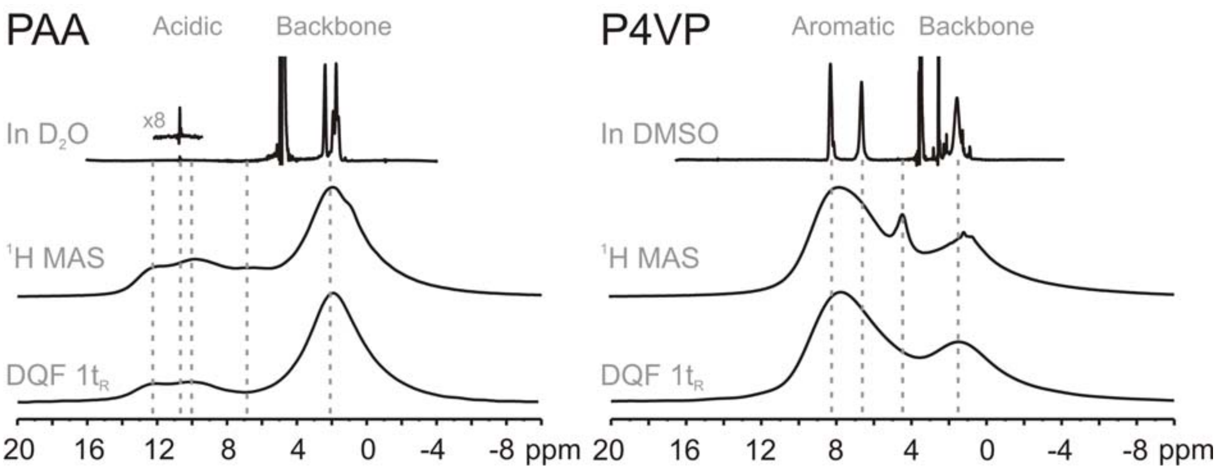

Figure 4.5: Comparison of ^{1}H NMR spectra of PAA and P4VP in solution and in solid state, using single-pulse ^{1}H MAS, and using double quantum filtration. Solution state spectra were recorded at 250 MHz proton Larmor frequency, and solid state spectra were recorded at 30 kHz spinning frequency, at 700 MHz proton Larmor frequency, and at room temperature. PAA was dissolved in D_2O and P4VP was dissolved in DMSO.

In Figure 4.5, a comparison of one-pulse and double-quantum filtration ^{1}H spectra is displayed together with liquid state spectra for PAA and P4VP. In the one dimensional ^{1}H DQ filtered MAS spectrum of PAA recorded at room temperature, most of the resonances observed in the ^{1}H MAS spectra are present except from two resonances at around 1 ppm and 7 ppm, which are from the backbone and the free carboxylic acid groups. The strong hydrogen bonded protons remain unchanged after DQ filtration. It can then be concluded that, they are rigid and have strong dipolar couplings on the timescale of one rotor period (66 μs). For P4VP, only the resonance at ~4.5 ppm, due to residual water in the sample, disappeared after DQ filtration. Aromatic resonances did not show any change as the side groups are rigid.

The comparison of ^{1}H MAS spectra with the solution spectra of the parent polymers, as shown in Figure 4.5, reveals interesting observations, especially for PAA. In the solution spectrum of PAA, a very weak resonance observed at ~11 ppm is attributed to carboxylic acid protons of dissolved PAA being in fast exchange between different hydrogen bonded forms with PAA or water molecules. In the solid state, however, instead of one resonance three resonances are observed, two of them are at 10 and 12 ppm which are shifted significantly downfield compared to free –COOH resonance (at 7-8 ppm). For P4VP, on the other hand, no significant difference in chemical shifts was observed.

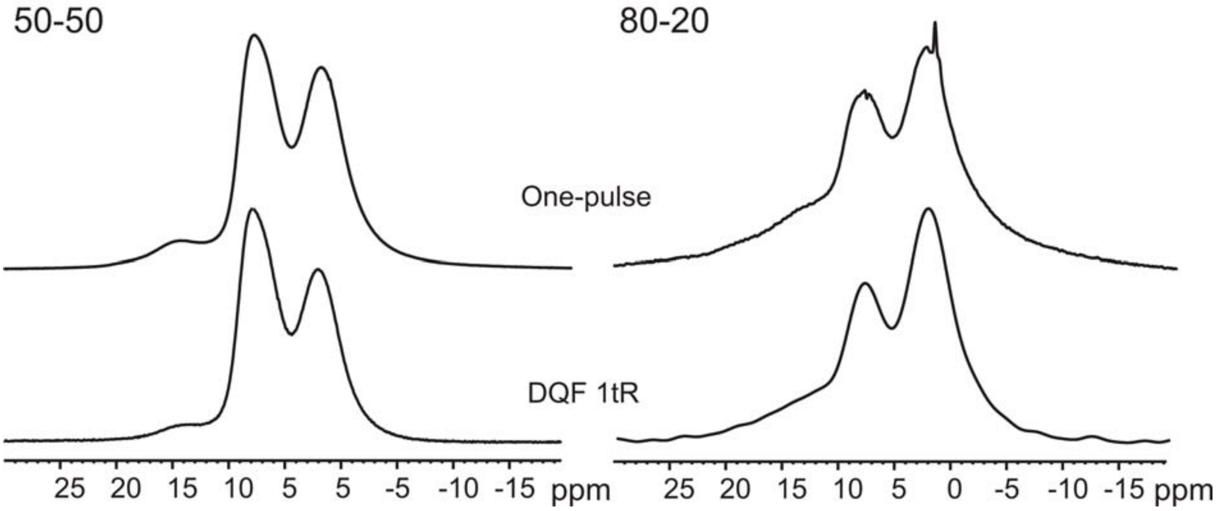

Figure 4.6: Comparison of ^{1}H MAS and ^{1}H DQF NMR spectra of 50PAA-50P4VP and 80PAA-20P4VP complex. Spectra were recorded at 30 kHz spinning frequency, at 700 MHz proton Larmor frequency, and at room temperature. The DQF spectra were recorded by using 1 t_R period of BaBa recoupling pulse sequence.

Another interesting observation is that the hydrogen-bonded –OH protons (c3-type) appear even after the application of DQF (see in Figure 4.5), which shows the “rigid” character of these protons on the timescale of the experiment. This rigid character occurs due to strong hydrogen-bonding of –COOH groups, as for example by dimer formation. The resonance at 10 ppm (c2-type), due to the exchange of hydrogen-bonded and free –COOH protons, is reduced but remains after DQF which shows that the motional averaging between the bonded and non-bonded arrangements is not isotropic and this does not lead to a complete loss of this particular resonance at room temperature. This situation changes with increasing temperature (The spectra are not shown), so that at higher temperatures both resonances disappear after DQF. The resonance around 7-8 ppm (c1-type), which disappears after DQF, is attributed to either “mobile” or isolated free –COOH protons. The dipolar interactions of these types of protons are significantly reduced due to their high molecular mobility, while the rigid ones remain unchanged. The interpretation of “rigid” and “mobile” protons is also confirmed by a recent DQ-CRAMPS (combined rotation and multiple-pulse spectroscopy) study of the pure PAA (Baohui 07). The comparison of ^{1}H MAS and ^{1}H DQF spectra for the complexes, 50-50 and 80-20, see Figure 4.6, shows that there is essentially no change for both complexes after the application of DQF, indicating that the proton sites of complexes including the hydrogen-bonded ones are rigid on the timescale of the NMR experiment at room temperature.

4.3.4 ^{1}H MAS Variable Temperature Studies of the System and Relation to Conductivity:

Variable temperature (VT) ^{1}H MAS and ^{1}H DQF NMR experiments yield valuable information about the nature of hydrogen bonding in the system, as well as local proton mobility. The VT ^{1}H SQ and DQ experiments were carried out in the temperature range of 275-405 K, at 30 kHz MAS frequency.

The VT ^{1}H MAS NMR spectra of parent polymers (PAA and P4VP) and their complexes (50-50 and 80-20) are shown in Figure 4.7. As temperature is increased from 270 K to 400 K, a continuous narrowing is observed for the resonances of hydrogen bonding protons, especially in PAA. Moreover, two different types of aromatic protons of P4VP are resolved at elevated temperatures, due to increased ring motion. An additional resonance in P4VP, due to residual water protons, significantly sharpens at 400 K. At 320 K, this sharp resonance appears at ~4.5 ppm and shifts up-field gradually with temperature to 3.5 ppm (at 400 K). The backbone proton motion in both samples is not affected by temperature elevation as much as the hydrogen-bonded proton groups in the parent polymers.

More interesting features are observed in dry PAA, thus a detailed discussion will only be provided for dry PAA (the effect of temperature in semi-hydrated PAA is also interesting and will be discussed in section 4.3.6). The relative intensities of the resonances of PAA at ~7-8 ppm, 10 ppm, and 12 ppm depend significantly on temperature. From room temperature to lower temperatures (270 K), the resonance at ~7-8 ppm (C1: free COOH proton) nearly disappears. This indicates that this type of proton is somehow incorporated in hydrogen-bonding at lower temperatures and is not free anymore. From 270 K up to 400 K, the –COOH resonance at 10 ppm exhibits a remarkable line narrowing with increasing temperature. Moreover, it shifts to higher-field and appears at 9 ppm at 400 K, due to the change in the population of the free and hydrogen-bonded acidic protons. The resonance at 12 ppm gradually disappears without any change in chemical shift. The signal at 9 ppm indicates that at 400 K there is a fast exchange between the hydrogen-bonded protons and the free ones. The observed chemical shift value is between the chemical shift value of hydrogen-bonded proton chemical shift and free acidic proton chemical shift, and depends on the ratio of these two types at a particular temperature. The intensity and position of the weak 7-8 ppm resonance (attributed to free acidic protons, c1 type) does not change from room temperature to high temperatures, and still exists at 400 K. This phenomenon can be explained by assuming regions with isolated –COOH groups which are not able to form strong hydrogen-bonds and/or are not affected by temperature increase.

All of the above observations are consistent with the carboxylic acid protons being in exchange between a hydrogen-bonded and a free state:

$$\mathrm{RCOOH^{\cdot\cdot}HOOCR} \underset{k_b}{\overset{k_f}{\rightleftarrows}} \mathrm{2RCOOH} \qquad (1)$$

k_f and k_b refer to the rate constants of the forward and backward reactions, and $K=\frac{k_f}{k_b}$. As far as the timescale of the motion is concerned, three different regimes are of particular importance in order to understand the NMR spectra: Fast, intermediate, and slow exchange limits (Spiess 85, Harris 94). Three parameters are needed to identify these regimes: $\Delta\nu$ is the frequency difference between the two resonances in exchange, the exchange rate k, and the effective transverse relaxation time T_2*. The correlation time (τ_c) of the motion is equal to the inverse of the rate constant ($\tau_c=1/k$). When $k>>\Delta\nu$, the system is in the fast exchange limit (µs to ns motion). The lineshape becomes independent of the exchange rate, and the position of the resonance appears at an average position given by the relative populations of the exchanging sites. For slow exchange (slower than millisecond motion), $k<<\Delta\nu$, the separated lines are well resolved, but broadened due to the exchange motion. In the intermediate motional exchange regime (µs to ms motion), $k\approx\Delta\nu$, an increase in temperature causes the two slow-exchange resonances to broaden and change their frequency in the direction of the weighted average frequency, until the rate constant will be equal to $k=\pi\Delta\nu/\sqrt{2}$ at the coalescence point, where a single broad resonance is observed. For PAA, in Figure 4.7, passage from slow exchange (at low temperatures) to fast exchange can be monitored. Above 380 K, the molecular motion is in the fast exchange limit and only one sharp resonance is

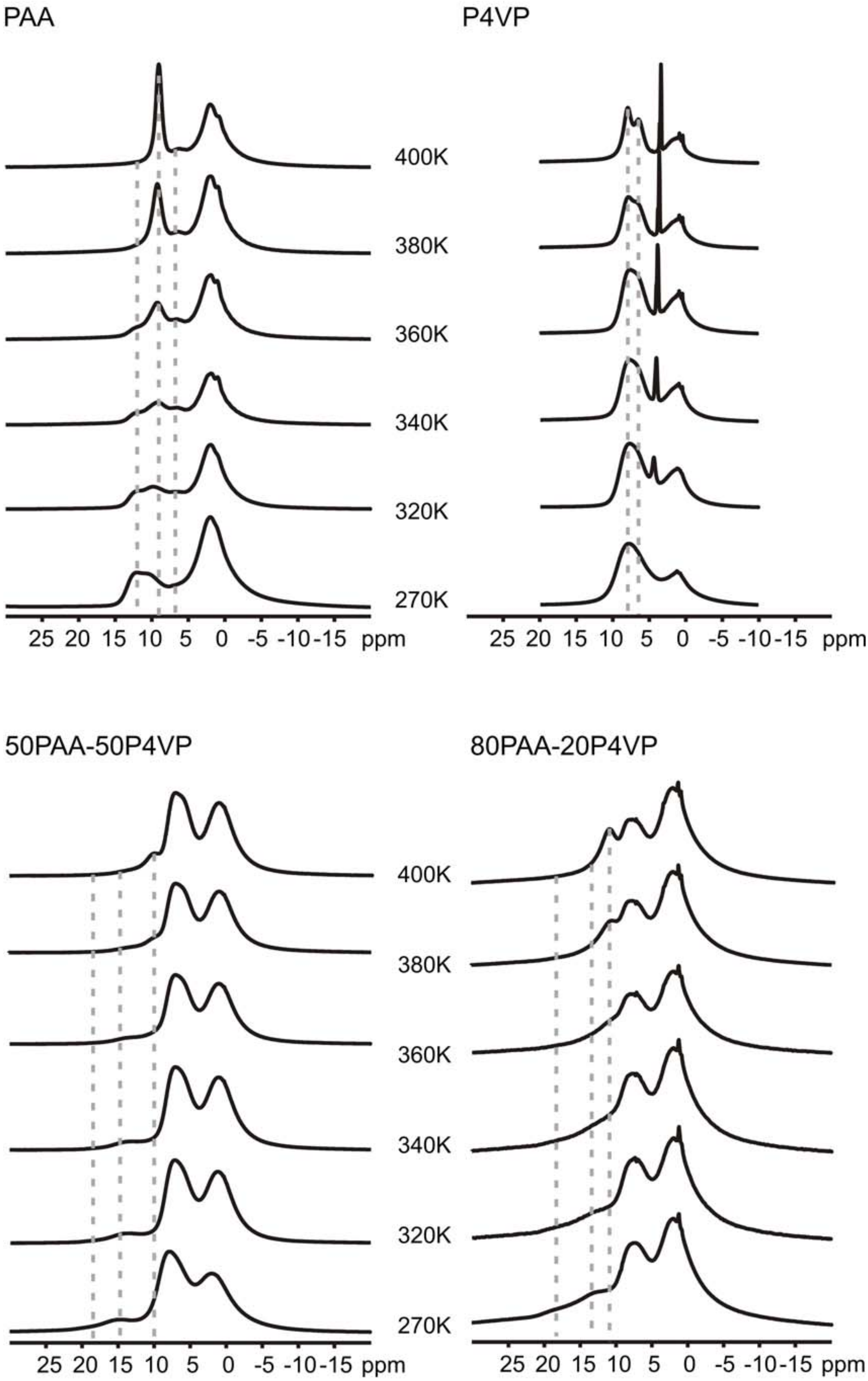

Figure 4.7: ^{1}H variable temperature NMR spectra of dried PAA, P4VP, 50PAA-50P4VP, and 80PAA-20P4VP samples at 30 kHz MAS frequency. The samples were dried at 60^{o}C under vacuum.

observed (Spiess 04, Traer 06), instead of two separated resonances.

The effect of temperature on the complexes is less pronounced compared to the effect of temperature on pure PAA. The conversion of hydrogen-bonded protons can still be observed, but the final averaged acidic proton resonances appear at higher ppm values, at around 10 ppm for a ratio of 1:1 (50-50 complex) and at 11 ppm for the 4:1 ratio (80-20 complex). Comparison of the spectra of PAA and the complex 80-20 at room temperature shows that despite the cut-off at 13 ppm in PAA, the chemical shift of the 80-20 complex goes up to 20 ppm. The increased chemical shift values indicate the presence of c4-type hydrogen bonding sites and their inhomogeneous distribution in the complex. With increasing temperature, the broad resonance at 270 K becomes much sharper at 400 K and appears at around 11 ppm. Because of the stabilization effect of complexation, hydrogen-bonded species exist at 400 K, which results in an averaged resonance appearing at higher chemical shift value. Because of the same effect, the pyridine ring motion is inhibited and no spectral resolution is observed at pyridine sites different from pure P4VP. In the 1:1 complex, c4-type of protons can more easily be observed as a more intense peak appears around 15 ppm different than other types of acidic protons. This is reasonable due to the increased ratio of PAA-P4VP interaction in the 1:1 compared to the 4:1 complex. The effect of temperature increase is similar to the 4:1 case, in which again finally at 400 K a sharper resonance at 10 ppm is observed, indicating the existence of hydrogen bonded protons (c2 type) in exchange.

Moreover, temperature has a pronounced effect on proton DQF signal intensity where the signal intensity lowers dramatically with increasing temperature. The variable temperature ^{1}H DQF spectra of the parent polymers and complexes are shown in Figure 4.8. In PAA, the weakly hydrogen bonded proton resonance at 10 ppm loses ~60% of its intensity at 400 K compared to room temperature. The strongly hydrogen bonded proton resonance at 12 ppm, nearly vanishes at 400 K and loses ~95% of its intensity. The different intensity loss of different acidic proton resonances can be explained in terms of the increased mobility at high temperatures and also due to the fast chemical exchange of the different hydrogen bonded proton sites. For PAA, a small resonance at ~9 ppm still exists even at 400 K. moreover, for 80-20 complex, again at ~11 ppm the hydrogen bonded proton resonance remains at highest temperature. For 50-50 complex, however, no low-field proton resonance remains at high temperature.

For the P4VP polymer, the aliphatic backbone proton resonance in DQF spectra shows nearly no intensity change upon heating. The proton resonance of water sharpens from RT to 400 K and in all cases is not observed in the DQ filtered NMR spectra because of its

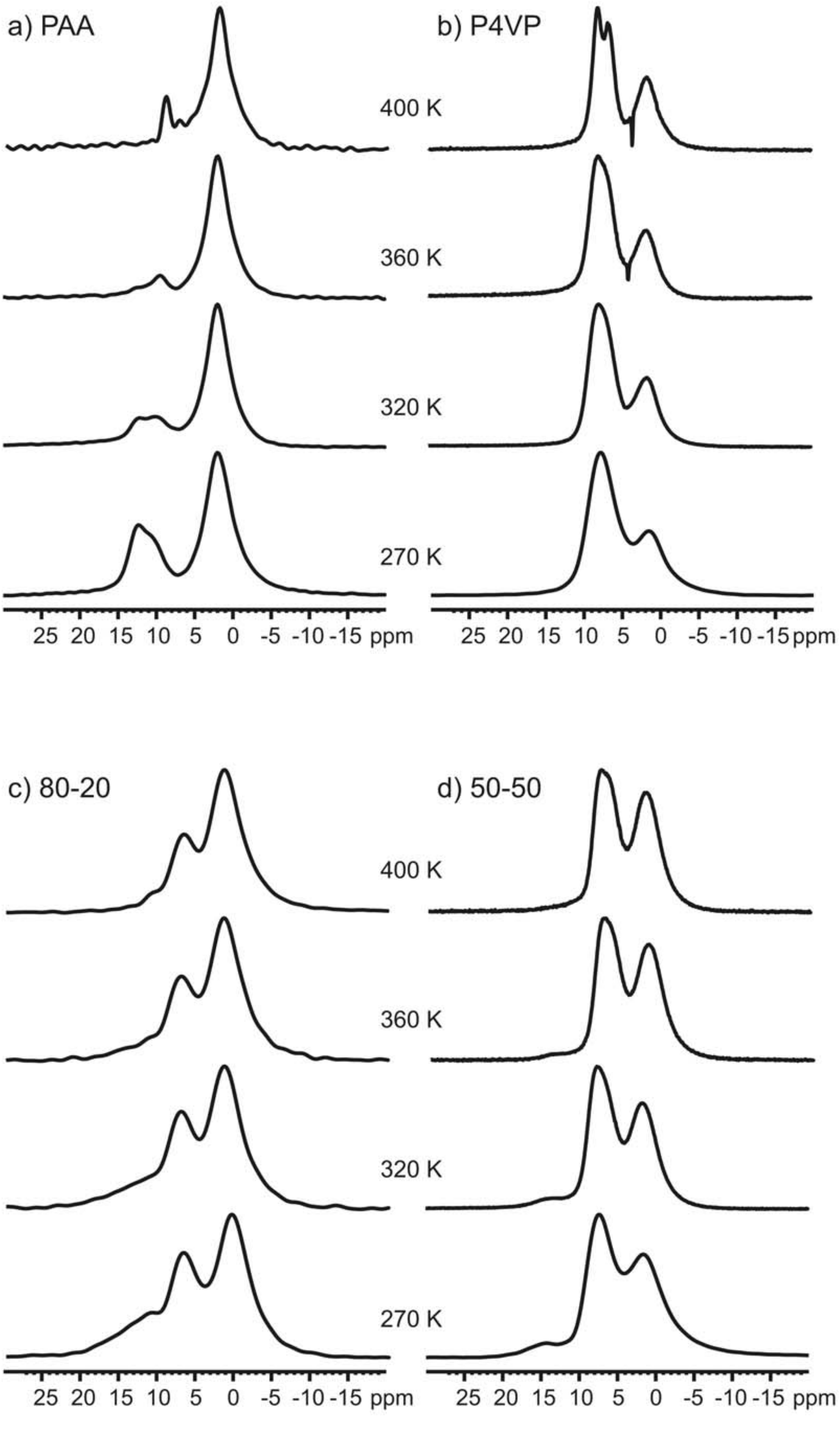

Figure 4.8: Variable temperature ^{1}H DQF spectra of the parent polymers and complexes recorded with one rotor-period of BaBa homonuclear recoupling pulse sequence at 30 kHz.

high mobility. Finally, the aromatic proton resonances become more mobile, especially at 400 K. Despite the increased ring dynamics which provides spectral resolution between the two aromatic ^{1}H sites, the dipolar coupling of ring protons is still sufficient to give a DQ signal, because the intermolecular dipole-dipole coupling is not affected by the ring motion.

The effect of heating in complexes is less pronounced compared to pure PAA because of the stabilizing complexation effect. By complexation the mobility is decreased, as observed in the high temperature spectra, where the pure polymers show sharper resonance lines (Figure 4.7). At 270 K and RT the patterns of ^{1}H MAS and DQF NMR spectra of both complexes, 50-50 and 80-20, are similar which implies that the samples are rigid at these temperatures. At 360 K, the 50-50 complex shows similar structure in both spectra; however, the 80-20 spectra change after the application of DQ filtration in a way that the hydrogen-bonded proton region, from 10 ppm up to 20 ppm, shows a loss in intensity which implies that these proton sites exhibit increasing mobility, but the dipole-dipole coupling remains strong enough to give rise to a DQ signal. At 400 K, the broad acidic proton resonances become sharper because of the conversion of hydrogen-bonded protons to mobile free acidic protons.

4.3.5 2D ^{1}H DQ MAS NMR Spectra: Spatial Proximities and Proton Connectivity in Systems

In order to determine the protons involved in the DQC, a 2D DQ spectrum is needed in which the DQ frequency, w_{DQ} given by the sum of two ^{1}H resonance frequencies involved is correlated with the conventional ^{1}H SQ frequency. DQCs between like spins give rise to the so called auto-peak located on the diagonal of the DQ spectra, while the DQCs between unlike spins give rise to pairs of cross-peaks symmetrically arranged on either side of the diagonal. One important point that should be kept in mind while analyzing the DQ spectra is that, an isolated ^{1}H spin as well as a mobile ^{1}H will not contribute to the 2D DQ NMR spectrum (Gottwald 95, Brown 01).

First, the DQ spectra with short excitation times emphasizing strong dipole-dipole couplings will be interpreted. Subsequently, the effect of temperature will be analyzed. The $1t_R$ 2D DQ spectrum of the pure samples clarifies the assignment of the peaks at elevated temperatures and at longer excitation times. In Figure 4.9, the 2D ^{1}H DQ spectra of PAA, P4VP, 50-50 and 80-20 samples recorded with 1 t_R BaBa recoupling time at room temperature are shown.

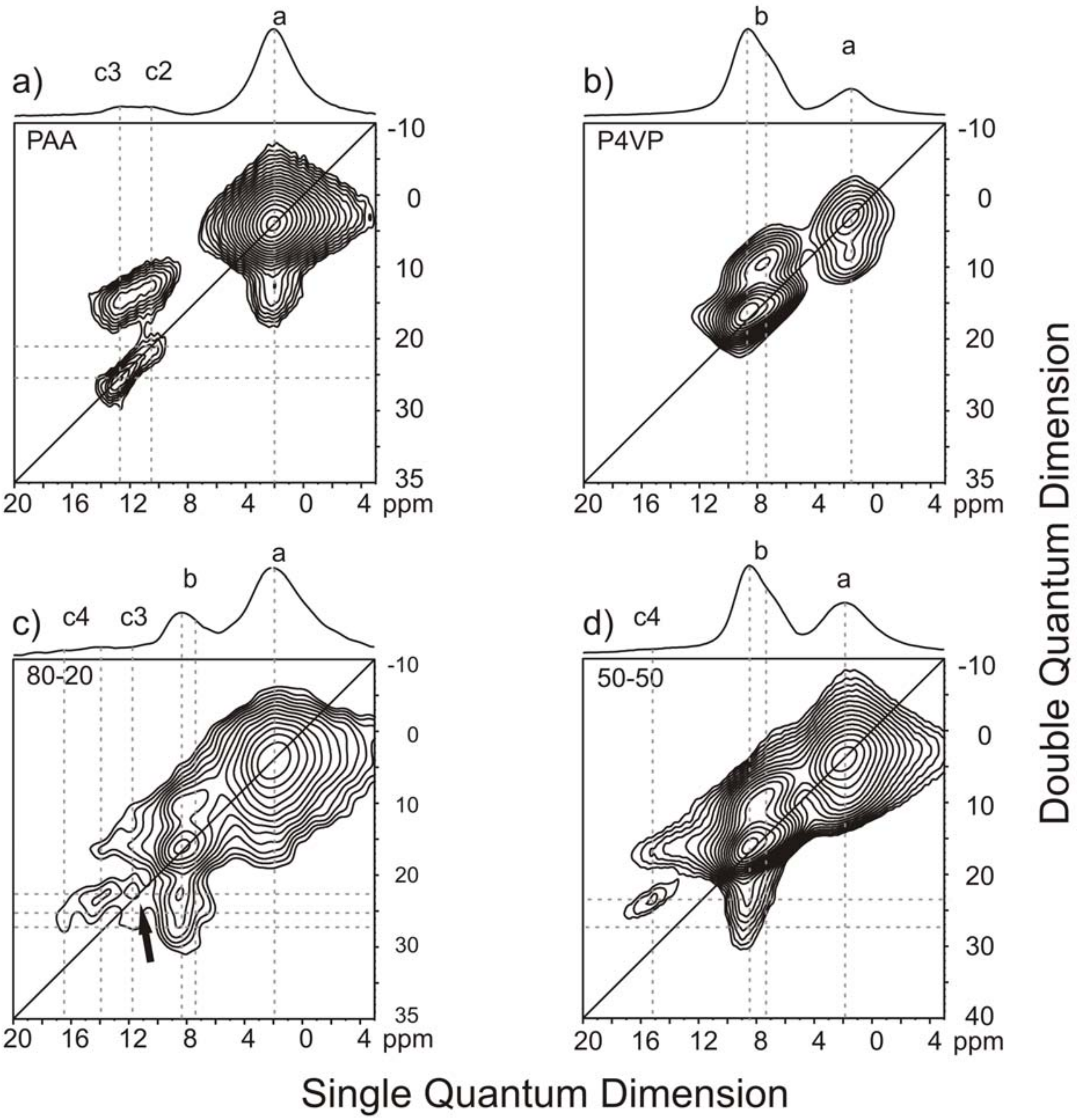

Figure 4.9: 2D ^{1}H DQ MAS NMR spectra of **a)** PAA, **b)** P4VP, **c)** 80PAA-20P4VP, and **d)** 50PAA-50P4VP. The spectra recorded with rotor-synchronized t_1 increments at 320K, 30 kHz MAS frequency, and with 1 rotor period of BaBa dipolar double-quantum recoupling pulse sequence.

For PAA, which is shown in Figure 4.9a, three auto peaks (a-a, c2-c2, and c3-c3) and two cross peaks (a-c2. a-c3) are observed. The strong auto-peak a-a appears at 2/4 ppm in SQ/DQ dimension is very broad, due to the strong couplings of the aliphatic protons and the amorphous nature of the polymer backbone. The auto-peaks c2-c2 and c3-c3 occur due to the acidic protons which are close in space to each other. The cross-peaks a-c2 and a-c3 appear in the DQ dimension at values which equal to the sum of individual SQ values of a, c2, and c3 (at 2, 12, and 14 ppm). It is interesting to note that there is no correlation between c2 and c3 type protons observed in the DQ spectra of pure PAA, most likely due to the dynamic process of the c2 sites, which leads to the fast exchange between the dimer and the free form. The hydrogen bonding in carboxylic acids occur by dimer formation in which the protons exist in pairs with typical through-space separation between 250 and 280 pm, corresponding to dipolar couplings of 5-8 kHz (Brown 01). Thus, the presence of the strong carboxylic auto peak c3-c3 in the 2D ^{1}H-^{1}H DQ spectrum is a clear proof of the hydrogen bonded dimers of carboxylic acid groups. For P4VP two proton signals are observed which are assigned to backbone protons (a-type) and aromatic pyridine protons (b-type). In this case, two auto-peaks and one cross-peak appear in the DQ spectrum. The signals of a-type protons located at 2/4 ppm in the SQ/DQ dimensions and two types of b-type protons at around ~8/16 ppm in SQ/DQ dimensions.

A closer inspection of the DQ spectra of the 4:1 complex (shown in Figure 4.9c) indicates the complexation of acid and base polymers. A new type of hydrogen bonding is formed between carboxylic acid protons and the pyridine nitrogen. The presence of this new interaction manifests itself as a cross-peak due to the interaction of carboxylic acid protons (c4 type) with the aromatic ring protons, appearing beyond 20 ppm in the DQ dimension (~23, ~25 and ~27 ppm in the DQ dimension). The presence of this resonance confirms the mixing of the materials at a molecular level. The absence of an auto-peak along the diagonal at the c4 type proton resonance indicates that the strongly hydrogen bonded –COOH protons with –N are not close to each other in space, but in fact are separated by at least one repeat unit, in both complexes. In the 4:1 system there is an excess of acid and the pairing is only available for 25% of the PAA with P4VP, which leaves 75% of PAA un-complexed. This fact differentiates the spectra of 1:1 and 4:1 complexes immediately. In Figure 4.9c, a weak auto peak along the diagonal (indicated by the arrow) due to the –COOH dimer formation by the excess acid sites in the system is still observed. This auto peak appears at 12/24 ppm in the SQ/DQ dimensions and is indicating strong hydrogen bonding, c3-type. Despite the excess acid, this auto peak is relatively weak, showing the prohibited interactions of –COOH pairs in the complex.

In the 1:1 complex (Figure 4.9d), two cross-peaks appear at around ~23 and ~27 ppm in the DQ dimension because of the interaction between aromatic protons (b-type, ~8 ppm in the SQ dimension) and acidic protons (c-types). The acidic protons contributing to the 23 and 27 ppm DQ signals can be calculated to be at ~15 and ~18 ppm, which are the c4-type acidic protons. In addition, there is no signal observed at ~12/24 ppm in SQ/DQ dimension for –COOH dimers, which was still the case in the 4:1 complex. This observation confirms the complete complexation where all PAA sites are interacting with P4VP sites, indicating that the systems are miscible and do not show any phase separation.

To be able to understand changes due to temperature variations, 2D ^{1}H-^{1}H DQ spectra were recorded as a function of temperature. When the temperature of the parent polymers and complexes was increased, substantial changes in spectra are observed, as is shown in Figure 4.10. The room temperature spectra are shown separately in Figure 4.9. For $1t_R$ excitation, from 320K to 400 K no big change was observed for the aliphatic backbone auto-peak a-a, and only a little change was observed in the aromatic region, as opposed to the carboxylic acid region.

For the PAA homopolymer, the c2-c2 auto-peak at 10 ppm is nearly invisible at 360 K, however, the c3-c3 auto-peak at the SQ dimension of 12 ppm corresponding to the strongly hydrogen bonding species can still be identified at the same temperature. On further heating, at 400 K, both of these resonances disappear because of the fast exchange noted above. In the ^{1}H MAS spectrum (Figure 4.7) an averaged signal was found at around 9 ppm for temperatures above 360 K. At lower temperature (T=270K), however, the acidic auto- and cross- peaks gain intensity relative to the aliphatic peaks because of the stabilization of hydrogen bonded sites, making them more rigid.

Upon complexation (for 1:1 and 4:1 samples), the mobility of the samples at a given temperature is reduced, as indicated already by the temperature dependence of the peak intensity in the spectra. The temperature effect is not as pronounced for the complexes as for the pure polymers. From room temperature to 400 K, the acidic ^{1}H interacting with aromatic protons giving rise to a cross-peak (b-c) decrease in intensity but can still be observed on the right side of the diagonal line. The existence of cross-peaks in the low field region (~23 and ~27 ppm in the DQ dimension) indicates that hydrogen bonds persist even at high temperature.

For the 4:1 complex, a weak auto peak still exists at ~12/24 ppm in the SQ/DQ dimensions due to excess PAA molecules. This type of auto peak is absent at increased temperatures for both PAA and 4:1. The cross peak at ~23 ppm in the DQ dimension (due to the interaction of 15 ppm PAA –COOH acidic proton resonance to the P4VP ring protons) in both complexes is detected at elevated temperatures, showing the stability of this kind of hydrogen bonding. More interestingly, the cross peak at ~27 ppm in the 4:1 complex is still strong at 400 K. This resonance is due to the interaction of a high chemical shifted hydrogen bonded proton, and mostly exists at the complex with excess amount of PAA. The thermal stability of hydrogen-bonding in the P4VP-PAA complex is higher than in PAA itself, as

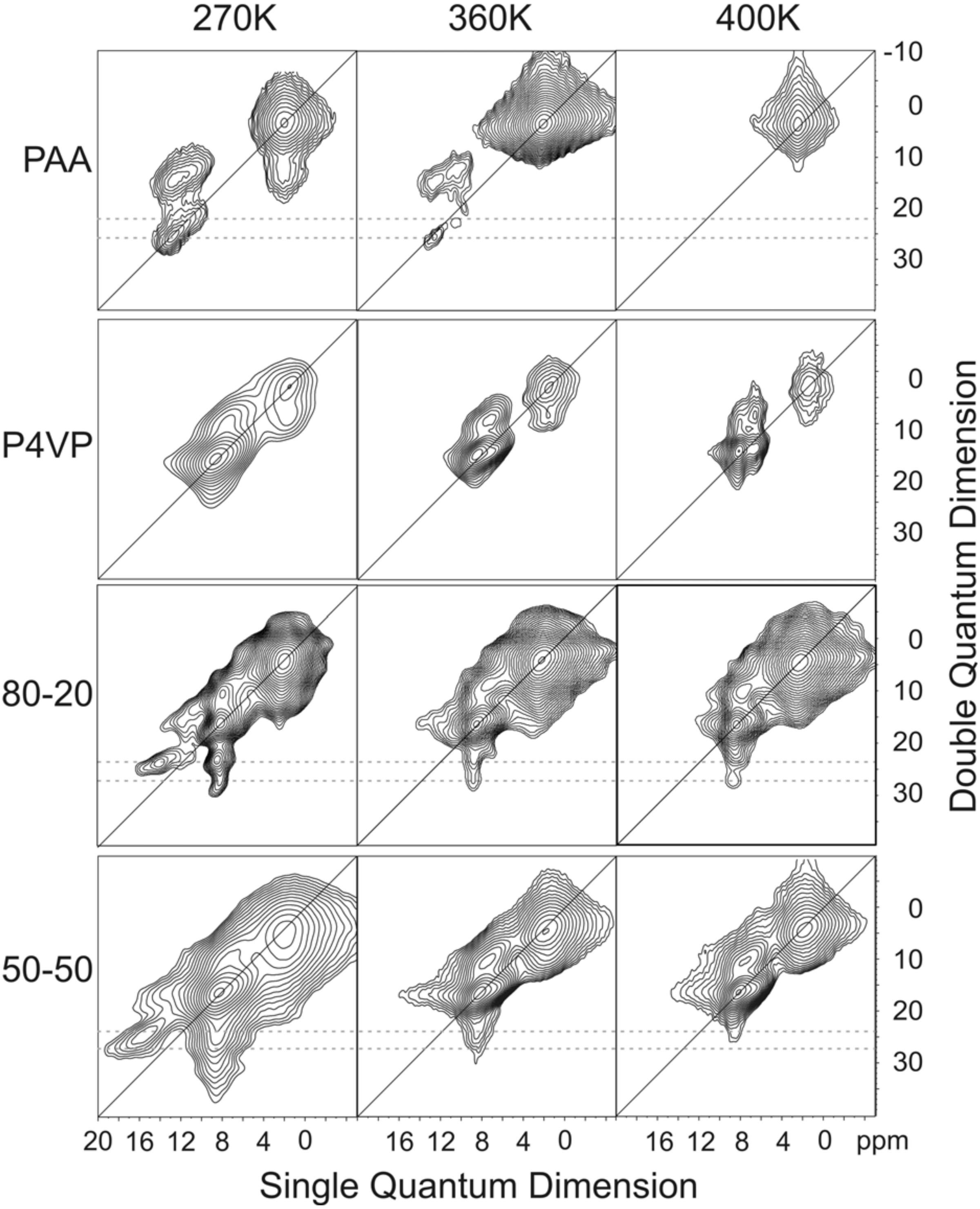

Figure 4.10: Temperature dependence of the 2D ^{1}H-^{1}H double-quantum MAS NMR spectra of dried parent PAA, P4VP, and their complexes 50-50 and 80-20, recorded at 30 kHz with $1t_R$ period of recoupling time.

indicated by the overall higher DQ intensity observed in the complexes compared with PAA at higher temperatures (400 K).

Another feature to be noted in Figure 4.10 is the missing cross peaks on one side of the diagonal at higher temperatures. For example, for PAA at 360K the cross peaks at ~15 ppm in the DQ dimension exist on the left side of diagonal only. They are missing on the right side of the diagonal. Also for the two complexes, at higher temperatures the cross peaks of the hydrogen bonded protons are missing on the left side of the diagonal lines. Normally, a DQC between unlike spins should give rise to two cross-peaks either side of the diagonal. These kind of missing peaks at one side of the diagonal have been observed before (Schnell 98), and indicates that different molecular mobilities of interacting sites present in the system.

4.3.6 Effect of Hydration to the Systems

Water has an enormous effect on the polymer complex structure, hydrogen-bonding, proton-transfer and proton-conductivity. Therefore, the water content should be precisely known and a homogeneous water distribution must be achieved prior to further analysis and experiments. Samples with known water content can be prepared by simply keeping the samples in an environment of desired humidity level. For complete hydration, the samples are kept in a desiccator with a water reservoir, and for lower water content with a saturated solution of calcium nitrate ($Ca(NO_3)_2.4H_2O$) which has a relative humidity of 55% at room temperature. The dried samples are prepared by keeping the samples in the oven under vacuum at 60^{o}C. The water permeation in PAA is fast enough to generate a homogeneous sample within several hours, but a heterogeneous distribution due to insufficient equilibration of water cannot be excluded.

The distribution and diffusion of water has particularly a big effect on the acidic protons of PAA. This effect becomes less important in the complexed samples when a basic polymer P4VP is added. In Table 4.3, the hydration levels for different samples are given. With increasing water content, PAA becomes softer and stickier, whereas the complexes did not show a significant softening upon hydration.

Table 4.3: Water contents of the samples investigated: PAA and complexes 50-50 (1:1) and 80-20 (4:1).

	PAA	**80-20**	**50-50**
Level A (Fully Hydrated)	53 %	20 %	28 %
Level B (Controlled)	11 %	9 %	11 %
Level C (Dried)	0 %	0 %	0 %

In Figure 4.11, ^{1}H MAS and ^{13}C CP-MAS spectra of PAA samples with different hydration levels at room temperature are plotted. In Figure 4.11a, the sharp peak at ~6 ppm in the sample with 53% water content is due to the free carboxylic acid proton surrounded by water molecules. This resonance appears at an intermediate chemical shift value between free carboxylic acid protons (~7-8 ppm) and the water proton resonance (~5), indicating an exchange of acidic protons and water. A small amount of hydrogen bonded protons exist even at high hydration levels, as indicated by the very weak resonance at ~9 ppm. The sample with 11% water content has an intense peak at around ~7.5 ppm indicating free carboxylic groups, previously referred to c1-type hydrogen-bonding proton, similar to the one obtained in pure PAA by increasing the temperature up to the complete conversion temperature, at above 340 K. In addition, there is a very small amount of hydrogen bonded protons in partially hydrated PAA appearing around 10 ppm. Upon lowering the hydration level, the acidic protons convert to c2 and c3 types of protons, and by further decreasing the water content, the dried situation is obtained in which c2 and c3 types are the dominant acidic protons with an additional tiny amount of free c1 type. Thus, changing the amount of water in pure PAA changes the hydrogen bonding strength and configuration.

The water adsorption has two effects which enhance proton conductivity. First, the chain mobility increases with increasing water content which is reflected in a better spectral resolution of carboxylic and aliphatic groups. Second, it leads to rapid proton exchange between water molecules and carboxylic acid groups. The second effect is the basis for efficient proton transport in hydrated materials.

Inefficient equilibration, on the other hand, results in an inhomogeneous water distribution throughout the sample as indicated by sharp intense resonances. In Figure 4.11a, such sharp peaks of the spectrum of PAA can be seen in the 4:1 complex. These peaks arise from very mobile regions inside the amorphous sample. The aliphatic region shows four sharp lines at 2.3, 1.4, 1 and 0.7 ppm originate from the backbone CH and CH_2 sites of the polymer and can also be seen in the liquid-state NMR spectrum of PAA.

The effect of hydration on the complexes is also shown in Figure 4.11a. The ^{1}H spectra of the 4:1 complex show a similar pattern as PAA in terms of sharper resonances in the aliphatic region. The shoulder at ~10 ppm at 20% hydration level indicates the presence of hydrogen bonding. When the complexation is complete, in the 1:1 sample, the sharp components disappear despite the same period of time spend for equilibrating the samples in the desiccator. In the 1:1 complex all the PAA are complexed with the P4VP so that the water permeation is limited and the partial hydration effect is less pronounced. The c4 type

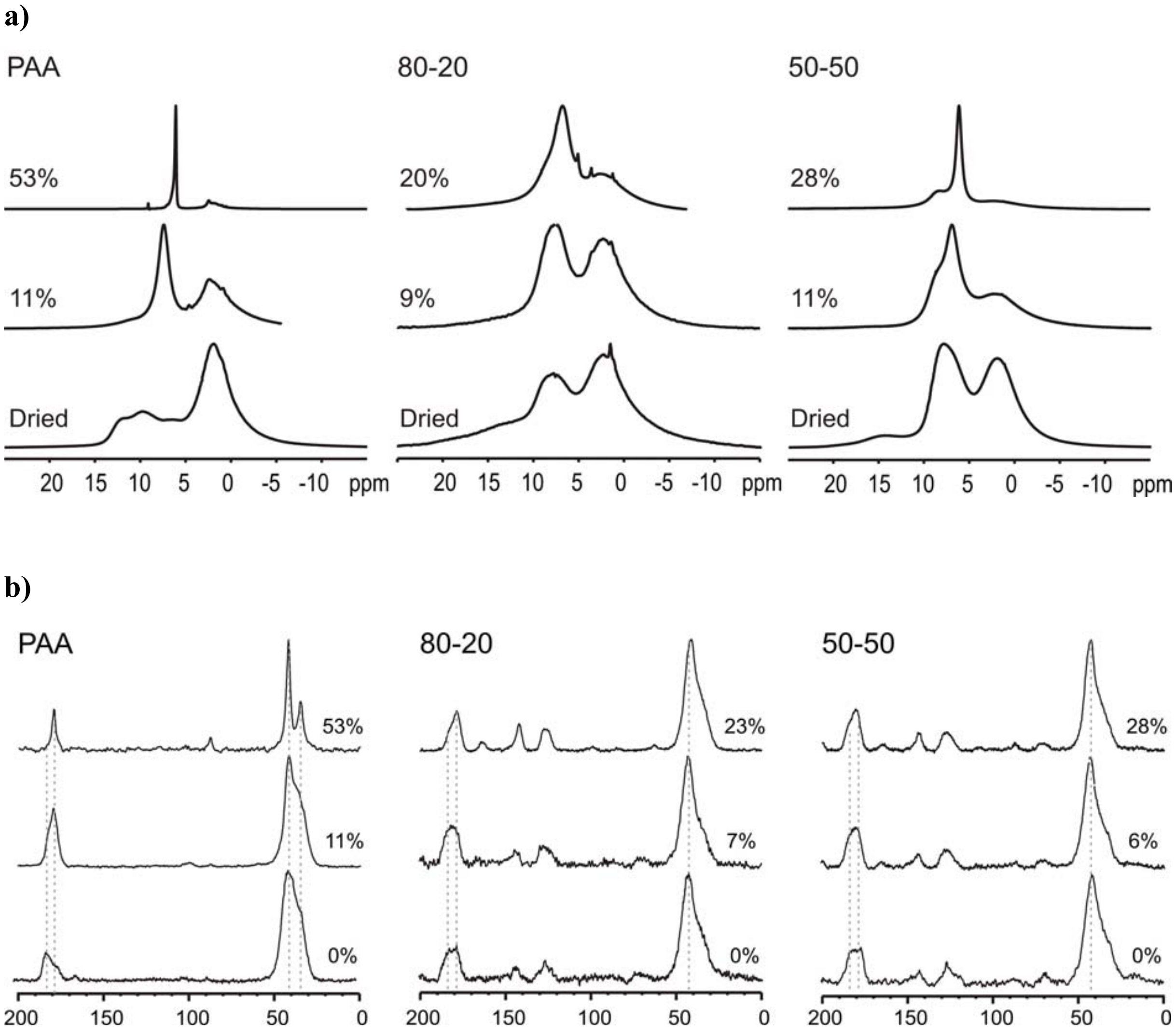

Figure 4.11: ^{1}H MAS and ^{13}C CP-MAS NMR spectra of PAA, and 50-50 (1:1) and 80-20 (4:1) complexes at room temperature with different hydration levels. The hydration levels are given at the top-right side of each spectrum. **a)** ^{1}H MAS spectra recorded at 30 kHz MAS, and **b)** CPMAS spectra recorded at 10 kHz MAS frequency, at room temperature, and with 1 ms CP contact time.

hydrogen bonding between PAA and P4VP, as well as other strong hydrogen bonding structures, are mostly absent in hydrated samples with a water content higher than ~10%.

^{13}C CP-MAS NMR spectra further clarify the effect of water on the materials noted above. This effect is twofold; it leads to changes in the carboxylic acid region around ~180 ppm and in the aliphatic region around ~30-50 ppm. In Figure 4.11b, ^{13}C CP-MAS NMR spectra of PAA, 1:1 and 4:1 samples with different hydration levels are shown, which enable us to monitor the conversion from the hydrogen bonded form of –COOH group to the free form with increasing water content. For PAA in its dried form, the resonance from the dimer type structure (c3 type) appears at around 184 ppm and resonance from the free carboxylic carbon (c1-type) appears at around 178 ppm. When the sample is hydrated to a certain level (11% or 53%), the amount of the hydrogen bonded carboxylic acid groups is decreased and converted into the c1-type, so the ratio of the 179/182 ppm signals changes. The effect of hydration is similar to the conversion with temperature increase. However, in this case, the carboxylic acid regions are surrounded by water molecules which inhibit the formation of hydrogen bonding. At 11% water content the two species can still be seen, however, only the free form is observed at 53% water content. For the complexes the effect of water is much less pronounced, and even at highest water contents (23% for 4:1, and 28% for 1:1 complex) two type of –COOH resonances can be seen.

Considering the aliphatic carbon resonances, a similar trend can be observed. With an increase in hydration level, at 53% water content, the two different peaks at 35 and 45 ppm become well resolved which appear as a broad peak with a shoulder in the dried form. With hydration, the mobility in the backbone increases leading to better spectral resolution. From the pure PAA to the complexes, the effect of hydration becomes less apparent.

4.3.7 Deuterium NMR Results: Molecular Level Mobility

^{2}H NMR studies of proton conducting acid-base polymer complexes are studied under static and magic-angel spinning conditions. Deuterium is a nucleus which is perfectly fitting to be used as a molecular dynamics probe in the μs time-scale. This is an immediate result of its small quadrupolar interaction (~200 kHz) which is effected by the motion of the specific deuterium site. Static experiments allow determining the quadrupolar coupling of ^{2}H nucleus, which can also be informative about the motional jump types and timescales when combined with variable-temperature approach. Combining ^{2}H NMR with fast magic-angle spinning can resolve the specific deuterium sites. Rotor-synchronized and non-rotor-synchronized data acquisition methods, as a result, give insights into different aspects of the motional questions. Deuterium NMR is a well established method for studying molecular dynamics (Spiess 85). ^{2}H is a quadrupolar nuclei with a spin I=1, and the quadrupolar interaction dominated for it. With an analysis of one-dimensional lineshapes for static ^{2}H spectra dynamical processes can be probed, because any motion exists in the deuterium site causes decrease in the rigid quadrupolar coupling which is around 200 kHz. During the last few years, attention in deuterium NMR progress into magic-angle spinning methods, which allow better resolution for site specific studies (Hologne 04, Thrippleton 08). ^{2}H solid-state NMR spectra in current study, recorded at 46.07 MHz ^{2}H Larmor-frequency for static experiments, and at 107.47 MHz ^{2}H Larmor-frequency for MAS experiments. Solid-echo pulse sequence was used for the static ^{2}H NMR experiments with a 1 μs pulse length, 20 μs echo-delay, and 1 s of recycle delay. ^{2}H MAS NMR spectra were recorded at 30 kHz MAS frequency, with rotor-synchronized one-pulse experiment, 2.5 μs pulse length, and 2 s delay time. The samples have been prepared by reflux method which should result in the exchange of only acidic protons with deuterium nucleus in D_2O solvent.

4.3.7.1 Static ^{2}H NMR Results

In this part static NMR results will be presented. Solid-state ^{2}H NMR techniques can provide direct information on the dynamics of selectively deuterated sites in the molecules. ^{2}H NMR studies have been made in a broad range of temperature (300 K – 400 K) to investigate the dynamics in a more complete manner.

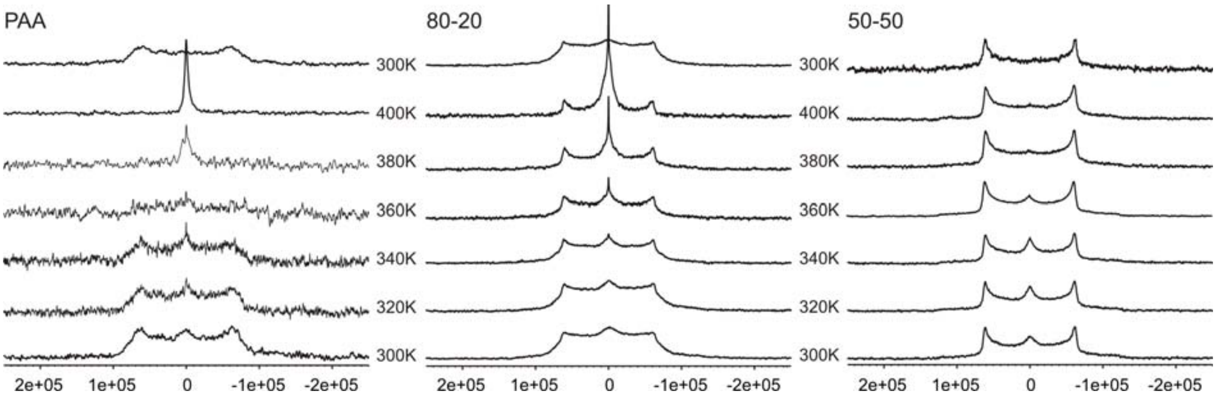

Figure 4.12: Solid-state ^{2}H NMR solid-echo spectra of PAA, and 80-20 and 50-50 complexes recorded in the temperature range 300-400 K. The echo delay used in solid echo experiments was 20 μs.

In Figure 4.12, variable temperature ^{2}H-static spectra of PAA and complexes are shown. At room temperature a rigid part and a more mobile part can be seen for PAA. The quadrupolar coupling of the rigid part, which may be assigned to the rigid hydrogen-bonded type of proton types is around 130 kHz. This value is simply extracted from the spectrum in Figure 4.12 by determining the splitting of two maxima of the 300 K spectrum by assuming this pattern is occurring due to a Pake-pattern. This pattern shows pronounced temperature dependence, i.e. becoming nearly invisible when the temperature reaches 360 K in the heating cycle. At 360 K because of the reorientation of deuterated species on the timescale of the echo delay the refocusing is incomplete so the signal disappears from the spectrum at this specific motional regime and temperature. This is a previously observed situation (Schmidt-

Rohr 94) and shows that the motion of the site is in the range of 1/ (20μs) = ~50 kHz. By further increasing the temperature, the motional rate of the deuterated site increases so the signal appears again but as a narrower line because of the much increased deuteron motion in the sample. During the cooling cycle the starting situation reappears, but in a rather different path. At 360 K on cooling a signal is observed similar to the one at 340 K in the heating cycle. Moreover, the narrower component in the room temperature spectra is missing. This is an indication of previously present water in the sample, which evaporated during the heating-cooling cycle.

The situation in 50-50 complex is quite different from pure PAA. In this case, above 360 K no narrow component is observed. Instead, the rigid part in the spectra with a quadrupolar coupling around 130 kHz determined. The rigid pattern is present even at the highest temperature, 400K, where PAA already showed motionally averaged sharp lineshape. This is a result of the complexation of PAA and P4VP, which gives a more rigid and stable structure to PAA in the complex with the formation of strong hydrogen bonding network. Similar to PAA, a narrower peak appears up to 380 K in 50-50, which is around the boiling point of water. This peak does not appearing after cooling the sample to 300 K. It can again be concluded that the narrower resonance is attributed to the residual D_2O in the sample which is bonded to the polymer, and removed during heating. After keeping 50-50 complex two weeks at room temperature in the rotor, the narrower component can be seen again at room temperature spectrum, which indicates the re-absorption of water.

Finally the same experiments were done for 80-20 complex. The situation in here can be described as a superposition of the spectra obtained for PAA and 50-50. The rigid part is like 50-50 sample and has a quadrupolar coupling of ~130 kHz, similar to others. The sharp component is originating from the PAA portion because of the excess non-complexed PAA in the sample and shows a similar sharp pattern at high temperature. After cooling back to room temperature, no change in the sharper component observed. This pattern indicates that the rigid component, due to the strong hydrogen bonded –OD, persists even at 400 K. Moreover, there is a more mobile component, whose mobility increases by increasing temperature and staying unchanged after heating cycle.

4.3.7.2 Spinning ^{2}H NMR Results

In Figure 4.13, ^{2}H MAS NMR spectra of deuterated PAA are plotted, recorded at 106 MHz Larmor frequency and at 30 kHz MAS spinning frequency. The deuterium spectrum at room temperature is extremely broad, beyond the observable spectral window. ^{2}H signal only becomes observable at higher temperatures. The absence of the ^{2}H signal at room temperature implies that reorientation of deuterium between different sites occur on the timescale of a rotor period (~33 µs) which prevents the refocusing of the anisotropic interactions by MAS. By increasing the temperature, the reorientation of the deuterated groups becomes much faster, as a result the interference disappears and ^{2}H signal re-appears. The same result also observed while cooling the sample.

The center frequency of the observed resonance at ~8-9 ppm proves the rapid exchange between free and hydrogen bonded –OD protons as also seen in the ^{1}H-NMR spectra. The activation energy for the deuteron dynamics is determined form the Arrhenius analysis of line width variation, which is ~31.7 kJ/mol.

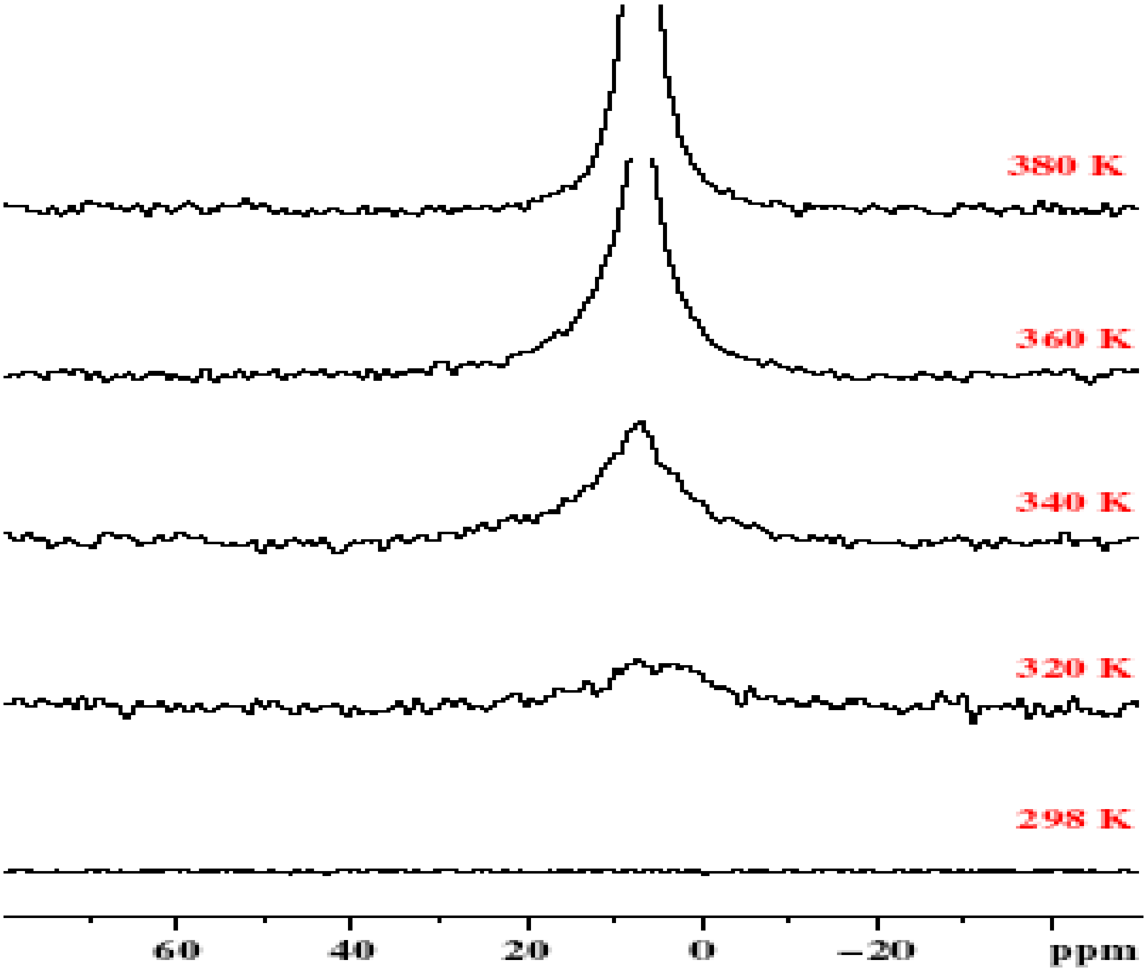

Figure 4.13: ^{2}H NMR spectrum of deuterated-PAA at 30 kHz MAS speed and at 106 MHz Larmor-frequency. Activation energy of proton exchange in deuterated PAA is ~31.7 kJ/mol.

4.4. Relation of NMR Observations to Proton Conductivity

The pure PAA shows the highest proton conductivity of ~3.70.10^{-5} S/cm at room temperature in wet conditions compared to all systems discussed here. Moreover, the 1:1 complex has a slightly higher conductivity (~1.65.10^{-5} S/cm) compared to the 4:1 complex (~1.20.10^{-5} S/cm) (Chu 08).

The high conductivity of pure PAA is easy to understand, however, the higher conductivity of 50-50 compared to 80-20 is more difficult to rationalize. In the PAA material, dimer formation results in different types of hydrogen bonded proton. Moreover, the free form of carboxylic acid is still present in the pure PAA. This type of hydrogen bonding is not as strong as that observed in the presence of P4VP (as indicated by higher chemical shifts).

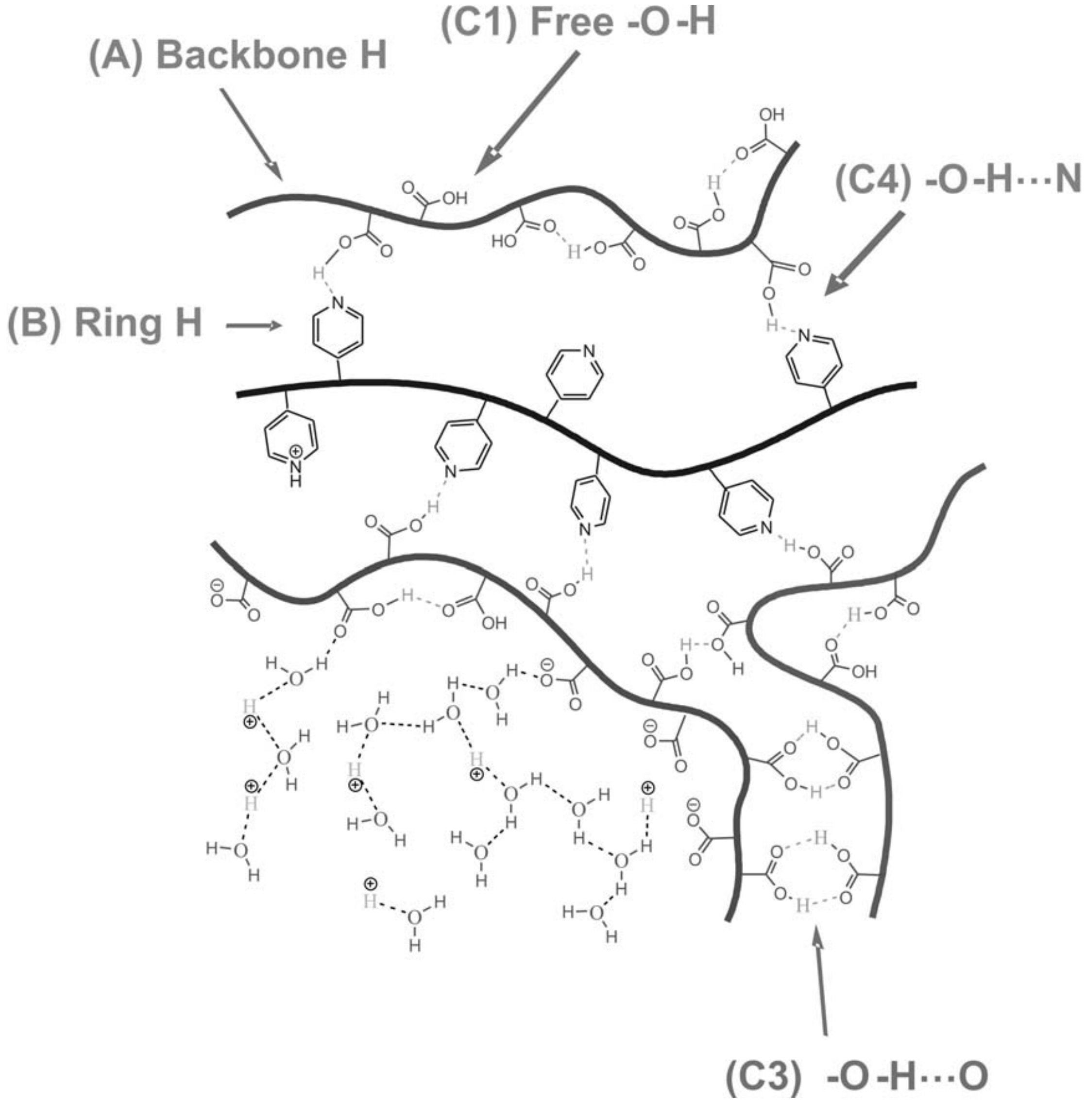

Figure 4.14: General scheme of PAA-P4VP system with all possible interactions and with the representation of the effect of water.

With the addition of P4VP to PAA a complex is formed as demonstrated by the NMR results, which might result in formation of more ordered domains and in facilitated proton conductivity, observed in partially wet materials. The presence of the strongest hydrogen bonding configurations (~18-19 ppm) in the 4:1 complex rather than in the 1:1 complex, is consistent with the higher conductivity of the 1:1 material. The stronger the hydrogen bonding, the more difficult it is for the protons to be transferred through the ordered domains (via a Grotthuss mechanism in the conduction channels).

In the presence of water in the systems, the proton conduction can simultaneously be achieved by a vehicle mechanism and proton hopping (Grotthuss), due to the excess of proton donor and acceptor sites. In the water-free samples, however, proton transfer must occur through the hydrogen-bonding network of PAA-P4VP via proton hopping between proton donor (PAA and protonated P4VP) and proton acceptor (P4VP and de-protonated PAA) sites. The later process is facilitated at elevated temperatures.

4.5. Conclusions

Acid-base polymer complex electrolytes provide a new design for achieving proton conductivity in essentially water free environments at elevated temperatures. The manner by which protons transport is achieved is closely related to the hydrogen bonding. Therefore, the formation of hydrogen bonding studied here is an important issue to better understand the proton transport mechanism.

The structure and dynamics of PAA-P4VP anhydrous acid-base polymer complexes have been studied with various solid-state MAS NMR techniques. The applied spectroscopic methods involve ^{1}H and ^{13}C and SQ as well as ^{1}H DQ methods. The results from ^{1}H NMR measured under fast magic angle conditions and additional aspects from ^{13}C CP-MAS NMR were combined to complete the picture, which is summarized in Figure 4.14.

The structure of the PAA-P4VP system was determined mainly by ^{1}H MAS solid-state NMR spectroscopy, where one non-hydrogen-bonded proton (c1) and three different types of hydrogen bonded protons were identified in PAA homo-polymer and its complexes. The spatial proximity of the acid and base groups in the polymer complex was monitored by 2D ^{1}H-^{1}H double quantum NMR methods in a semi-quantitative way. The miscibility of PAA and P4VP is also an important issue to understand the complex formation. From the 2D DQ NMR spectra direct evidence for a complete miscibility on the molecular level of PAA and P4VP was obtained.

The stability of the hydrogen bonded species against temperature has been investigated in the range of 270-400 K. In PAA, conversion of carboxylic acid dimers to free acid protons was observed. This conversion is accomplished at around ~380 K in dry samples and occurs at lower temperatures in hydrated samples, ~360 K (for 11% water content) and ~340 K (for 36% water content). The stability of hydrogen-bonding strongly depends as well on the hydration level in the complex. Hydration particularly has a strong effect on PAA due to the ease of the water and carboxylic acid proton interactions. This effect is smaller for the complexes. In the hydrated materials, a chemical exchange of acidic –COOH proton with water was observed, especially for PAA.

^{2}H NMR spectroscopy was used to investigate the dynamics of the systems. However, insufficient information about the hydration level of the deuterated samples prevents further conclusions on the timescales and types of motions of acidic sites. Nevertheless, it can still be said that, from static ^{2}H NMR results, the stabilization effect of complexation of PAA with P4VP is proved which can be seen by the persisting ^{2}H Pake-pattern at higher temperatures. The Pake-pattern is lost at elevated temperatures leaving only the narrower component for PAA. The complexes have much more stability compared to PAA, which manifest itself as an un-disturbed Pake pattern at high temperatures in static ^{2}H spectra. From the spinning ^{2}H NMR results the deuterated sites observed with an increased resolution gained by MAS. After the heating cycle the irreducible broadening of the peaks observed. The activation energy for the deuteron motion in deuterated-PAA is determined form the Arrhenius analysis of the line width change upon heating, which is ~31.7 kJ/mol.

The rational design of proton conductors requires insights on the molecular level structure, the interaction between complexed groups, and intrinsic dynamics related to the building blocks. Advanced solid-state NMR provides detailed information on structure and dynamics of such systems. In conclusion, hydrogen bonding mediated proton conduction is present in PAA-P4VP polymer blend systems. The conductivity values are still short of an immediate application, but the current study provides a detailed understanding of the acid-base polymer blend approach. Similar systems with different acid-base configurations are being under investigation which will help to reveal the conductivity phenomenon even better.

Chapter 5:

Hydrogen Bonding and Proton Conduction of Anhydrous Poly(2,5-benzimidazole)-Poly(vinyl-phosphonic acid) Acid-Base Polymer Blends

In this chapter, the acid polymers blended with basic polymer are studied which belongs to acid-base polymer blends approach with the aim of preventing the problem of acid leaching, whose examples are studied before (Kerres 99, Akbey 08). The system is based on the complexation of acidic poly (vinyl-phosphonic acid) (PVPA) and basic poly (2,5-benzimidazole) (ABPBI) polymers which form self assembled arrays driven by hydrogen-bond formation (Shown in Figure 5.1). Since the acid groups are fixed to the polymer backbone, this system does not suffer from the leaching of acidic groups. This concept might lead to a new fuel cell material type which still conducts protons at intermediate temperatures. Hydrogen bonding is an important issue to elucidate in these proton conducting materials, which is the driving force for the complex formation. Moreover, Grotthuss type proton conduction mechanism is established by the hydrogen-bonding network. Different hydrogen bonding arrangements of the current system are shown in Figure 5.2.

To meet the required goals, several design concepts have been proposed. One concept is the use of basic polymers to achieve high anhydrous conduction at higher temperatures. Kerres et. al. reported materials based on the phosphoric acid doping of poly-benzimidazole (Kerres 96). The main problem in this category of materials is the leaching of the dopant acid, due to the un-stabilized nature.

A similar study of poly (acrylic acid) – poly (4-vinyl pyridine) (PAA-P4VP) was performed recently with similar NMR techniques in our group (Akbey 08), which showed different hydrogen-bonding arrangements in that system. The current system is based on PVPA, which is a stronger acid compared to PAA, and as a result supplying a stronger interaction with basic ABPBI polymer. Lee et al. (Lee 07) and Unugur et al. (Unugur 08) have reported a similar solid-state NMR study of pure PVPA and its copolymers with PVTri, which are suffering from the crosslinking of the phosphorous groups. With this study the effect of the complexation with basic polymer on the anhydrate formation will be investigated.

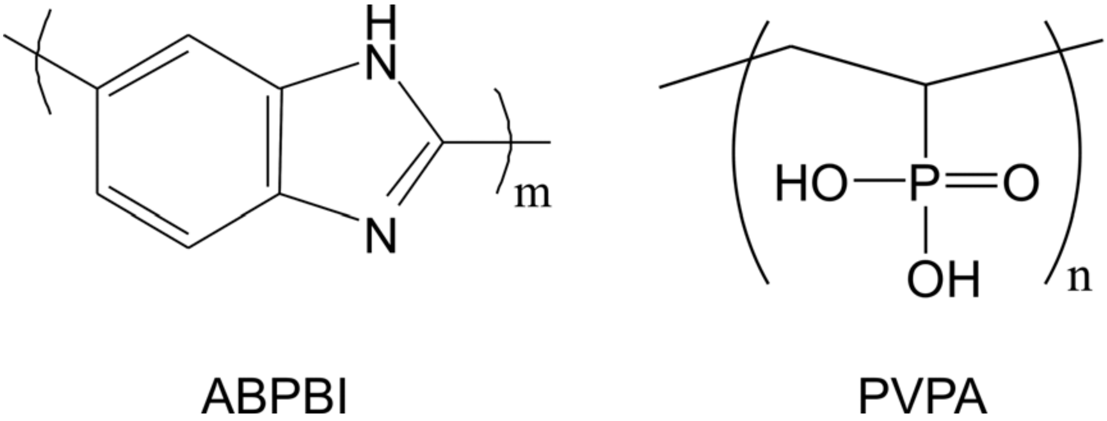

Figure 5.1: Schematic chemical structures of the parent polymers: Poly(2,5-benzimidazole) (henceforth referred to as ABPBI) and Poly(vinyl-phosphonic acid) (henceforth referred to as PVPA).

The aim of the current study is to understand the acid-base complexation of the ABPBI-PVPA system at different mixing ratios, and to elucidate the resulting structural and dynamics effects. This information will be compared with conductivity results. ^{1}H, ^{13}C and ^{31}P MAS NMR methods were used to investigate the systems. This will be combined with the molecular dynamics studies by variable temperature ^{1}H MAS and one-dimensional (1D) double-quantum (DQ) methods. Two-dimensional (2D) ^{1}H DQ correlation experiments will be used to probe spatial proximities which are very important to fully solve the mixing and complexation of the system, as well as the molecular level mixing of the two different polymer components. The existence of anhydride formation will be probed by ^{31}P MAS NMR.

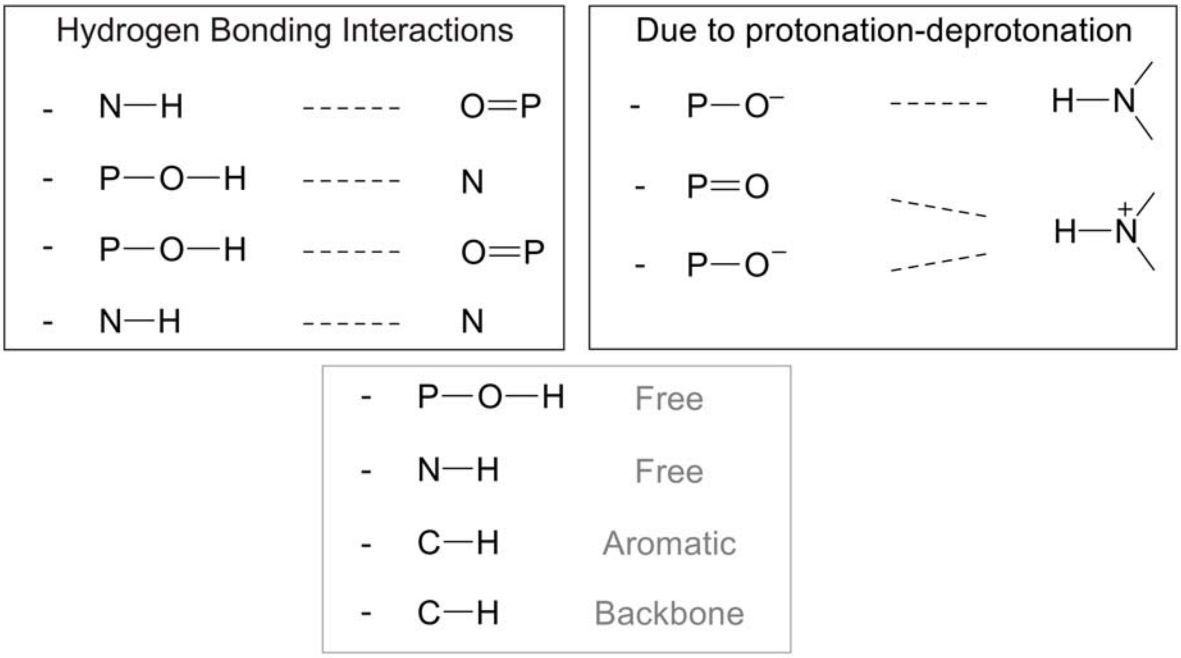

Figure 5.2: Different types of protons in the ABPBI-PVPA systems, and their possible arrangements. The hydrogen bonding arrangements of protonated or de-protonated molecules are shown separately. Protons which are not participating hydrogen-bonding interactions are additionally shown below.

5.1. Materials:

The materials studied here were prepared by Peter P. Chu, and details of the synthesis procedures will be given elsewhere (Chu 08). As a short note, Poly(vinyl phosphonic acid) was purchased from Polyscience (Mw = 24000) and used as received. ABPBI was synthesized in the laboratory of Peter Chu. The polymer materials were prepared by the addition of appropriate mole percent of ABPBI and PVPA in methanesulfonic acid, followed by an evaporation of solvent.

5.2. Results:

5.2.1 One-Dimensional ^{1}H MAS Spectra: Molecular Structure of the System

Figure 5.3 represents the one-dimensional ^{1}H MAS NMR spectra of the parent polymers ABPBI and PVPA recorded at 320 K and at 30 kHz MAS frequency. The specific resonances can be seen originating from different types of protons in the polymers. For ABPBI, one very sharp and dominating resonance at 7.2 ppm is originating from the ring C-H and free ring N-H protons. A much less intense peak at 1.4 ppm is also observed originating from the residual solvent methyl sulfonic acid, nevertheless, the amount of this resonance is very small and only appearing in this parent polymer. More interestingly, a broad shoulder appearing at around 12 ppm is observed which is due to the hydrogen bonded ring N-H proton in ABPBI. From the low intensity of the 12 ppm resonance, one can conclude that in the ABPBI polymer there is hydrogen-bonding present, due to the interaction of successive ABPBI pairs (inter-chain interactions). However, the amount of hydrogen bonded ring NH protons is not much compared to the non hydrogen-bonded proton resonances, understood from the intensity ratio in the ^{1}H MAS spectrum.

It is evident from the hydrogen-bonded proton resonance that ABPBI system arranges in such a way that the NH···N type of hydrogen-bonding is formed through the inter-chain benzimidazole units. This kind of arrangement is also evident from the X-ray studies of pure ABPBI, showing an inter-chain spacing of ~3.9 A (Chu 08). In the same chain (intra-chain), however, because of the large distance of adjacent N-H and N sites, the hydrogen-bonding is not possible.

The PVPA has resonances with different chemical shift values compared to the ABPBI proton resonances. The 2.2 ppm proton resonance is due to the backbone -CH_2 protons, residual water is observed at 6.8 ppm (with a very low intensity even after drying), and the hydrogen-bonded acidic -P-OH protons appear at 10.6 ppm (inter or intra chain hydrogen bonding). The water molecules which still exist in PVPA are coordinated water molecules, different from bulk water, as indicated the higher chemical shift value. The high chemical shift value of the –P-OH resonance is clearly showing the presence of hydrogen-bonding in PVPA (Lee 07, Unugur 08).

The different proton sites and possible interactions between them in the ABPBI-PVPA system are shown in Figure 5.2. This is a list which contains all possible arrangements, however, it should be noted that not all of them may exist in the current systems. We need to clarify the existence of specific interactions experimentally. Hydrogen bonding is possible between acidic protons like P-OH, N-H and electron rich groups like –P=O or ring –N.

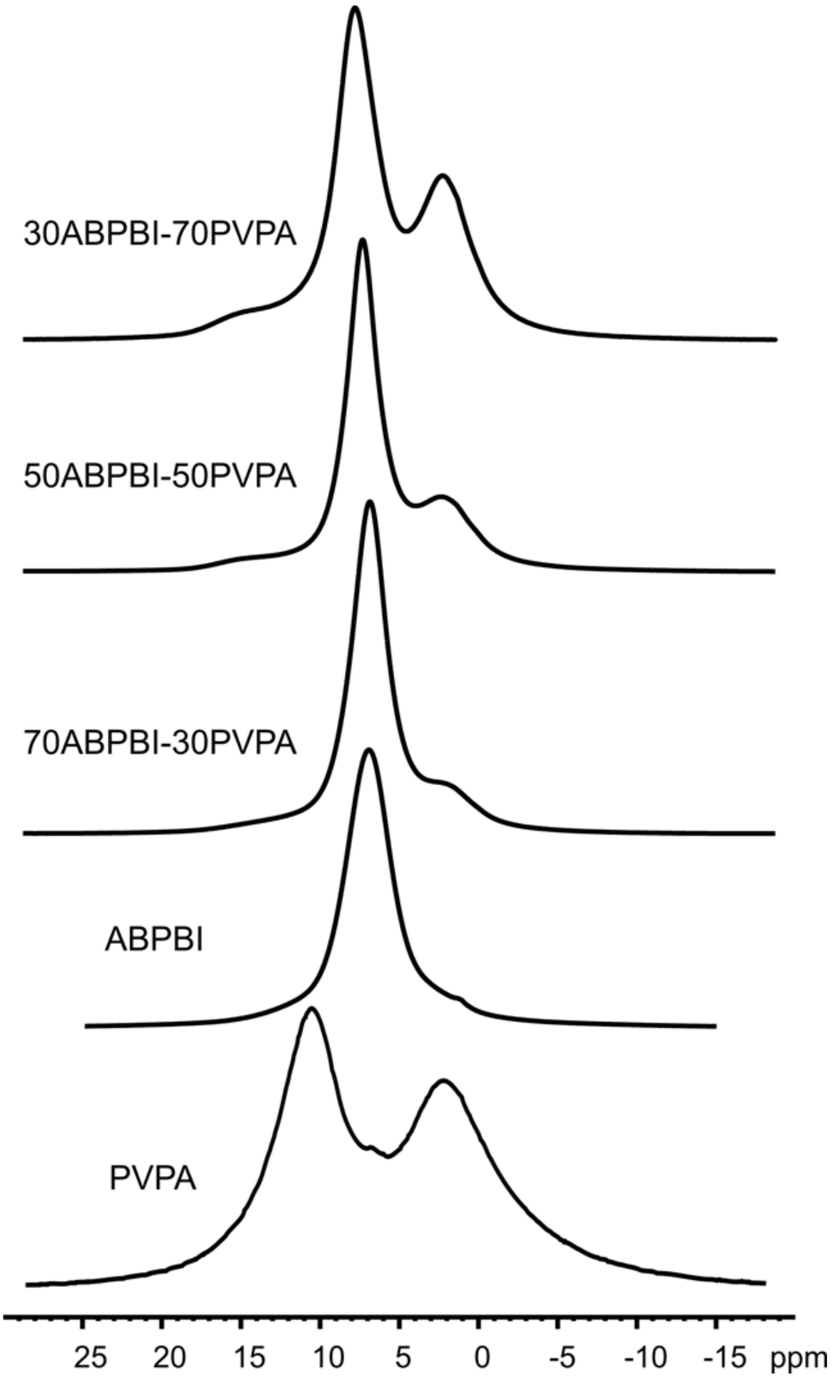

Figure 5.3: ^{1}H MAS NMR spectra of all samples with different mixing ratios (70-30, 50-50, 30-70) and parent polymers recorded at room temperature (325K, after the correction of additional heating caused by high spinning speed) and at spinning speeds of 30 kHz, at 700 MHz.

Different combinations may occur with possible pairing configurations in different complexes.

The ^{1}H MAS spectra depending on the complexation are given in Figure 5.3. The resonances of the aliphatic and aromatic region are consistent with a superposition of the ^{1}H

MAS spectra of the parent polymers, however in the case chemical shift region of hydrogen-bonding protons new signals are observed. The broad new resonance covers a chemical shift region from 10 ppm up to ~18 ppm, which corresponds to a distribution of hydrogen-bonded protons with different types and strengths. The high chemical shift values of this broad resonance indicate the presence of strong hydrogen bonded proton sites in the complexes. Due to the polymeric nature of the sample, the hydrogen-bonding network is not well defined, and can not adopt ideal organization. Different strengths of the same hydrogen-bonded pairs can exist at different sites of the polymer system, which cause an additional broadening of specific chemical shifts, covering ~8 ppm width.

A closer inspection of the aromatic resonances (~7 ppm) shows that different linewidths and chemical shift values are observed in different mixing-ratios of acid and base polymers, which implies different mobility of the ABPBI rings at different mixing-ratio complexes due to different packing. The narrowest aromatic resonance is observed in the 50-50 complex which has 1.6 kHz linewidth at half maximum height (1.8 kHz in 70-30, 2.2 kHz in 30-70, and 2.3 kHz in ABPBI), showing the most mobile nature of aromatic protons. Moreover, there is a shift in aromatic resonance with the addition of acidic polymer. In 70-30 complex this resonance appears at ~7.3 ppm, in 50-50 complex at ~7.5 ppm, and in 30-70 complex at ~7.8 ppm.

The pure ABPBI has the strongest packing arrangement within inter-chain benzimidazole units and its ring proton chemical shift value is 7.2 ppm. A gradual low-field shift occurs towards higher chemical shift values (up to 7.8 ppm for 30-70 complex) by the introduction of acidic polymer for three complexes depending on the PVPA content. The introduction of strong hydrogen-bonding interactions decreases the packing effect and causes weakening of ABPBI inter-chain interactions driven by the dominating hydrogen-bonding interaction between ABPBI and PVPA.

Despite the sharper hydrogen bonded proton resonance in PVPA, at 10.6 ppm, in the acid-base polymer complexes (even at the highest acidic polymer mixing-ratio, 30ABPBI-70PVPA) there is only a very broad resonance from 10 ppm up to 18 ppm. This shows the broad distribution of hydrogen-bonding formation in PVPA after complexion with ABPBI. This only leaves the hydrogen bonding arrangements which are formed with the corresponding ABPBI polymer chain and also with the intra-chain interactions of adjacent –P-OH groups in the same chain. The intra-chain hydrogen bonded –P-OH protons do not result in a sharper resonance.

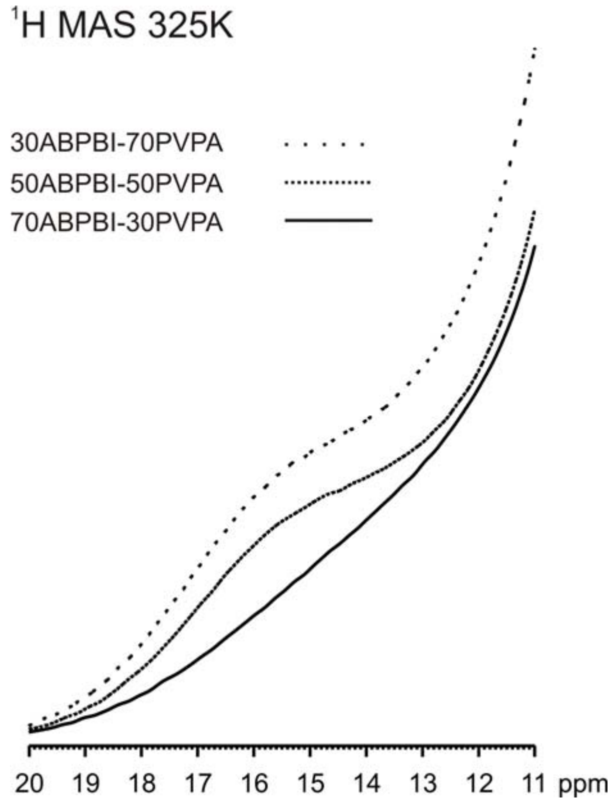

Figure 5.4: ^{1}H MAS NMR spectra of complexes with 70-30, 50-50 and 30-70 ABPBI-PVPA mixing ratios, recorded at 325K at 30 kHz spinning speeds. Spectrum is showing the zoomed hydrogen-bonded region of the full spectra shown in **Fig. 5.3**, from 11 ppm up to 20 ppm.

The broad resonance appearing in the low-field region can be more easily understood considering the different possible hydrogen-bonding combinations in the current system shown in Figure 5.2. In previous studies, some of these hydrogen-bonding structures (Goward 02, Hughes 04, Unugur 08) could be used to assign the chemical shift values in the current systems. In the study of Goward et al., it was shown that the N-H ··· N hydrogen bonding pair has a chemical shift value of 16 or 14.7 depending on being intra-pair or inter-pair interaction in the imidazole-2-ethyleneoxide system. In a more recent study of Hughes et al. on phosphoric acid doped Poly[2,2′-(*m*-phenylene)-5,5′-bibenzimidazole], the proton of the N-H ··· O-P hydrogen bond was shown to have a chemical shift value of 14 ppm, and P-OH ··· O-P having a lower chemical shift value of ~11-13 ppm. In PVPA-PVTri copolymer systems (Unugur 08), OH···O and OH···N types of hydrogen bonded protons were observed at ~12 and ~15 ppm, which are very similar chemical shift values to those of the current system. In both systems the aromatic protons of the ring containing nitrogen have the chemical shift value of around 7 ppm. It is evident from these previous studies that the very broad resonance from 10 ppm up to 18 ppm contains many different types of hydrogen-bonded structures.

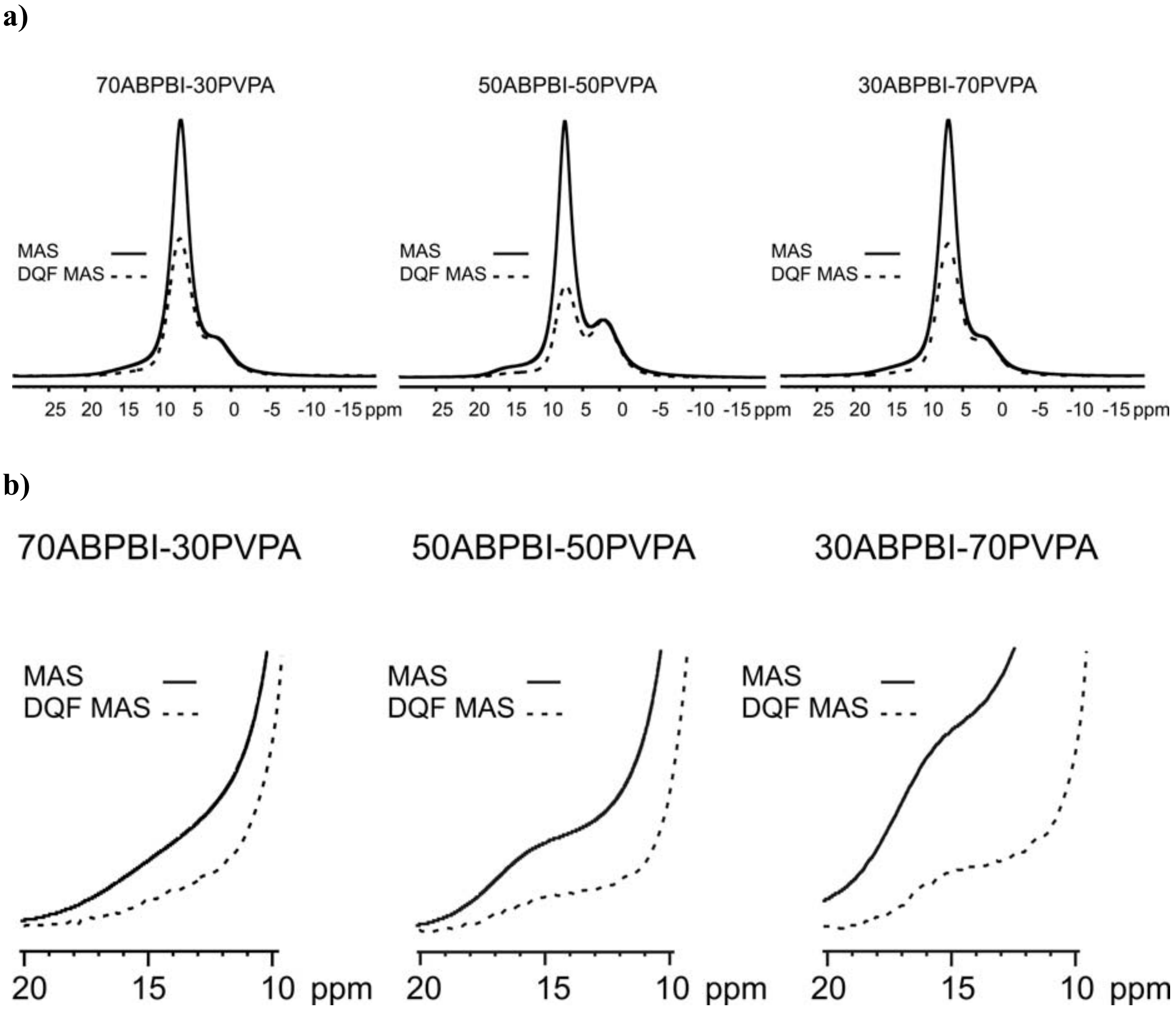

Figure 5.5: a) Comparison of ^{1}H MAS and ^{1}H DQF MAS spectra of the complexes with 70-30, 50-50 and 30-70 ABPBI-PVPA mixing ratio. The spectra recorded at 325 K and at 30 kHz MAS frequency. The intensity of the aliphatic region was the basis of comparison. It was set equal height in both spectra to make it easier to see the relative decrease of other peak intensities. **b)** The enlarged hydrogen-bonding region of the complexes.

The relative intensity of the broad hydrogen-bonded proton resonance increased with increasing PVPA content in the ABPBI-PVPA system. However, the most resolved lineshape of the broad hydrogen-bonding region is observed at a 1:1 acid-base mixing-ratio in 50-50 complex (Figure 5.4).

The low-field ^{1}H resonance of 30-70 mixing-ratio in Figure 5.4 is more intense compared to other two complexes, which results from the excess amount of acidic PVPA. When the 1:1 mixing ratio is obtained in the 50-50 complex, a more defined shoulder is observed at 15.5 ppm. This supports the formation of a more ordered hydrogen-bonding configuration, which has been obtained by other techniques (Chu 08).

5.2.2 ^{1}H DQ MAS NMR (one-dimensional DQ-filtered spectra): Mobility of Hydrogen Bonding Proton Sites

A comparison of ^{1}H MAS spectrum with ^{1}H double quantum filtered (DQF) spectrum allows us to distinguish between mobile and rigid proton types (Schnell 01a, Brown 01). It should be kept in mind that, the protons which are transferred from one site to another hydrogen-bonding site are in charge of the conductivity. The rigid acidic protons, however, are trapped in their places due to strong hydrogen bonding configuration. Rigid protons usually do not contribute to the proton conductivity. Still hydrogen bonding is necessary for proton conduction to facilitate protons to be transported via Grotthuss mechanism by a hydrogen-bond breaking process. The signals of mobile acidic protons are suppressed by double-quantum filtration. In some cases, a complete loss of the signal can be observed, as in the case of Imi-nEO materials (Goward 02).

The comparison of ^{1}H MAS and DQF spectra is shown in Figure 5.5a. The spectra are recorded at T=320 K, 30 kHz MAS rotation frequency and with one rotor period (33 μs) BaBa DQ excitation. When the intensity of the ^{1}H DQF spectra is normalized to aliphatic regions of ^{1}H MAS spectra, it can be seen that there is a more pronounced loss in intensity at the signals of the hydrogen-bonded protons as well as at the 7 ppm resonance assigned to aromatic ring of ABPBI and free P-OH of PVPA. Proton resonances loose intensity after the applications of DQ filtration because of the mobility present in those specific sites. However, their mobility is not sufficient to cause a complete removal of the signals after DQ filtration.

The most pronounced reduction is observed for the signals at ~7-8 ppm, which is strongest for the 50-50 complex. This mobility difference between the different complexes is also observed in ^{1}H MAS NMR spectra, manifesting itself as the narrowest aromatic resonance for the 50-50 sample (Figure 5.3). This mobility difference might also be the reason for the observed higher proton-conductivity of 50-50 complex at room temperature.

In Figure 5.5b, the enlarged ^{1}H MAS-DQF NMR spectra is shown, for a better comparison of hydrogen-bonded proton dynamics in different complexes. It can be seen that the relative intensity loss at hydrogen-bonded proton sites after DQF is most pronounced in 30-70 complex compared to ^{1}H MAS spectrum. It seems that the hydrogen bonding configurations formed by 30-70 complex is the most mobile one at room temperature. The other two complexes, on the other hand, are forming more stable hydrogen bonding arrangements, as indicated by their smaller decrease in intensity after DQ filtration.

5.2.3 ^{1}H DQ MAS NMR (two-dimensional rotor synchronized spectra): Molecular Level Proton Proximities

From one-dimensional ^{1}H DQF spectra shown in Figure 5.5, spatial proximities between dipolar coupled protons can hardly be determined. This information will be immediately available by two-dimensional rotor-synchronized ^{1}H DQ MAS experiments (Schnell 01a), which are shown for ABPBI and PVPA in Figure 5.6.

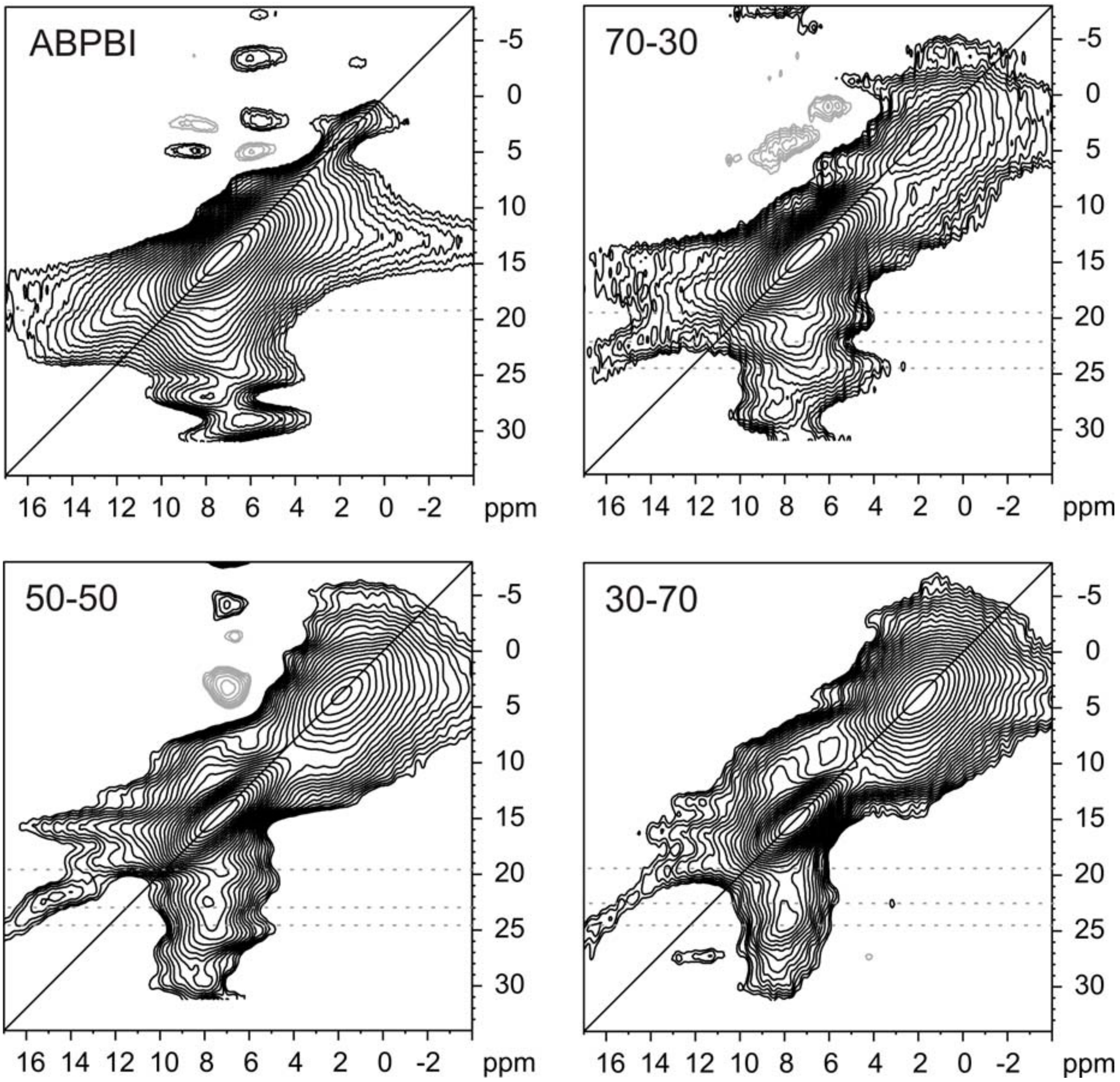

Figure 5.6: 2D DQ Spectra of the ABPBI parent polymer and 70-30, 50-50 and 30-70 ABPBI-PVPA complexes recorded at 325K and at 30 kHz spinning frequency. The spectra recorded by using BaBa DQ recoupling pulse sequence with 1 rotor period of excitation-reconversion recoupling time. The increase in PVPA content and induced changes can be seen. The contour levels set same in all spectra, so comparison can be done easily by comparing the intensities.

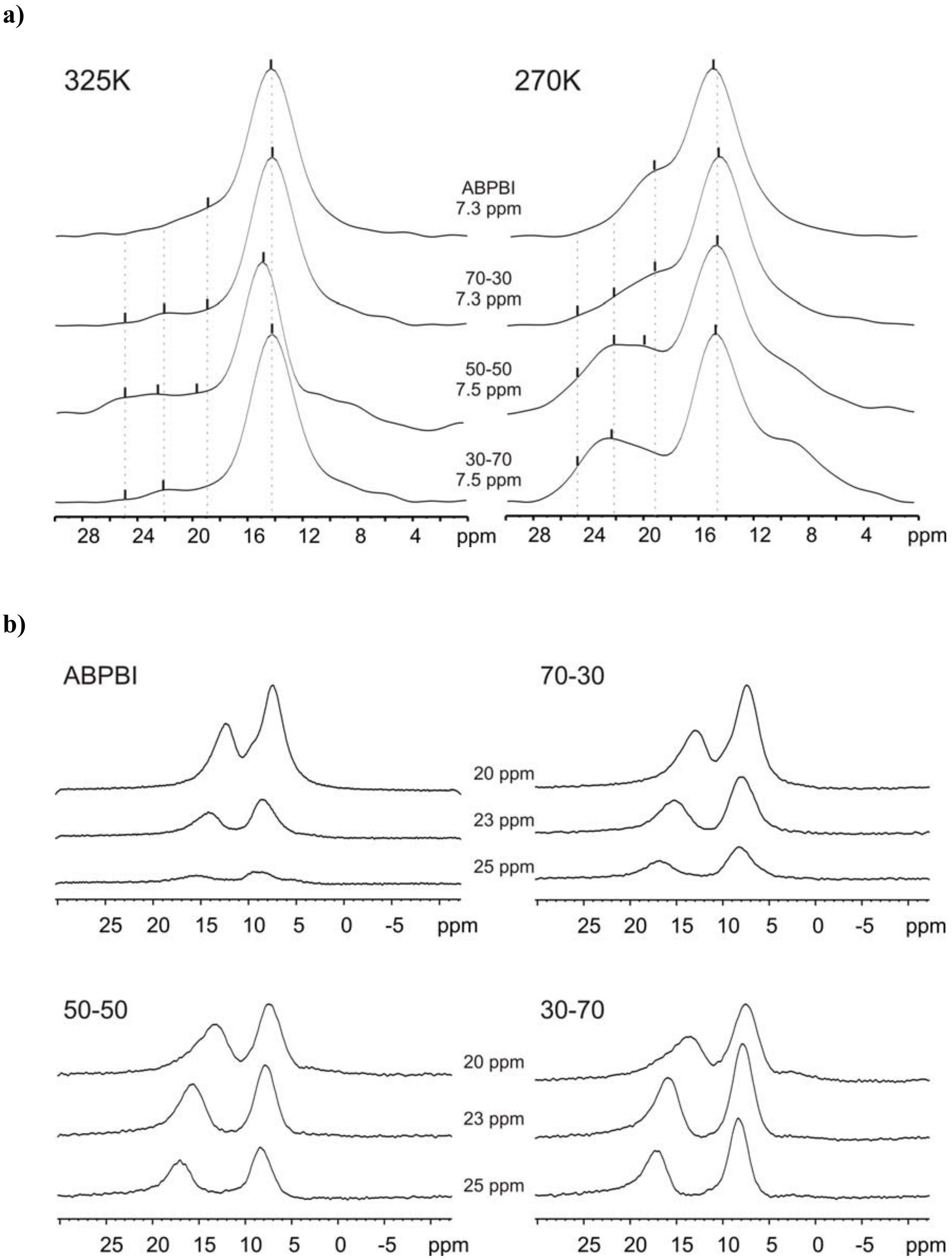

Figure 5.7: a) The slices taken from the of ^{1}H 2D DQ spectra of the pure ABPBI and the complexes recorded at 270 K and 325 K. The slices are taken from the given single-quantum dimension chemical shift values to more easily recognize the interactions of ABPBI ring protons with other proton types, especially with hydrogen-bonded acidic protons. **b)** The slices taken from the given double-quantum dimension chemical shift values of ^{1}H 2D DQ spectra recorded at 270 K. The chemical shift values, from which the slices are taken, are stated in the figures. The proton types resulting in the DQCs can much more easily be seen from these slices.

In the 2D DQ spectrum of ABPBI two auto peaks can be seen at ~1.4/2.8 ppm and ~7.3/14.6 ppm from residual methyl-sulfonic acid and imidazole ring NH in SQ/DQ dimensions, respectively. In addition to these two auto peaks, a broad cross peak at ~19 ppm in the DQ dimension is observed indicating the existence of the hydrogen-bonded proton species due to the ABPBI rings.

An auto peak of these kinds of strongly hydrogen-bonded protons, which should have a chemical shift of 12/24 ppm in SQ/DQ dimensions, could not be observed due to the lack of interaction of hydrogen-bonded ring –NH protons with each other. Hydrogen-bonding in pure ABPBI is only possible by the alignment of the imidazole chains close to each other to provide a close proximity for inter-chain hydrogen bonds. Keeping in mind that ABPBI chains in its homopolymer have an inter-chain spacing of ~3.9 Å for stacked pairs, this type of hydrogen-bonding can more easily be understood. The broad feature of this cross peak (from 18 ppm to 22 ppm in DQ dimension) is already observed in ^{1}H MAS spectrum (shown Figure 5.3), is due to the disordered hydrogen-bonding structure in the ABPBI polymer.

The PVPA polymer is recently studied as a homopolymer (Lee 07) and as a copolymer by MAS NMR, and its ^{1}H DQ spectrum is well known. In the 2D DQ spectrum of PVPA at low temperature, two auto peaks at 2.2/4.4 and 10.6/21.2 ppm in SQ/DQ dimension from the interactions of backbone protons and hydrogen bonded –P-OH protons are removed. Additionally, a cross peak due to close proximities of these two types of protons are observed. At room temperature, however, the resonances of –P-OH protons are absent due to the high mobility of these groups.

The ^{1}H 2D DQ NMR spectra of complexes with three different ABPBI-PVPA mixing-ratios recorded at 325 K with one rotor period of BaBa recoupling pulse sequence at 30 kHz spinning frequency are also shown in Figure 5.6. The slices taken from single and double-quantum dimensions of the ^{1}H 2D DQ spectra recorded at 270 K and 325 K are shown separately in Figure 5.7. This figure makes it much easier to identify the cross-peak between ABPBI ring protons and acidic protons. From a first look, one can easily realize the distinct patterns of complexes compared to ABPBI and PVPA homopolymers. With the complexation, new interactions between protons become possible, as already illustrated in Figure 5.2, and, the hydrogen bonding possibilities also increase.

On the top of the Figure 5.7, the spectrum of the system having 70-30 ABPBI-PVPA mixing-ratio is given. It should be kept in mind that the complexation between acid and base polymer is not complete yet at this mixing ratio. Some portion of the ABPBI, 30% mole ratio of the whole content, is interacting to the PVPA but the rest of the ABPBI (40% percent of the whole content), is still in the un-complexed state. Thus, the observed spectrum is similar to pure ABPBI. The auto peak at 2 ppm originates from the PVPA backbone protons, and the strong auto peak at ~7.3 ppm is from the ABPBI ring and non-hydrogen bonded–NH protons. The cross peak appearing at around ~9.3 ppm in DQ dimension results from the aliphatic backbone protons of PVPA and aromatic ABPBI ring protons, indicating that a partial complexation is already obtained at the molecular level. It is surprising that, still the P–OH groups of PVPA do not appear as an auto peak at low-field. Low temperature ^{1}H 2D DQ NMR experiments are needed to prove the existence of acidic auto peaks, which are shown in Figure 5.8. At the low field region of the spectrum, different cross peaks strongly overlap due to the existing of many possible hydrogen-bonding configurations, covering a wider spectral region compared to pure ABPBI [between 19 and 25 ppm in DQ dimension, at ~19-20 ppm (ABPBI ring –NH protons with ABPBI ring –N), ~22-23 ppm (ABPBI ring –NH protons with PVPA –P=O), and ~24-25 ppm (PVPA –P-OH with ABPBI ring –N)]. The cross peak at ~24-25 ppm is very weak, but becomes stronger at lower temperatures, shown in Figure 5.8.

The right hand side of the cross-peaks in DQ spectra is more intense compared to the left hand side of the diagonal at 325 K, which was observed before (Schnell 98). This is due to the more stable and rigid nature of the protons at 8 ppm, which are the ring protons of ABPBI and clearly shows a more rigid nature compared to hydrogen-bonded protons at 325K. One should also note here that the width of the observed DQ pattern at the high chemical shift part of the DQ spectra shown in Figure 5.8, cover nearly 8-10 ppm, is due to the hydrogen-bond distribution with different strengths. This asymmetry, however, disappears and symmetric cross peaks are observed in DQ spectra recorded at lower temperature (270 K), due to the stabilized hydrogen-bonding arrangements.

As mentioned above, the 30-70 ABPBI-PVPA mixing-ratio complex shows a similar pattern to the other two complexes. Only the intensity ratios are different due to different mole fractions of the ABPBI-PVPA polymers. Another interesting observation is the lower intensity of the cross peaks observed between 19-25 ppm in DQ dimension.

The remarkable observation comparing Figure 5.6 and 5.8 is that the cross peaks observed between 18 ppm and 25 ppm in the DQ dimension, due to the interaction of ring protons and hydrogen-bonded protons, are much more intense at lower temperature. Moreover, the intensity ratio between the right hand side and the left hand side of the diagonal is equilibrated, which is not equal at 320 K spectra.

In Figure 5.7, the slices taken from the 1H 2D DQ spectra of the studied materials are shown. The values from where the slices are taken are stated at every spectrum. The spectra in Figure 5.7a, were normalized according to the intense ABPBI aromatic proton resonance (at ~7 ppm/~14 ppm in the SQ/DQ dimensions). The remarkable intensity increase in the low field region cross peaks is due to the stabilized hydrogen-bonded protons at lower temperature. The positions of the cross-peaks are also specified in the spectra.

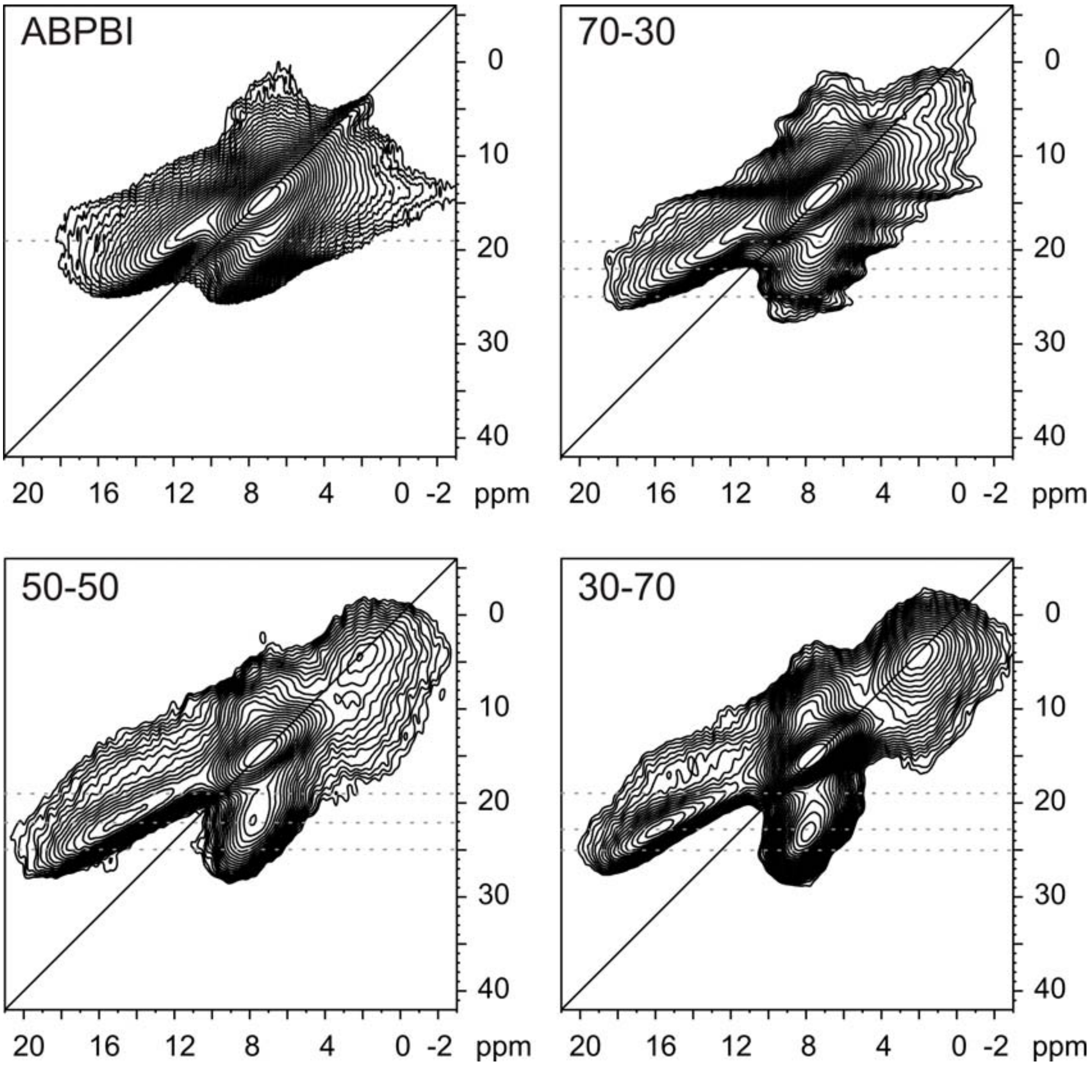

Figure 5.8: 2D DQ Spectra of the ABPBI parent polymer and 70-30, 50-50 and 30-70 ABPBI-PVPA complexes recorded at 270K and at 30 kHz spinning frequency. The spectra recorded by using BaBa DQ recoupling pulse sequence with 1 rotor period of excitation-reconversion recoupling time. The contour levels set same in all spectra, so comparison can be done easily by comparing the intensities.

Another remarkable observation is the lack of auto peaks due to acidic protons for the complexes which have a high amount of acid even at 270 K. These resonances are also absent at the 30-70 mixing ratio, which has an excess amount of acidic PVPA. This is clear indication of non-aggregating acid-base polymer morphology. The acidic polymer does not form self aggregates at none of the polymer mixing ratios and mixes well in the complex.

5.2.4 ^{13}C CPMAS NMR Results:

In Figure 5.9, ^{13}C CPMAS spectra of the ABPBI homopolymer and three ABPBI-PVPA complexes with different mixing-ratios are presented. Specific carbon sites are obvious in the spectra. By an increase in PVPA ratio, the aliphatic carbon resonances are increasing in intensity around ~32 ppm as expected. In the pure ABPBI and in the complexes, the ring carbon resonances (between 114 ppm and 153 ppm) are similar with two differences.

First, in pure ABPBI and in complexes the resonance appearing at ~142 ppm has different intensity. This specific resonance decreases in intensity with the addition of acidic PVPA, in 70-30 complex, e.g. Moreover, after the complete complexation, in the 50-50 complex, and in the excess content of PVPA, in the 30-70 complex, this resonance

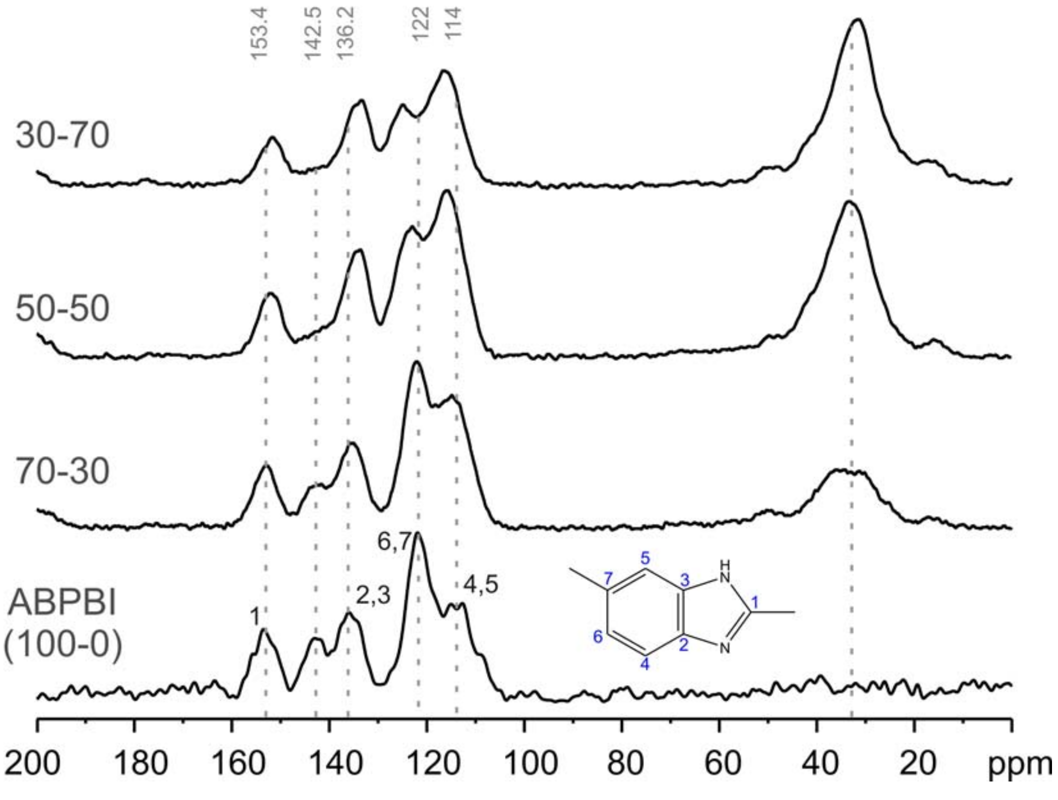

Figure 5.9: ^{13}C CPMAS spectra of the ABPBI parent polymer and the three complexes recorded at 125.76 MHz ^{13}C frequency, at room temperature, and at 15 kHz MAS frequency.

disappears. In a previous study of pure ABPBI, where remaining methyl sulfonic acid is present, the resonance at 142.5 was not observed which can be attributed to the increased mobility in the material due to remaining solvent.

The additional peak at 142 ppm in ABPBI is therefore associated with the stacking of PBI ring moiety. X-ray diffraction pattern reveals partial crystallinity with characteristic spacing of ~3.9 and ~3.3 Å in ABPBI. While 3.3 Å is closer to the monomer repeating unit, the spacing of 3.9 Å can originate from the separation of adjacent ABPBI in stacked chains. Independent of the local ABPBI configuration, the resonance at 142 ppm should be related to the local packing, as it disappears upon formation of hydrogen bonds between PVPA and ABPBI which deteriorates the local packing configuration.

Moreover, the X-ray diffraction signal is strongly reduced by the addition of PVPA which is in good agreement with the given explanation for the NMR signal at 142 ppm. In the 50-50 complex, only a broad halo (nearly amorphous) associated with the monomer repeat unit is observed, which results from the deterioration of the ABPBI stacking due to the hydrogen-bonding of ABPBI with PVPA.

With the addition of PVPA, the intensity-ratio of the two resonances at 122 and 114 ppm changes. This observation can be attributed to differences in the cross-polarization dynamics which originate from changes in molecular motion. Additional experiments with varying cross-polarization contact times were performed in pure ABPBI to study the intensity ratio change due to a change in dynamics (the spectra is not shown here). A variation of the CP contact-time 0.2 ms up to 2 ms, showed a change in the intensity-ratio of the resonances at 114 and 122 ppm. This indicates that a change in intensity-ratio observed in Figure 5.9 with the PVPA addition, is due to the change in dynamics at these two specific carbon sites in the 6-member benzene ring of ABPBI. The unchanged intensity of the 5-member imidazole ring part of ABPBI might originate from the stabilization effect of hydrogen bonding.

The 5-carbon ring gained more intensity than the 6-carbon ring with increasing PVPA content reflects the possibility that better cross polarization on the 5-carbon ring is achieved as the proton rich PVPA comes in close proximity to the ABPBI upon complexation. Other NMR features which change with increasing PVPA content provided direct evidence that hydrogen bonding is indeed established between the acid PVPA and the base ABPBI. In Figure 5.9, the ~136 ppm and the bridging ~153 ppm groups (in 5-membered imidazole ring) are found to shift upfield, while the 122 ppm and 114 ppm groups (in 6-membered ring) are shifted down field with increasing PVPA content.

5.2.5 Molecular Dynamics & Proton Mobility in the Systems at Elevated Temperatures:

The temperature dependence of the hydrogen-bonded ^{1}H resonances is investigated with variable temperature ^{1}H MAS NMR spectroscopy at 30 kHz MAS, and the spectra are recorded in a temperature range of 325K-405 K. The sample was kept at each specific temperature for 5-10 minutes to ensure temperature equilibration within the sample.

The variable temperature ^{1}H MAS NMR spectra of different mixing-ratios (70-30, 50-50, and 30-70 ABPBI-PVPA) are presented in Figure 5.10. The highest temperature available with the current instrumentation is still below the glass temperatures, T_g, of the samples. Nevertheless, temperature induced changes can be seen in the studied temperature-range.

In all of the three spectra shown here, significant line narrowing of the aromatic proton resonances of ABPBI is observed, indicating an increase in the mobility of the aromatic rings in the complexes (Table 5.1). The changes in the line widths of the aromatic resonances are different for three complexes. However, no significant temperature chemical shift was observed for the resonances of aromatic protons due to the temperature increase.

Table 5.1: Linewidths of the aromatic proton resonances (~7-8 ppm) at FWHM for all of the three acid-base polymer complexes at 325 and 405 K.

Material	325K	405K
70ABPBI-30PVPA	2070 Hz	1340 Hz
50ABPBI-50PVPA	1650 Hz	1030 Hz
30ABPBI-70PVPA	2130 Hz	1200 Hz

The aliphatic resonance, at ~2 ppm, in all three complexes did not show significant line narrowing. This may result from the unchanged molecular mobility of the PVPA backbone in the acid-base polymer complexes. This behavior is similar to that of pure PVPA (Lee 07), where no line narrowing was observed for polymer backbone. This result supports the presence of Grotthuss type ^{1}H conductivity, with the possible zip-unzip action of hydrogen-bonded acidic protons. The homopolymer and acid-base polymer blend approach resulted in a rigid backbone structure even at elevated temperatures, opposed to the copolymer approach (Unugur 08) with similar building blocks.

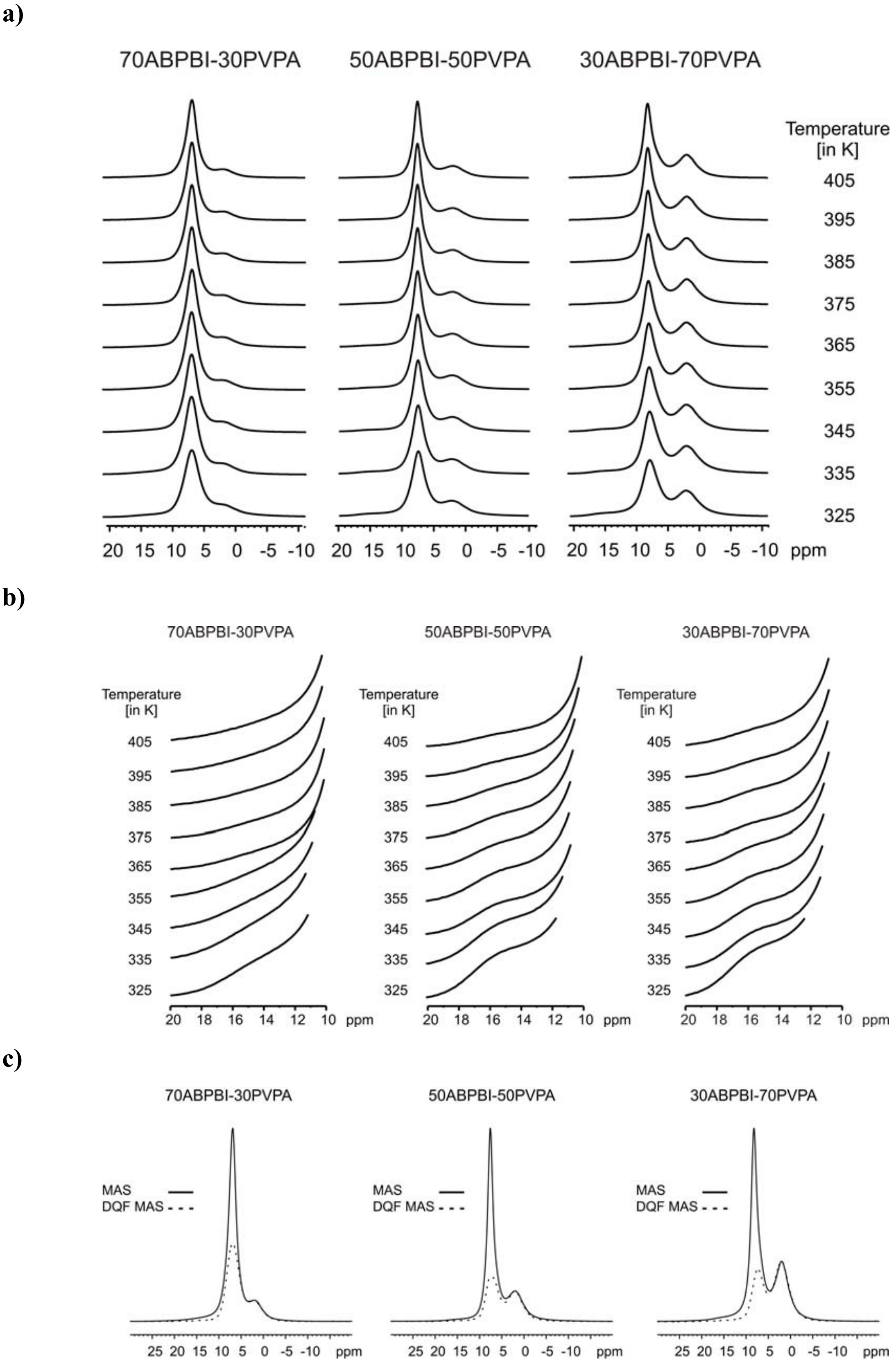

Figure 5.10: **a)** Full region of variable temperature ^{1}H MAS NMR spectra of the complexes with 70-30, 50-50 and 30-70 ABPBI-PVPA mixing ratio, recorded at 30 kHz MAS frequency. **b)** The low-field region of (10–20 ppm) figure a. **c)** The comparison of ^{1}H MAS and DQF spectra of the complexes at 405 K.

The low field regions of the spectra (which are displayed separately in Figure 5.10b), contain the resonances of hydrogen bonded protons. A loss in intensity of the hydrogen-bonded signals is observed with an increase in temperature. This indicates that, the hydrogen bonding arrangements formed by the interaction of acidic and basic polymers are deteriorating with increasing temperature due to molecular mobility at the specific hydrogen bonding sites and maybe due to the increased ring motion (can be seen also in Figure 5.10c). Finally, the gradual removal of the acidic proton resonances indicates, that the timescale of the proton hopping motion is in the order of kilohertz range, due to the destructive interference of the signal and MAS frequency which causes signal deterioration.

5.2.6 ^{31}P NMR Results: The anhydride formation in the system:

Figure 5.11 shows one-dimensional ^{31}P MAS and two-dimensional ^{1}H-^{31}P CP-MAS correlation spectra of the non-annealed and the annealed 50-50 complex. The phosphorous anhydride species present even in non-annealed materials (represented in Figure 5.11a) due to the synthesis procedures. After annealing at high temperatures for several hours, two distinct resonances are observed at 22 and 29 ppm. Nearly 60% of the phosphorous sites are from the anhydride species (signal at 22 ppm). The typical structures of the anhydride species were represented in the literature before (Lee 07). Additionally, a small amount of the phosphorous sites (~1-2%) are observed at -1 ppm in both of the non-annealed and annealed complex. The signal is assigned to cleaved phosphoric acid groups.

Spatial proximities of protons and phosphorous sites are elucidated by two-dimensional ^{1}H-^{31}P CPMAS correlation spectra, which are presented in Figure 5.11b. It can clearly be seen, that phosphorous nuclei are in proximity with acidic protons in both the normal as well as the anhydride species. Even after annealing, the acidic proton-phosphorous connectivities remain with slightly reduced intensity. However, in a former study of copolymers of PVPA with poly(vinyl triazole), PVTri, the anhydride species showed nearly no connectivities with acidic protons after annealing (Unugur 08). For the current ABPBI-PVPA system, acidic proton-phosphorous connectivities seem to remain unchanged due to the excess acidic protons and might contribute to the connectivity even after annealing.

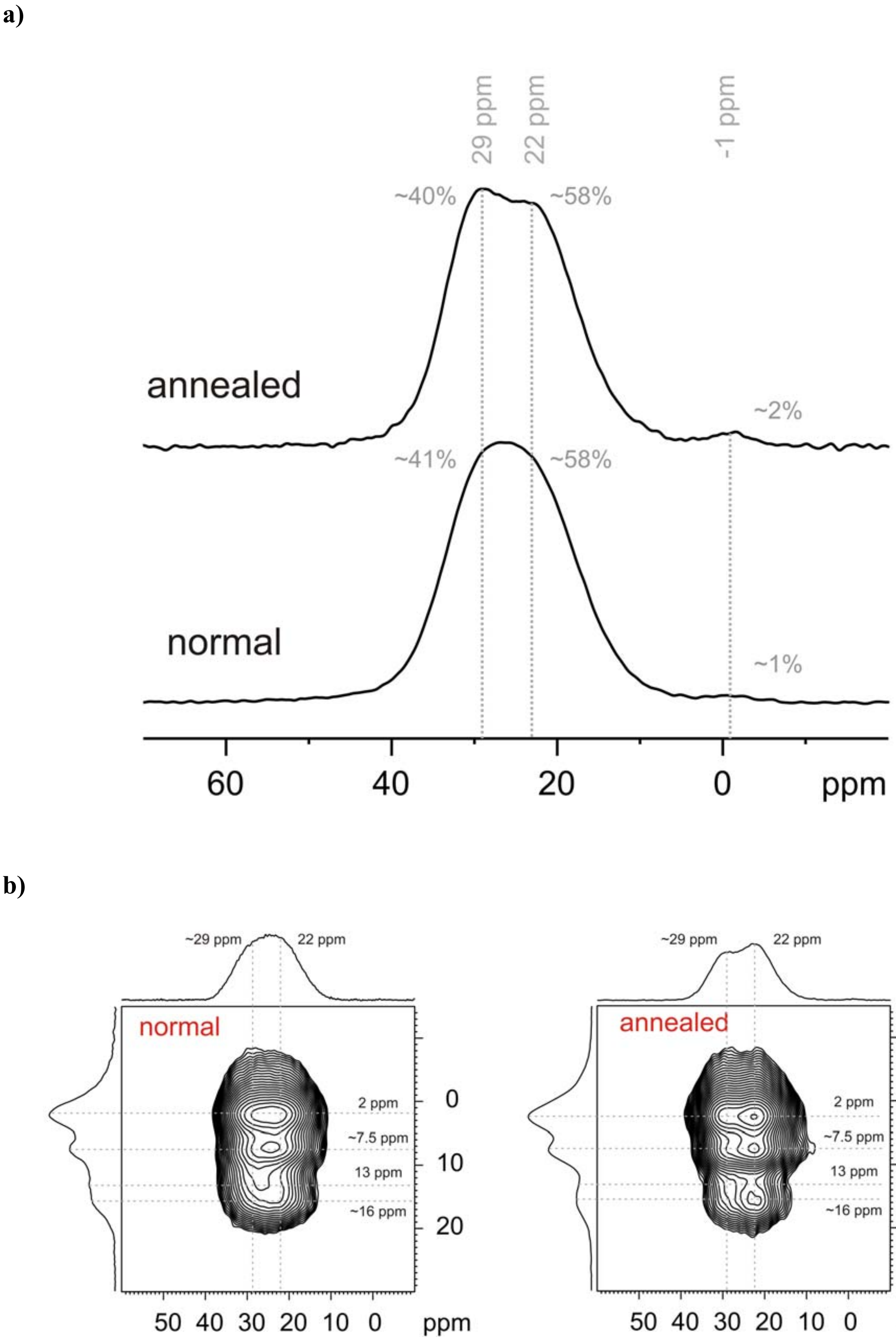

Figure 5.11: a) ^{31}P MAS spectra of non-annealed and annealed 50-50 ABPBI-PVPA complex. The spectra are recorded at 30 kHz MAS and with 10 s of relaxation delay. **b)** 2D ^{31}P-^{1}H CPMAS spectra recorded at 30 kHz with 2 ms of CP contact time.

5.3. Interpretation & Discussions:

5.3.1 Proton Chemical Shifts and Hydrogen Bonding Network

All chemical shift values observed in SQ experiments are given in Table 5.2 with the information of the assigned proton types. Previous studies (Goward 02, Hughes 04, Lee 07, Unugur 08) were taken into account in assigning the observed chemical shifts.

Table 5.2: The observed chemical shift values in the ABPBI-PVPA acid-base polymer complexes, and their assignments.

Chemical Shifts: (ppm, SQ)	Proton Assignments
2	PVPA backbone protons
7-8	ABPBI ring protons
~ 10.5	PVPA –POH ---- PVPA –POH
12-13	ABPBI –NH ---- ABPBI –N
14-15	ABPBI –NH ---- PVPA –P=O
~17	PVPA –P-OH ---- ABPBI –N

A schematic representation of all of the interactions for the homopolymers and complexes are shown in Figure 5.12. The breaking of the pi-stacked ABPBI network due to the formation of a hydrogen bonding network between acid and base polymer is represented. Moreover, in Figure 5.13, the nucleus independent chemical shift (NICS) map of the ABPBI monomer was performed (figure is not shown) to understand the extent of pi-stacking effect of one monomer, whose effect is reaching up to the nearby ABPBI chain.

5.3.2 Relation to Proton Conduction

Two major types of conduction mechanisms are contributing to the proton conduction in most systems, the vehicle and/or the Grotthuss type (Kreuer 82, Schuster 03). In anhydrous proton conductors, however, only the latter is contributing due to the lack of low molecular weight vehicle components in the systems. The Grotthuss type proton conduction is facilitated by the formation of hydrogen bonding networks. The presence of hydrogen-bonding is proved in the ABPBI-PVPA system with the current study, and its nature is identified with the help of ^{1}H MAS NMR spectroscopy. Different types of hydrogen-bonding identified between the acid-base polymers (shown in Figure 5.12), and listed in Table 5.2.

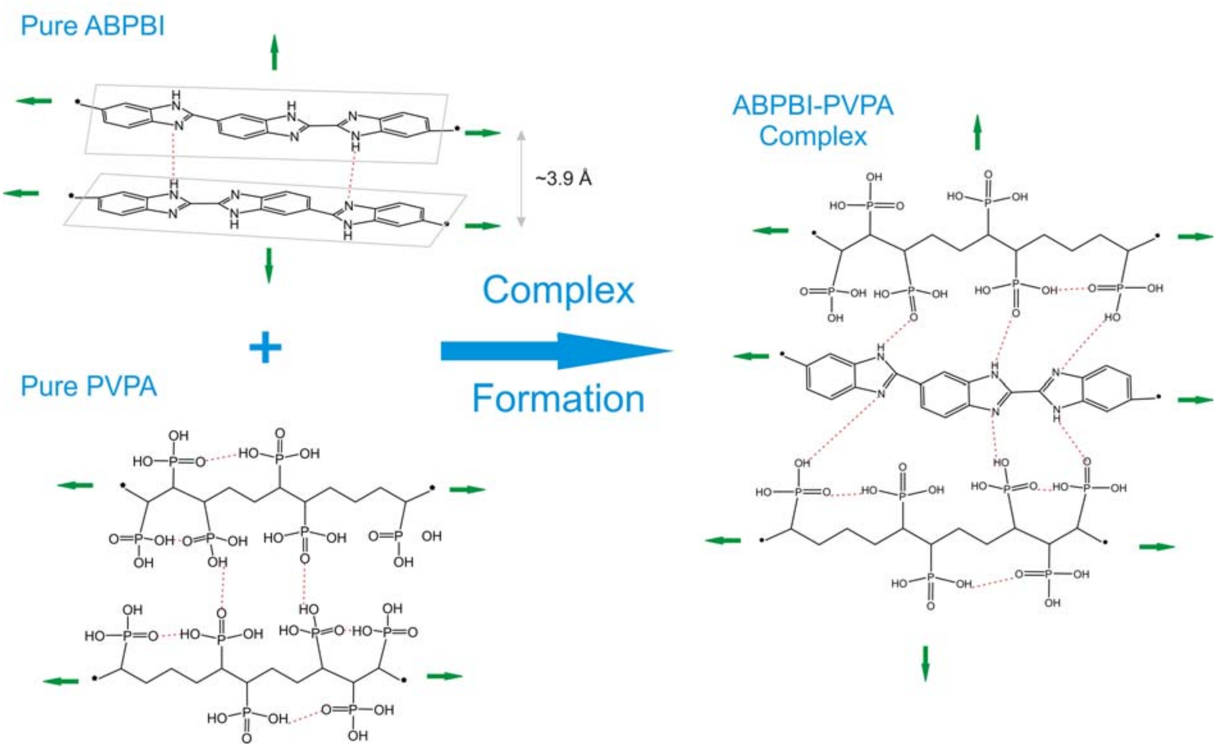

Figure 5.12: Schematic representation of the parent polymers ABPBI, PVPA and the complex formed from these two polymers.

The proton conduction is mediated by the acidic protons in the complexes. The movement of the acidic protons follows the pathway formed by the hydrogen-bonding via a Grotthuss type of mechanism in the anhydrous environments. Zip-unzip processes of the hydrogen-bonding between ABPBI and PVPA might occur and result in the conduction of protons from one end to the other end of a conduction channel formed by complexation.

The pure ABPBI has a significantly lower conductivity than the ABPBI-PVPA complexes, as expected due to the excess proton source (PVPA) in the complexes. Moreover, the conductivity values of the complexes at room temperature are increasing with the PVPA content reaching a maximum value of ~1.6.10^{-3} in the wet films of the 30-70 complex. However, under dry conditions, the 50-50 complex has an order of magnitude higher conductivity value (~10^{-7}) compared to the other two complexes at room temperature. This holds up to ~100 ^{o}C when the conductivity of the 30-70 complex becomes higher due to the higher acidic component. Remarkably, the 50-50 complex has much lower activation energy for the proton conduction compared to other complexes. This observation can be explained by the formation of more ordered proton conduction channels, which is suggested as well by the more resolved signals in the ^{1}H MAS and 2D ^{1}H DQ MAS spectra of 50-50 complex of the hydrogen-bonded protons. Observation of the more featured low-field resonance in

Figure 5.4 indicates the presence of more ordered hydrogen-bonding network in 50-50 sample, in which the complete complexation is achieved.

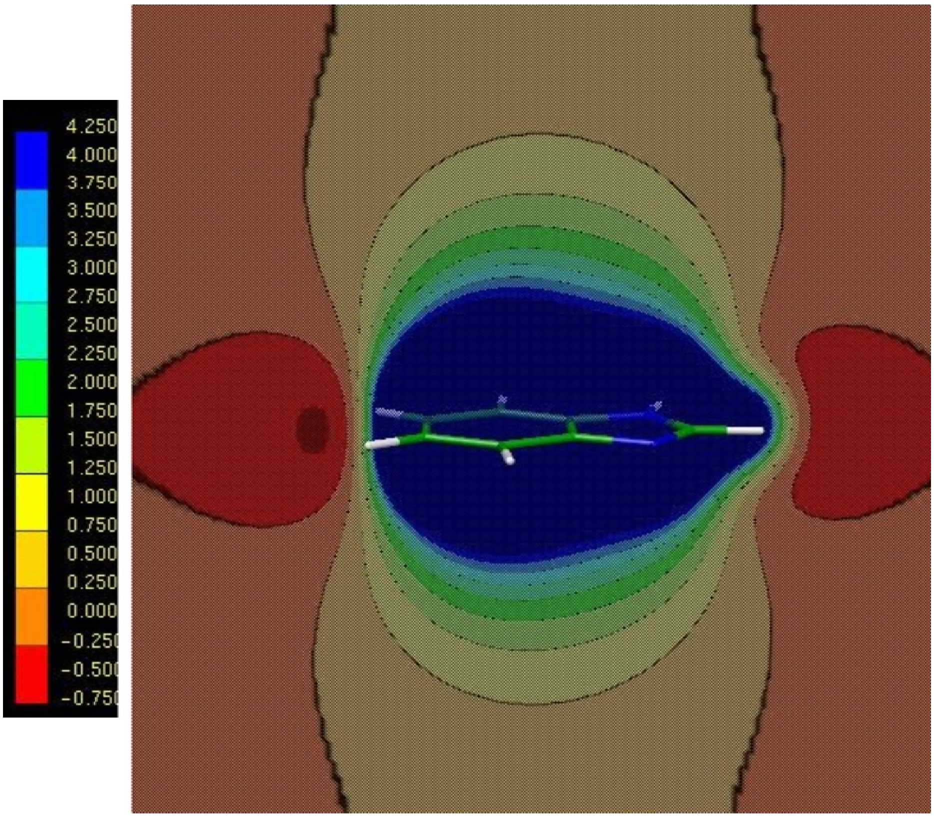

Figure 5.13: Nucleus independent chemical shift map of ABPBI.

The higher mobility of the hydrogen-bonding sites in the 30-70 complex leads to a high macroscopic (bulk-conductivity) conductivity value (Figure 5.5) at elevated temperatures. It has the highest conductivity of all three complexes at high temperatures. This shows that the proton conductivity at elevated temperatures does not so much depend on the local organization, which is best in the 50-50 complex, but depends on the number of proton donor sites. In the current system, the vehicle-like mechanism does not contribute to the proton conduction, opposed to the oligomeric imidazole systems studied previously (Goward 02).

5.4. Conclusions

The structural features governed by acid-base polymer complexation were studied in detail with solid-state NMR methods. Different types of hydrogen-bonding arrangements involving several hydrogen-bonding donor and acceptor groups were determined. By introducing acidic PVPA polymer to the basic ABPBI, the local-packing of the ABPBI is disturbed by the formation of a hydrogen bonding network. A broad distribution of hydrogen-bonding arrangements results in a broad low-field proton resonance ($\Delta\delta$=8 ppm) in the complexes. The complex with the highest PVPA content has the highest content of acidic protons.

The most structured resonance of hydrogen-bonded protons is observed for the 50-50 complex which shows the lowest activation energy. The 30-70 complex which shows the highest activation energy, exhibits the highest proton mobility at the elevated temperatures. The miscibility of the complexes on the molecular level is proven by 2D ^{1}H-^{1}H DQ NMR spectra. Moreover, in none of the complexes, aggregates of acidic PVPA are observed. Anhydride formation is present in current complexes, similar to the PVPA homopolymer. Nevertheless, a significant amount of acidic protons forming hydrogen-bonds are attached to phosphorous as observed with 2D ^{1}H-^{31}P CP-MAS experiments.

Chapter 6:

Anhydrous Proton Conducting Properties of Triazole-Phosphonic Acid Functional Copolymers

In this chapter, the copolymers of 1,2,4-triazole functional polymer with poly(vinyl phosphonic acid) are studied with advanced solid-state NMR methods. This system is an example to the copolymer approach to achieve high proton conduction under water-free conditions. It can also be said that the current system is an extension of the 1,2,3-triazole functional material, which was presented in chapter 3. The structure of the studied system is shown in Figure 6.1, and the compositions of the copolymers are given in Table 6.1.

1H-1,2,4-Triazole (Tri) is an promising alternative heterocyclic whose structure is similar to imidazole but contains three nitrogen atoms in the ring (Gunday 06). Recently, Tri was used as a protogenic solvent in a blend with an acidic polyelectrolyte to generate high temperature resistive and electrochemically stable free-standing films. Polymer electrolyte membranes consisting of an acidic polymer host and Tri allowed for long range proton transport via structural diffusion (Kim 07). One of the most important problems of such host/guest systems is the leaching of the protogenic solvent during cell operation (Xing 02). Immobilization of the protogenic solvents can achieved via copolymerization of an acidic monomer with a heterocyclic comonomer. It was previously reported, however, that copolymers of 4(5) vinylimidazole yielded low conductivities, because ionic complexation blocked the free nitrogens and long range proton diffusion was inhibited (Bozkurt 03). In order to avoid this problem, the use of a triazole based monomers containing free nitrogens in the heterocyclic ring can be explored.

In this work, novel copolymer membranes which were synthesized by free radical solution copolymerization of vinylphosphonic acid (VPA) and 1-Vinyl-1,2,4-triazole (VTri) (Figure 6.1) are studied. Copolymerization was conducted at several feed ratios to control the VTri and VPA contents which covalently form the backbone, as a result different copolymers were obtained and characterized by NMR. With the help of ^{31}P MAS NMR, insight into the coordination of -PO_3H_2 units in the copolymer was obtained. Proton conductivity of the copolymers was investigated by an impedance analyzer and the results are compared with previously reported systems and with NMR results. Finally, the proton dynamics and proximities were revealed by variable-temperature ^{1}H MAS NMR.

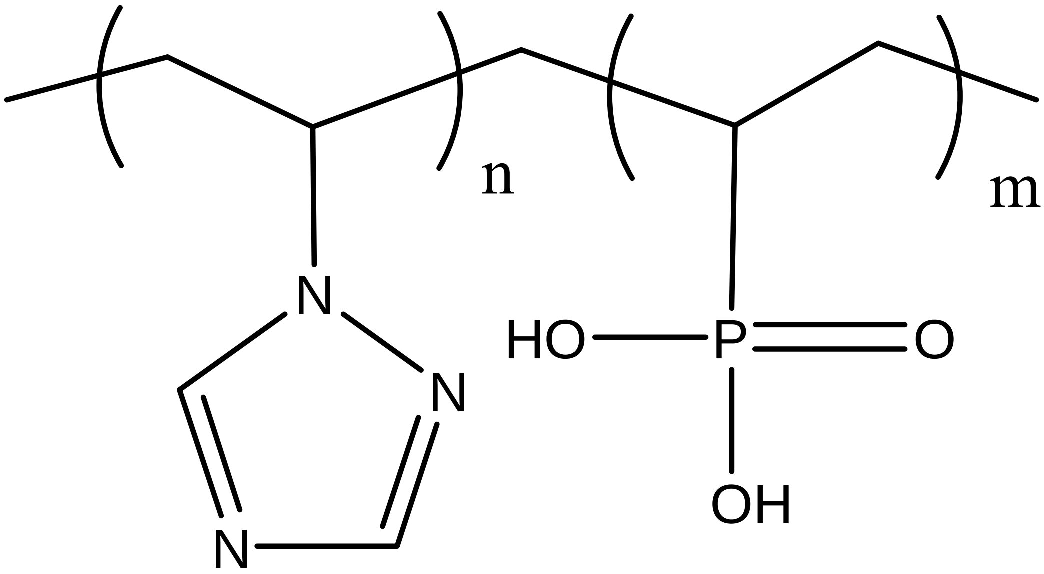

Figure 6.1: Structure of the copolymer, poly(VTri-*co*-VPA).

6.1. Proton Conductivity Properties of the Materials

Proton conductivities of the copolymers were determined by Unugur et. al (Unugur 08) via an AC impedance technique in the frequency range from 1 Hz to 3 MHz at various temperatures. The DC conductivity (σ_{dc}) of the samples was obtained from the plateaus of log σ_{ac} vs. log F by linear fitting of the data (10^3-10^5 Hz, at 120 °C and 10^2-10^4 Hz, at 50 °C). In the anhydrous state, the proton conductivities of the copolymer samples are displayed in Figure 6.2. Obviously, the conductivity of the samples increases with increasing the percent VPA content as well as with temperature up to 120 °C with a slight deviation from linearity. The higher conductivity of S1 is attributed to the high VPA mole percent as proton source in the copolymer where it is 60% for S1 and 50% for S3.

Table 6.1: Monomer VTri and VPA in the feed and composition of the copolymers.

Sample	Feed ratio (mol) VTri/VPA	T_g (°C)	Mol % of VTri in the Copolymers
Poly(VTri-co-VPA), S1	1:1	159	41
Poly(VTri-co-VPA), S2	1:2	169	33
Poly(VTri-co-VPA), S3	2:1	166	51

Previously, the relation between water uptake, self-condensation and proton conductivity of PVPA was investigated by Kaltbeitzel *et al.* (Kaltbeitzel 07). They suggested that even after annealing and drying the material, water takes part in the conductivity mechanism. The condensation limits the conductivity, as it reduces the phosphonic acid sites taking part in the proton transport. Thus, maximum proton conductivity of 10^{-3} S/cm was reached under 1 bar H_2O atmosphere.

The structure and the local proton mobility of the homopolymer, PVPA, were studied by solid-state NMR under fast magic angle spinning (Lee 07). The study concluded that the proton migration of PVPA is mediated by acidic protons through hydrogen bonding network and condensation of acidic units blocked the proton transport resulting in a decrease in the proton conductivity. A copolymer including a heterocyclic monomer, poly(1,2,4-

vinyltriazole-*co*-5-vinyltetrazole-*co*-acrylonitrile) was prepared by click chemistry and the copolymers become proton conductive only after doping with phosphoric acid (Pu 07).

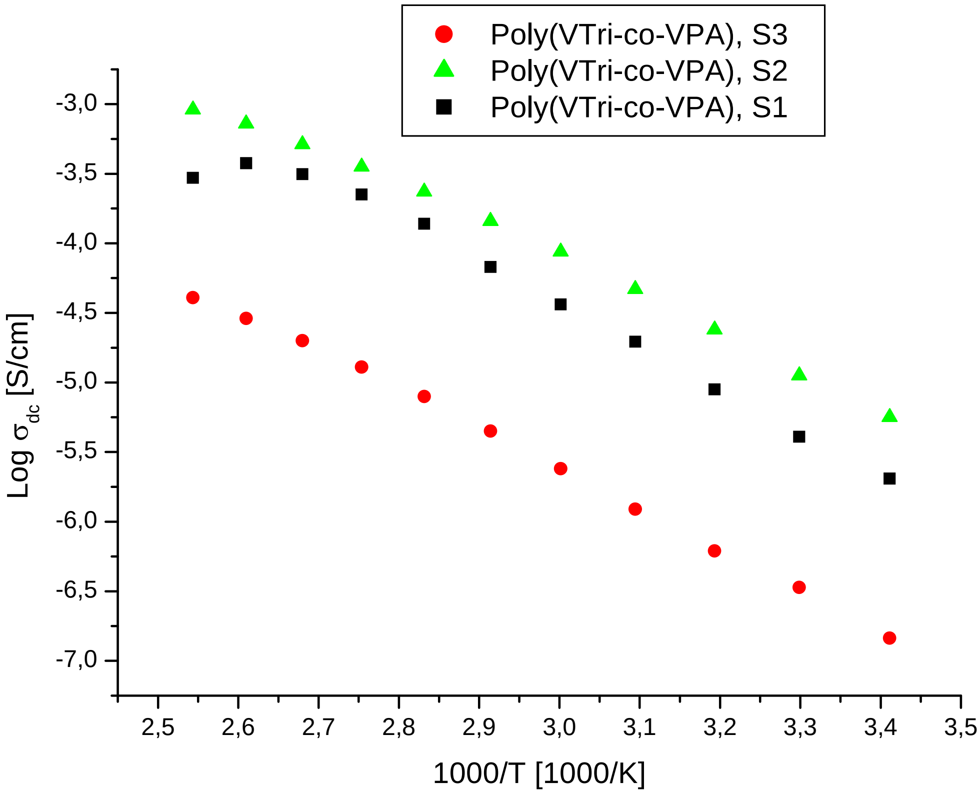

Figure 6.2: The DC conductivity versus reciprocal temperature for the copolymer membranes (Reproduced from Unugur 08).

Copolymerization of monomers bearing acidic units as proton source and heterocyclic units as charge carrier is a rather interesting and new methodology. In this context, copolymers of 4(5)-vinylimidazole and vinylphosphonic acid have previously been reported (Bozkurt 03). The DC conductivities of this copolymer were in the range from 10^{-6} to 10^{-12} S/cm within the measured temperature regime. The conductivities of the copolymer samples increased with increasing imidazole content which were immobilized in the polymer backbone. The improvement of the σ_{dc} was attributed to an increase in the free nitrogen sites. Such a behavior supports the idea of complete protonation of imidazole resulted in the blocking of the heterocycles. Since a defect type conduction occurs through intermolecular proton exchange reactions between neighboring heterocyclic molecules (Munch 01).

To get improved proton conductivity, here VTri and VPA monomers were used and novel copolymers were produced. From FT-IR, copolymer composition as well as conductivity data, it can be concluded that a Grotthuss mechanism (structural diffusion) produces a pathway for proton diffusion. As expected, the conductivity of these novel systems is at least three orders of magnitude higher than that of imidazole based copolymers. The proton conductivity of Poly(VPA-*co*-VTri), **S2** is ~ 10^{-3} S/cm at 120 ^{o}C, in the anhydrous state. This value is very close to the conductivity of hydrated PVPA under 1 bar H_2O atmosphere (Kaltbeitzel 07).

6.2. NMR Results:

6.2.1 ^{13}C and ^{31}P MAS NMR Results: Structure of the Copolymers & Coordination Behavior

The ^{13}C CPMAS spectra of the pure PVTri and the poly(VPA-*co*-VTri) copolymers are shown in Figure 6.3. In the homopolymer of PVTri, the specific resonances from the different carbon sites can easily be identified. The resonances due to backbone carbons appear at approximately 40 and 55 ppm. The two ring carbon resonances appear at higher chemical shift values, at 145 and 153 ppm.

Copolymerization of VPA with VTri generates new resonances. The backbone carbons of PVPA appear at 32 and 35 ppm as sharper resonances, indicating higher mobility of the PVPA backbone compared to the PVT backbone. By further increasing the PVPA content in the copolymer, these two sharp resonances become less resolved due to the possible effect of hydrogen bonding between different side groups and/or due to possible crosslinking, see below.

After the introduction of PVPA into the copolymer, a new resonance starts to appear at ~165 ppm. The relative amount of this resonance increases with the addition of PVPA, and becomes comparable in intensity with the ring carbon resonances. The nature of this resonance was clarified with the help of quantum chemical calculations by using Gaussian 03 program package (Gaussian 03). It is most probably due to crosslinking of the ring of PVTri with a PVPA side group in a way as ring C-O-P, which was found to have a higher carbon chemical shift value compared to the un-bridged ring C. The intensity of the resonance at 153 ppm decreases with addition of PVPA, whereas, the intensity of the 165 ppm resonance increases. This observation also gives an additional hint to the possible structure of the crosslinking. The P-O of PVPA is somehow connected to the ring via the carbon atom which is shifted to higher chemical shift values in the spectra.

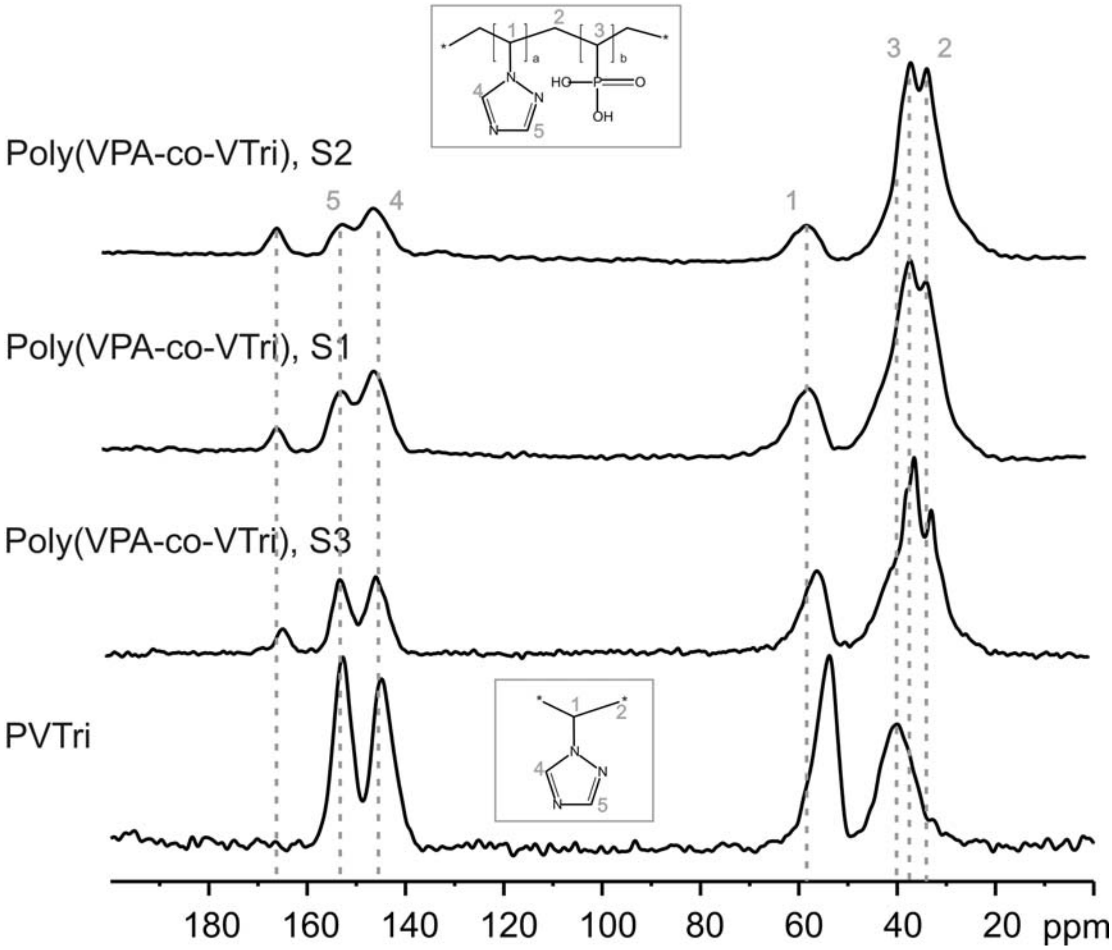

Figure 6.3: ^{13}C CPMAS spectra of pure PVTri and Poly(VTri-*co*-VPA) copolymers. The spectra recorded at room temperature at 176.05 MHz ^{13}C Larmor frequency and with an MAS frequency of 20 kHz. Contact time for the CPMAS experiment was 2 ms.

The ring carbon resonances of PVTri become broader and less resolved with increased amount of PVPA in the copolymers. This is an additional indication of hindered mobility of the heterocycle ring due to the crosslinking of different side groups and/or hydrogen bonding interactions between VTri and VPA.

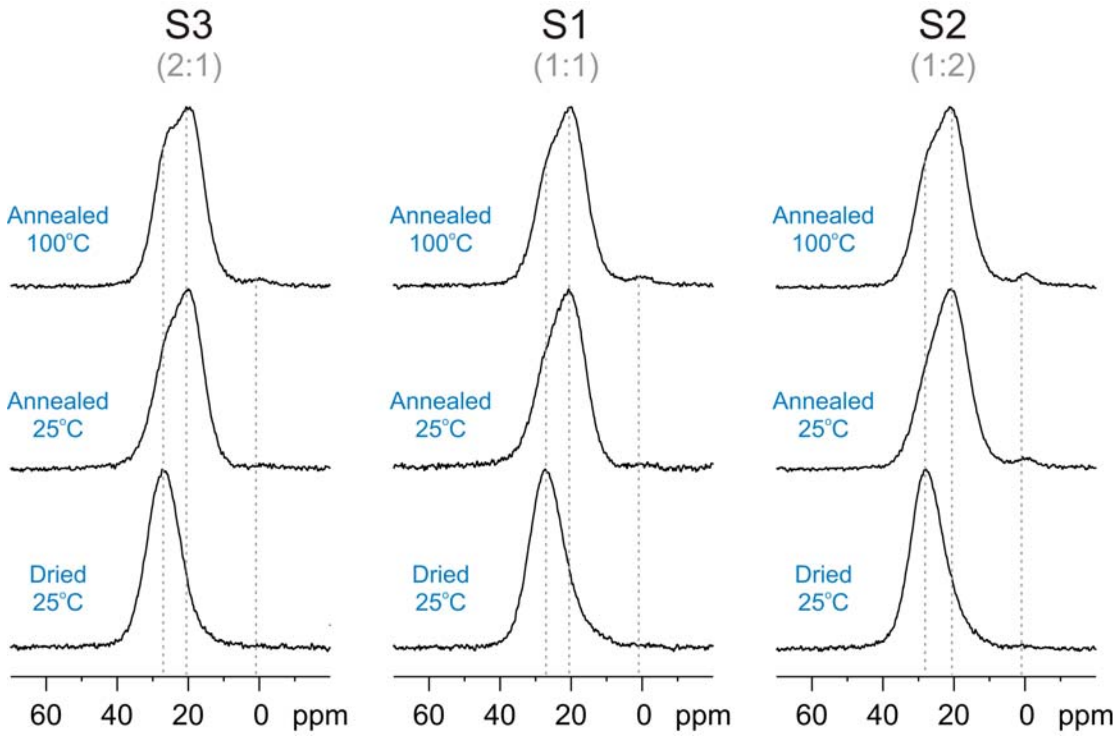

Figure 6.4: ^{31}P MAS NMR spectra of the annealed and the non-annealed dried copolymer, **S1**, **S2**, and **S3** recorded at 25°C and 100°C. The spectra recorded at 283.42 MHz ^{31}P Larmor frequency and at 25 kHz MAS frequency. The procedures of annealing and drying are explained in the text. A relaxation delay of 5 seconds was used in the single-pulse experiment.

^{31}P MAS NMR spectra are presented in Figure 6.4, the dry as-synthesized copolymers do not have a resolved resonance due to a phosphonic acid anhydride species. However, the asymmetry of the resonances implies that there are indeed phosphorous anhydride species present (Lee 07). From a line fitting analysis, which was performed using the DMFIT program package (Massiot 02), the amount of different type of phosphorous sites becomes clearer. Before annealing, anhydride species are present at ~ 30-40% and after annealing their fraction increases up to ~60%. In the pure PVPA system, the formation of the anhydride species has already been reported with a similar condensation fraction (Lee 07). The formation of anhydride species is not desired as they block the proton transport pathways. It seems that by copolymerization of PVPA and PVT, anhydride formation is still active, reducing conductivity. After annealing the copolymers 160°C for 10-12 hours, the resonance due to phosphonic acid anhydride (at ~22 ppm) become much more clear, whose possible structures are shown in detail elsewhere (Lee 07). At higher temperatures (above 160°C), condensation is even more probable, as a weight loss is observed in the TGA. NMR experiments at higher temperatures could not be performed due to the instrumental limitations. As a last point, a weak resonance appearing at ~0-2 ppm is observed for the annealed materials. This resonance is due to the cleavage of phosphonic acid functional groups from the polymer backbone. The removal is rather modest indicated by the very low intensity of this resonance (~1-3%), and only appears after intense annealing for several hours.

6.2.2 ^{1}H MAS SQ and DQ NMR: Hydrogen Bonding Network and Proton Proximities

Figure 6.5 shows the ^{1}H MAS spectra of the homopolymer, PVTri and copolymers poly(VTri-*co*-VPA) (**S1**, **S2** and **S2**) recorded at 300K. Three different proton resonances can easily be recognized: backbone protons (at ~3 ppm: A-type), PVTri ring protons (at ~8 ppm: B-type), and hydrogen bonded acidic protons (from 10 ppm up to 17 ppm: C1- and C2-types). The width of the hydrogen bonded proton resonances implies that the hydrogen bonding in copolymers, does not have a well defined arrangement, but instead displays a broad distribution in terms of structures and strengths. Due to the lack of acid protons PVTri itself does not display hydrogen bonding. In PVPA, at ambient temperatures, the hydrogen bonded P-OH protons are observed at a chemical shift of ~10.5 ppm (Lee 07). In the copolymer structure, the hydrogen bonded region is extended, covering a region from 10 ppm up to 17 ppm. The patterns observed in the three copolymer compositions are broad, but still easily identified. Two different types of hydrogen bonding arrangements are possible, O-H¨O between P-OH and P=O, and O-H¨N between P-OH and VTri ring N (as depicted in Figure 6.6). If protonation of the PVTri ring occurs, additional arrangements will be possible. It is most likely that the broad ^{1}H NMR pattern consist of two resonances, which are easy to identify in the 2D ^{1}H DQ spectra, shown in Figure 6.6. With the help of the 2D ^{1}H DQ NMR spectrum, the connectivity of protons can be deduced as well. In the copolymers two cross-peaks are observed designated as AC1 and AC2 which indicate two different types of hydrogen-bonding protons. The AC2 cross-peak appears at ~15 ppm in the DQ dimension (3 ppm+12 ppm) on both sides of the diagonal. Because the A-type polymer backbone protons have a chemical shift value of ~3 ppm, the C2-type P-OH should have a chemical shift value of ~12 ppm, O-H¨O. The other cross-peak, AC1, appears at a slightly higher chemical shift value at ~17 ppm in DQ dimension. This again clearly shows that, the C1 type of proton has a chemical shift value of ~14 ppm, and probably reflect the interaction of the P-OH proton and the nitrogen of PVTri ring, O-H¨N.

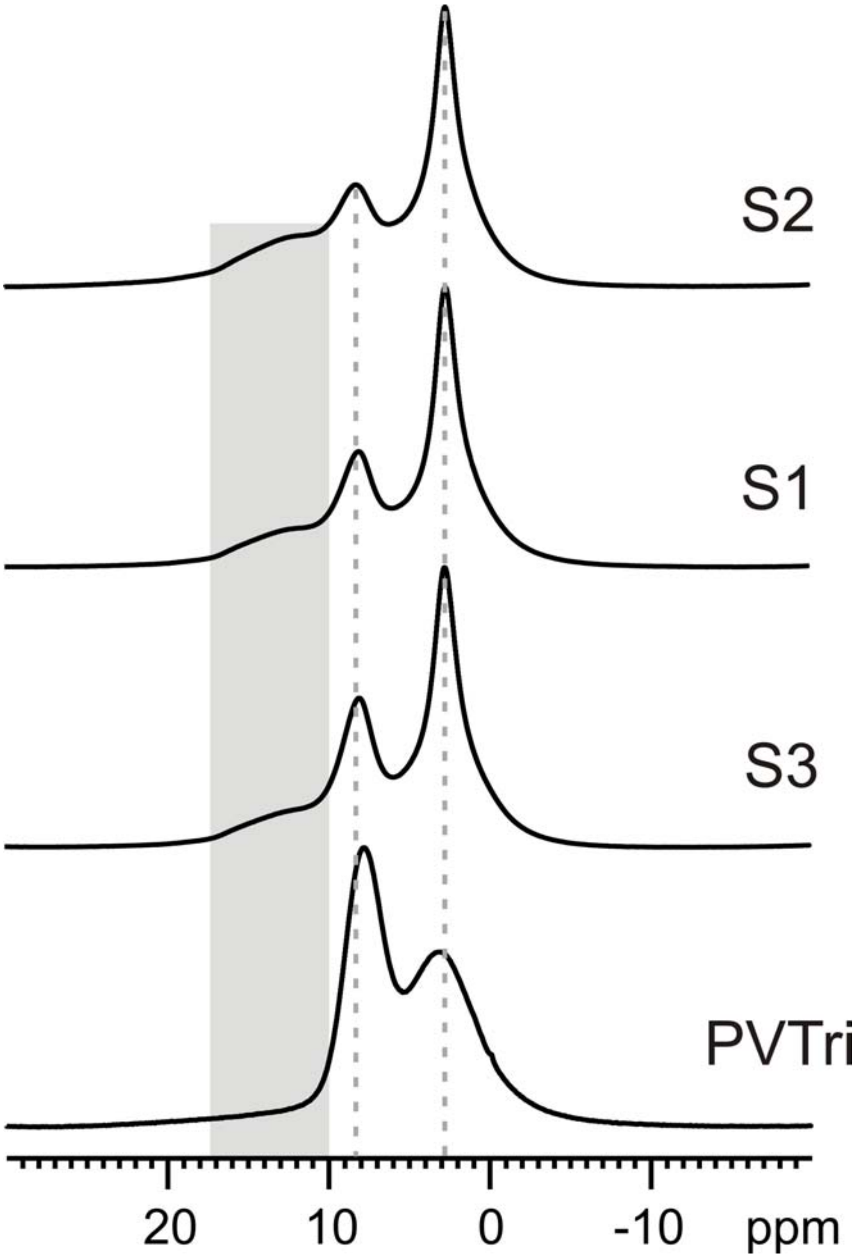

Figure 6.5: ^{1}H MAS spectra of PVTri and its copolymers with PVPA at three different mixing ratios. The spectra were recorded at 300K, and at 25 kHz MAS frequency.

This conclusion is further supported with a similar study on benzimidazole and Nafion™ composites (Kim 07). In this study, the hydrogen-bonded ring-NH of imidazole with another imidazole ring-N appears at ~14 ppm. With an introduction of additional oxygen sites, an additional type of hydrogen-bonded proton appeared due to the interaction of ring-NH to –P=O at ~12 ppm, confirming our assignment.

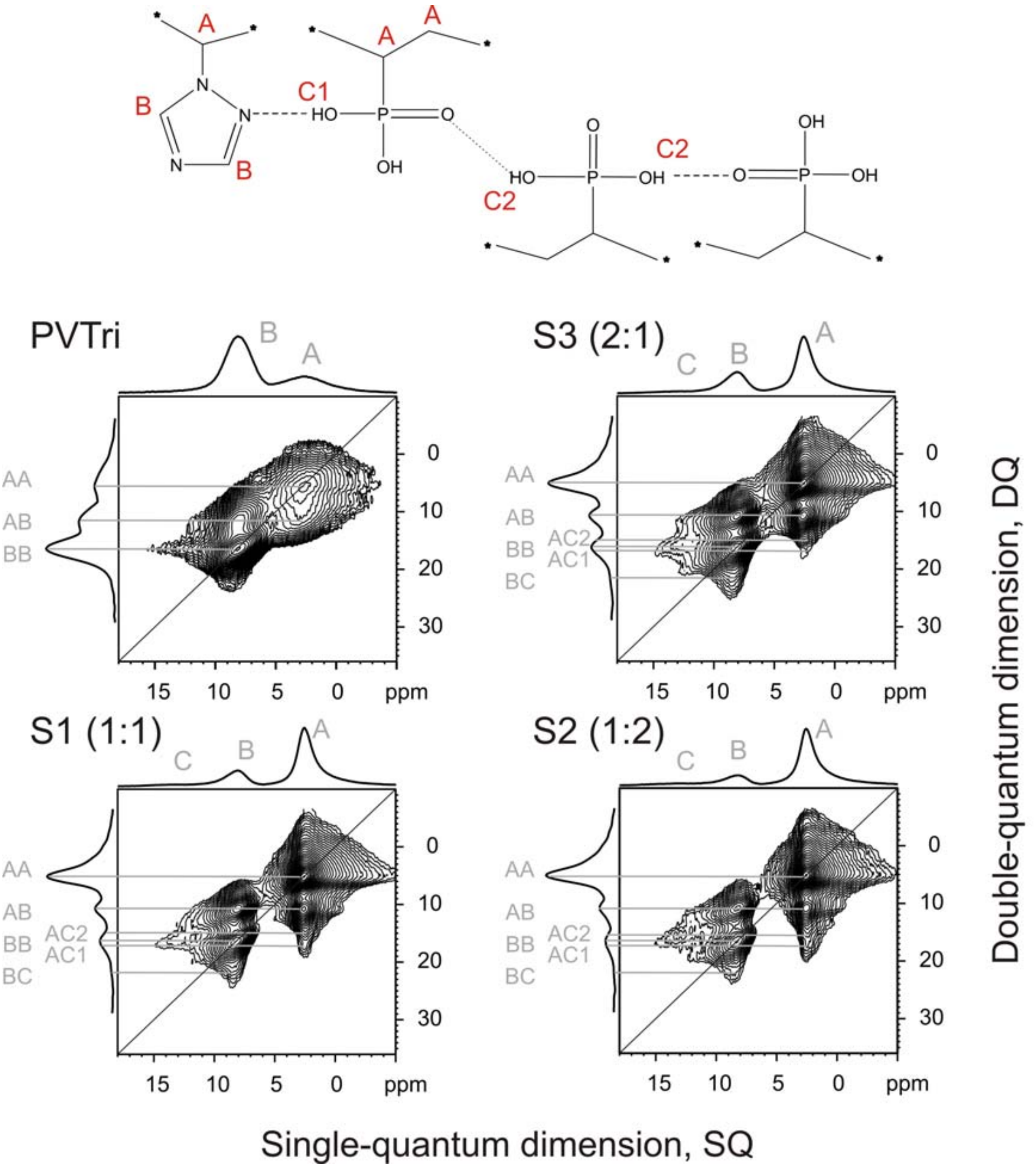

Figure 6.6: 2D ^{1}H DQ MAS NMR spectra of PVTri and its copolymers. The spectra were recorded with one rotor-period of recoupling time, at 25 kHz MAS frequency and at 300 K. Different types of protons are visible: Backbone (A-type, ~3 ppm), triazole ring (B-type, ~8 ppm), and hydrogen-bonded protons (C-types, ~10-17 ppm).

For an even more detailed spectral assignment, a two-dimensional ^{1}H-^{31}P heteronuclear correlation experiment was performed, as shown in Figure 6.7 for the as-synthesized 1:1 (S1) copolymer and its annealed form. It reveals proximities of the phosphorous and the hydrogens of PVPA, which are established via through-space dipolar interactions between the nuclei. Spatial proximities of ^{31}P are expected to the

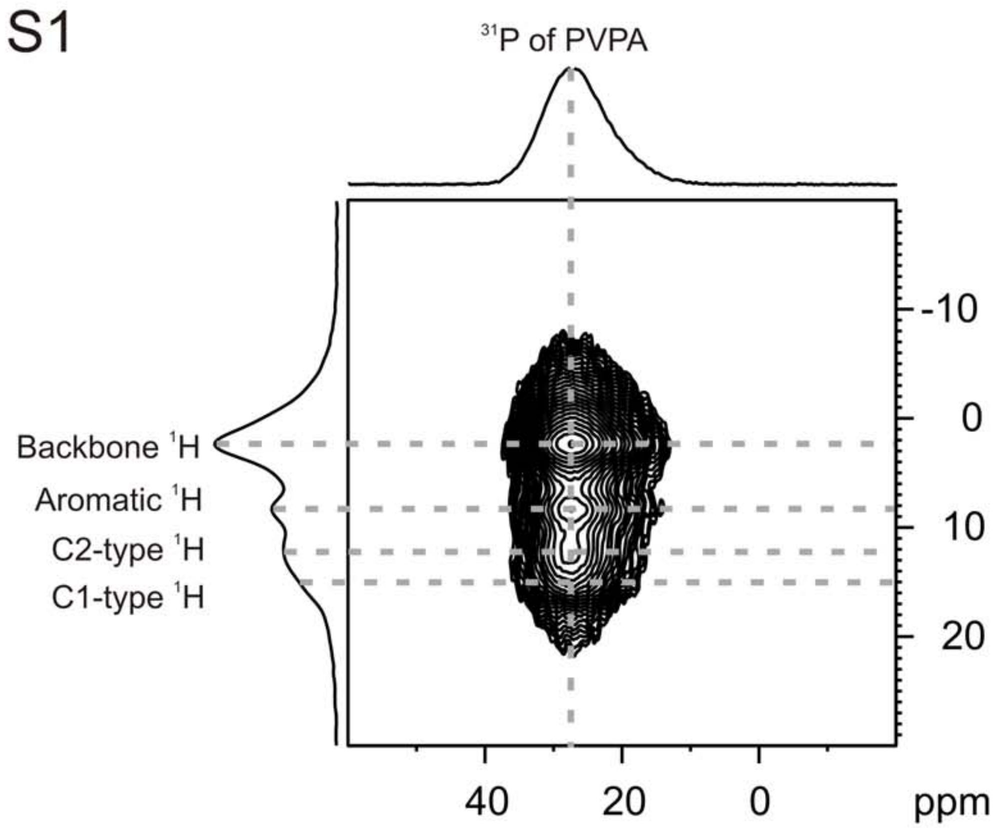

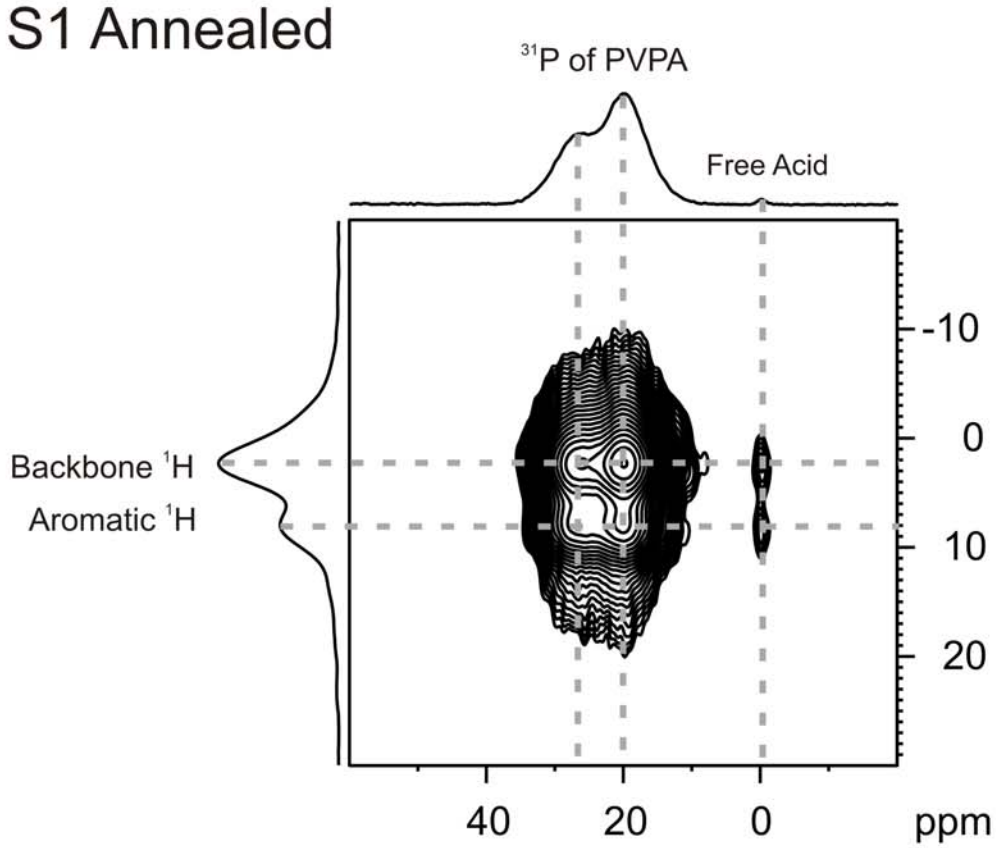

Figure 6.7: 2D ^{1}H-^{31}P CPMAS spectrum of dried and annealed S1 (1:1 ratio of polymers) recorded at 300K and at 30 kHz MAS frequency. The contact times for the cross-polarization experiments were 2 ms.

polymer backbone –CH_2, the ring ^1H of PVPA, and ^1H of phosphoric acid group (P-OH). Here different types of acidic protons C1- and C2- types, have to be distinguished. The clearly resolved C2-type of hydrogen bonding proton shows a much higher intensity compared to the C1-type which appears only as a shoulder. For the annealed sample, more interactions are present due to the additional phosphorous sites. The interactions due to the hydrogen-bonded protons are nearly removed due to anhydride formation. A small amount of trapped H_3PO_4 is detected in the annealed sample, in close proximity to the polymer backbone and triazole ring.

6.2.3 ^1H Variable Temperature MAS NMR: Proton Mobility

For the desired proton conductivity, proton mobility is most important. It can easily be probed by variable-temperature (VT) ^1H MAS and ^1H DQF MAS NMR. For ^1H double-quantum coherence (DQC) to be present in a ^1H double-quantum filtered (DQF) spectrum, the proton site should be rigid on the timescale of the NMR experiment (μs) and should interact with other protons. After the application of a DQF, no peak disappeared for PVTri or the three copolymers. This shows that, at room temperature no highly mobile proton (e.g. in fast exchange) is present in the system. Even the hydrogen-bonding proton signals remain after the double-quantum filtration at 300 K, due to their rigid structure, with fixed hydrogen bonds.

The ^1H VT MAS spectra of the copolymer, S1, with 60% PVPA mole percentage, are shown in Figure 6.8. Increasing the temperature from 300 K up to 410 K makes the broad hydrogen-bonded proton resonance sharper. At 410 K, only one proton resonance is observed at ~11.5 ppm, indicating exchange between different hydrogen-bonding and free sites. However, there is no indication of ^1H in O-H$\cdots$N sites anymore. This suggests that the motions in those sites move with rates comparable to the MAS spinning frequency leading to destructive interference and signal loss (Suwelack 80). Consistent with this, the sharp signal does not occur at the average of all ^1H chemical shifts at low field, but its chemical shift is characteristic of the O-H$\cdots$O site. This indicates that, the acidic protons move between many different PVPA sites, which are the origin of high proton conductivity (Lee 07). It can not be excluded, however, that ^1H in dissociated hydrogen-bonds of OH$\cdots$N sites contribute to this signal as well. The mobility difference of the acidic proton can also clearly be seen in Figure 6.8b. This figure represents the comparison of ^1H MAS and DQF NMR spectra of the **S1** copolymer.

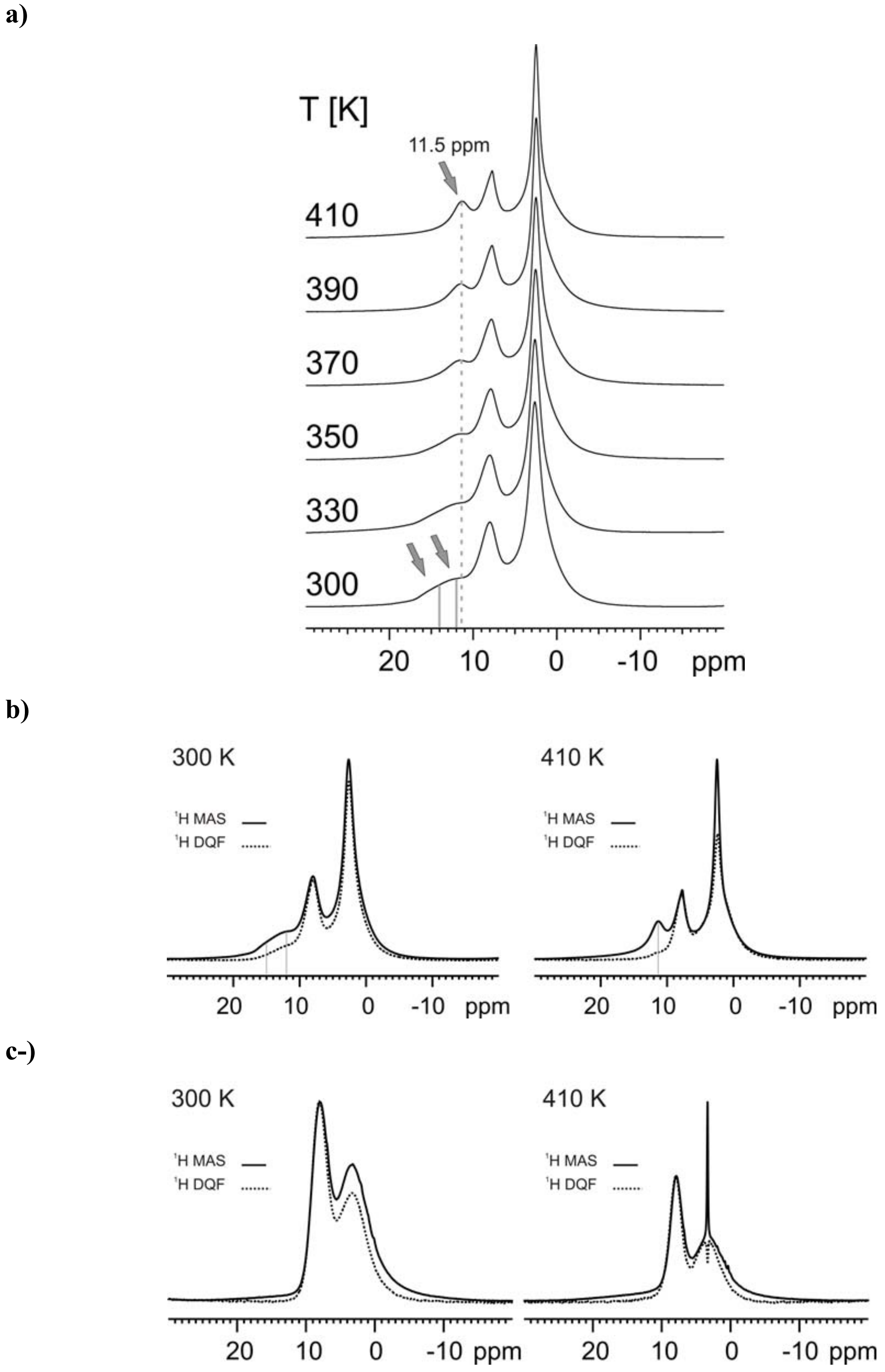

Figure 6.8: a) The variable temperature ^{1}H MAS spectra of Poly(VTri-co-VPA), S1 recorded at 25 kHz MAS frequency, from 300K up to 410 K. **b)** The comparison of ^{1}H MAS and DQF NMR spectra of **S1** recorded at 300 and 410 K under 30 kHz MAS. The DQF spectra were recorded with 1 t_R of BaBa recoupling pulse sequence. **c)** The comparison of ^{1}H MAS and DQF NMR spectra of PVTri recorded at 300 and 410 K under 30 kHz MAS.

At room temperature all hydrogen-bonded proton resonances can still be seen after the application of DQF. At 410 K, however, the mobility increase due to increased exchange rate results in intensity loss in the DQF spectra. Aliphatic and ring protons additionally become more mobile, and show line narrowing, but no significant changes in chemical shift values are observed. This behavior is different from PVPA itself (Lee 07), where no indication of mobility in the polymer backbone was observed. The introduction of PVTri clearly induces additional mobility to the polymer backbone, which may further facilitate proton conduction. In addition, ^{1}H MAS and DQF spectra of PVTri are represented in Figure 6.8c, recorded at 300 and 410 K. In particular for the ring ^{1}H line narrowing is observed, but even at 410 K no resonance disappeared after the application of DQ filtration.

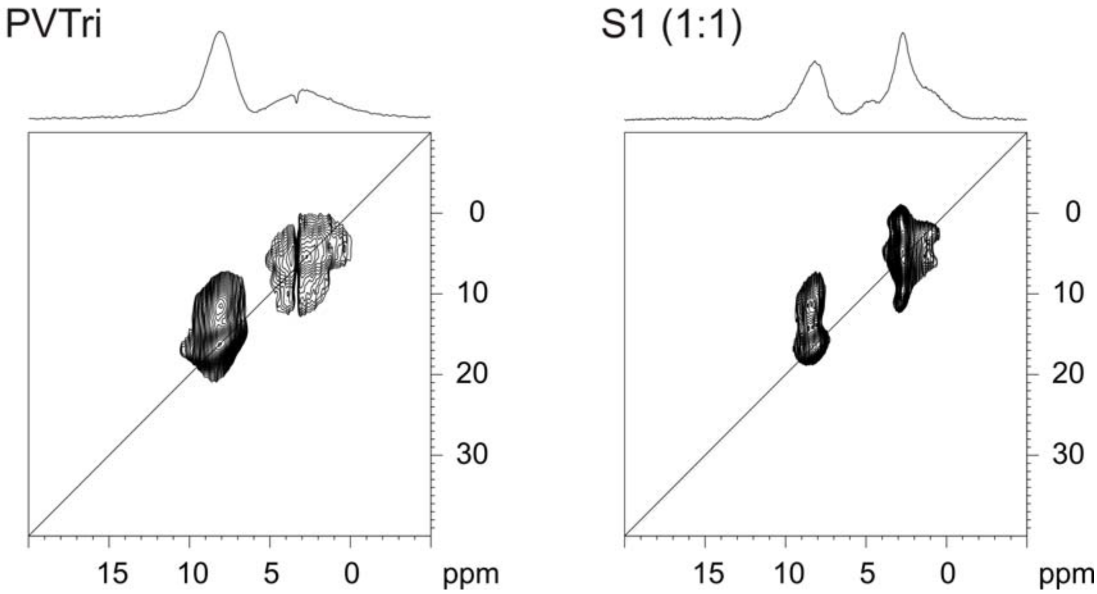

Figure 6.9: 2D ^{1}H DQ MAS NMR spectra of PVTri and **S1**. The spectra were recorded with one rotor-period of recoupling time, at 25 kHz MAS frequency and at 410 K.

Information about the packing of the heterocyclic groups is obtained from the ring auto peak at the ^{1}H DQ spectra at 300 K and even at 410 K (Figure 6.6 and 6.9). Normally there should not be an auto peak from the PVTri ring under these conditions, because of their large distance (~4 Å). This then means that the auto peak indicates ring packing in the PVTri and in the copolymers. At room temperature the auto peak at 8/16 ppm in SQ/DQ dimension is the dominating resonance for PVTri (Figure 6.6). The same resonance in the copolymers is reduced in intensity, but still present. This represents the remaining packing arrangements even in the copolymers. At elevated temperature, 410 K (Figure 6.9), the relative amount of this auto peak is much reduced due to the mobility increase at the ring sites, nevertheless it still can be observed for both PVTri and S1. The distance between the aromatic protons was probed by ^{1}H-^{1}H sideband pattern (see Supplementary Information). A ^{1}H-^{1}H dipole-dipole coupling of 4.6 kHz at 300 K and 4 kHz at 410 K was determined. This relates to ~2.97 Å at 300 K and allows only highly restricted ring mobility at elevated temperatures. Thus the packing remains essentially intact. For the S1 copolymer, a slightly reduced dipolar of 4.4 kHz was observed at 300 K. However, at 410 K the dipolar coupling was removed completely which did not allow fitting to obtain the dipolar coupling, whereas in PVTri still a dipolar coupling of ~3.8 kHz is present. This shows that the molecular mobility in the S1 copolymer is higher at elevated temperatures compared to the PVTri homopolymer.

6.2.4 ^{1}H DQ Sideband-Patterns:

From an analysis of the sideband patterns, dipolar coupling constant can be extracted which can be converted to distance information (Brown 00). The nature of the observed pattern is very sensitive to the product of the excitation/reconversion time, $N*t_R$, and dipolar coupling. The recorded ^{1}H sideband patterns are shown in Figure 6.10.

While performing the fitting, the simulated spectra is produced by using a DQC between an isolated spin-pair, as a result no even-order sidebands are produced. However, in the real spectra, in Figure S1, the presence of the even-order sidebands is clear. Nevertheless, previous studies have showed that still reliable information can be extracted at high spinning frequencies (Graf 97, Brown 99, Brown 00). In the current case, the aliphatic protons lead to centerband and even-order sidebands. Moreover, the aliphatic protons nearby the ring CH protons produce DQCs which cause the observation of an additional shoulder (marked by *) in the odd-order (first and third) sidebands on the right side of the original pattern.

The dipolar couplings given in the Figure S1 are extracted from the sideband-patterns by only fitting the intensities of odd-order sidebands in the ^{1}H DQ MAS spectra. For PVTri homopolymer, at 300 K, a dipolar-coupling of 4600 Hz was extracted, which corresponds to a distance of ~0.297 nm between the neighbor CH protons. Because the distance between ring-CH protons in the same triazole ring is too much (~0.41 nm) to give a DQC, the calculated dipolar coupling, is due to the distance between the pi-packed aromatic triazole rings. At 410 K, however, the same dipolar coupling is reduced to 4000 Hz, due to the increased triazole ring mobility. For the S1 copolymer, at 300 K, the third order sidebands are

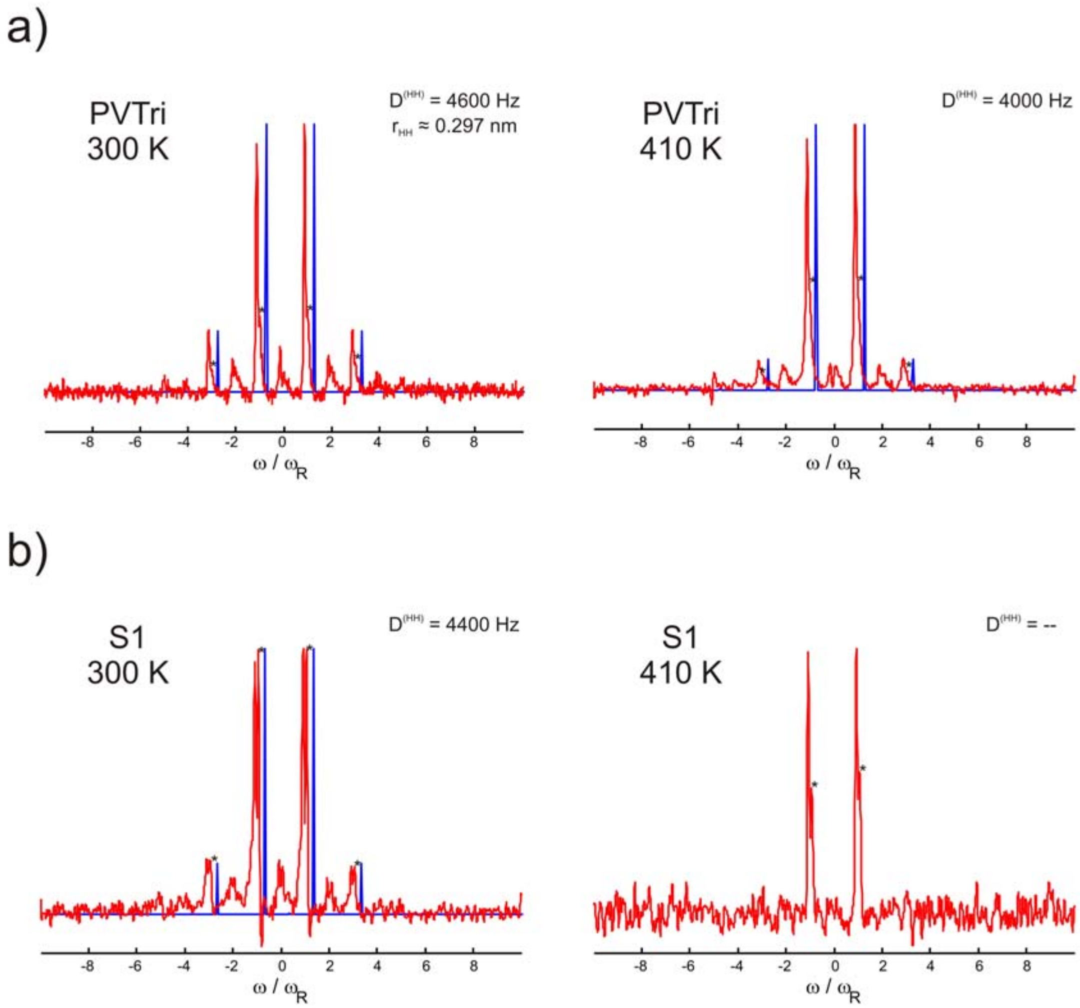

Figure 6.10: Extracted columns (red) from ^{1}H DQ sideband-pattern MAS spectra of PVTri homopolymer (**a**) and S1 copolymer (**b**) recorded at 300 K and 410 K at ~7.8 ppm (corresponds to the chemical shift of the ring CH). In each spectrum, the bets-fit spectrum (blue) is additionally included to the right side of the spectra which was generated by assuming an isolated spin-pair. The resonances marked by * correspond to DQCs between the ring CH protons and other nearby protons. The calculated dipolar couplings and resulting proton distances are included on top right of each spectrum.

slightly reduced and a dipolar coupling of 4400 Hz was extracted. This dipolar coupling is slightly higher compared to the pure PVTri. Moreover, at 410 K, the dipolar coupling of the copolymer was much reduced which is evident from the fact that the third order sidebands are already disappeared for the copolymer.

It can be concluded from these results that the ring distances in the S1 copolymer is slightly higher compared to pure PVTri. This result might be due to a dilution of the PVTri moieties from each other, which might eventually increase the molecular mobility at the triazole ring sites of PVTri, by the addition of PVPA. Additionally, at high temperature, 410

K, the third-order sidebands are missing in the S1 copolymer, which are still present for pure PVTri. This observation states that the molecular mobility in the S1 copolymer is much higher compared to the pure PVTri.

6.3. Conclusions:

In this work, we have investigated novel proton conducting copolymers based on vinylphosphonic acid (VPA) and 1-Vinyl-1,2,4-triazole (VTri). The copolymers, poly(VPA-*co*-VTri) were prepared by conventional free radical polymerization of the corresponding monomers. Low molecular weight copolymers were produced and their structures were confirmed by ^{13}C CP-MAS NMR spectroscopy. The materials became more stable against phosphonic acid anhydride formation, but condensation could not be completely prevented as shown by ^{31}P MAS NMR. The proton conductivity increased with the content of phosphonic acid units in the polymer chain. Poly(VPA-*co*-VTri), S2 (~70% PVPA mole ratio) show a conductivity of ~ 10^{-3} S/cm at 120 °C, in the anhydrous state. The hydrogen-bonding nature of the copolymers was analyzed with the help of ^{1}H MAS NMR. The presence of two different types of hydrogen-bonding arrangements, $O\text{-}H\cdots O$ and $O\text{-}H\cdots N$, was proved with the assistance of double-quantum ^{1}H MAS NMR. Moreover, the molecular dynamics present in the system were elucidated by variable-temperature ^{1}H NMR techniques, which revealed that at high temperature (410 K) highly mobile acidic protons are only present in $O\text{-}H\cdots O$ arrangement, and as a result a single resonance is observed at an averaged chemical shift of 11.5 ppm. At elevated temperatures, no evidence for protons in $O\text{-}H\cdots N$ bond with dominant shifts up to 15 ppm was found. Opposed to the PVPA homopolymer, increased mobility in the polymer backbone was observed. This suggests that the triazole containing copolymers provide defect sites facilitating proton conduction. A related behavior was previously observed in proton conducting imidazole oligomers (Goward 02), where only the weakly hydrogen-bonded regions were responsible for the proton conductivity. Similarly, in pure PVTri, increased ring and backbone mobility was observed, which facilitate proton conduction in the systems. Thus, copolymerization of VTri with VPA yielded promising polymer electrolyte membrane (PEM) materials that showed better conductivities compared to imidazole comprising copolymers, and similar conductivity compared to homopolymer of PVPA under dry conditions (Steininger 07).

Chapter 7:

Structure and Dynamics of Self-Organizing Supramolecular Conductors: Perylenebisimide Derivatives

This chapter explains the results obtained by using the previously described advanced solid-state MAS NMR methods (chapter 2) to study structure and dynamics of perylenebisimide materials whose general structure is represented in Figure 7.1. The detailed information especially on the structure and the dynamics of different perylenebisimide will be presented. Perylene derivatives are very promising systems in the field of electron conducting functional materials for organic electronic applications.

In section 7.1, a general introduction to the system will be given with an emphasis on the phase behavior of the materials investigated. The materials investigated were provided by Prof. Percec and his coworkers, whose names are listed in the acknowledgement section at the end. As a result, the synthesis procedures are not explained in the text, and can be found in the literature (Percec 08).

7.1: Introduction to Perylenebisimide Derivatives:

Great interest in supramolecular assemblies (Lehn 95, Philp 96) has been inspired by examples from nature like the light harvesting system (LHS) (McDermott 95) in purple bacteria. Chlorophyll molecules in natural supramolecular assembly organize in cyclic arrangements and control the electronic coupling of the dye molecule and allow accommodation of the photosynthesis reaction (McDermott 95). Due to the crucial importance of self-assembled molecules in biology, efforts have been devoted to the building and control of similar organizations of artificial molecules for their promising applications in organic electronic devices (Wurthner 00).

Some discotic liquid crystalline materials have been proposed showing the desired optical and electronic properties, like columnar liquid-crystalline hexabenzocoronanes (HBCs) (Pisula 06, Hill 04), which may be used as conducting layers in organic electronic devices (van de Craats 99). Triphylenylenes (Adam 94). Furthermore, well-organized assemblies of p- and n- type semiconducting π-electron systems have been constructed for efficient charge carrier mobility (van der Boom 02, Debije 05). Perylene bisimide (PBI) derivatives based on colorants are from similar types and have received great attention due to their ability to form supramolecular aggregates and its application areas in the industry (Zollinger 03, Herbst 97). Most recent applications of these materials are mostly in the field of electronic materials, among which perylene bisimides are one of the best n-type semiconductor available to date (Struijk 00, Demitrakopoulos 02). These dyes and their assemblies find application as functional units in artificial light harvesting systems (DeSchryver 05, Sautter 05), photo induced electron transfer (OTNeil 92, Prodi 05), and organic electronic devices such as organic light emitting diodes (OLED) (Kraft 98, Pan 05), organic thin-film transistors (OTFT) (Wurthner 06), and solar cells (Tang 86, Schmidt-Mende 01).

Non-covalent interactions, particularly π-π stacking in the current systems, play a crucial role in the arrangements of self-assembly structure of polycyclic aromatic materials in condensed matter (Dessiraju 89). The nature of these preferred arrangements in different derivatives will be the main focus of this chapter. Another important property of the materials determined also by π-π stacking is their liquid crystallinity (LC) which leads to the formation of columnar dye stacks which can enable 1D charge carrier mobility (Wurthner 01). Liquid crystallinity is very important in terms of obtaining well-organized layers in which the columnar organization can be controlled and self-healing of structural defects can occur (van de Craats 99).

Previous studies have shown that the un-substituted PBIs exhibit flat π-systems as confirmed by X-ray diffraction of several single crystals (Graser 80, Zugenmaier 00). Substitutions made at the bay positions can impose twisting of the planar molecule (Chen

04). The exact conformation of the molecule is not clear when the substitution is made at the imide positions of PBIs. In the solid state, for the tetraphenoxy-substituted perylene bisimides, a racemic mixture is observed and the phenoxy groups adopt an extended orientation that allows the most compact packing of these dyes (Wurthner 02). However, in the self-assembled architectures of these molecules, the conformation preferences are unclear.

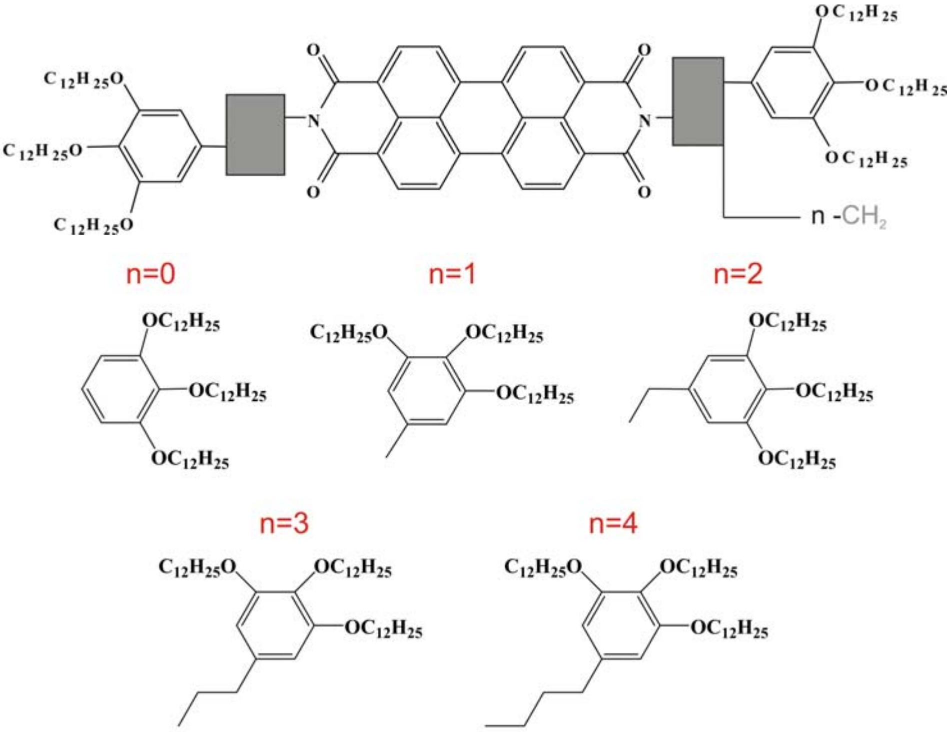

Figure 7.1: General structure of perylenebisimide derivatives. The outer phenyl groups are attached to the perylene core with n –CH_2 spacer ($0 \leq n \leq 4$) (n=0 is EM177, n=1 is EM261, n=2 is EM266, n=3 is EM248, n=4 is EM341).

Packing behavior of the PBI in the crystal has been studied previously (Graser 80). It has been found that for different imide substitutions different stacking distances (3.34 – 3.55 A, whereas this distance is 3.35 A in graphite (Graser 80)) and different longitudinal and translational offsets between neighboring PBIs were determined with a planar geometry of perylene bisimide. The color of the system is determined by the stacking distance and conformation due to different interactions of π-systems in the crystal lattice (crystallochromy; color changes resulting from the interaction of the π-systems in the crystal lattice). This is the origin of the quest of finding the best combination, which would results in best electron mobility value in the system with the best π interactions of successive PBI molecules (Wurthner 04).

The structure of the PBI derivatives (as shown in Figure 7.1) is composed of a rigid perylene core which is attached from both sides to the outer phenyl by $–CH_2$ spacer groups. The $–OC_{12}H_{25}$ side chains (tridodecyloxyphenyl) are introduced to the outer phenyl groups to obtain the liquid crystalline mesophases. Five different PBI derivatives were investigated which are differing by the length of spacer group (from n= 0 to n=4).

The structural design of perylene bisimide derivatives has some specific functional properties. One molecule is composed of four different parts: perylene core, spacer group, outer phenyl, and –R groups attached to the phenyl. The perylene core supplies the origin of the electron mobility in the supramolecular complex, by the effect of π-π stacking between repeating PBI molecules. Surrounding the PBI core, insulating $(CH_2)_n$ spacer exist on the both sides of the core. Outer phenyls and the attached R groups supply the desired liquid crystalline properties. Moreover, additional control of molecular packing can be managed by fine-tuning the packing with changing the substituents attached to the PBI core. As shown before, the perylene dendrons at the outside have pronounced effect on the stacking of the chromophores (Percec 02, 07).

Table 7.1: Electron mobility values and phase transition temperatures of the materials studied.

Sample	CH_2 Unit in between	Phase transition temp.[K]			Mobility of e^- cm^2/Vs
			T_g	T_m	
EM177	0	244	640	-	15.10^{-2}
EM261	1	246	498	-	$(1.7 - 4).10^{-2}$
EM266	2	251	374	407	$(1 - 2).10^{-2}$
EM248	3	253	361	399	$(80 – 110).10^{-2}$
EM341	4	258	361	386	-

The electron mobility was measured for the different materials and the results are listed in Table 7.1. The conductivity values are measured at 20°C. Values listed here strongly depend on the thermal history of the samples. Nevertheless, the conductivity strongly depends on the spacer length, and particularly reached to a maximum in the material with n=3 molecule (three $–CH_2$ units as spacer units). The perylene bisimide derivative having three $–CH_2$ in the spacer group, shows mobility values exceeding 1 cm^2/Vs in the room temperature phase compared to the other materials. These values are in the same range as HBC derivatives, and approach the value for the graphite (~ 3 cm^2/Vs) (Dresselhaus 81).

All of the PBI materials studied (with changing spacer $–CH_2$ units), form thermotropic mesophases (columnar liquid-crystalline phases) over a broad temperature range. Due to the extended aromatic surfaces, PBIs are expected to enter the mesophase at relatively high temperatures. However, with the disturbing effect of side chains on packing of the aromatic part of the molecules, lowering of the LC phase entering temperature is observed. The phase transition temperatures of the materials studied are also listed in Table 7.1.

Differential scanning calorimetry (DSC) shows that the transitions from room temperature phases occur at different temperatures for the materials having different spacer lengths. The studied materials are divided into two general groups in terms of their phase transition temperatures. The materials with spacer length of n=0 and 1, are designated as *high phase-transition temperature materials*, and materials with longer spacer groups are designated as *low phase-transition temperature materials*. For the high phase-transition materials (n=0, and n=1), this transition occurs at 640 K for n=0, while at 498 K for n=1. For the low phase-transition materials (n=2-4), however, this transition occurs at 374 K for n=2, at 361 K for n=3, and at 361 K for n=4.

The high phase-transition materials have very high phase-transition temperatures which are far beyond the temperature range accessible with the used NMR instrumentations (maximum temperature is 400 ^{o}K). However, for the low phase-transition materials, the phases above the transition temperatures could be studied, as well as room temperature phases.

7.2: PBI Derivatives with High Phase Transition Temperatures: Structural Investigation

The structural features of the high phase-transition perylene derivatives are determined with the application of single-quantum and double quantum ^1H NMR under fast MAS. 2D DQ ^1H experiments will provide proton proximities and valuable information on the molecular organization can be gathered. With the help of the higher chemical shift dispersion of carbon nucleus, more site specific features will be revealed.

7.2.1: ^1H SQ-DQ MAS NMR results:

Figure 7.2 presents ^1H MAS spectra of the room temperature phases of high-T_g materials with n=0 and n=1 at an MAS frequency of 30 kHz and 850 MHz ^1H Larmor frequency. The very intense resonance at 1.1 ppm is originating from the aliphatic protons. The resonance at around 3.6-3.7 ppm is due to O-CH_2 protons of the sidechains. For n = 1 material (EM261), the –CH_2 spacer appears at ~5.5 ppm in the spectrum in close proximity to aromatic resonances of the outer phenyl. In all other materials with –CH_2 spacer, this signal is observed at ~3.7 ppm. The outer phenyl aromatic protons have chemical shifts of around 6.7-6.9 ppm (similar to the values observed in the liquid state). The detailed list of the chemical shift values observed in the solid and liquid states are given in Table 7.2.

Table 7.2: Comparison of solid and solution state chemical shift for different PBIs. The values in parenthesis are solution values ($CDCl_3$), others are solid-state values.

Proton Type	**n=0**	**n=1**	**n=2**	**n=3**	**n=4**
Aliphatic	1.1	1.1	1.1	1.1	1.1
O-CH_2 in sidechains	3.7	3.6	3.6	3.6	3.6
Spacer –CH_2–	~3.6	~3.6, ~5.3	~3.6	~3.6	~3.6
Outer phenyl	6.9 (6.9)	6.7 (6.9)	6.4 (6.5)	6.2 (6.5)	6.1 (6.4)
Perylene core	(8.3, 8.5)	(8.5, 8.6)	(8.6, 8.7)	(8.6, 8.7)	(8.6, 8.7)

The aromatic regions of the perylene core have the most diverse chemical shift ranges, changing severely from one molecule to other. From Figure 7.2 it can be immediately realized that depending on the length of the –CH_2 spacer remarkable changes are observed in the aromatic regions of ^{1}H MAS spectra of the materials. In liquid-state NMR, the protons of the perylene core are observed as two different resonances separated by ~0.1-0.2 ppm (at ~8.6 ppm, slightly changing for the different samples), due to the two different proton sites at the bay position of the perylene core (which leads to the two-fold symmetry of the perylene core). This difference in chemical shift can hardly be resolved in the solid-state NMR spectra due to dipolar couplings between protons in the system. Only one broad resonance should have been observed. However, instead of one distinct resonance, four (6.2, 7.5, 8.1, and 9 ppm for n=0) and three (6.1, 7.3, and 8.1 ppm for n=1) aromatic resonances were observed in the case of high-T_g materials (n = 0 and 1). These additional resonances result from different arrangements (packing) of the perylene molecules and different π-shifts experienced by the aromatic resonances (Brown 99, 00).

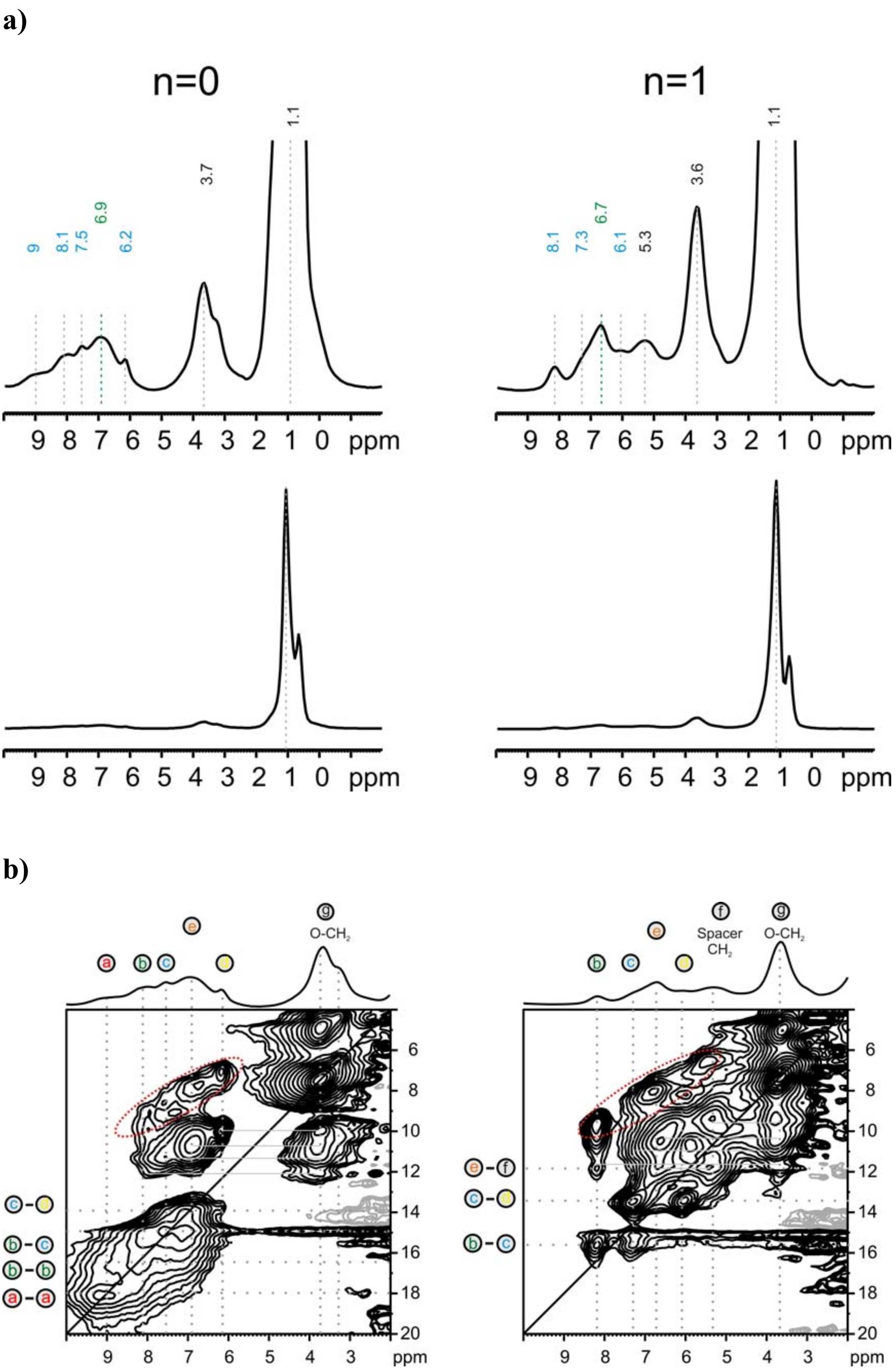

Figure 7.2: a) ^{1}H MAS single quantum spectra of perylene bisimide derivatives with a spacer length of n=0 and n=1. b) ^{1}H 2D DQ MAS NMR spectra. All spectra recorded at 30 kHz MAS frequency, at 850 MHz ^{1}H Larmor frequency and at 320K.

The studied perylene molecules have extended aromatic cores. This structure forms a π-electron system and possesses ring currents to the surroundings causing shielding or deshielding effects. This phenomenon was demonstrated by Waugh and Fessenden in the early 1956 (Waugh 56), who showed that a proton located above an aromatic ring system experiences a large shielding effect which causes a high-field shift. Many examples of high-field shifts were observed in HBC derivatives (Brown 99, 00), for example. The observation of more than one aromatic resonance (in the high-T_g materials) is a clear indication of the presence of π-packing effects, which makes resonances of chemically identical protons appear at different spectral positions.

For the PBI derivative with n= 1, instead of one resonance at solution-state chemical shift, 8.5-8.6, three resonances shifted to high-field are observed. The amount of shifting depends on the strength of the experienced packing by that particular proton. The stronger the external field experienced by a proton, the bigger is the shift in chemical shift value. As a result, it is obvious that, there are three distinct proton sites experiencing this external field due to pi-packing differently. More interestingly, in the n=0 material, in addition to these three high-field shifted proton resonances, there is also one low-field shifted proton resonance at 9 ppm (~0.5-0.7 ppm shifted). This result is a manifestation of a different packing arrangement in n=0 material compared to n=1 material. The origin of these shielding effects can more clearly be understood in the following sections when discussing the results of quantum chemical calculations. At the moment, a more complete understanding can be obtained by ^{1}H 2D double-quantum NMR spectroscopy.

From one-dimensional ^{1}H spectra, it is not possible to determine the interactions between dipolar-coupled protons. By performing two-dimensional rotor-synchronized ^{1}H double-quantum MAS experiment (Schnell 01, Brown 01), this information will immediately be available. This technique has proven to be particularly useful to investigate the packing in columnar systems like HBCs, triphnylenes, and dendrimers (Brown 99, Kranig 90, Percec 02). Such spectra recorded with one rotor-period (τ_R) of BaBa recoupling (Feike 96) for DQ excitation and reconversion at T=320K, are alkyl regions of the spectra which are dominated by the intense signals from sidechain protons are not shown here. The given spectra focus the more informative aromatic region better.

In Figure 7.2b, the proton resonances are named with letters (**a** to **g**) to ease the description. Four different strong interactions can be seen for the *n=0* perylene derivative. The pattern at the low-field region is broadened due to the possible strong dipolar interactions of protons, and the resonances are less apparent. A strong auto peak (**a**-**a**, 9-18 ppm) is observed due to the low-field shifted protons. Another auto peak is observed (**b**-**b**, 8-16 ppm) due to the least high-field shifted proton which appears at 8.1 ppm in SQ dimension. Two cross peaks are observed which are due to the close proximity of **b**-**c** and **c**-**d** type of protons. **b**-**c** peak appears at 15 ppm and **c**-**d** peak appears at 14 ppm in the DQ dimension. With the introduction of one –CH_2 spacer group to the PBI molecule (n=1 molecule), a symmetry brake in the molecule happens and different molecular organization is preferred which represents itself as two well resolved cross-peaks in the spectrum. The **b**-**c** (at 15.5 ppm in the DQ dimension) and **c**-**d** (at 13.5 ppm in the DQ dimension) type of cross peaks are due to the interaction of low-field shifted three different types of perylene aromatic core protons. Interestingly, no aromatic auto-peak is observed for ***n=1*** molecule, and the observed cross-peaks are well resolved compared to the ***n=0*** material.

Many interactions between unlike protons are seen as cross-peaks. Perylene core protons form dipolar correlations to the O-CH_2 and/or spacer –CH_2 groups which are shown in the figure with grey-solid lines, whereas, the interactions of core protons and sidechain protons are marked with red dashed circles. Apart from the **a**-type of low-field shifted proton of n=0 material, all other core protons have cross peaks to the sidechains or spacer protons. This is indicating that **a**-type of protons are placed in a more isolated region in the molecular packing, and have no contact with the alkyl side chains within 0.3-0.4 nm.

7.2.2: ^{13}C MAS NMR results:

After clarifying many aspects by ^{1}H SQ and DQ MAS results, which is relatively quick to obtain (within a hour or so), a second step in the structural determination is using ^{13}C nucleus. With the help of ^{13}C CPMAS and ^{1}H-^{13}C heteronuclear correlation experiments (HETCOR) a better resolution can be achieved due to the larger chemical shift range and inherently narrower line widths (Schnell 01) and as a result the assignment procedure will be easier. Additionally, one can determine the chemical shifts of ^{1}H bound to particular carbons with the help of dipolar ^{1}H-^{13}C correlation experiments. Without the enrichment of the samples, in natural abundance, these spectra can be obtained in longer experiment times (~10 hours with 10-20 mg of sample) due to the poor sensitivity of ^{13}C compared to ^{1}H.

In Figure 7.3 the ^{13}C CPMAS spectra of the ***n=0*** and ***n=1*** material is shown with the assignment of specific carbon sites. Much better resolution obtained for different sites is obvious. Different carbon atoms of different outer phenyl and perylene core sites appear as separate resonances, which makes the site-specific analysis easier. In the perylene core region the signals are overlapping, but nevertheless, the resonances can still be identified.

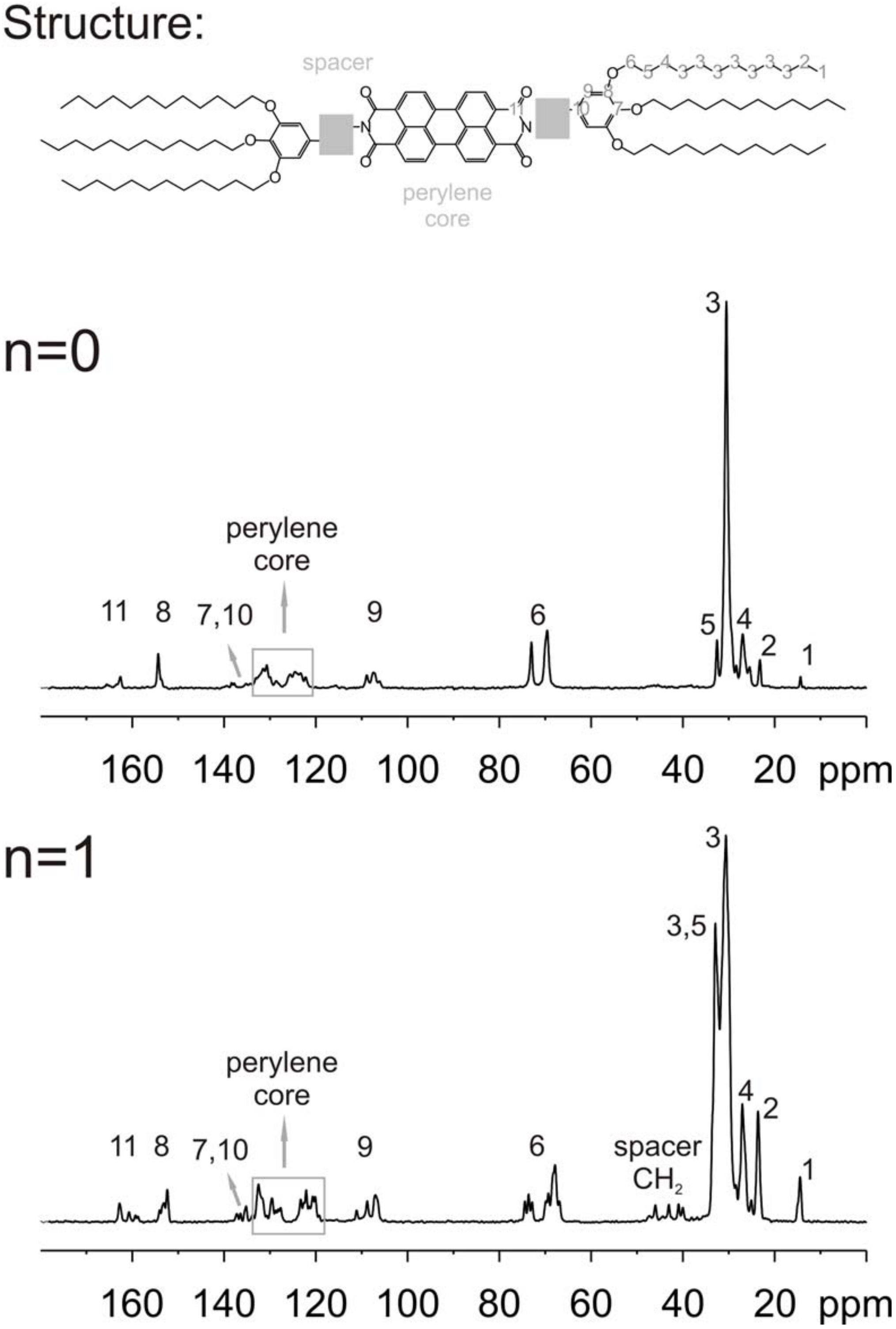

Figure 7.3: ^{13}C CPMAS NMR spectra of n=0, and n=1 perylene derivative. The spectra recorded at 176.05 MHz ^{13}C Larmor frequency, at 15 kHz MAS frequency, and at room temperature. The contact time for the CPMAS experiment was 1 ms. 15k scans were accumulated to get these spectra.

With the assignment of carbon sites in hand (Figure 7.3), we can further gain insight about the connectivities of different carbon atoms with protons. This will supply additional information about the packing arrangements of the materials by knowing the chemical shifts (also π-shifts) of specific protons attached to certain carbons. In Figure 7.4 and 7.5, the Rept-HSQC spectra of *n=0* and *n=1* are shown. The perylene core region is enlarged and shown separately. Additionally, the lines at specified specific carbon chemical shift values are extracted to visualize the attached protons more easily, which are also shown in the figure as obtained from ^{13}C CPMAS NMR separately with more number of scans.

In the 2D Rept-HSQC spectrum which is shown in Figure 7.4 and 7.5, five different regions can be distinguished: the aliphatic, the spacer –CH_2, the Ar-OCH_2, outer phenyl, and the perylene core region. Even the perylene core and the carbonyl carbons are obvious, some of which do not have a directly bonded proton due to the long recoupling time used in recording the spectrum ($2t_R$ at 30 kHz). The assignment for the individual carbon sites is also given with the numbering which is shown in the structure in Figure 7.3.

Carbon sites of the aliphatic region have contacts with the aliphatic protons at 1 ppm as expected. In the –O-CH_2 region, different types of groups can be distinguished, corresponding to the molecular structure of the perylene derivatives (the meta-positions (3, 5-sites) of the outer phenyl appear at ~70 ppm, whereas the para-position (4-site) appears at ~73 ppm). For the ***n=1*** molecule, the proton chemical shift of the spacer –CH_2 unit can be assigned based on the very same experiment performed with only $1t_R$ recoupling time (the spectra is not shown here). The proton chemical shift value was assigned to ~5.3 ppm as indicated before. The outer phenyl carbons have interaction with the close by attached O-CH_2 protons and its own ring proton. The outer phenyl proton chemical shift can be assigned to ~6.9 ppm for both ***n=0*** and ***n=1*** material. The interesting observation of outer phenyl carbon site at the position of 9 is that it split into two resonances (even into three for n=1). This observation indicates different π-shifts for this carbon site, resulting from at least two different positions of C-9 is visualized in the packing arrangement of both ***n=0*** and ***n=1***.

For a better understanding of the packing arrangements, the perylene core region is analyzed in a more detailed manner. When the connectivities of the carbon sites with the protons are compared for ***n=0*** and ***n=1***, the interacting protons range from ~ 6 to 9 ppm for ***n=0***, whereas for ***n=1*** they cover a range from ~ 4 to 8 ppm. Thus for ***n=1***, the π-shifts to the high field region are much more pronounced. The different types of packing arrangements in these two different molecules are also clear in the ^{1}H DQ spectra shown in Figure 7.2, where different types of auto- and cross- peaks are observed. Moreover, in terms of the ^{13}C chemical

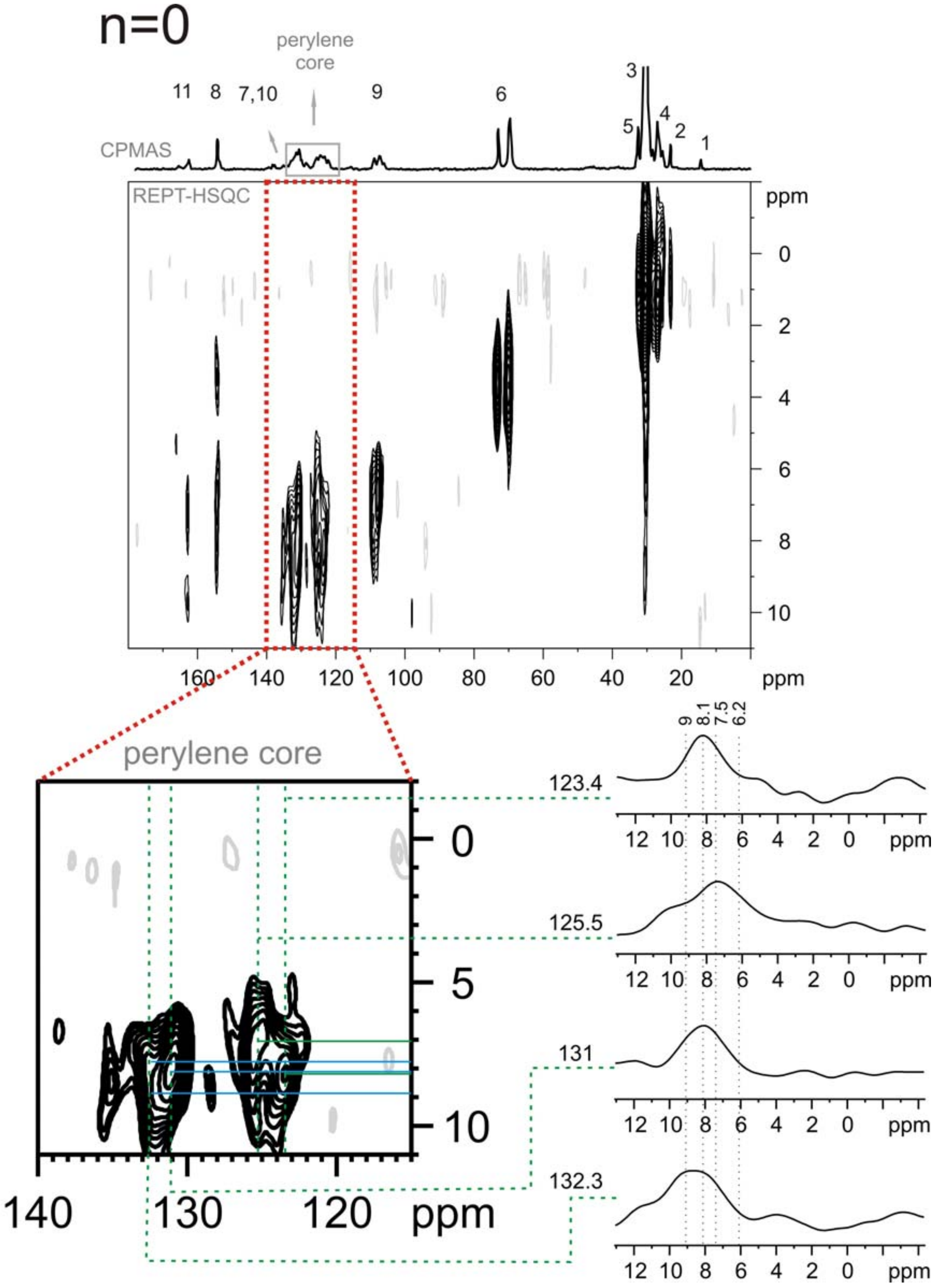

Figure 7.4: Rept-HSCQ spectrum of n=0 perylene derivatives. The spectra recorded at 850 ^{1}H Larmor frequency, 30 kHz MAS frequency, at 320K and with 2 t_R period of recoupling time.

shift values, two molecules have different ranges, once again. ***n=0*** molecule covers a chemical shift range from ~123 to 132 ppm, whereas ***n=1*** molecule this region starts from a much smaller chemical shift value, from ~119 ppm. The exact chemical shift values of the ^{1}H-^{13}C interactions are given at the figures.

As it can bee seen from the spectra in Figure 7.4 and 7.5, especially in the enlarged region of the spectra, the specific carbon resonances from perylene core have protons with different ^{1}H chemical shift values. As a result different proton-carbon correlations were observed. It is clear that the *n=0* and *n=1* derivative of the current PBI compounds have significantly different packing arrangements, which additionally manifests itself as different observed ^{1}H 2D DQ patterns, in Figure 7.2. The *n=1* derivative experienced stronger π-shifts and as a result lower ^{1}H chemical shifts were observed.

7.3: PBI Derivatives with Low Phase Transition Temperatures: Structural Investigation

In this section, the structural properties of the low phase-transition materials will be discussed. Moreover, structural differences compared to the high phase-transition PBI derivatives will be pointed out.

7.3.1: ^{1}H SQ-DQ MAS NMR Results:

The recorded ^{1}H and ^{1}H-^{1}H DQ MAS spectra are presented in Figure 7.6. Despite the features observed in the ^{1}H MAS spectra of high-T_g materials (Figure 7.2a), the spectra of the low-T_g materials are less featured especially in the aromatic proton region where local packing arrangements show the strongest influence. A resonance is observed for all of the materials with a ^{1}H chemical shift around 8 ppm for the perylene core and ~6.1 ppm for the protons of the outer phenyl ring. This observation is already an indication of an increased mobility in the system with a less ordered structure, resulting in averaged aromatic proton resonances with a less broad width at the aromatic proton region in the spectra.

In addition to the differences in ^{1}H MAS spectra of high and low phase-transition perylene derivatives, there are also remarkable differences in the two different material groups when a comparison of the 2D ^{1}H DQ MAS NMR spectra is done. These spectra are represented in Figure 7.6b for low phase-transition materials. First thing to be compared is the lack of resolution in these spectra compare to the ones in Figure 7.2b. Much more averaged patterns are observed for *n=2-4*, especially for *n=2* and *n=3,* due to the interfering mobility of materials with the experiment as a result of lower phase transition temperatures.

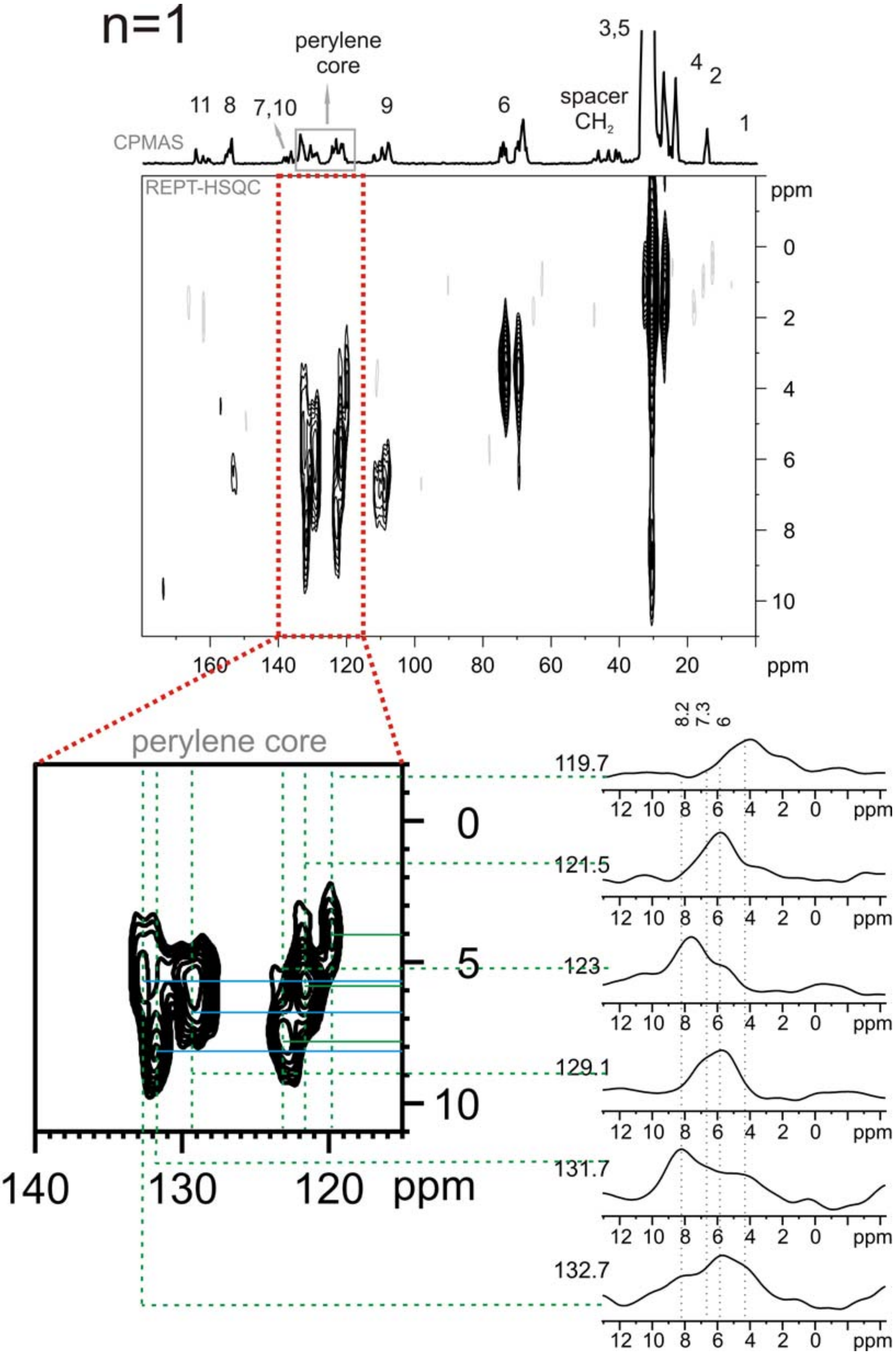

Figure 7.5: Rept-HSCQ spectrum of n=1 perylene derivatives. The spectra recorded at 850 ^{1}H Larmor frequency, 30 kHz MAS frequency, at 320K and with 2 t_R period of recoupling time.

7.3.2: ^{13}C MAS NMR Results:

In Figure 7.7 the ^{13}C CP-MAS spectra of the perylene derivatives (***n= 2-4***) are represented. Despite of the resolved carbon resonances for ***n=0*** and ***n=1*** materials, much broader resonances are observed for ***n=2*** and ***n=3*** derivatives. For ***n=4***, however, again the resonances are more resolved. This observation might be due to the lack of rigid organization for ***n=2*** and ***n=3*** perylene derivative and due to their higher molecular mobility.

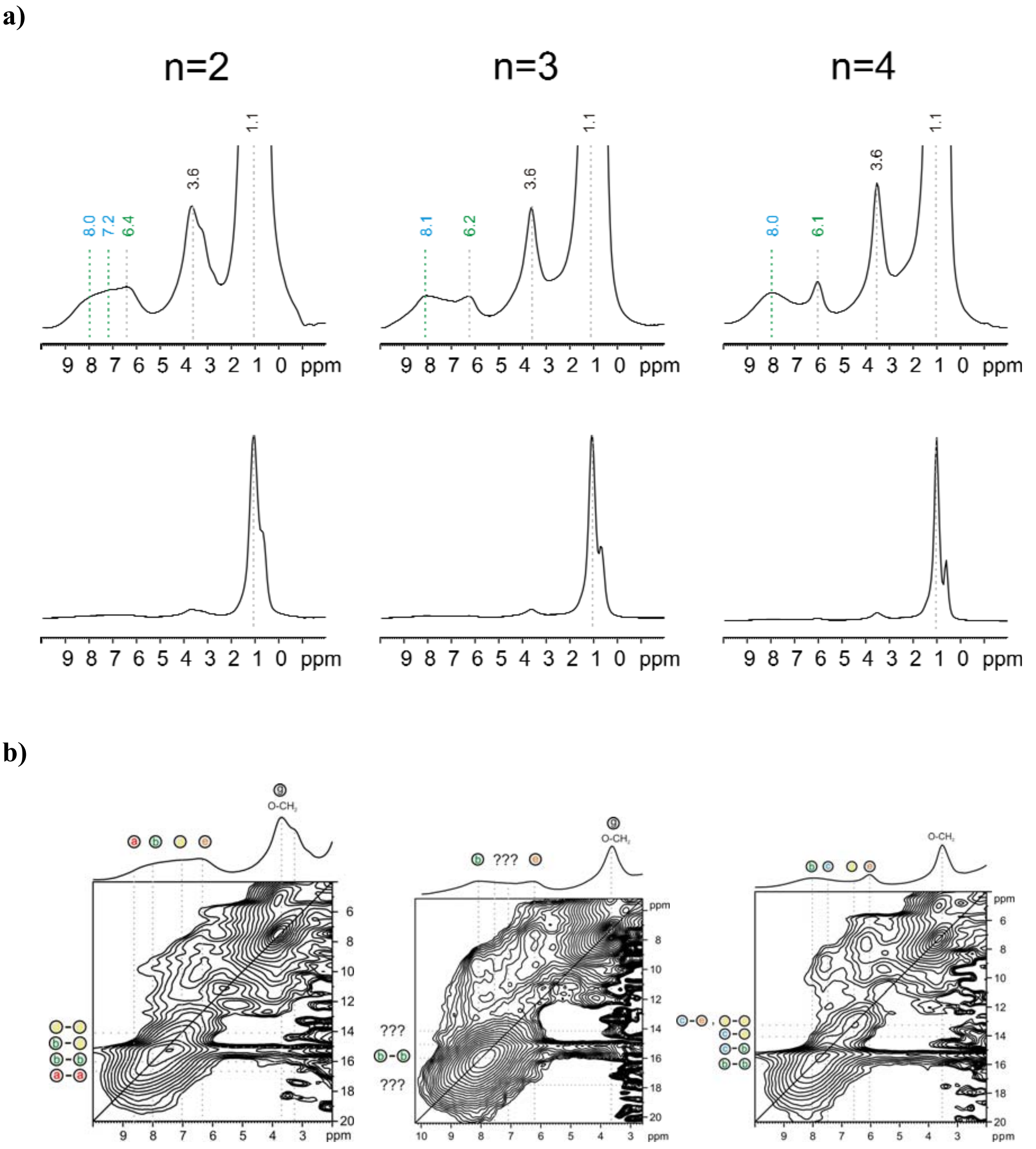

Figure 7.6: a) ^{1}H MAS single quantum spectra of perylene bisimide derivatives with a spacer length of n=2, n=3 and n=4. b) ^{1}H 2D DQ MAS NMR spectra of the same compounds. All spectra recorded at 30 kHz MAS frequency, at 850 MHz ^{1}H Larmor frequency and at 320K.

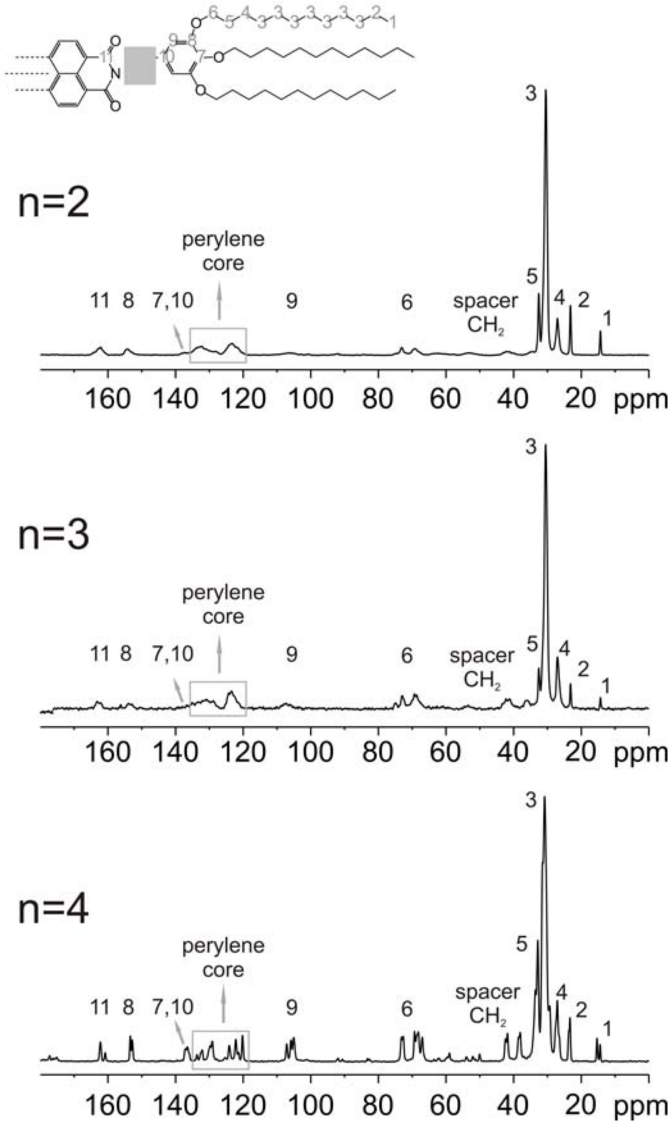

Figure 7.7: ^{13}C CPMAS NMR spectra of n=2, n=3, and n=4 perylene derivative. The spectra recorded at 176.05 MHz ^{13}C Larmor frequency, at 15 kHz MAS frequency, and at room temperature. The contact time for the CPMAS experiment was 1 ms. 15k scans were accumulated to get these spectra.

The two-dimensional ^{1}H-^{13}C Rept-HSQC correlation experiments are represented in Figure 7.8-7.10 for ***n=2-4*** materials. The resonances observed for n=2 and ***n=3*** are very similar in the perylene region, despite one fact. The ^{1}H-^{13}C spectrum for ***n=3*** perylene derivative could not obtained at 30 kHz MAS, which is the case for all of the other correlation experiments. However, the spectrum could be obtained at a higher MAS frequency, 50 kHz (with only 5 t_R recoupling period). This feature is representing the unique behavior of ***n=3*** material in terms of motional timescales, which led to destructive interference and complete signal loss at 30 kHz, nevertheless this interference was eliminated at a higher MAS rate. This behavior was observed only for the ***n=3*** PBI derivative.

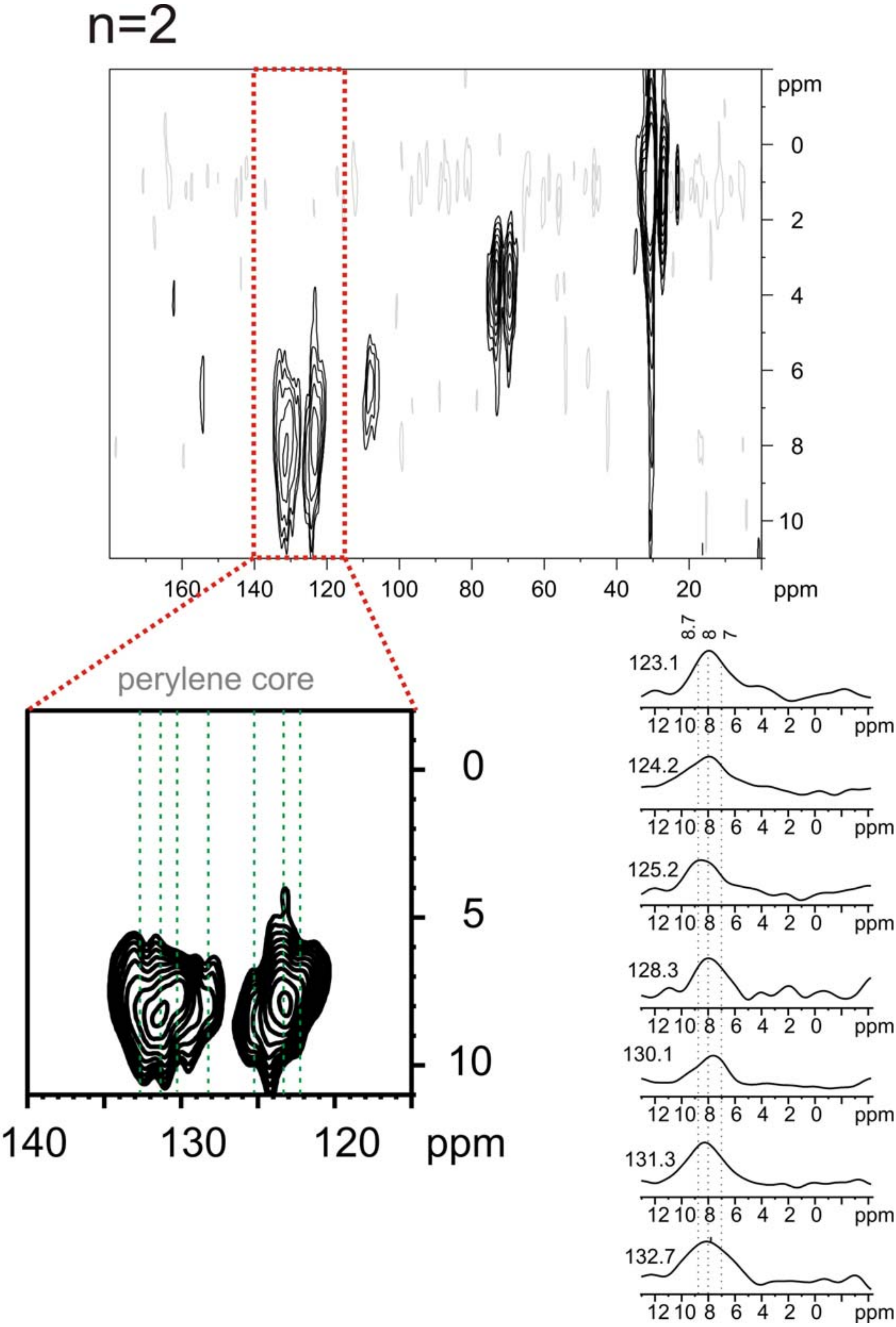

Figure 7.8: Rept-HSCQ spectrum of n=2 perylene derivatives. The spectra recorded at 850 ^{1}H Larmor frequency, 30 kHz MAS frequency, at 320K and with 2 t_R period of recoupling time.

When the ^{1}H-^{13}C correlation spectra are compared, it can be seen that the patterns obtained for ***n=2*** and ***n=3*** are similar, however the pattern obtained for ***n=4*** is different from those two and more similar to ***n=1*** derivative which has distinct ^{1}H-^{13}C correlations in the lower chemical shift region of perylene resonances. From these correlation patterns, the existence of different packing arrangements for different PBI derivatives is clear. A more complete understanding of the molecular arrangements and the observed chemical shifts will be more easily understood after the consideration of calculated ring-current effects.

7.4: Molecular Dynamics of Perylenebisimide Derivatives

In this section, insights about the dynamics of the PBI derivatives will be revealed by using advanced solid-state NMR techniques. First a comparison of ^{1}H MAS and DQF MAS will be presented, to visualize the mobile fractions of proton resonances. Then, the Rept 1D results will be represented which were recorded at different recoupling times, to increase the site selectivity by the use of carbon nucleus. Finally, variable temperature ^{1}H MAS and DQF-MAS results will be shown to follow the dynamical processes at elevated temperatures, after the phase transition temperatures for some materials.

7.4.1: Qualitative investigation of local molecular dynamics: Comparison of ^{1}H MAS and ^{1}H DQF MAS and 1D Rept Experiments

Following, one can see the results obtained with advanced NMR methods with the highest magnetic fields available in our laboratories with 700 MHz and 850 MHz proton Larmor frequencies. The variable temperature (315K-405K) ^{1}H MAS and ^{1}H DQF MAS NMR experiments recorded at the 700 MHz magnet. The 2D DQ MAS NMR experiments are recorded at 850 MHz magnet. 30 kHz magic angle spinning was applied to all experiments to elucidate sufficient resolution for specific structural information. The heating effect of fast MAS was considered according to previous study done in our group (Langer 99). The heating and cooling rate was set to 1°C/min and the samples were kept at the specific temperature around 30 minutes to ensure proper temperature equilibration.

In Figure 7.11 the comparison of ^{1}H MAS and DQF-MAS spectra are represented for all of the perylene derivatives. In all compounds, remarkable mobility exists for the aliphatic sidechains, which leads to a reduction of the aliphatic resonances (~1 ppm) after DQ-filtration. For the spacer-CH$_2$ and O-CH$_2$ resonances (~3.6 ppm), apart from the ***n=0*** compound which has a rigid spacer at room temperature, there exist some mobility which is again indicated by the intensity loss in that region. For the mobility of the outer phenyl, it can

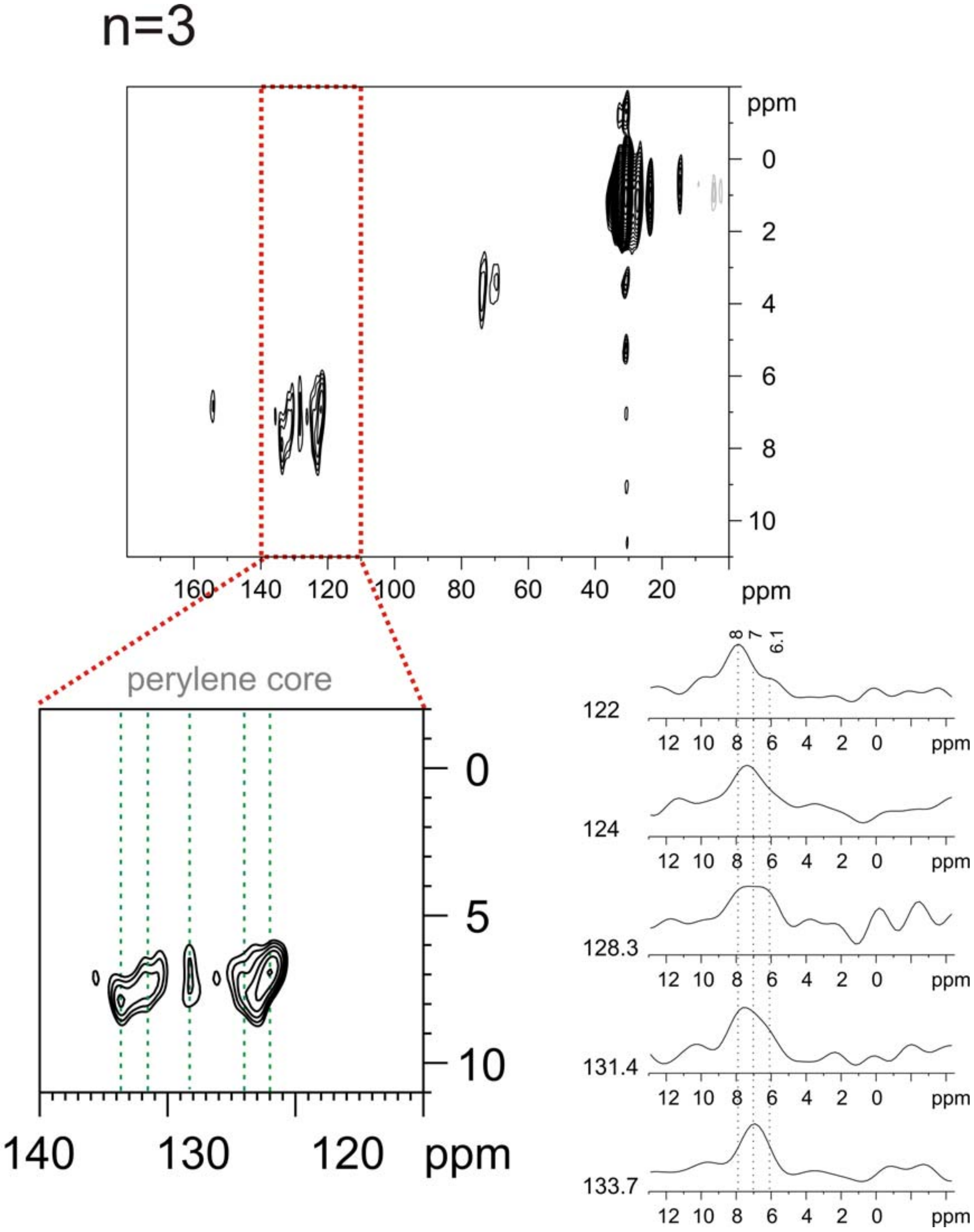

Figure 7.9: Rept-HSCQ spectrum of n=3 perylene derivatives. The spectra recorded at 850 ^{1}H Larmor frequency, 50 kHz MAS frequency, at 320K and with 5 t_R period of recoupling time.

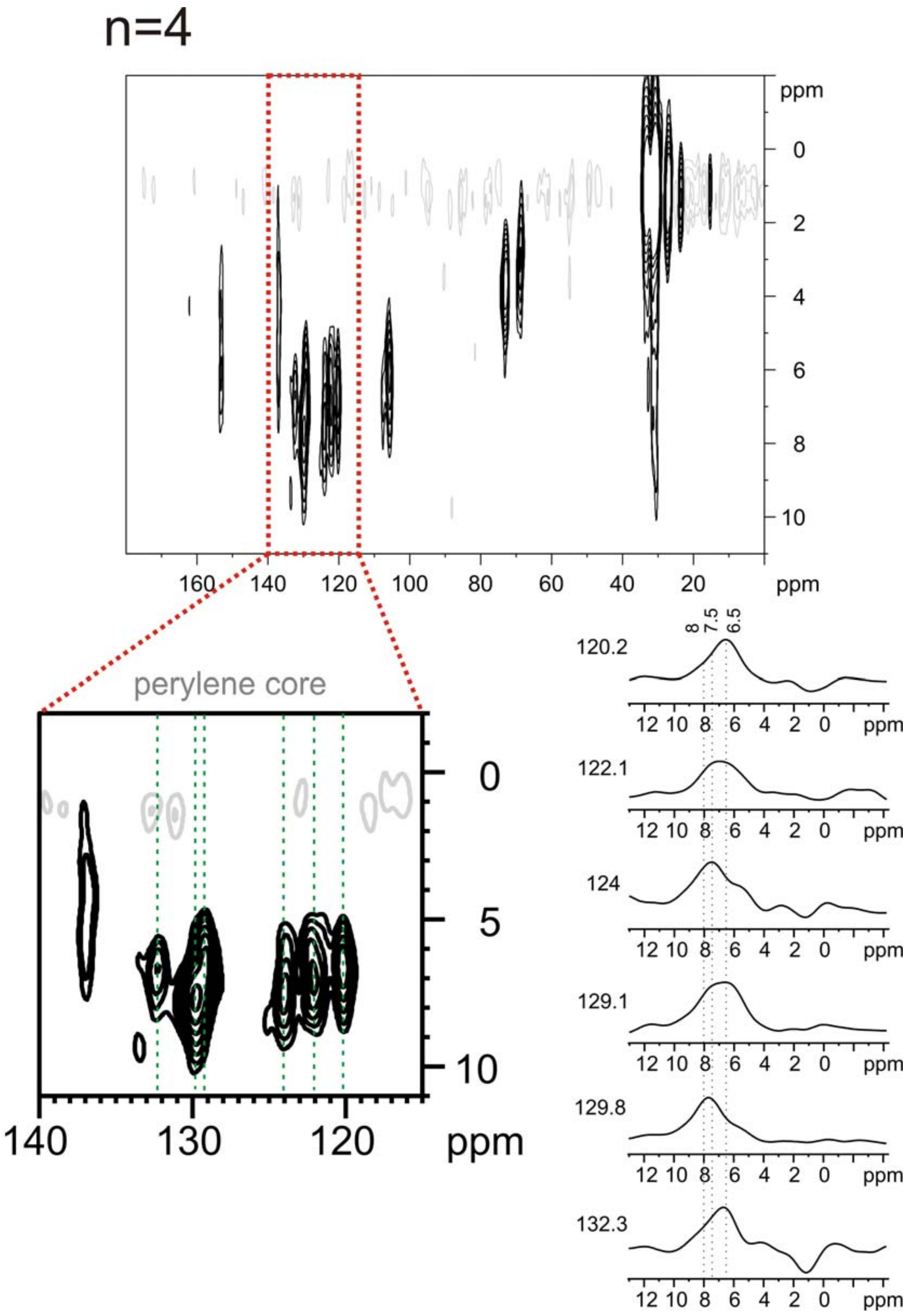

Figure 7.10: Rept-HSCQ spectrum of n=4 perylene derivatives. The spectra recorded at 850 ^{1}H Larmor frequency, 30 kHz MAS frequency, at 320K and with 2 t_R period of recoupling time.

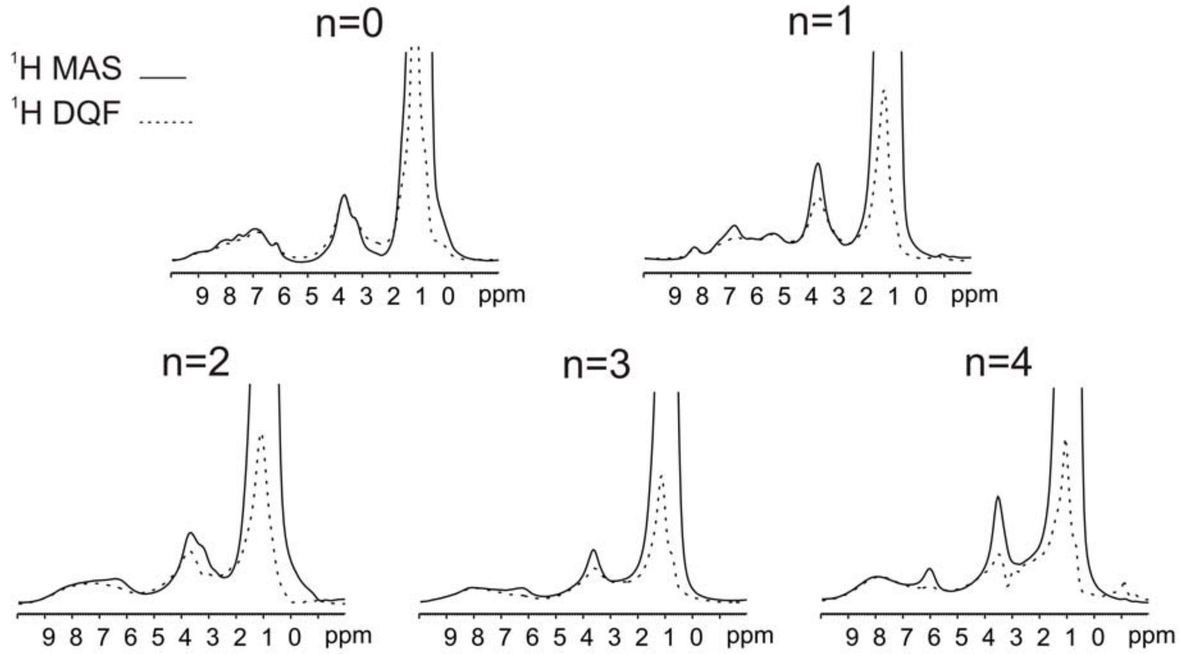

Figure 7.11: The comparison of ^{1}H MAS and DQF-MAS spectra for different perylene derivatives. The spectra are recorded at 320K and 30 kHz MAS.

be concluded that the ***n=0*** compound (which have very high phase-transition temperature) do not have significant mobility in ^{1}H spectrum, however, for ***n=1-4*** again an intensity loss is seen for the proton signal of the outer phenyl.

The ^{1}H-^{13}C heteronuclear dipolar couplings can be probed with improved site resolution due to the bigger spread of chemical shift using the Rept sequence. The one-dimensional Rept spectra are presented in Figure 7.12, recorded at different recoupling times. One remarkable observation is that the signal-to-noise ratio for the *n=3* compound is much worse compared to the other compounds. The resolution difference of *n=2* and *n=3* material was already observed before with ^{13}C CPMAS spectra represented in Figure 7.3 and 7.7. With a different timescale of the Rept experiment, additionally the difference in the motional timescale of *n=3* perylene derivative is determined which result in a very poor signal intensity. It should be noted here that the Rept signal for *n=3* is particularly poor for perylene core resonances at 30 kHz, however it reappears at 50 kHz MAS (Figure 7.9).

7.4.2: Mobility changes due to the elevation of temperature: ^{1}H VT MAS and DQF-MAS NMR

For the low-T_g samples, temperatures far above the phase transition temperatures can be reached by the instrumentations available in our laboratory. For the high-T_g materials,

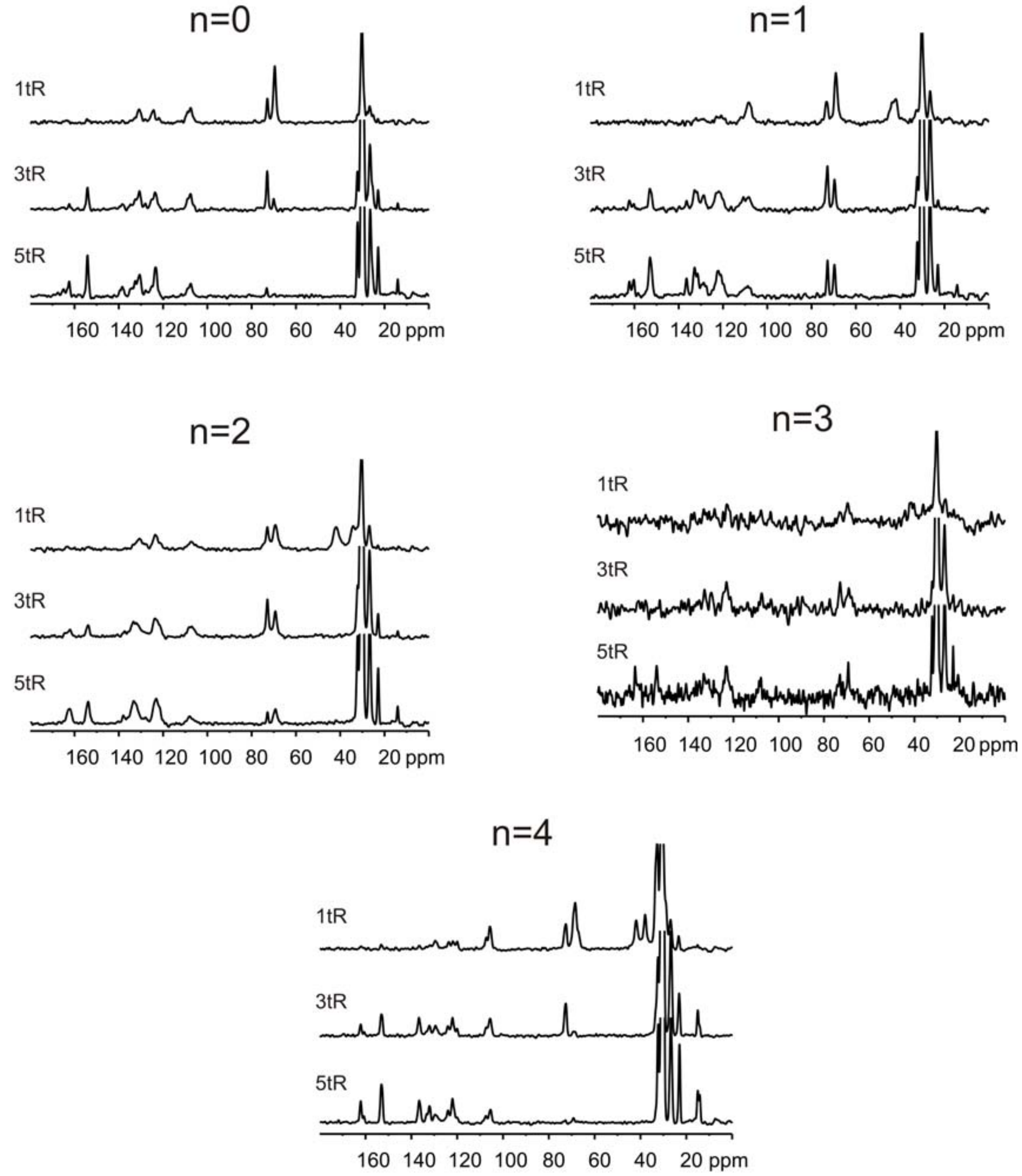

Figure 7.12: The 1D Rept spectra with different recoupling periods, recorded at 320K and 30 kHz MAS for different perylene derivatives.

however, the phase transition temperatures are far above the instrumental limit. Nevertheless even for the high-T_g materials, some changes in lineshapes are observed. The variable temperature ^{1}H MAS spectra of all of the perylene derivatives are shown in Figure 7.13. The liquid state chemical shift values of the outer phenyl and the perylene core protons are indicated by grey dashed-lines in the figure. The black solid-lines represent the final chemical shift values of the outer phenyl and perylene core aromatic protons.

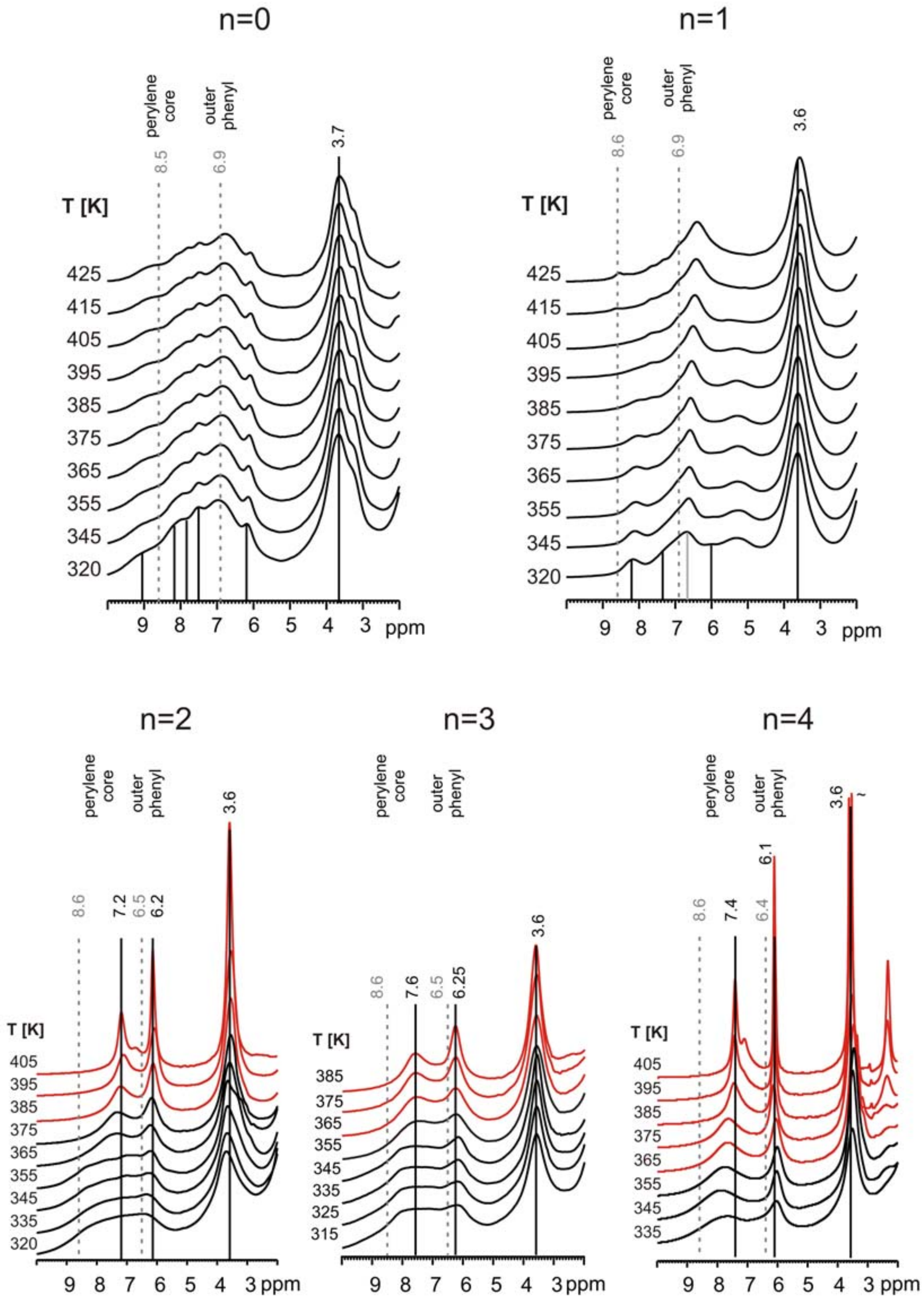

Figure 7.13: Variable temperature ^{1}H MAS spectra of all of the perylene derivatives. The spectra were recorded at 30 kHz MAS. The spectra recorded after the phase transitions are represented as red colors.

For the ***n=0*** material, the ^{1}H lineshapes for the spacer, O-CH$_2$, and aromatic regions basically remained unchanged even at the highest temperature, 425 K. For ***n=1***, however, some changes for the aromatic proton resonances are observed, meaning that some changes occur upon heating of the sample. The very broad resonance observed at the aromatic region represents many different aromatic proton sites available due to the different influence of ring-currents. They basically remain unchanged even at the highest temperatures. More interestingly, for the low phase-transition materials, ***n=2-4*** much more pronounced changes were observed upon heating. This might result from the fact that the temperatures above the phase transition are also covered in the temperature range. The spectra above the phase transition temperatures are presented in red color. In all cases, a very broad aromatic resonance covering more than 2 ppm range, especially for ***n=2***, narrow above the phase transition temperatures and two relatively sharp resonances are observed at high temperatures. The chemical shift values of these two resonances, at the perylene core and outer phenyl protons, are marked with back solid lines for clarity.

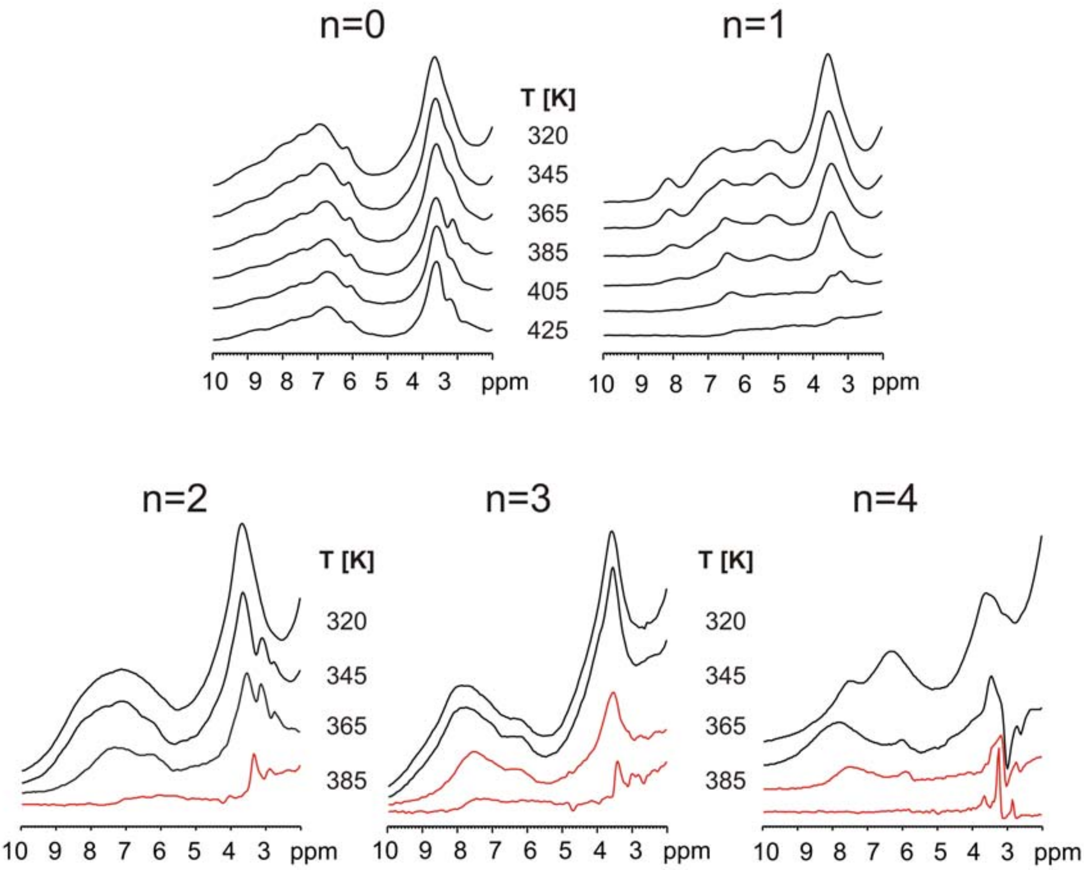

Figure 7.14: Variable temperature ^{1}H DQF-MAS spectra of the perylene derivatives. The spectra were recorded at 30 kHz MAS and with 1t_R of BaBa recoupling period.

It should be noted that the averaged sharp resonances do not appear at the chemical shift values of liquid-state NMR. The protons of outer phenyl are appearing very close to liquid-state values, but, the proton resonances of perylene core are appearing at ~1-1.5 ppm high-field shifted compared to liquid-state values. This clearly shows that even in the very mobile phase above the phase transition, the packing effect for perylene core protons is still present. The origin of this observation will be explained basically by the maintenance of the packing arrangement by still allowing escape of individual perylene molecules (temporarily forming trimer structures with 180° flip motion along the long axes of the perylene molecule) without destructing the overall packed structure, see below.

Finally, the variable temperature ^{1}H DQF-MAS results are represented in parallel to the variable temperature ^{1}H MAS results, to visualize the mobility increase upon heating at specific resonances (Figure 7.14). Only for the ***n=0*** compound, there is nearly no changes in the signal intensity upon heating the sample. For ***n=1*** material and especially for ***n=2-4*** materials, at high temperatures significant decrease in signal intensity is observed especially above the phase transition temperatures. These demonstrations clearly state once again the increased mobility at elevated temperatures for specific perylene derivatives.

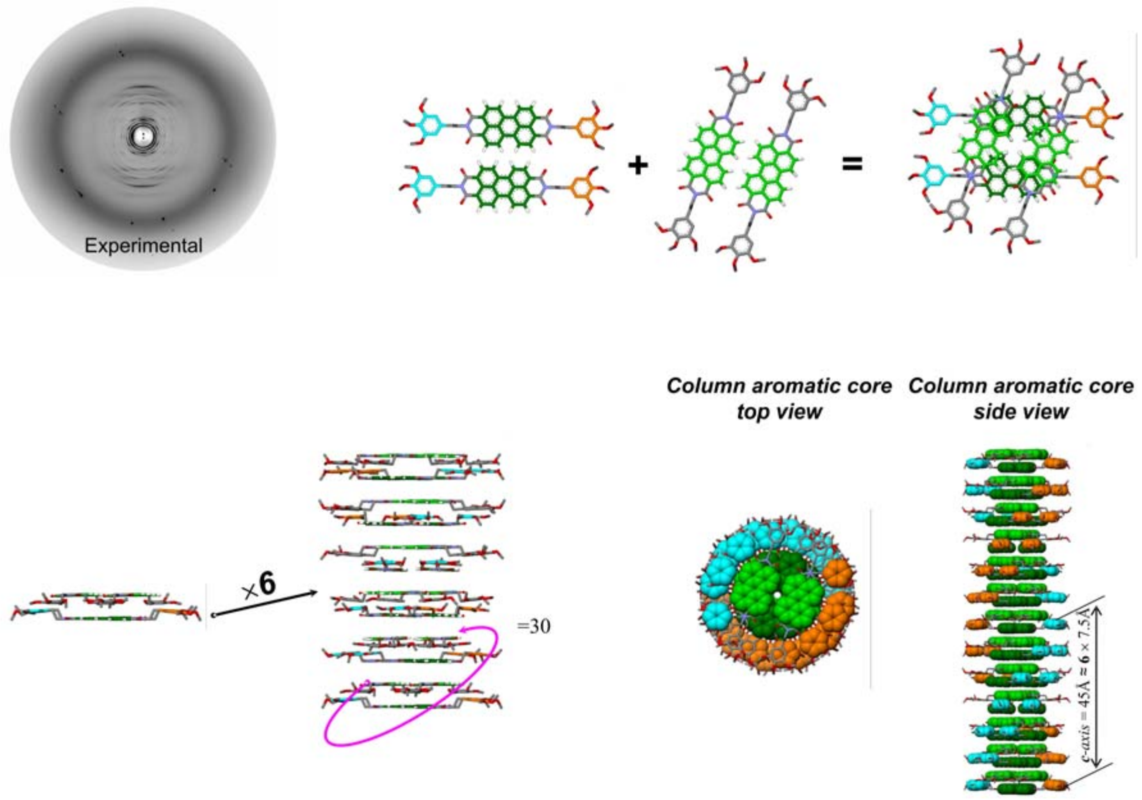

Figure 7.15: X-Ray structure of the n=2 PBI derivative, the x-ray pattern was recorded at room-temperature (Obtained from Ungar et. al.).

7.5: Structure of Packing: Revealed by combination of NMR Results with Quantum Chemical Calculations, and X-Ray Results

In this section, the structure proposed by X-Ray results will be presented with additional Car-Parinello molecular dynamics (CPMD) calculations of this structure (Hutter 95). Chemical shift values obtained from quantum chemical calculations will be compared with the experimental values and the validity of the proposed structure will be analyzed. Moreover, nucleus-independent chemical shift (NICS) maps will be presented to visualize the ring-current effects for various sites of perylene derivatives (Schleyer 96, Sebastiani 05).

7.5.1 Proposed X-Ray Structures for n=2 (EM266) PBI derivative:

From the X-Ray results, represented in Figure 7.15, it can be understood that *n=2* PBI derivative is forming tetramer structures at room temperature and these tetramer structures are arranged to a three-dimensional helical columnar structure, as represented in the figure.

This structure was used in the CPMD calculations (obtained from Sekheran), which will be represented in the following section. The combination of the structural information from x-ray and molecular dynamics simulations based on this structure will help us to elucidate the assignment of the observed chemical shifts, as well as the dynamics observed in the system.

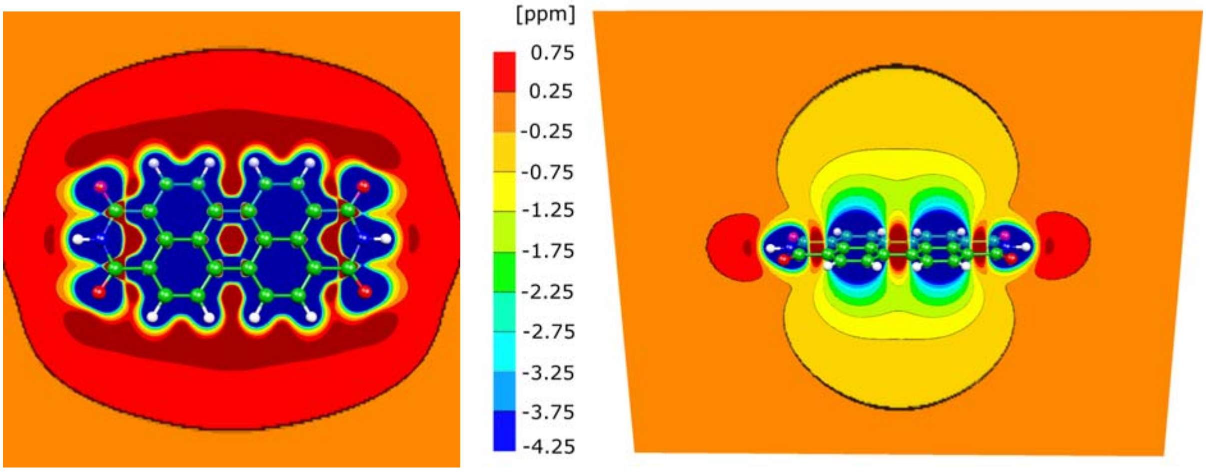

Figure 7.16: Nucleus-independent chemical shift maps of the perylene molecule without the spacer and outer phenyl (Sebastiani 08).

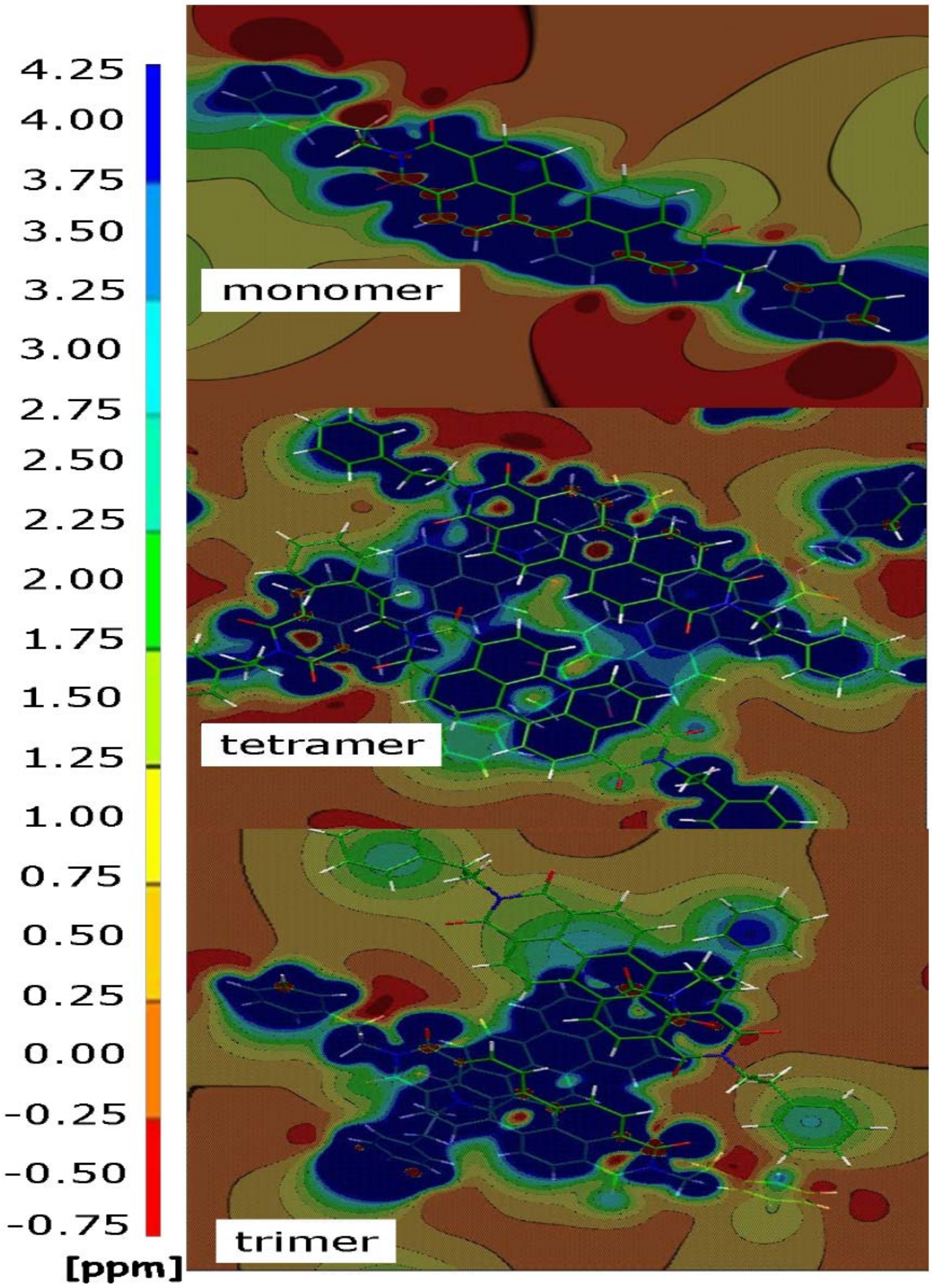

Figure 7.17: Nucleus independent chemical shift maps of n=2 perylene derivative in its monomer, trimer, and tetramer conformations. Red color represents Upfield-shifts, blue-green-yellow represent Downfield-shifts.

7.5.2 NICS Maps:

By additionally performing the nucleus-independent chemical shift maps calculations, which are much easier compared to the CPMD calculations, one can obtain additional information on the insights of the packing easily. In Figure 7.16, the results of NICS maps are represented, with a color code next to them to visualize the effect of chemical shift changes at different positions in space around perylene molecule. On the left side of the figure a view from top of the molecule is shown and on the right side of the figure a view from the side of the molecule is shown.

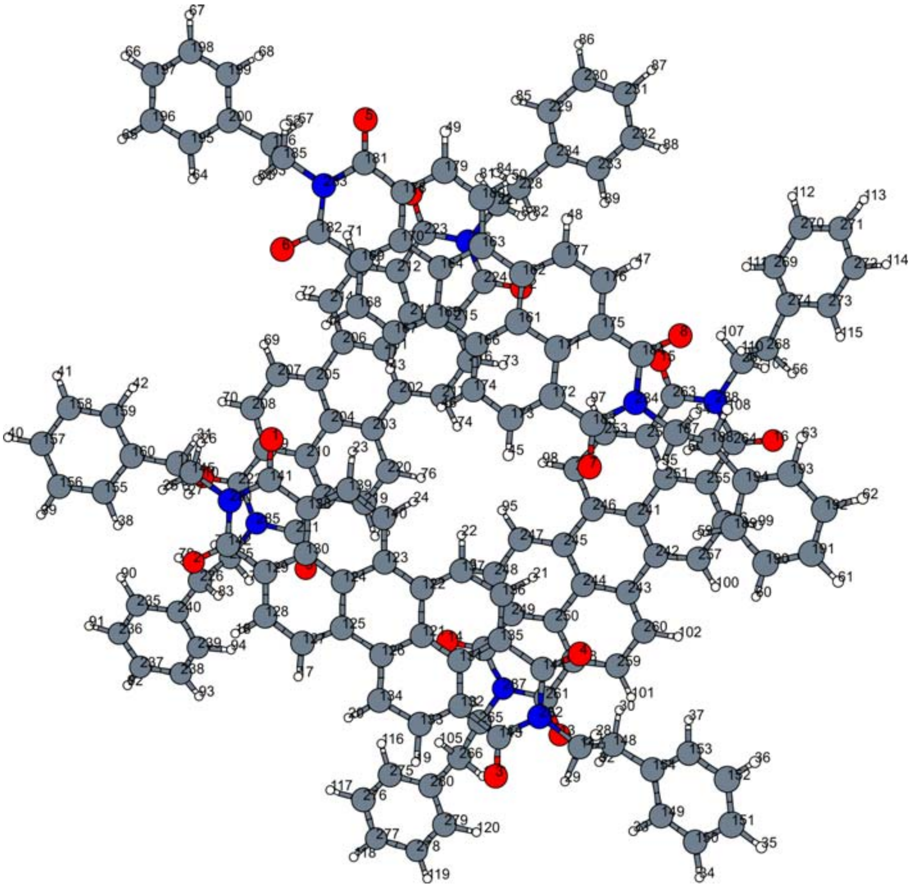

Figure 7.18: Structure of the perylene tetramer structure obtained from X-ray studies (Obtained from Sekharan 08).

The red color represents the areas in space (bay positions of the perylene core) in which the chemical shift value of an approaching atom increases. And the yellow to orange colors represents the areas in where the approaching atom's chemical shift value decrease (up and down of the perylene surface). So, it is clear that if two perylene molecules are located next to each other then the chemical shifts of the protons at the bay positions between two molecules move to higher chemical shifts. And if the two perylene molecules are located on top of each other, then the chemical shifts of the protons of each perylene derivative mostly move to lower chemical shifts due to the ring-current effects of the upper/below PBI molecule. In Figure 7.17, the NICS maps of the PBIs are represented for monomer, trimer and tetramer configurations.

7.5.3 CPMD Calculation:

In order to get a better insight in the molecular dynamics of the systems and to understand the line narrowing at elevated temperatures (are represented in section 7.4), molecular dynamics simulations of the *n=2* material (EM266) were performed based on the proposed X-ray structure (Unger 08). The tetramer arrangement (shown in Figure 7.15 and 7.18) obtained from the X-ray provided the starting point for CPMD computations (Shekharan 08). The resulting electron structures were analyzed in terms of NMR chemical shift values.

The values of the calculated chemical shift values for the Monomer structure of ***n=2***

	Spread	**Average δ**	**Standard Dev.**
Outer	0.24 ppm	7.42	0.09
Inner	0.31 ppm	7.16	0.11

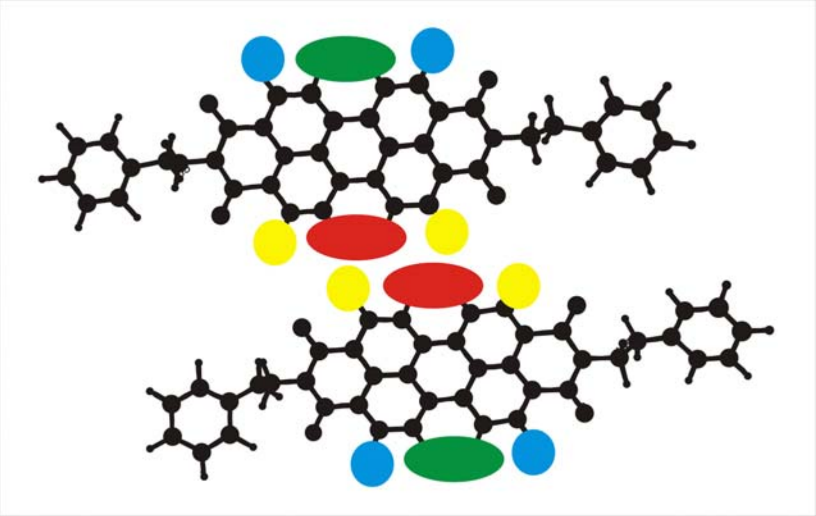

Figure 7.19: Nomenclature of the specific sites of the interacting perylene which are used throughout the text: **Blue**; outer-periphery (OP), **Green**; inner-periphery (IP), **Yellow**; outer-core (OC), **Red**; inner-core (IC).

For the calculated chemical shift values for the Tetramer structure of *n=2* (Figure 7.20, up):

	Spread	**Average δ**	**Standard Dev.**
Outer Periphery	1.3 ppm	6.18	0.42
Inner Periphery	1.06 ppm	6.20	0.33
Outer Core	0.86 ppm	4.42	0.30
Inner Core	0.9 ppm	4.48	0.31

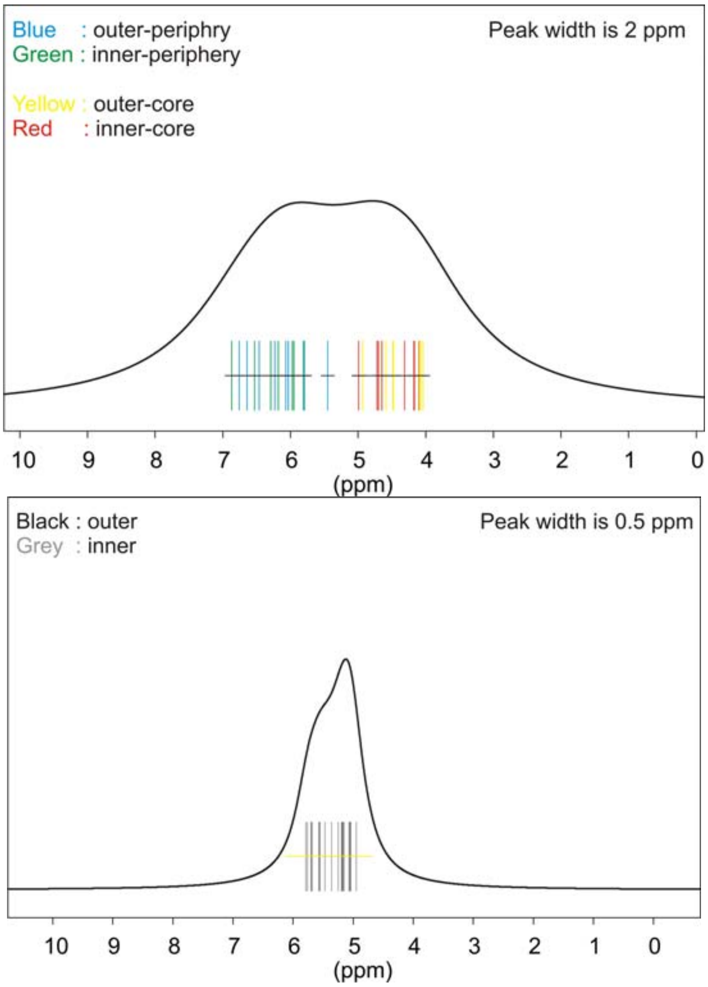

Figure 7.20: Schematic representation of the calculated chemical shift values for the perylene molecule with two –CH_2 spacer groups, n=2. **Up:** The chemical shift values of a perylene molecule in a tetramer with 2 ppm line broadening. **Down:** The chemical shift values of the perylene core in a tetramer with 0.5 ppm line broadening (taking the higher local mobility at elevated temperature into account), where the perylene core is undergoing a 180° flip motions around the long axes of the molecule.

For the averaged chemical shift values for the same **Tetramer** (**Figure 7.14, down**):

	Spread	**Average δ**	**Standard Dev.**
Outer	0.65 ppm	5.30	0.26
Inner	0.84 ppm	5.34	0.30

And for the averaged chemical shift values for the same **Trimer** (**Figure 7.14, down**):

	Spread	**Average δ**	**Standard Dev.**
Outer	5.41 ppm	5.49	1.76
Inner	4.58 ppm	5.12	1.52

The computation of the chemical shifts shows that the packing in the columns makes the protons in the core and at the periphery of the columns inequivalent. The calculated spread of chemical shifts agrees with the experimentally observed. To adjust the absolute values of the calculated chemical shifts some rescaling is still needed, nevertheless, the general trend of the chemical shift values can be recognized. For the regular perylene tetramer structure, after convoluting the calculated chemical shifts with a line width, we could obtain a similar pattern as observed in the ^{1}H MAS spectrum of n=2 material (EM266). The protons between two perylene molecules (‘core protons’) are shifted to lower ppm values, compared to those of the periphery of the tetramer. It should be noted, that an in plane motion of the individual molecules may lead to an exchange between chemical shifts of inner- and outer-protons but not between chemical shift of core- and periphery protons. This type of exchange, however, is needed to explain the motional narrowing to a single peak of the ^{1}H MAS spectra at elevated temperatures (see Figure 7.13, ^{1}H VT).

The averaging between core and periphery positions of molecules requires a 180^o flip motion around the long axes of the PBI molecule, which will be difficult to be accomplished in the column. Therefore, we propose that the individual molecules can escape from the tetramer structure in the column, leave the center of the column and return to it with an arbitrary orientation. A similar type of motion has been observed in other columnar perylene systems by ^{2}H NMR, (see Spiess 04, Fig. 3), which is reproduced here below for convenience.

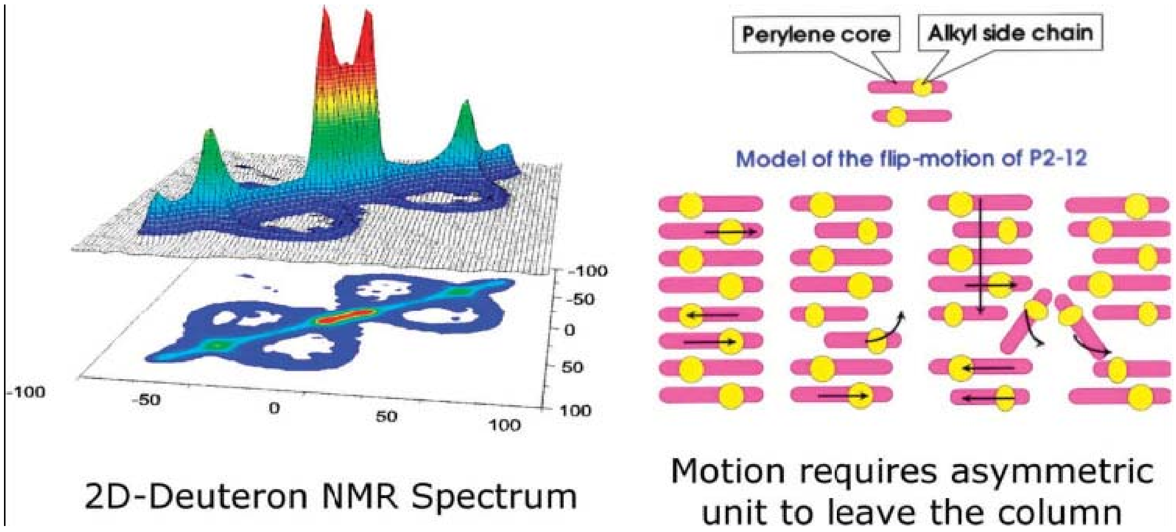

Figure 7.21: Schematic representation of the motion of perylene system which was studied previously by ^{2}H NMR (Adopted from Spiess 04). The going-out and returning-back into the column motion of perylene is illustrated.

In order to probe this model, additional simulations have been performed with defects in the tetramer structure (the values of the chemical shift values are given above). Remarkably, the structure is able to stabilize itself, even if one perylene molecule is missing in every tetramer arrangement. This surprising stability of the defect tetramer structure (trimer structure, partially shown in Figure 7.17) show that an exchange between individual molecules and the environment between the columns is feasible in the tetrameric columnar architecture and indicates the capability of this system to self-reorganize without loosing the overall molecular organization. Obviously, such a process will be able to avoid long-lived defects by self-healing.

7.6: Conclusions

In this chapter the structure and dynamics of perylenebisimide derivatives have been studied by using ^{1}H-^{1}H and ^{1}H-^{13}C recoupling experiments under fast MAS. The work has been done without isotopic labeling at natural abundance of the nuclei studied. The present work particularly focuses on how the molecular packing and structure changes by changing the molecular structure of the perylene derivatives in a way that the spacer length between the outer phenyl and perylene core is altered. By doing so, substantial changes occurred in the NMR spectra of that particular material. With the help of the X-Ray studies and quantum chemical calculations, the packing in the studied materials (spacer length; n=2) were revealed by NMR and found that a structure formed from four PBI units is established (tetramer structure) in the solid state of the material.

The PBI materials with high-T_g (n=0, 1) has more featured pattern in the ^{1}H NMR spectrum compared to the low-T_g materials (n=2-4). This can be explained with the different magnitude of packing effects felt by the materials. Less shielding and de-shielding effects are observed for low-T_g materials. From the 2D ^{1}H DQ spectra it is clear that the n=1 PBI is even more unique in terms of its packing behavior which represented well resolved resonances. The low-T_g materials represent mostly broad less featured resonances for the aromatic region. Especially the n=3 material, which showed the highest electron mobility, has interestingly the least resolved resonances at room temperature.

The outer phenyl ring in PBI materials is relatively mobile and shows signal loss with DQF, expect for the n=0 PBI which has a rigid outer phenyl in the timescale of the performed NMR experiment. All of the materials have considerable mobility at the aliphatic side groups starting from ambient temperatures. The perylene core region of the PBIs shows no mobility at room temperature.

With increasing temperature, increased mobility was observed for the studied PBIs. For n=0 and 1, not too much change was observed due to their high phase transition temperatures. However, for n= 2-4, remarkable effects were observed, manifesting themselves as line narrowing. For these later materials, the very broad width (~2 ppm) at room temperature ^{1}H NMR spectra reduced to ~0.5 ppm width by still appearing at a chemical shift value much lower compared to the liquid state chemical shift value. This is showing the conserved packing effects at elevated temperatures, despite the increased mobility in those systems. So, at elevated temperatures, due to the mobility increase, the materials have more degrees of freedom to move and they perform a dynamical process in such a way that, one particular PBI is released from the tetramer structure, go out, turn 180^o and come back to its original place. This observation was further proved by the quantum chemical calculations as stated before. This kind of situation, as stated before, was observed in slightly different perylene molecules studied by ^{2}H NMR (Spiess 2004).

In conclusion, this study represents that valuable structural and dynamics information can be extracted from the supramolecular systems by the use of advanced solid-state NMR techniques. NMR approach has indispensable importance to have deeper understanding on the self-assembly process of supramolecular systems. It was also clear that by changing the spacer length in the PBI derivatives, dramatic changes are observed in the molecular ordering.

Chapter 8:
Conclusions

The aim of this work is to understand the structure, supramolecular order, and molecular dynamics of various functional macromolecular materials. The studied materials can be divided into two main sub-groups: proton conducting polymers and photo-reactive perylene derivatives. Advanced solid-state NMR techniques combined with fast-magic-angle spinning provide sufficient spectral resolution so that important information about molecular dynamics encoded in the dipolar-couplings was obtained. The applied NMR methods proved to be powerful and convenient to use since they do not rely on isotropic labeling.

Structural investigations were performed by the use of ^{1}H, ^{13}C and ^{31}P cross-polarization, and ^{1}H-^{1}H and ^{1}H-^{13}C and correlation solid state NMR spectroscopy. The information obtained from these experiments has been used to understand the structural details of the investigated materials. Dynamics studies were performed applying ^{1}H DQ and ^{2}H NMR methods in a variable-temperature manner. The ^{1}H NMR measurements have been preformed under fast magic angle conditions to achieve sufficient resolution. The applied ^{1}H NMR methods include simple ^{1}H MAS spectroscopy as well as ^{1}H-^{1}H DQF methods and two dimensional ^{1}H DQ spectroscopy. Different types and timescales of molecular motions have been identified. Especially for the proton conducting polymers, the local mobility of the acidic protons is determined and compared to the macroscopic conductivity behavior of those materials. The dynamic behavior of the systems has been investigated on some of the selectively deuterated samples using ^{2}H NMR techniques under static and MAS conditions.

The study of the proton conducting polymers provides detailed information on the structural and dynamic factors governing the proton conduction and the hydrogen-bonding. An investigation on the types of proton conducting mechanisms which are active in the systems was gained, as well as the existing types of hydrogen-bonding pairs and the effects of the local structures (e.g. hydrogen-bonding) and dynamics (e.g. local proton mobility). A correlation of the microscopic proton mobility to the macroscopic conductivities obtained by impedance spectroscopy has been made.

In chapter 3, a triazole functional polysiloxane polymer was investigated. The organization of the polymers in the solid state was determined and interpreted in the light of the present strong hydrogen-bonding. The absence of hydrogen-bonded –NH dimers has been proven, which is the case in pure PAA. All molecular sites of the system were affected from temperature increase and became more mobile at high temperatures. More surprisingly, the acidic NH proton was experiencing molecular exchange with different timescales at different temperature ranges, and all of the slow, intermediate and fast exchange regimes were observed. A motion in the kHz range is observed in the fast exchange regime (301-373 K) for the acidic NH proton. Fast ring-flipping process is proved while NH proton is attached to the ring, whereas the breaking of NH hydrogen-bonds is in the same orders of magnitude as the ring-flipping. Only the latter process is responsible for proton conduction in Triazole material. The similar activation energy values obtained from different methods for the acidic NH proton motion indicate that there is no phase separation in the triazole material which would give different activation energies at the macroscopic (E_a value obtained from impedance spectroscopy) and microscopic level (E_a value obtained from NMR) (as reported previously, Goward 02).

In chapter 4 and 5, acid-base polymer complexes were investigated. Different acidic –OH resonances were detected and related to different hydrogen-bonded and free –OH protons in PAA-P4VP and PVPA-ABPBI systems. An insight on the effect of the acid-base complexation on the structure and dynamics was gained. With the addition of the basic polymer (P4VP) new types of hydrogen-bonding was obtained in both systems. It was found that the complexation has a stabilization effect on the hydrogen bonding, and a more ordered hydrogen-bonding network is formed with the addition of basic polymers to the acidic ones. Especially with a 1:1 mixing ratio, in which complete pairing is achieved between the two components of the materials, a more resolved low-field lineshape is observed in the ^{1}H MAS NMR spectra. Mixing at the molecular level in the acid-base polymer systems was also proven. The conductivity values of the acid-base polymer complexes do not allow immediate application purposes, however finding better acid-base pairs is a key to solve this problem.

In chapter 6, copolymers of triazole and vinyl phosphonic acid as proton conducting polymer was presented. It was found that the condensation of the phosphonic acid units being a severe problem in the pure poly(vinyl phosphonic acid) system could not be completely prevented by the introduction of the triazole as a copolymer. The presence of two different types of hydrogen-bonding arrangements, O-H···O and O-H···N, was proved using double-quantum ^{1}H MAS NMR spectroscopy. At elevated temperature (410 K) highly mobile acidic protons are only present in O-H···O arrangement resulting in a single resonance with an average chemical shift of 11.5 ppm. Finally, increased mobility in the polymer backbone was observed opposed to the PVPA homopolymer. This suggests that the triazole containing copolymers provide defect sites facilitating proton conduction.

The second type of investigated functional supramolecular materials is a photoconducting perylenebisimide derivative. A detailed knowledge about their supramolecular structure and molecular dynamics is crucial for understanding their electronic properties. Details on the properties of these materials were given in chapter 7. A change in the spacer length of the PBI materials introduced significant changes in the ^{1}H MAS NMR spectra, which is a sign of different packing arrangements in those materials. The PBI derivatives with high-T_g (n=0, 1) have more featured pattern in the ^{1}H NMR spectrum compared to the low-T_g materials (n=2-4). Less shielding and de-shielding effects are observed for low-T_g materials. n=1 PBI is even more unique in terms of its packing behavior which leads to well resolved resonances. The low-T_g materials exhibit mostly broad and less featured resonances for the aromatic region. This is particularly true for the n=3 material, which has the highest electron mobility and the least resolved resonances at ambient conditions. Outer phenyl, spacer groups and the perylene core have different dynamic behaviors for different PBI derivatives. These sites also show mobility increase as a function of temperature.

At elevated temperatures, due to the mobility increase, the PBI materials have more motional degrees of freedom. A dynamical process where one particular PBI molecule is released from the tetramer structure, goes out, performs a 180° jump and comes back to its original place is proposed. This has been further confirmed by quantum chemical calculations. Similar observation has been previously reported for slightly different perylene molecule studied by ^{2}H NMR (Spiess 2004).

The results obtained in this work supply a deeper understanding of the supramolecular materials, in particular for proton-conductors and photo-active packed aromatic systems. Important structural and dynamics properties induced by hydrogen-bonding and π- π interactions were determined. The results also show that solid-state NMR is a powerful tool for the investigation of similar supramolecular functional materials to understand the structure-property relationship, especially when it is combined with other characterization techniques and quantum chemical calculations.

Bibliography

[Abragam 61] A. Abragam. The Principles of Nuclear Magnetism. Oxford Univ. Press, Oxford (1961).

[Abramowitz 72] M. Abramowitz, I. A. Stegun. Handbook of Mathematical Functions. Dover Publications, Inc., New York (1972).

[Adam 94] D. Adam, P. Schuhmacher, J. Simmerer, L. Häussling, K. Siemensmeyer, K. H. Etzbach, H. Ringsdorf, D. Haarer. Fast Photoconduction in the Highly Ordered Columnar Phase of a Discotic Liquid-Crystal. Nature 371, 141-143 (1994).

[Akbey 08] U. Akbey, R. Graf, P. P. Chu, H. W. Spiess, Submitted to J. Poly. Sci. B.

[Andrew 58] E. R. Andrew, A. Bradbury, R. G. Eades. Nuclear Magnetic Resonance Spectra from a Crystal Rotated at High Speed. Nature 182, 1659 (1958).

[Antonucci 99] Antonucci, P. L.; Arico, A. S.; Creti, P.; Ramunni, E.; Antonucci, V. Investigation of a direct methanol fuel cell based on a composite Nafion (R)-silica electrolyte for high temperature operation. Solid State Ionics 125, 431-437 (1999).

[Antzutkin 94] O.N. Antzutkin, Z. Song, X. Feng, M.H. Levitt. Suppression of Sideband in Magic-Angle-Spinning NMR –General Principles and Analytical Solutions. J. Chem. Phys. 100-1, 130-140. (1994).

[Antzutkin 99] O. N. Antzutkin, Sideband manipulation in magic-angle-spinning nuclear magnetic resonance. Progress in Nuclear Magnetic Resonance Spectroscopy. 35, 203–266, (1999).

[Apple 96] A. Appleby, J. Philos. Trans. R. Soc. London 354, 1681 (1996).

[Bak 00]	M. Bak, J. T. Rasmussen, N. C. Nielsen. SIMPSON: A General Simulation Program for Solid-State NMR Spectroscopy. J. Magn. Res.. 147, 296–330 (2000).
[Baohui 07]	L. Baohui, L. Xu, Q. Wu, T. Chen, P. Sun, Q. Jin, D. Ding, X. Wang, G. Xue, A. C. Shi. Various Types of Hydrogen Bonds, Their Temperature Dependence and Water-Polymer Interaction in Hydrated Poly(Acrylic Acid) as Revealed by ^{1}H Solid-State NMR Spectroscopy. Macromolecules 40, 5776-5786 (2007).
[Becker 96]	Becker, E. D. Encyclopedia of Nuclear Magnetic Resonance; Wiley: Chichester, Vol:4, 2409 (1996).
[Becker 96b]	Becker, E. D.; Hydrogen bonding, Wiley, Chichester, Ch. 4, 2409–2415 (1996).
[Benedict 98]	H. Benedict, H. H. Limbach, M. Wehlan, W. P. Fehlhammer, N. S. Golubev, R. Janoschek. Solid State ^{15}N NMR and Theoretical Studies of Primary and Secondary Geometric H/D Isotope Effects on Low-Barrier NHN-Hydrogen Bonds. J. Am. Chem. Soc. 120, 2939-2950 (1998).
[Bennett 95]	A. E. Bennett, C. M. Rienstra, M. Auger, K. V. Lakshmi, R. G. Griffin. Heteronuclear Decoupling in Rotating Solids. J. Chem. Phys. 103, 6951–6958 (1995).
[Berglund 80]	B. Berglund, R. W. Vaughan. Correlations between Proton Chemical Shift Tensors, Deuterium Quadrupole Couplings, and Bond Distances for Hydrogen Bonds in Solids. J. Chem. Phys. 73, 2037–2043 (1980).
[Bingol 06]	B. Bingol, W. H. Meyer, M. Wagner, G. Wegner. Synthesis, microstructure, and acidity of poly (vinylphosphonic acid). Macromol. Rapid Commun. 27, 1719- 1724 (2006).
[Bloch 46]	F. Bloch. Nuclear Induction. Phys. Rev. 70, 460–474 (1946).
[Bloembergen 53]	N. Bloembergen, T. J. Rowland. On the Nuclear Magnetic Resonance in Metals and Alloys. Acta Metall. 1, 731–746 (1953).
[Blumich 90]	B. Blumich, A. Hagemeyer, D. Schaefer, K. Schmidt-Rohr, H.W. Spiess. Solid State NMR Spectroscopy in Polymer Science. Adv. Mat. 2, 72–81 (1990).
[Bodenhausen 79]	G. Bodenhausen. Multiple-Quantum NMR, Progress in Nuclear Magnetic Resonance Spectroscopy 14, 137-173, (1980).

[Bodenhausen 81] G. Bodenhausen. Simple Digital Phase-Shifter for Multiple-Quantum NMR. J. Mag. Reson. 34, 357-360, (1979).

[Bozkurt 03] A. Bozkurt, W. H. Meyer, J. Gutmann, G. Wegner. Proton conducting copolymers on the basis of vinylphosphonic acid and 4-vinylimidazole. Solid State Ionics 164, 169-176 (2003).

[Brinkmann 00] A. Brinkmann, M. Eden, M. H. Levitt. Synchronous Helical Pulse Sequences in Magic-angle Spinning Nuclear Magnetic Resonance. J. Chem. Phys. 112, 8539–8554 (2000).

[Brown 99] S. Brown, I. Schnell, J. Brand, K. Mullen, H. W. Spiess. An investigation of pi-pi packing in a columnar hexabenzocoronene by fast magic-angle spinning and double-quantum ^{1}H solid-state NMR spectroscopy. J. Am. Chem. Soc. 121, 6712-6718 (1999).

[Brown 00] S. P. Brown, I. Schnell, J. D. Brand, K. Mullen and H. W. Spiess. The competing effects of pp packing and hydrogen bonding in a hexabenzocoronene carboxylic acid derivative: A ^{1}H solid-state MAS NMR investigation. Phys. Chem. Chem. Phys., 2, 1735-1745 (2000).

[Brown 01] S. P. Brown, H. W. Spiess. Advanced Solid-state NMR Methods for the Elucidation of Structure and Dynamics of Molecular, Macromolecular and Supramolecular systems. Chem. Rev. 101, 4125–4155 (2001).

[Bruker 97] Bruker. Commercial MAS probeheads capable of $\omega r/2\pi$ = 35 kHz. Rapport technique, Bruker GMBH, Karlsruhr, Germany (1997).

[Brunner 98] E. Brunner, U. Sternberg. Solid-state NMR investigations on the nature of hydrogen bonds. Prog. Nuc. MAg. Res. Spec. 32, 21-57 (1998).

[Carravetta 00] M. Carravetta, M. Eden, X. Zhao, A. Brinkmann, M. H. Levitt. Symmetry Principles for the Design of Radiofrequency Pulse Sequences in the Nuclear Magnetic Resonance of Rotating Solids. Chem. Phys. Lett. 321, 205–215 (2000).

[Carette 01] L. Carrette, K. A. Friedrich, U. Stimming. Improvement of CO tolerance of proton exchange membrane (PEM) fuel cells by a pulsing technique. Fuel Cells 1, 5-39 (2001).

[Carr 53] H. Y. Carr, PhD Thesis, Harvard University, 1953.

[Celik 08] S. U. Celik, U. Akbey, R. Graf, A. Bozkurt, H. W. Spiess, Proton-Conducting Properties of Acid-Doped Poly(glycidyl methacrylate)-

1,2,4-Triazole Systems. Macromolecular Chemistry and Physics 209-6, 593 – 603 (2008).

[Chen 04] Z. Chen, M. G. Debije, T. Debaerdemaeker, P. Osswald and F. Würthner. Tetrachloro-substituted perylene bisimide dyes as promising n-type organic semiconductors: Studies on structural, electrochemical and charge transport properties. ChemPhysChem, 5, 137–140 (2004).

[Chu 08] P. P. Chu. In preparation.

[Colombon 92] P. Colomban (Ed). Proton Conductors: Solids, Membranes, and Gels - Materials and Devices; Cambridge University Press: Cambridge (1992).

[Davis 76] J. H. Davis, K. R. Jeffrey, M. Bloom, M. I. Valic, T. P. Higgs. Quadrupolar Echo Deuteron Magnetic Resonance Spectroscopy in Ordered Hydrocarbon Chains. Chem. Phys. Lett. 42, 390–394 (1976).

[de Greef 2008] T. F. A. de Greef and E. W. Meijer. Supramolecular Polymers Nature 453, 171-173 (2008).

[deAzavedo 99] E. R. deAzevedo, W.-G. Hu, T. J. Bonagamba, K. Schmidt-Rohr. Centerband-Only Detection of Exchange: Efficient Analysis of Dynamics in Solids by NMR. J. Am.Chem. Soc. 121, 8411–8412 (1999).

[Debije 05] M. G. Debije, Z. Chen, J. Piris, R. B. Neder, M. M. Watson, K. Mullen, F. Wurthner. Dramatic increase in charge carrier lifetime in a liquid crystalline perylene bisimide derivative upon bay substitution with chlorine. J. Mater. Chem. 15, 1270 –1276 (2005).

[Demitrakopoulos 02] C. D. Dimitrakopoulos and P. R. L. Malenfant. Organic thin film transistors for large area electronics. Adv. Mater.14-2, 99–117 (2002).

[DeSchryver 05] F. C. De Schryver, T. Vosch, M. Cotlet, M. van der Auweraer, K. M;llen, J. Hofkens. Energy dissipation in multichromophoric single dendrimers. Acc. Chem. Res. 38, 514 – 522 (2005).

[Dessiraju 89] G. R. Dessiraju. Crystal Engineering: The design of organic solids; Elsevier: Amsterdam, (1989).

[Detken 02] A. Detken, E. H. Hardy, M. Ernst, B. H. Meier. Simple and Efficient Decoupling in Magic-angle Spinning Solid-state NMR: the XiX Scheme. Chem. Phys. Lett. 356, 298–304 (2002).

[Dixon 82]	W. T. Dixon. NMR Spectra in Spinning Samples (TOSS). J. Chem. Phys. 77, 1800–1809 (1982).
[Dong 97]	J. Dong, Y. Ozaki, K. Nakashima. Infrared, Raman, and Near-Infrared Spectroscopic Evidence for the Coexistence of Various Hydrogen-Bond Forms in Poly(acrylic acid). Macromolecules 30, 1111-1117 (1997).
[Dresselhaus 81]	M. S. Dresselhaus, G. Dresselhaus. Intercalation Compounds of Graphite. Adv. Phys. 31, 139-326 (1981).
[Duer 04]	M. J. Duer, Introduction to Solid State NMR Spectroscopy, Blackwell Publishing, Oxford, (2004).
[Dusold 00]	S. Dusold, A. Sebald. Dipolar Recoupling under Magic-Angle Spinning Conditions. In Annual reports on NMR spectroscopy, Volume 41, pp. 185–264. Academic Press (2000).
[Eden 99]	M. Eden, M. H. Levitt, Pulse sequence symmetries in the nuclear magnetic resonance of spinning solids: Application to heteronuclear decoupling. J. of Chem. Phy. 111, 1511-1519, (1999).
[Ernst 87]	R. R. Ernst, G. Bodenhausen, A. Wokaun. Principles of Nuclear Magnetic Resonance in One and Two Dimensions. Clarendon Press, Oxford (1987).
[Ernst 01]	M. Ernst, A. Samoson, B. H. Meier. Low-power Decoupling in Fast Magic-angle Spinning NMR. Chem. Phys. Lett. 348, 293–302 (2001).
[Ernst 03]	M. Ernst. Heteronuclear Spin Decoupling in Solid-state NMR under Magic-angle Sample Spinning. J. Magn. Reson. 162, 1–34 (2003).
[Feike 96]	M. Feike, D. E. Demco, R. Graf, J. Gottwald, S. Hafner, H. W. Spiess. Broadband Multiple-Quantum NMR Spectroscopy. J. Magn. Reson. A 122, 214–221 (1996).
[Fischbach 03]	I. Fischbach, PhD Thesis, Mainz University (2003).
[Fischbach 04]	I. Fischbach, H. W. Spiess, K. Saalwa1chter, G. R. Goward. Solid state NMR spectroscopic investigations of model compounds for imidazole-based proton conductors. J. Phys. Chem. B 108, 18500-18508 (2004).
[Fischbach 04b]	I. Fischbach, F. Ebert, H. W. Spiess, I. Schnell. Rotor Modulations and Recoupling Strategies in 13C Solid-State Magic-Angle-Spinning NMR Spectroscopy: Probing Molecular Orientation and Dynamics. ChemPhysChem 5, 895-908 (2004).

[Friedrich 98] U. Friedrich, I. Schnell, S. P. Brown, A. Lupulescu, D. E. Demco, H. W. Spiess. Spinning-sideband patterns in multiple-quantum magicangle spinning NMR spectroscopy. Mol. Phys. 95, 1209–1227 (1998).

[Fontanella 93] J. J. Fontanella, Mclin, M. G.; Wintersgill, M. C. Electric-Impedance Studies of Acid Form Nafion Membranes. Solid State Ionics 66, 1-4 (1993).

[Fung 00] B. M. Fung, A. K. Kithrin, K. Ermolaev. An Improved Broadband Decoupling Sequence for Liquid Crystals and Solids. J. Magn. Res. 142, 97–101 (2000).

[Gan 97] Z. Gan, R. R. Ernst. Frequency- and Phase-modulated Heteronuclear Decoupling in Rotating Solids. Solid State Nucl. Magn. Res. 8, 153–159 (1997).

[Gaussian 03] Gaussian 03, Revision D.02, M. J. Frisch, G. W. Trucks, H. B. Schlegel, G. E. Scuseria, M. A. Robb, J. R. Cheeseman, J. A. Montgomery, Jr., T. Vreven, K. N. Kudin, J. C. Burant, J. M. Millam, S. S. Iyengar, J. Tomasi, V. Barone, B. Mennucci, M. Cossi, G. Scalmani, N. Rega, G. A. Petersson, H. Nakatsuji, M. Hada, M. Ehara, K. Toyota, R. Fukuda, J. Hasegawa, M. Ishida, T. Nakajima, Y. Honda, O. Kitao, H. Nakai, M. Klene, X. Li, J. E. Knox, H. P. Hratchian, J. B. Cross, V. Bakken, C. Adamo, J. Jaramillo, R. Gomperts, R. E. Stratmann, O. Yazyev, A. J. Austin, R. Cammi, C. Pomelli, J. W. Ochterski, P. Y. Ayala, K. Morokuma, G. A. Voth, P. Salvador, J. J. Dannenberg, V. G. Zakrzewski, S. Dapprich, A. D. Daniels, M. C. Strain, O. Farkas, D. K. Malick, A. D. Rabuck, K. Raghavachari, J. B. Foresman, J. V. Ortiz, Q. Cui, A. G. Baboul, S. Clifford, J. Cioslowski, B. B. Stefanov, G. Liu, A. Liashenko, P. Piskorz, I. Komaromi, R. L. Martin, D. J. Fox, T. Keith, M. A. Al-Laham, C. Y. Peng, A. Nanayakkara, M. Challacombe, P. M. W. Gill, B. Johnson, W. Chen, M. W. Wong, C. Gonzalez, and J. A. Pople, Gaussian, Inc., Wallingford CT, 2004.

[Gebel 97] G. Gebel, J. Lambard. Small-angle scattering study of water-swollen perfluorinated ionomer membranes. Macromolecules 30, 7914-7920 (1997).

[Geen 94] H. Geen, J.J. Titman, J. Gottwald, H.W. Spiess. Solid-state proton multiplequantum NMR spectroscopy with fast magic angle spinning. Chem. Phys. Lett. 227, 79–86 (1994).

[Geen 95] H. Geen, J. J. Titman, J. Gottwald, H.W. Spiess. Spinning Sidebands in the Fast-MAS Multiple-Quantum Spectra of Protons in Solids. J. Magn. Reson. A 114, 264–267 (1995).

[Gottwald 95] J. Gottwald, D. E. Demco, R. Graf, H. W. Spiess. High-Resolution Double-Quantum NMR-Spectroscopy of Homonuclear Spin Pairs and Proton Connectivities in Solids. Chem. Phys. Lett. 243, 314-323 (1995).

[Goward 01] G. R. Goward, I. Schnell, S. P. Brown, H. W. Spiess, H. D. Kim, H. Ishida. Investigation of an N· · ·H hydrogen bond in a solid benzoxazine dimer by 1H–15N NMR correlation techniques under fast magic-angle spinning. Magn. Reson. Chem. 39: S5–S17 (2001).

[Goward 02] G. R. Goward, M. F. H. Schuster, D. Sebastiani, I. Schnell, H. W. Spiess. High-resolution solid-state NMR studies of imidazole-based proton conductors: Structure motifs and chemical exchange from H-1 NMR. J. Phys. Chem. B 106, 9322-9334 (2002).

[Graf 98a] R. Graf. Hochauflosende Doppelquanten-NMR-Spektroskopie an amorphen Polymeren. Dissertation, Universitat Mainz (1998).

[Granados-Focil 07] S. Granados-Focil, R. C. Woudenberg, O Yavuzcetin, M. T. Tuominen, E. B Coughlin. Water-Free Proton-Conducting Polysiloxanes: A Study on the Effect of Heterocycle Structure. Macromolecules 40, 8708-8713 (2007).

[Graser 80] F. Graser and E. Hädicke. Crystal-Structure and Color of Perylene-3,4-9,10-Bis(Dicarboximide) Pigments. Ann. Chem. 1994–2011 (1980).

[Gregory 95] D. M. Gregory, D. J. Mitchell, J. A. Stringer, S. Kiihne, J. C. Shiels, J. Callahan, M. A. Mehta, G. P. Drobny. Windowless Dipolar Recoupling- The Detection of Weak Dipolar Couplings Between Spin-1/2 Nuclei with Large Chemical-Shift Anisotropies. Chem Phys Lett. 246: 654–663 (1995).

[Gullion 89a] T. Gullion, J. Schaefer. Detection of Weak Heteronuclear Dipolar Coupling by Rotational-Echo Double-Resonance Nuclear Magnetic Resonance. Adv. Magn. Reson.13, 57–83 (1989).

[Gullion 89b] T. Gullion, J. Schaefer. Rotational-Echo Double-Resonance NMR. J. Magn. Reson. 81, 196–200 (1989).

[Gullion 90] T. Gullion, D. B. Baker, M. S. Conradi. New, Compensated Carr-Purcell Sequences. J. Magn. Reson. 89, 479–484 (1990).

[Gullion 97] T. Gullion. Measurement of Heteronuclear Dipolar Interactions by Rotational-Echo, Double-Resonance Nuclear Magnetic Resonance. Magn. Reson. Rev. 17, 83–131 (1997).

[Gunday 06] Gunday S. T.; Bozkurt A.;, Meyer W.M.; Wegner G. Effects of different acid functional groups on proton conductivity of polymer-1,2,4-triazole blends. J. of Poly. Sci. Part B: Poly. Phys. 44, 3315-3322 (2006).

[Haeberlen 76] U. Haeberlen, High Resolution NMR in Solids, Academic Press, New York, (1976)

[Hahn 50] E. L. Hahn. Spin Echoes. Phys. Rev. 80, 580–594 (1950).

[Hafner 98] S. Hafner, H. W. Spiess, Advanced Solid-State NMR Spectroscopy of Strongly Dipolar Coupled Spins Under Fast Magic Angle Spinning. Conc. In Magn. Reson. 10, 99-128, (1998).

[Haile 97] S. M. Haile, P. M. Calkins and D. Boysen Superprotonic conductivity in β-Cs3(HSO4)2(Hx(P,S)O4) Solid State Ionics, 97, 1-4, 145-151(1997)

[Haile 98] S. M. Haile, P. M. Calkins and D. Boysen. Structure and Vibrational Spectrum of β-$Cs_3(HSO_4)_2[H_2-x(P_{1-x},S_x)O_4](x \sim 0.5)$, a New Superprotonic Conductor, and a Comparison with α-$Cs_3(HSO_4)_2(H_2PO_4)$. Journal of Solid State Chemistry,139, 2, 373-387, (1998).

[Hamilton 98] W. C. Hamilton, J. A. Ibers. Hydrogen Bonding in Solids; Benjamin: New York (1968).

[Harris 88] R. K. Harris, P. Jackson, L. H. Merwin, B. J. Say, G. Hagele. Perspectives in High-resolution Solid-state Nuclear Magnetic Resonance, with Emphasis on Combined Rotation and Multiple-pulse

Spectroscopy. Chem. Soc. Faraday Trans. I. 84(11), 3649-3672 (1988).

[Harris 94] R. K. Harris, Nuclear Magnetic Resonance Spectroscopy, A Physicochemical View, Pitman, London (1994).

[Hartmann 62] S. R. Hartmann, E. L. Hahn. Nuclear Double Resonance in Rotating Frame. Phys. Rev. 128, 2042 (1962).

[Helmer-Metzmann 93] F. Helmer-Metzmann. EP 0 574 791 A2, Hoechst AG (1993).

[Herbst 97] W. Herbst and K. Hunger, Industrial Organic Pigments: Production, Properties, Applications, 2nd edn., WILEY-VCH, Weinheim (1997).

[Herzfeld 80a] J. Herzfeld, A. E. Berger. Sideband Intensities in NMR Spectra of Samples Spinning at the Magic Angle. J. Chem. Phys. 73, 6021–6030 (1980).

[Herzfeld 80b] J. Herzfeld, X. Chen, Sideband analysis in magic angle spinning NMR of solids, in: D.M. Grant, R.K. Harris (Eds.), Encyclopedia of Nuclear Magnetic Resonance, Wiley, Chichester, (1996).

[Hill 04] J. P. Hill, W. Jin, A. Kosaka, T. Fukushima, H. Ichihara, T. Shimomura, K. Ito, T. Hashizume, N. Ishii, T. Aida. Self-assembled hexa-peri-hexabenzocoronene graphitic nanotube. Science 304, 1481 – 1483 (2004).

[Hing 92] A. W. Hing, S. Vega, J. Schaefer. Transferred-Echo Double-Resonance NMR. J. Magn. Reson. 96, 205–209 (1992).

[Hologne 04] M Hologne, J Hirschinger. Molecular dynamics as studied by static-powder and magic-angle spinning H-2 NMR. Solid State Nuclear Magnetic Resonance 26, 1–10 (2004).

[Hong 00] M. Hong. Solid-state NMR Determination of 13Cα Chemical Shift Anisotropies for the Identification of Protein Secondary Structure. J. Am. Chem. Soc. 122, 3762–3770 (2000).

[Hong 05] L. Q. Hong, L. Qi-zhi, Y. Zheng-long. A new anhydrous proton conducting material based on phosphoric acid doped polyimide. European Polymer Journal 41, 2505 –2510 (2005).

[Honma 99] I. Honma, S. Hirakawa, K. Yamada, J. M. Bae. Synthesis of Organic/Inorganic Nanocomposites Protonic Conducting Membrane Through Sol-Gel Processes. Solid State Ionics 118, 29-36, (1999).

[Hughes 04] C. E. Hughes, S. Haufe, B. Angerstein, R. Kalim, U. Malhr, A. Reiche, M. Baldus. Probing Structure and Dynamics in Poly[2,2-(m-phenylene)-5,5□-bibenzimidazole] Fuel Cells with Magic-Angle Spinning NMR. J. Phys. Chem. B 108, 13626-13631 (2004).

[Hutter 95] J. Hutter, P. Ballone, M. Bernasconi, P. Focher, E. Fois, S. Goedecher, M. Parrinello, M. Tucherman. CPMD Computer Code (1995).

[Jaroniec 00] C. P. Jaroniec, B. A. Tounge, C.M. Riestra, J. Herzfeld, R. G. Griffin. Recoupling of Heteronuclear Dipolar Interactions with Rotational-Echo Double-Resonance at High Magic-Angle Spinning Frequencies. J. Magn. Reson. 146, 132–139 (2000).

[Jeffrey 86] G. A. Jeffrey, Y. Yeon, The Correlation Between Hydrogen-Bond Lengths and Proton Chemical-Shifts in Crystals, Acta Crys. B Strc. Sci. 42: 410-413, (1986).

[Kaltbeitzel 07] A. Kaltbeitzel, S. Schauff, H. Steininger, B. Bingöl, G. Brunklaus, W. H. Meyer, H. W. Spiess. Water sorption of poly(vinylphosphonic acid) and its influence on proton conductivity. Solid State Ionics 178, 469 (2007).

[Kerres 96] J. Kerres, G. Eigenberger, D. Bevers, W. Schnurnberger, A. Fischer, H. Wendt, "Hydrogen Energy", Proceedings of the 11th Hydrogen Conference, T. N. Veziroglu, C. J. Winter, J. P. Baselt, G. Kreysa, 23-28, 1951, Stuttgart, Germany, (1996).

[Kerres 99] J. Kerres, A. Ullrich, F. Meier, T. Haring. Synthesis and Characterization of Novel Acid-Base Polymer Blends for Application in Membrane Fuel Cells. Solid State Ionics 125, 243-249 (1999).

[Kim 07] J. D. Kim, T. Mori, S. Hayashi, I. Honma. Anhydrous proton-conducting properties of Nafion-1,2,4-triazole and Nafion-benzimidazole membranes for polymer electrolyte fuel cells. J. Electrochem. Soc. 154, A290-A294 (2007).

[Kimura 00] H. Kimura, A. Shoji, H. Sugisawa, K. Deguchi, A. Naito, H. Saito. Determination of N-H Bond Lengths of 15N-Labeled Poly(L-alanines) by 1H CRAMPS NMR. Macromolecules 33, 6627-6629 (2000).

[Kraft 98] A. Kraft, A. C. Grimsdale, A. B. Holmes. Electroluminescent conjugated polymers - Seeing polymers in a new light. Angew. Chem. Int. Ed. 37, 402 –428 (1998).

[Kranig 90]	W. Kranig, C. Boeffel, H. W. Spiess. H-2 NMR-Studies of Molecular Motions and Alignment Process of Discotic Liquid-Crystalline compounds Based on Substituted Triphenylenes. Macromolecules 23, 4061-4067 (1990).
[Kreuer 82]	K. D. Kreuer, A. Rabenau, W. Weppner, Vehicle mechanism, a new model for the interpretation of the conductivity of fast proton conductors. Angew. Chem. Int. Ed. Engl. 21, 208 (1982).
[Kreuer 96]	K. D. Kreuer. Proton conductivity: Materials and applications. Chem. Mater. 8, 610-641 (1996).
[Kreuer 97]	K. D. Kreuer. On the development of proton conducting materials for technological applications. Solid State Ionics 97, 1-15 (1997).
[Kreuer 98]	K. D. Kreuer, A. Fuchs, M. Ise, M. Spaeth, J. Maier. Imidazole and Pyrazole Based Proton Conducting Polymers and Liquids. Electrochimica Acta 43, 1281-1288 (1998).
[Langer 99]	B. Langer, I. Schnell, H. W. Spiess, A. R. Grimmer. Temperature calibration under ultrafast MAS conditions. J. Magn Reson. 138, 182 (1999).
[Lassegues 89]	C. J. Lassegues, B. Desbat, O. Trinquet, F. Cruege, C. Poinsignon. From Model Solid-State Protonic Conductors to New Polymer Electrolytes. Solid State Ionics, 35, 17-25, (1989).
[Lassegues 92]	C. J. Lassegues, P. Colomban. Proton Conductors: Solids, Membranes and Gels - Materials and Devices, Cambridge University Press, Cambridge (1992).
[Lee 95]	Y. K. Lee, N. D. Kurur, M. Helmle, O. G. Johannessen, N. C. Nielsen, M. H. Levitt. Efficient Dipolar Recoupling in the NMR of Rotating Solids. A Sevenfold Symmetric Radiofrequency Pulse Sequence. Chem. Phys. Lett. 242, 304–309 (1995).
[Lee 05]	S. Y. Lee, G. Scharfenberger, W. H. Meyer, G. Wegner. A novel water-free proton-conducting solid electrolyte based on an organic/inorganic hybrid. Adv. Mater. 17, 626 (2005).
[Lee 07]	Y. J. Lee, B. Bingol, T. Murakhtina, D. Sebastiani, W. H. Meyer, G. Wegner, H. W. Spiess. High-resolution solid-state NMR studies of poly(vinyl phosphonic acid) proton-conducting polymer: Molecular

structure and proton dynamics. J. Phys. Chem. B 111, 9711-9721 2007).

[Lehn 95] J. M. Lehn. Supramolecular Chemistry. VCH, Weinheim (1995).

[Linkous 93] C. A. Linkous. Development of Solid Polymer Electrolytes for Water Electrolysis at Intermediate Temperatures. Int. J. Hydrogen Energy 18(8),641-646 (1993).

[Lowe 59] I. J. Lowe. Free Induction Decays of Rotating Solids. Phys. Rev. Lett. 2, 285–287 (1959).

[Macho 01] V. Macho, L. Brombacher, H.W. Spiess. The NMR-WEBLAB: an Internet Approach to NMR Lineshape Analysis. Appl. Magn. Res. 20, 405–432 (2001).

[Makhija 90] S. Makhija, E. M. Pearce, T. K. Kwei, F. Liu. Miscibility Studies in Blnds of Polybenzimidazoles and Poly(4-vinyl pyridine). Polymer Eng Sci. 30, 798-801 (1990).

[Maricq 79] M. M. Maricq, J. S. Waugh. NMR in Rotating Solids. J. Chem. Phys. 70, 3300–3316 (1979).

[Marion 83] D. Marion, K. Wuthrich. Application of Phase Sensitive Two-dimensional Correlated Spectroscopy (COSY) for Measurements of H-1 H-1 Spin-spin Coupling constants in Proteins. Biochem. Biophys. Res. Commun. 113, 967–974 (1983).

[Marion 89] D. Marion, M. Ikura, R. Tschudin, A. Bax. Rapid Recording of 2D NMR-Spectra without Phase Cycling- Application to the Study of Hydrogen-Exchange in Proteins. J. Magn. Res. 85, 393–399 (1989).

[Massiot 02] D. Massiot, F. Fayon, M. Capron, I. King, S. Le Calvé, B. Alonso, J. O. Durand, B. Bujoli, Z. Gan, G. Hoatson. Modelling one- and two-dimensional solid-state NMR spectra. Magn. Reson. Chem. 4, 70 (2002).

[Mauritz 04] K. A. Mauritz, R. B. Moore. State of Understanding of Nafion . Chem. Rev. 104, 4535 (2004).

[McDermott 95] G. McDermott, S. M. Prince, A. A. Freer, A. M. Hawthornthwaite-Lawless, M. Z. Papiz, R. J. Cogdell and N. W. Isaacs. Crystal-Structure of an Integral Membrane Light-Harvesting Complex from Photosynthesis Bacteria. Nature 374, 517 (1995).

[McQuade 97] D. T. McQuade, S. L. McKay, D. R. Powell, S. H. Gellman. Indifference to hydrogen bonding in a family of secondary amides. J.Am. Chem. Soc. 119, 8528-8532 (1997).

[Mehring 83] M. Mehring. High Resolution NMR of Solids. Springer-Verlag, Berlin (1983).

[Metz 94] G. Metz, X. Wu, S. O. Smith. Ramped-Amplitude Cross Polarization in Magic-Angle-Spinning NMR. J. Magn. Reson. A 110, 219–227 (1994).

[Mingos 04] D. M. P. Mingos. Supramolecular Assembly via Hydrogen Bonds 1. Springer, Germany (2004).

[Munch 01] W. Munch, K. D. Kreuer, W. Silvestri, J. Maier, G. Seifert. The diffusion mechanism of an excess proton in imidazole molecule chains: first results of an ab initio molecular dynamics study. Solid State Ionics 145, 437-443 (2001).

[Munowitz 87] M. Munowitz, A. Pines. Principles and Applications of Multiple-Quantum NMR. Adv. Chem. Phys. 66, 1–152 (1987).

[Nielsen 94] N. C. Nielsen, H. Bildsoe, H. J. Jakobsen, M. H. Levitt. Double-Quantum Homonuclear Rotary Resonance – Efficient Dipolar Recovery in Magic-Angle Spinning NMR. J. Chem. Phys. 101-3: 1805– 1812 (1994).

[OTNeil 92] M. P. OTNeil, M. P. Niemczyk, W. A. Svec, D. Gosztola, G. L. Gaines III, M. R. Wasielewski. Picosecond Optical Switching Based on Biphotonic Excitation of an Electron Donor-Acceptor-Donor Molecule. Science 257, 63 –65 (1992).

[Pake 48] G. E. Pake. Nuclear Resonance Absorption in Hydrated Crystals: Fine Structure of the Proton Line. J. Chem. Phys. 16, 327–336 (1948).

[Pan 05] J. Pan, W. Zhu, S. Li, W. Zeng, Y. Cao, H. Tian. Dendron-functionalized perylene diimides with carrier-transporting ability for red luminescent materials. Polymer 46, 7658 –7669 (2005).

[Parkinson 07] M. J. Parkinson, PhD Thesis, Imperial College, (2007).

[Pena 04] E. Dıez-Pena, I. Quijada-Garrido, J. M. Barrales-Rienda, I. Schnell, H. W. Spiess. Advanced 1H Solid-State NMR Spectroscopy on Hydrogels. The Effect of Hydrogen Bonding in the Collapse of

Poly(methacrylic acid) (PMAA) Hydrogels. Macromol. Chem. Phys. 205, 430–437 (2004).

[Percec 02] V. Percec, M. Clodde, T. K. Bera, Y. Miura, I. Shiyanovskaya, K. D. Singer, V. S. K. Balagurusamy, P. A. Heiney, I. Schnell, A. Rapp, H. W. Spiess, S. D. Hudson, H. Duan. Self-organization of supramolecular helical dendrimers into complex electronic materials. Nature 419, 384-387 (2002).

[Percec 08] In preparation.

[Philp 96] D. Philp, J. F. Stoddart. Self-assembly in natural and unnatural systems. Angew. Chem., Int. Ed. Engl. 35, 1155-1196 (1996).

[Pines 73] A. Pines, M. G. Gibby, J. S. Waugh. Proton-enhanced NMR of Dilute Spins in Solids. J. Chem. Phys. 59, 569–590 (1973).

[Pisula 06] W. Pisula, M. Kastler, D. Wasserfallen, J. W. F. Robertson, F. Nolde, C. Kohl, K. Mullen. Pronounced supramolecular order in discotic donor-acceptor mixtures. Angew. Chem., Int. Ed. Engl. 45-5, 819-823 (2006).

[Pourcelly 90] G. Pourcelly, A. Oikonomou, H.D. Hurwitz, C. Gavach. Influence of the Water-Content on the Kinetics of Counterion Transport in Perfluorosulfonic Membranes. J. Electroanal. Chem. 287, 43-59, (1990).

[Powles 63] J. G. Powles, J. H. Strange. Zero Time Resolution Nuclear Magnetic Transients in Solids. Proc. Phys. Soc. Lond. 82, 60 (1963).

[Prodi 05] A. Prodi, C. Chiorboli, F. Scandola, E. Iengo, E. Alessio, R. Dobrawa, F. Wurthner. Wavelength-Dependent Electron and Energy Transfer Pathways in a Side-to-Face Ruthenium Porphyrin/Perylene Bisimide Assembly. J. Am. Chem. Soc. 127, 1454 –1462 (2005).

[Pu 03] H. Pu. Polymer Int. Studies on polybenzimidazole/poly (4-vinylpyridine) blends and their proton conductivity after doping with acid. 52-9, 1540-1545 (2003).

[Pu 07] H. Pu, S. Ye, D. Wang. Anhydrous proton conductivity of acid doped vinyltriazole-based polymers. Electrochimica Acta 52, 5879-5883 (2007).

[Purcell 46] E. M. Purcell, H. C. Torrey, R. V. Pound. Resonance Absorption by Nuclear Magnetic Moments in Solids. Phys. Rev. 69, 37–38 (1946).

[Rapp 03] Almut Rapp, Ingo Schnell, Daniel Sebastiani, Steven P. Brown, Virgil Percec, Hans Wolfgang Spiess. Supramolecular Assembly of Dendritic Polymers Elucidated by ^{1}H and ^{13}C Solid-State MAS NMR Spectroscopy. J. Am. Chem. Soc. 125, 13284–13297 (2003).

[Rose 57] M. E. Rose. Elementary Theory of Angular Momentum. Wiley, London (1957).

[Saalwachter 01a] K. Saalwachter, R. Graf, H. W. Spiess. Recoupled Polarization-Transfer Methods for Solid-State ^{1}H-^{13}C Heteronuclear Correlation in the Limit of Fast MAS. J. Magn. Reson. 148, 398–418 (2001).

[Saalwachter 01b] K. Saalwachter, H. W. Spiess. Heteronuclear ^{1}H-^{13}C Multiple-spin Correlation in Solid-state Nuclear Magnetic Resonance: Combining Rotationalecho Double-resonance Recoupling and Multiple-quantum Spectroscopy. J. Chem. Phys. 114, 5707–5728 (2001).

[Saalwachter 02] K. Saalwachter, I. Schnell. REDOR-based Heteronuclear Dipolar Correlation Experiments in Multi-spin Systems: Rotor-encoding, Directing and Multiple Distance and Angle Determination. Solid State Nucl. Magn. Res. 22, 154–187 (2002).

[Sakurai 85] J. J. Sakurai, Modern Quantum Mechanics, Addison-Wesley, New York (1995).

[Samoson 03] A. Samoson, T. Tuherm. High performance MAS (2003). Poster contribution at the ENC (2003).

[Samoson 04] A. Samoson, T. Tuherm, J. Past, A. Reinhold, T. Anupold, I. Heinmaa. New Horizons for Magic-Angle Spinning NMR. Topics in Current Chemistry 246, 15–31 (2004).

[Sautter 05] A. Sautter, B. K. Kaletas, D. G. Schmid, R. Dobrawa, M. Zimine, G. Jung, I. H. M. Van Stokkum, L. De Cola, R. M. Williams, F. Wurthner. Ultrafast Energy-Electron Transfer Cascade in a Multichromophoric Light-Harvesting Molecular Square. J. Am. Chem. Soc. 127, 6719 –6729 (2005).

[Schaefer 76] J. Schaefer, E. O. Stejskal. C-13 Nuclear Magnetic-Resonance of Polymers Spinning at Magic Angle. JACS, 98, 1031-1032, (1976).

[Schleyer 96] P.v.R. Schleyer, C Maerker, A Dransfeld, H Jiao, N.J.R.v.E. Hommes. Nucleus Independent chemical shifts: A simple and efficient aromaticity probe. J. Am. Chem. Soc. 118, 6317–6318 (1996).

[Schmidt 06] J. Schmidt, A. Hoffmann, H. W. Spiess, D. Sebastiani. Bulk Chemical Shifts in Hydrogen-Bonded Systems from First-Principles Calculations and Solid-State-NMR. J. Phys.Chem. B. 110, 46, 23205-23210 (2006).

[Schmidt-Mende 01] L. Schmidt-Mende, A. Fechtenkçtter, K. Mullen, E. Moons, R. H. Friend, J. D. MacKenzie. Self-organized discotic liquid crystals for high-efficiency organic photovoltaics. Science 293, 1119 – 1122 (2001).

[Schmidt-Rohr 94] K. Schmidt-Rohr, H. W. Spiess. Multidimensional Solid-State NMR and Polymers. Academic Press, London (1994).

[Schnell 98] I. Schnell, S. P. Brown, H. Y. Low, H. Ishida, H. W. Spiess. An Investigation of Hydrogen Bonding in Benzoxazine Dimers by Fast Magic-Angle Spinning and Double-Quantum 1H NMR Spectroscopy. J. Am. Chem. Soc. 120, 11784- 11795 (1998).

[Schnell 01a] I. Schnell, H. W. Spiess. Advances in Magnetic Resonance. High resolution 1H NMR Spectroscopy in the Solid State: Very Fast Sample Rotation and Multiple-quantum Coherences. J. Magn. Reson. 151, 153–227 (2001).

[Schnell 01b] I. Schnell, A. Watts, H. W. Spiess. Double-Quantum Double-Quantum MAS Exchange NMR Spectroscopy: Dipolar-Coupled Spin Pairs as Probes for Slow Molecular Dynamics. J. Magn. Reson. 149, 90–102 (2001).

[Schuster 01] M. Schuster, W. H. Meyer, G. Wegner, H. G. Herz,; M. Ise, M. Schuster, K. D. Kreuer, J. Maier. Proton mobility in oligomer-bound proton solvents: imidazole immobilization via flexible spacers. Solid State Ionics 145, 85- 92 (2001).

[Schuster 03] M. F. H. Schuster, W. H. Meyer. Anhydrous Prootn Conducting Polymers. Annu. Rev. Mater. Res. 33, 233-261 (2003).

[Sebastiani 05] D. Sebastiani. Current Densities and Nucleus-Independent Chemical Shift Maps from Reciprocal-Space Density Functional Perturbation Theory Calculations. ChemPhysChem 7-1, 164 – 175 (2005).

[Sebastiani 08] Personal communications.

[Sekharan 08] Personal communications.

[Serpico 02] J. M. Serpico, S. G. Ehrenberg, J. J. Fontanella, X. Jiao, D. Perahia, K. A. McGrady, E. H. Sanders, G. E. Kellogg, G. E. Wnek. Transport and

Structural Studies of Sulfonated Styrene-Ethylene Copolymer Membranes. Macromolecules 35, 5916-5921 (2002).

[Slichter 96] C. P. Slichter. Principles of Magnetic Resonance. Springer-Verlag, Berlin (1996).

[Smith 92] S. A. Smith, W. E. Palke, J. T. Gerig. The Hamiltonians of NMR. Concepts in Magn. Reson. 4, 107-144 (1992).

[Sorensen 83] O. W. Sorensen, G. W. Eich, M. H. Levitt, G. Bodenhausen, R. R. Ernst. Product Operator Formalism for the Description of NMR Pulse Experiments. Progr. NMR Spectrosc. 16, 163–192 (1983).

[Sommer 95] W. Sommer, J. Gottwald, D. E. Demco, H. W. Spiess. Dipolar Heteronuclear Multiple-Quantum NMR Spectroscopy in Rotating Solids. J. Magn. Reson. 113, 131-134 (1995).

[Spiess 78] H. W. Spiess. Rotation of Molecules and Nuclear Spin Relaxation. In P. Diehl, E. Fluck, R. Kosfeld (eds.), NMR Basic Principles and Progress, Volume 15, pp. 55–214. Springer-Verlag, Berlin (1978).

[Spiess 85] H. W. Spiess, Deuteron NMR – A New Tool for Studying Chain Mobility and Orientation in Polymers. Adv. in Poly. Sci. 66, Springer-Verlag Berlin (1985).

[Spiess 04] E D. Pena, I. Q. Garrido, J. M. B. Rienda, I. Schnell, H. W. Spiess. Advanced 1H Solid-State NMR Spectroscopy on Hydrogels-1: The Effect of Hydrogen Bonding in the Collapse of Poly(methacrylic acid) (PMAA) Hydrogels. Macromol. Chem. Phys., 205, 430–437, (2004).

[Stejskal 77] E. O. Stejskal, J. Schaefer, J. S. Waugh. Magic-Angle Spinning and Polarization Transfer in Proton-Enhanced NMR. J. of Magn. Reson. 28, 105-112 (1977).

[Steininger 07] H. Steininger, M. Schuster, K. D. Kreuer, A. Kaltbeitzel, B. Bingol, W. H. Meyer, S. Schauff, G. Brunklaus, J. Maier, H. W. Spiess. Intermediate temperature proton conductors for PEM fuel cells based on phosphonic acid as protogenic group: A progress report. Phys. Chem. Chem. Phys. 9, 1764-1773 (2007).

[Struijk 00] C. W. Struijk, A. B. Sieval, J. E. J. Dakhorst, M. Van Dijk, P. Kimkes, R. B. M. Koehorst, H. Donker, T. J. Schaafsma, S. J. Picken, A. M. van de Craats, J. M. Warman, H. Zuilhof and E. J. R. Sudhölter. Liquid

Crystalline Perylene Diimides: Architecture and Charge Carrier Mobilities. J. Am.Chem. Soc. 122, 11057–11066 (2000).

[Suwelack 80] D. Suwelack, W. P. Rothwell, J. S. Waugh. Low Molecular-Motion Detected in the NMR Spectra of Rotating Solids. J. Chem. Phys 1980. 73, 2559- 2569.

[Takahashi 76] T. Takahashi, S. Tanese, O. Yamamoto. Proton Conduction in Triethylenediamine-Sulfate and Hexamethylenetetraamine-Sulfate. Journal of Solid State Chemistry 17, 353-361, (1976).

[Tang 86] C. W. Tang. 2-Layer Organic Photovoltatic Cell. Appl. Phys. Lett. 48, 183–185 (1986).

[Tiitu 05] M. Tiitu, M. Torkkeli, R. Serimaa, T. Makela, O. T. Ikkela. Self-assembly and flow alignment of protonically conducting complexes of polystyrene-block-poly(4-vinylpyridine) diblock copolymer with phosphoric acid. Solid. State Ionics, 176, 1291-1299, (2005).

[Traer 06] J. W. Traer, E. Montoneri, A. Samoson, J. Past, T. Tuherm, G. R. Goward. Unraveling the Complex Hydrogen Bonding of a Dual-Functionality Proton Conductor Using Ultrafast Magic Angle Spinning NMR. Chem. Mater. 18, 4747-4754 (2006).

[Thrippleton 08] M J. Thrippleton, M Cutajar, S Wimperis. Magic angle spinning (MAS) NMR linewidths in the presence of solid-state dynamics. Chemical Physics Letters 452, 233–238 (2008).

[Tycko 89] R. Tycko, G. Dabbagh, P. A. Mirau. Determination of Chemical-Shift-Anisotropy Lineshapes in a Two-Dimensional Magic-Angle-Spinning NMR Experiment. J. Magn. Reson. 85, 265–274 (1989).

[Tycko 91] R. Tycko, G. Dabbagh, Double-Quantum Filtering in Magic-Angle Spinning NMR Spectroscopy: An Approach to Spectral Simplification and Molecular Structure Determination. JACS, 113, 9444-9448, (1991).

[Ungar 08] Personal communications.

[Unugur 08] S. Unugur, U. Akbey, R. Graf, A. Bozkurt, H. W. Spiess. Anhydrous proton-conducting properties of triazole–phosphonic acid copolymers: a combined study with MAS NMR. PCCP, DOI: 10.1039/b807659f (2008).

[van de Craats 1999] van de Craats AM, Warman JM, Fechtenkotter A, Brand JD, Harbison MA, Mullen K. Record charge carrier mobility in a room-temperature discotic liquid-crystalline derivative of hexabenzocoronene. Adv. Mat. 11-17, 1469-1472 (1999).

[van der Boom 02] T. van der Boom, R. T. Hayes, Y. Zhao, P. Bushard, E. A. Weiss, M. R. Wasielewski. Charge transport in photofunctional nanoparticles self-assembled from zinc 5,10,15,20-tetrakis (perylenediimide) porphyrin building blocks. J. Am. Chem. Soc. 124-32, 9582-9590 (2002).

[Vold 79] R. R. Vold. Nuclear magnetic relaxation in coupled spin systems. Prog. NMR Spect. 12, 79-133 (1979).

[Wang 96] J. T. Wang, R. F. Savinell, J. S. Wainright, M. Litt, H. Yu. A H2/O2 Fuel Cell Using Acid Doped Polybenzimidazole as Polymer Electrolyte. Electrochimica Acta. 41, 193-197, (1996).

[Wainright 95] J. S. Wainright, J. T. Wang, D. Weng, R. F. Savinell, M. J. Litt. Acid-Doped Polybenzimidazoles: A New Polymer Electrolyte. Electrochem. Soc. 142, L121-L123 (1995).

[Wainright 79] J. S. Wainright, J. T. Wang, D. Weng, R. F. Savinell, M. Litt, "Proton Conduction of the Membranes Based on the Poly(Benzimidazole)", Journal of Electrochemical Society, 142, 121-132 , (1995).

[Walker 99] M. Walker, K. M. Baumgaertner, M. Kaiser, J. Kerres, A. Ullrich, E. Raeuchle. Proton-conducting polymers with reduced methanol permeation. J. Appl. Polym. Sci. 74-1, 67-73 (1999).

[Waug 56] J. S. Waugh, R. W. Fessenden. Nuclear Resonance Spectra of Hydrocarbons: The Free Electron Model. J. Am. Chem. Soc. 79, 846 (1956).

[Wei 99] Y. Wei, A. E. McDermott, Effects of Hydrogen Bonding on ^{1}H Chemical Shifts. Modeling NMR Chemical Shifts, ACS Symposium Series 732, Edited by J. C. Facelli, A. C. deDios. 177-193, (1999).

[Weitekamp 82] D. P. Weitekamp, J. R. Garbow, A. Pines. Determination of Dipole Coupling Constants Using Heteronuclear Multiple Quantum NMR. J. Chem. Phys. 77, 2870–2883 (1982).

[Wurthner 00] Wurthner F. A. Sautter. Highly fluorescent and electroactive molecular squares containing perylene bisimide ligands. Chem. Commun. 445–446 (2000,).

[Wurthner 01] F. Würthner, C. Thalacker, S. Diele, C. Tschierske. Fluorescent J-type Aggregates and Thermotropic Columnar Mesophases of Perylene Bisimide Dyes. Chem. Eur. J. 7-10, 2245-2253 (2001).

[Wurthner 02] F. Würthner, A. Sautter, J. Schilling, J. Org. Chem., 67, 3037–3044 (2002).

[Wurthner 04] F. Wurthner. Perylene bisimide dyes as versatile building blocks for functional supramolecular architectures. Chem. Commun. 14, 1564–1579 (2004).

[Wurthner 06] F. Wurthner, R. Schmidt. Electronic and crystal engineering of acenes for solution-processible self-assembling organic semiconductors. ChemPhysChem 7, 793 – 797 (2006).

[Xing 02] B. Z. Xing, O. Savadogo. Development of Pt-alloy and Pt-metal oxide mixed anodes for direct acetal/oxygen polymer electrolyte membrane fuel cell (DAPEMFC). J. New Mat. Electrochem. Syst. 5-1, 9-13 (2002).

[Yamada 05] M. Yamada, I Honma. Proton conductivity of zwitterionic-type molecular solids under intermediate temperature and anhydrous conditions. Chem. Phys. Chem. 402, 324-328, (2005).

[Yamauchi 00] K. Yamauchi, S. Kuroki, K. Fujii, I. Ando. The amide proton NMR chemical shift and hydrogen-bonded structure of peptides and polypeptides in the solid state as studied by high-frequency solid-state H-1 NMR. Chem. Phys. Lett. 324, 435–439 (2000).

[Ye 06] G. Ye, N. Janzen, G. R. Goward. Solid-State NMR Study of Two Classic Proton Conducting Polymers: Nafion and Sulfonated Poly(ether ether ketone)s. Macromolecules 39, 3283-3290 (2006).

[Yeo 83] R. S. Yeo, J. C. McBreen. Ion Clustering and Proton Transport in Nafion Membranes and Its Applications as Solid Polymer Electrolyte. J. Electrochem. Soc. 130, 533-538 (1983).

[Yu 98] Y. Yu, B. M. Fung. An Efficient Broadband Decoupling Sequence for Liquid Crystals. J. Magn. Res. 130, 317–320 (1998).

[Yuan 05] C. H. Yuan, S. J. Tu, M. H. Gelb, M. D. Tsai. Unusual four-bond secondary H/D isotope effect supports a short-strong hydrogen bond between phospholipase A(2) and a transition state analogue inhibitor. Biochemistry, 44 -12, 4748-4754 (2005).

[Zhao 01] X. Zhao, M. Eden, M. H. Levitt. Recoupling of Heteronuclear Dipolar Interactions in Solid-state NMR Using Symmetry-based Pulse Sequences. Chem. Phys. Lett. 342, 353–361 (2001).

[Zhou 06] Z. Zhou, R. Liu, J. Wang, S. Li, M. Liu, J. L. Bredas. Intra and Intermolecular Proton Transfer in 1H(2H)-1,2,3-Triazole Based Systems. J. Phys. Chem. A,110-7, 2322-2324 (2006).

[Zollinger 03] H. Zollinger, Color Chemistry, 3rd edn., VCH, Weinheim (2003).

[Zugenmaier 00] P. Zugenmaier, J. Duff, T. L. Bluhm. Crystal and molecular structures of six differently with halogen substituted bis (benzylimido) perylene. Cryst. Res. Technol. 35-9, 1095–1115 (2000).